Germanium Doping of Aluminum-Containing Cubic Group III-Nitride Heterostructures

Dem Department Physik
der Universität Paderborn
zur Erlangung des akademischen Grades eines
Doktors der Naturwissenschaften
(Dr. rer. nat.)
vorgelegte

Dissertation

von

Michael Deppe

Paderborn, Juli 2020

Kurzfassung

Die Gruppe III-Nitride sind ein wichtiges Halbleitermaterialsystem mit vielen Anwendungen in der Optoelektronik und in der Leistungselektronik. Insbesondere für optoelektronische Anwendungen ist die metastabile Zinkblende-Phase eine vielversprechende Alternative zu der üblicherweise verwendeten Wurtzit-Phase, da hier Polarisationsfelder, die die Rekombinationseffizienz beeinträchtigen, nicht vorhanden sind. Die Herstellung der meisten Bauelemente erfordert eine präzise Kontrolle der p- und n-Typ-Dotierung. Für die n-Typ-Dotierung wird üblicherweise Si verwendet, das jedoch bei hohen Dotierungskonzentrationen für eine Zugverspannung sorgt und dadurch die Kristallqualität verschlechtert. Kürzlich wurde berichtet, dass Ge eine geeignete Alternative zu Si für die n-Typ-Dotierung von Nitriden in der Wurtzitstruktur ist. Hohe Donatorkonzentrationen konnten erreicht werden, ohne die strukturelle Qualität der Schichten zu beeinträchtigen.

In dieser Arbeit wird Ge als Donator für GaN und $Al_xGa_{1-x}N$ bis zu $x = 0{,}6$ in der Zinkblende-Struktur untersucht. Es wurden Ge- und Si dotierte GaN-Schichten mit Dotierkonzentrationen über mehrere Größenordnungen hergestellt und hinsichtlich ihrer optischen, strukturellen und elektrischen Eigenschaften untersucht. Die maximal erreichbaren freien Elektronenkonzentrationen liegen bei $3.7 \times 10^{20}\,\mathrm{cm}^{-3}$ bzw. $4.3 \times 10^{20}\,\mathrm{cm}^{-3}$ für die Ge- und Si-Dotierung. Die strukturelle Qualität von Ge- und Si-dotierten Schichten ist im Bereich des Dotierungsmaximums vergleichbar. Die Elektronenbeweglichkeiten bei höchster Dotierung sind im Rahmen der Messgenauigkeit ebenfalls vergleichbar für beide Dotieratome. Bei niedrigerer Dotierung sind die Beweglichkeiten in Ge-dotierten Schichten etwa $20\,\%$ höher als die in Si-dotierten Schichten. Der Einbau von Ge in Zinkblende-$Al_xGa_{1-x}N$ ist nahezu unabhängig von x, aber der unbeabsichtigte Einbau von Sauerstoff, der ebenfalls ein Donator ist, wird mit steigendem x verstärkt. Der Einbau von Ge verläuft proportional zur Dampfdruckkurve von Ge. Die maximal erreichte Donatorkonzentration in $Al_{0.25}Ga_{0.75}N$ beträgt $1.4 \times 10^{20}\,\mathrm{cm}^{-3}$, aber die Qualität der Schichten verschlechtert sich oberhalb von $3 \times 10^{19}\,\mathrm{cm}^{-3}$. Die optische Emission von Schichten mit $x > 0{,}25$ stammt von einem tiefen Defektniveau, welches $0.9\,\mathrm{eV}$ unterhalb der indirekten Bandlücke liegt. Dieses steht jedoch nicht mit dem Einbau von Ge im Zusammenhang. Die Wachstumsraten von GaN fallen bei hohen Dotierungsniveaus um bis zu $40\,\%$ ab, was höchstwahrscheinlich auf die Ansammlung von Dotierungsmaterial an der Probenoberfläche während des Wachstums zurückzuführen ist. Bei $Al_xGa_{1-x}N$-Schichten ist keine Reduktion der Wachstumsraten zu beobachten. Erste Ge-dotierte GaN/AlN-Übergitterstrukturen wurden hergestellt und hinsichtlich ihrer optischen Intersubbandabsorption im infraroten Spektralbereich untersucht. Die Strukturen sind von hoher Qualität und es konnte eine Intersubbandabsorption um $1.55\,\mu\mathrm{m}$ beobachtet werden. Es wurde zudem der Einfluss des Substrats auf das Absorptionsvermögen der Strukturen untersucht.

Abstract

The group III-nitrides are an important semiconductor material system with many applications in optoelectronics and power devices. Especially for optoelectronic applications, the metastable zinc blende phase is a promising alternative to the commonly employed wurtzite phase, as polarization fields which impair the recombination efficiency are absent here. The fabrication of most devices requires precise control of p- and n-type doping. For n-type doping mostly Si is used, which however introduces tensile strain at high doping concentrations and deteriorates the crystal quality. Recently, Ge was found to be a well-suited alternative to Si for n-type doping of wurtzite nitrides, which allows for high donor concentrations without impairing the structural quality.

In this work Ge is investigated as a donor in zinc blende GaN and $Al_xGa_{1-x}N$ up to $x = 0.6$. Ge- and Si-doped GaN layers with doping levels spanning over several orders of magnitude were fabricated and investigated regarding their optical, structural, and electrical properties. The maximum achievable free electron concentrations are $3.7 \times 10^{20}\,cm^{-3}$ and $4.3 \times 10^{20}\,cm^{-3}$ for Ge- and Si-doping, respectively. The structural quality of Ge- and Si-doped layers is comparable in the range of the doping limit. Electron mobilities are also comparable within measurement accuracy for highest doped layers using both dopants, and mobilities of Ge-doped layers are about $20\,\%$ higher than those of Si-doped layers for lower doping. The incorporation of Ge in zinc blende $Al_xGa_{1-x}N$ is found to be almost independent on x, but the unintentional incorporation of O, which acts as a donor as well, is enhanced with rising x. The incorporation of Ge proceeds proportionally to the vapor pressure curve of Ge. The maximum achieved donor concentration in $Al_{0.25}Ga_{0.75}N$ is $1.4 \times 10^{20}\,cm^{-3}$, but quality of the layers degrades when the doping level exceeds $3 \times 10^{19}\,cm^{-3}$. The optical emission of layers with $x \geq 0.25$ is found to originate from a deep defect level $0.9\,eV$ below the indirect band gap, which is however not related to the incorporation of Ge. Growth rates of GaN drop at high doping levels by up to $40\,\%$, most probably due to accumulation of dopant material at the sample surface during growth. The growth rate reduction is not observed for $Al_xGa_{1-x}N$ layers. First Ge-doped GaN/AlN superlattice structures were fabricated and investigated regarding optical intersubband absorption in the infrared spectral region. Structures are of high quality and intersubband absorption around $1.55\,\mu m$ could be observed. A study on the influence of the substrate on the absorption capabilities of the structures is presented.

Contents

Acronyms

Notation	Description
AFM	atomic force microscope
APB	antiphase boundary
APD	antiphase domain
BEP	beam equivalent pressure
BGR	band gap renormalization
BMS	Burstein-Moss shift
CV	capacitance-voltage
CVD	chemical vapor deposition
DFT	density functional therory
DHJ	double heterojunction
EDX	energy-dispersive X-ray spectroscopy
FWHM	full width at half maximum
HRXRD	high resolution X-ray diffraction
HV	high vaccum
HVPE	hydride vapor phase epitaxy
ISBT	intersubband transition
LED	light emitting diode
MBE	molecular beam epitaxy
MOVPE	metal organic vapor phase epitaxy
MQW	multiple quantum well
n.i.d.	not intentionally doped
PAMBE	plasma-assisted molecular beam epitaxy
PBN	pyrolytic boron nitride
PL	photoluminescence
PPC	persistent photoconductivity

Notation	Description
QCSE	quantum-confined Stark effect
QMS	quadrupole mass spectrometer
QW	quantum well
RHEED	reflection high-energy electron diffraction
RMS	root mean square
RSM	reciprocal space map
SEM	scanning electron microscope
SIMS	secondary ion mass spectrometry
SL	superlattice
TEM	transmission electron microscope
TOF-SIMS	time-of-flight secondary ion mass spectrometry
UHV	ultra high vaccum

List of Symbols

Notation	Description
a	lattice constant
d	quantum well thickness
E_D	donor binding energy
E_g	band gap
ε_r	relative permittivity
f	lattice mismatch
I_A	flux impinging on the substrate
k_B	Boltzmann constant
m_0	electron mass
m_e^*	effective electron mass
m_h^*	effective hole mass

Notation	Description
μ	sticking coefficient
n	free electron concentration
N_D	donor concentration
x	mole fraction

CHAPTER 1

Introduction

Group III-nitrides are nowadays used in many different areas due to their unique properties. By utilizing ternary compounds of AlN, GaN, and InN, the band gap can be varied over a large range, enabling to fabricate optoelectronic devices operating over the entire visible spectrum, as well as in the infrared and ultraviolet spectral range. Especially in the blue and ultraviolet spectral range, nitrides are without any alternative for fabricating devices like LEDs or lasers operating with high efficiency. Only progress in the development of group III-nitrides made the production of white LEDs possible, which are used in almost all lighting applications today. Although the band gap of ternaries containing In can be small enough to cover the infrared spectral range utilizing interband transitions, the efficiency of these structures would be poor due to several difficulties associated with the incorporation of In [1–3]. However, intersubband transitions within the conduction band of GaN-based quantum wells feature energies suited for infrared applications. Conceivable devices are for example quantum cascade lasers operating at high powers or at high frequencies [4, 5], or fast infrared detectors [6].

For the fabrication of nearly all semiconductor devices, precise control of p- and n-type doping is required. Especially for unipolar devices operating in the conduction band, in part high doping levels are required. The most commonly used donor for III-nitrides in their thermodynamically stable wurtzite phase is Si, which however impairs the structural quality of the semiconductor crystal at high doping concentrations [7]. Recently, Ge has found to be a well-suited alternative to Si in GaN and $Al_xGa_{1-x}N$, allowing to achieve high doping concentrations without introducing additional crystal defects [8–11].

One drawback of the wurtzite phase of nitrides is, that the recombination efficiency in heterostructures can be reduced due to spontaneous and piezoelectric polarization fields. There are several approaches to fabricate structures where these fields are absent, one of which is growing structures in the metastable zinc blende phase [12–14]. The zinc blende phase of the III-nitrides is significantly less investigated than the wurtzite phase. Regarding Ge doping hardly any experiments are reported. Thus, in this work Ge is investigated as an alternative to Si for n-type doping of zinc blende GaN and $Al_xGa_{1-x}N$, and first Ge-doped structures featuring intersubband transitions in the infrared spectral region are fabricated and characterized.

CHAPTER 2

Fundamentals

This work covers the growth by molecular beam epitaxy (MBE), doping and characterization of cubic group III-nitride layers and heterostructures. In this chapter first the basic properties of cubic GaN (c-GaN) and the ternary alloy cubic $Al_xGa_{1-x}N$ (c-$Al_xGa_{1-x}N$) are explained. Next, a description of the MBE growth principle itself is given. Finally, the physics of multiple quantum wells (MQWs) and superlattices (SLs) as well as their ability to absorb light via intersubband transitions (ISBTs) are treated.

2.1 Properties of group III nitrides

Group III nitrides are compounds that in equal shares consist of N and elements of the third main group (the boron group) of the periodic table of elements. More specifically, in semiconductor physics the term *group III nitrides* mostly refers to compounds containing In, Ga, and Al. The binary compounds are indium nitride (InN), gallium nitride (GaN), and aluminum nitride (AlN), but also ternary compounds such as $In_xGa_{1-x}N$ and $Al_xGa_{1-x}N$ or quaternaries like $In_xGa_yAl_{1-x-y}N$ can be prepared. In the case of ternaries and quaternaries, the metal elements sum up to the same quantity as the N atoms and their respective mole fractions are given by x (and if necessary y).

Group III nitrides can occur in the (hexagonal) *wurtzite*, (cubic) *zinc blende*, and *rock salt* crystalline structure [16, p. 1]. These structures are visualized by means of GaN in
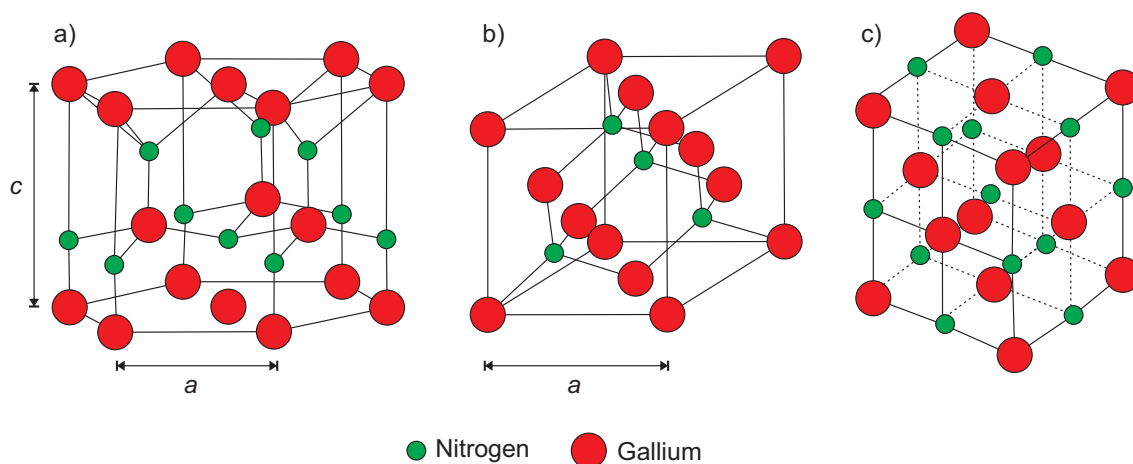

Figure 2.1: The three crystal structures of GaN. a) wurtzite (hexagonal); b) zinc blende (cubic); c) rock salt. After [15].

Figure 2.1. The only difference between the wurtzite and the zinc blende phase is the bond angle of the second nearest neighbor, resulting in a different stacking order. The wurtzite structure is characterized by a AaBb stacking sequence and is mirrored without in-plane rotation. In the zinc blende structure, the in-plane rotation between stacks is 60°, resulting in a AaBbCc stacking sequence [16, p. 4]. The following relations regarding equivalent directions of wurtzite and zinc blende crystals hold [17]:

$$[0001]_{\mathrm{wz}} \parallel [111]_{\mathrm{zb}}$$

$$[11\bar{2}0]_{\mathrm{wz}} \parallel [10\bar{1}]_{\mathrm{zb}}$$

$$[1\bar{1}00]_{\mathrm{wz}} \parallel [1\bar{2}1]_{\mathrm{zb}}$$

The thermodynamically stable phase of InN, GaN, and AlN is the wurtzite structure [16, pp. 1f], but in case a cubic substrate and adequate ambient conditions are provided also the metastable zinc blende phase (in the following referred to as *cubic* or, e.g., c-GaN) can be prepared by epitaxial growth. Due to the metastable nature of the cubic phase, the hexagonal phase still can form at defect sites [16, p. 2] or if the growth conditions are not met. The rock salt phase only forms under high pressures [16, p. 1] and is thus irrelevant for epitaxially grown layers.

The lattice constants of InN, GaN, and AlN in their hexagonal and cubic phase are listed in Table 2.1. With help of *Vegard's law* the lattice constant of ternary alloys can be estimated by linear interpolation [18, 19], e.g.:

$$a(\mathrm{Al}_x\mathrm{Ga}_{1-x}\mathrm{N}) = xa(\mathrm{AlN}) + (1-x)a(\mathrm{GaN}) \tag{2.1}$$

Due to the different crystalline structure, band gaps E_g of the hexagonal and cubic nitrides differ slightly. In general the band gaps of the cubic nitrides are slightly smaller. The values are listed in Table 2.1. InN, GaN, AlN, and their ternaries are direct semiconductors both in the hexagonal and cubic phase, except c-AlN and Al-containing cubic ternaries. In c-AlN, the direct $\Gamma_v \rightarrow \Gamma_c$ transition has an energy of 5.93 eV, while the indirect $\Gamma_v \rightarrow X_c$

Table 2.1: Lattice parameters a and c and direct band gaps E_g of the zinc blende (zb) and wurtzite (wz) group III nitrides at $T = 300$ K.

	InN	**GaN**	**AlN**
a_{zb}	5.01 Å [20]	4.503 Å [21]	4.373 Å [22]
a_{wz}	3.538 Å [16]	3.189 Å [16]	3.1106 Å [16]
c_{wz}	5.703 Å [16]	5.1864 Å [16]	4.9795 Å [16]
$E_{g,\mathrm{zb}}$	0.595 eV [20]	3.23 eV [23]	5.93 eV [24, 25] indirect: 5.3 eV [24, 25]
$E_{g,\mathrm{wz}}$	0.78 eV [16, 26]	3.42 eV [16]	6.03 eV [16]

has an energy of merely $5.3\,\text{eV}$. The transition between direct and indirect in c-Al$_x$Ga$_{1-x}$N is calculated to be between $x = 0.64$ and 0.69 by means of density functional therory (DFT) and is experimentally determined to occur at $x = 0.71$ [25]. For c-Al$_x$In$_{1-x}$N the transition is calculated to occur at $x = 0.24$ [27, 28].

To calculate the band gap of a ternary alloy, it can be interpolated between the values of the binary band gaps. However, linear interpolation is not sufficient in this case, thus the empirical *bowing parameter b* is introduced to account for a parabolic contribution [16, p. 90]:

$$E_g(\text{Al}_x\text{Ga}_{1-x}\text{N}) = xE_g(\text{AlN}) + (1-x)E_g(\text{GaN}) - bx(1-x) \tag{2.2}$$

In case of c-Al$_x$Ga$_{1-x}$N, the bowing parameters are $b = 0.85$ for the direct and $b = 0.01$ for the indirect transition [25].

An overview of the band gaps E_g versus the lattice constant a of all wurtzite and zinc blende ternaries is displayed in Figure 2.2. Additionally, also values of plenty other common III-V semiconductors are shown. The band gaps of the nitrides cover the whole visible spectral range and extend both into the infrared and ultraviolet spectral range and thus enable them to be used in manifold areas of application. It is noteworthy that for achieving light emission in the green spectral region a smaller In mole fraction is required in cubic InGaN compared to hexagonal InGaN, due to the smaller band gaps of the cubic nitrides. This is relevant to the extent that several factors complicate the growth of In-rich InGaN [1–3].

The band gap of a semiconductor is temperature-dependent and can be calculated by Varshni's empirical equation [32, 33]:

$$E_g(T) = E_g(0\,\text{K}) - \frac{AT^2}{T + \Theta} \tag{2.3}$$

For c-GaN the low-temperature band gap is $E_g(0\,\text{K}) = 3.293\,\text{eV}$ [23] and the Debye-temperature is $\Theta = 600\,\text{K}$ [33]. A is a fitting parameter with the value of $6.697 \times 10^{-4}\,\text{eV K}^{-1}$ for c-GaN [33].

Due to the symmetry of the wurtzite structure, large built-in spontaneous polarization fields are present within layers grown on the c-plane (0001) [34]. In addition, piezoelectric polarization fields occur when the layers are strained [34], which is the case when layers are grown on foreign substrates or heterostructures like quantum wells are grown. In heterostructures the difference in polarization of well and barrier material causes that a potential is built up inside the well. As a result of the quantum-confined Stark effect (QCSE) electrons and holes transfer to opposite sides of the quantum well, so that the maxima of their wave functions do not match up anymore. As the recombination probability of an electron-hole pair is proportional to the spatial overlap of electron and hole wave functions, the efficiency of photon emission is reduced. Furthermore, the photon energy is slightly reduced by this effect [16, p. 264]. It is possible to grow on non-polar planes of the wurtzite structure that are perpendicular to the c-plane, namely the $(11\bar{2}0)$ a-plane and the $(10\bar{1}0)$ m-plane, where these field are nearly absent. Also, polarization effects
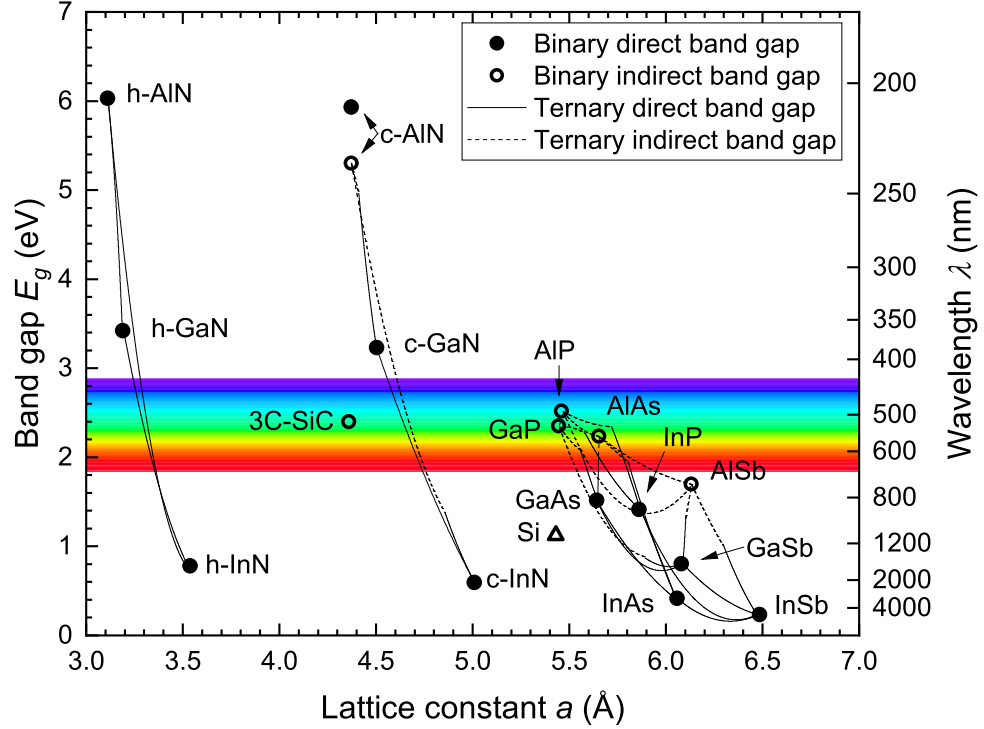
Figure 2.2: Band gaps E_g of hexagonal and cubic nitride binaries and ternaries and other important III-V semiconductors versus their lattice constant a. Based on [29] with some updated parameters: Band gaps for cubic nitrides see Table 2.1. For c-InGaN the bowing parameter is $b = 0.6\,\mathrm{eV}$ [30]. Bowing parameters of c-AlGaN are $b = 0.85\,\mathrm{eV}$ and $b = 0.01\,\mathrm{eV}$ for the direct and indirect band gaps, respectively, and the crossover is at $x = 0.71$ [25]. Bowing parameters of the direct and indirect c-InAlN band gaps are $b = 2.729\,\mathrm{eV}$ and $b = 3.624\,\mathrm{eV}$, respectively, and the crossover is at $x = 0.24$ [27]. Values for hexagonal nitrides taken from [16, 26, 29] and parameters for the remaining III-V semiconductors are taken from [29]. Parameters for 3C-SiC, which is used as a substrate for cubic nitrides, and Si after [31]. ▭

are reduced in semi-polar planes, which are located between polar and non-polar planes. However, the fabrication of structures on these planes is not as mature as on the c-plane [35]. The polarization fields are also absent in the zinc blende phase in (001) growth direction [36–38], which is employed in this work. Spontaneous polarization is forbidden in the zinc blende phase [39, p. 308], and piezoelectric polarization does not occur for (001) layers [40, pp. 69ff], unless shear strain is applied [41]. No noteworthy polarization-induced separation of wave functions occurs in cubic heterostructures [14]. In Figure 2.3 the band structure of an AlN/GaN quantum well in wurtzite and zinc blende phase is drawn schematically to illustrate the effect. The cubic nitrides are therefore promising alternatives to the non-polar wurtzite planes for fabricating devices with increased efficiency. For example, it has been

demonstrated that the radiative recombination rate of cubic GaN quantum dots is about two orders of magnitude higher than that of their hexagonal counterparts [42, 43].
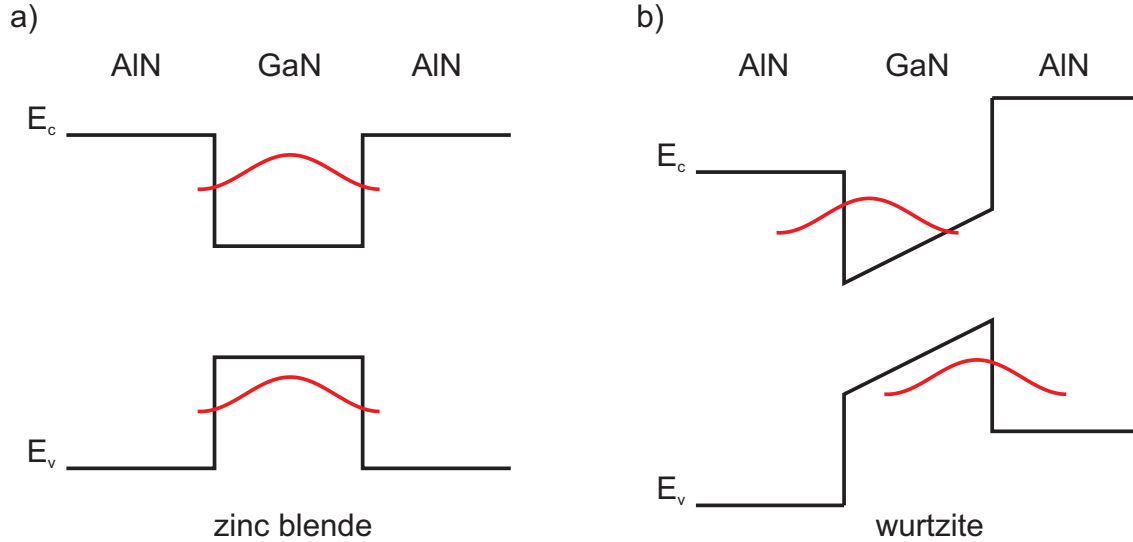

Figure 2.3: Simplified drawing of the distribution of electron and hole wave functions in an AlN/GaN quantum well. a) zinc blende structure; b) wurtzite structure with polarization fields.

2.2 Doping

2.2.1 General

The doping of a semiconductor means to intentionally incorporate impurities into the crystal to have an influence on the electrical properties of the material. This can be accomplished in various ways, e.g., implanting ions into the semiconductor crystal or by introducing dopants by diffusion. The most common and simplest way to dope epitaxially grown layers is to provide the dopant material during growth. In MBE chambers dopants are provided from separate effusion cells (see section 2.3).

There are several ways how impurities can affect the electrical properties of a semiconductor. For group III nitrides, the most relevant impurities are shallow, substitutional impurities [16]. *Substitutional* means, that impurity atoms are incorporated in place of group III or N atoms in the crystal lattice. The relevant impurity atoms have one excess or deficit electron compared to the atom they replace. Atoms that provide excess electrons to the semiconductor are called *donors*. In this case, the excess electron is not required for bond formation. It is weakly bound to the donor atom and is released to the conduction band, if the donor binding energy E_D is provided. If this energy is in the order of the thermal energy at room temperature $k_B T \approx 26\,\text{meV}$ or lower, the donor is *shallow* [44, p. 6]. That means at room temperature nearly all of the donor electrons are ionized. After the excess electron is released to the conduction band, the donor atom remains positively charged. A semiconductor with excess electrons is called *n-type*. In the other case of an impurity featuring a deficit electron (*acceptor*), an electron from the valence band can be excited to be localized at the impurity atom, if the acceptor binding energy E_A is

provided. A *hole* (deficit electron) is created in the valence band, which contributes to the electrical conductivity like an electron in the conduction band. A semiconductor with deficit electrons (or excess holes) is called *p-type.*

Since a shallow donor, simply put, consists of an electron and a positively charged ionized impurity, it can be approximated as a hydrogen-like atom. The donor binding energy E_D is then calculated analogously to the ionization energy of the hydrogen atom and one obtains [44, p. 20]:

$$E_D = \frac{m_e^*}{m_0 \varepsilon_r^2} E_{\mathrm{Ryd}} \tag{2.4}$$

The term m_e^*/m_0 accounts for the effective electron mass, ε_r is the relative permittivity and $E_{\mathrm{Ryd}} = 13.6\,\mathrm{eV}$ is the Rydberg energy.

The fabrication of almost all devices requires doping of the semiconductor. Light emitting diodes (LEDs) or bipolar transistors for example base on pn-junctions, i.e., control over both n- and p-type doping are necessary. For some applications also unipolar devices, which only require n- or p-type layers, are suitable. These are, e.g., quantum fountain lasers or quantum cascade lasers [45].

Apart from shallow dopants, there is the possibility that impurities create states located deeply inside the band gap, called *deep defects.* These are disadvantageous for many applications, as they are centers for non-radiative recombination, reduce the carrier lifetime, can compensate doping, and reduce the carrier drift velocity [44, pp. 54ff]. A special type of deep defects, the DX center, is described briefly in the appendix on page 124.

2.2.2 Temperature dependence of carrier concentration

Due to the fact that the ionization of an impurity can amongst others be accomplished by thermal activation, it is obvious that the carrier density is temperature-dependent. Figure 2.4 schematically shows the dependence of the carrier concentration n on the temperature T for an n-type semiconductor (solid line) and an intrinsic semiconductor (dashed line). The temperature-dependence for an n-type semiconductor differs within three temperature ranges. At temperatures near $0\,\mathrm{K}$ neither electrons from the valence band nor from donor states can be excited to the conduction band, meaning the semiconductor is insulating. With increasing temperature, more and more donors are ionized. The band-to-band transition is impossible, because the thermal energy is much smaller than the band gap energy $k_B T \ll E_g$. The free electron concentration in this *ionization regime* depends on the temperature as follows [44, pp. 120ff]:

$$n \approx \sqrt{\frac{N_D N_c}{g}} \exp\left(-\frac{E_D}{2 k_B T}\right) \tag{2.5}$$

Here N_D is the donor concentration, N_c the effective density of states at the conduction band edge, and $g = 2$ the ground-state degeneracy of hydrogen-like donors. With further increasing temperature, at some point all donors are ionized. As still no band-to-band excitation is possible, the carrier concentration cannot rise further. This is called the
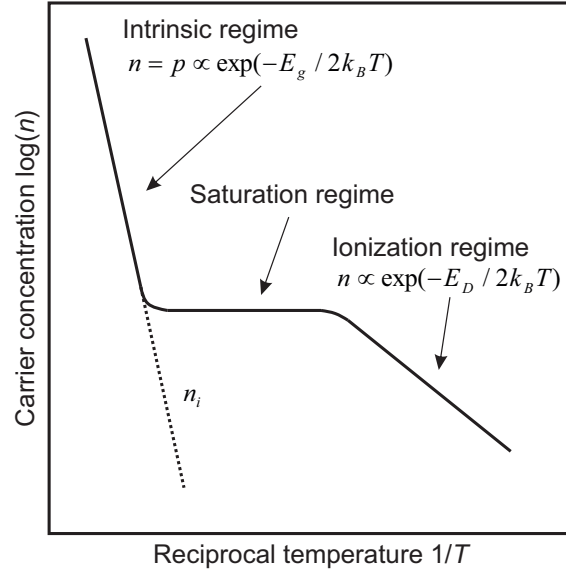
Figure 2.4: Temperature-dependence of the carrier density of intrinsic (dashed line) and doped (solid line) semiconductors. After [44].

saturation regime and the free electron concentration is equal to the donor concentration [44, pp. 120ff]:

$$n = N_D \tag{2.6}$$

At some point with further increasing temperature, the thermal energy is high enough to excite carriers directly from the valence to the conduction band. The carrier concentration now depends on the temperature analogously to an intrinsic semiconductor [44, pp. 120ff]

$$n_i = p_i = \sqrt{N_v N_c} \exp\left(-\frac{E_g}{2k_B T}\right) \tag{2.7}$$

with N_v the effective density of states at the valence band edge.

2.2.3 Effects at high doping levels

Several effects can occur at high doping levels, that can drastically change the properties of a semiconductor. The **Mott transition** is an insulator-to-metal transition [44, pp. 34ff], that occurs due to a reduction of the impurity ionization energy at high doping levels. Normally, e.g., in an n-type semiconductor, all donors are neutral at temperatures near 0 K and the semiconductor is insulating. If due to a high N_D donors are so close together that their Coulomb potentials overlap, the energy barrier between two donors can be lower than E_D. Tunneling or thermal emission over the barrier allows electrons to transfer between donor states, which becomes more likely with increasing N_D [44]. Second, high free electron concentrations will screen the coulomb potentials of the donors, which also lowers the ionization energy [44]. The extreme case is a reduction of the effective ionization energy to

zero, which allows for charge transfer even near $0\,\mathrm{K}$ - comparable to metals. The Mott transition starts to emerge when the distance between impurities becomes comparable to the effective Bohr radius a_B^* [44]:

$$N_{\mathrm{crit}}^{-1/3} = \frac{4\pi}{3} a_B^*$$
(2.8)

where N_{crit} is the critical impurity concentration.

The **Burstein-Moss** or **Moss-Burstein effect** [46, 47] is a shift of the absorption edge due to band-filling effects. The band structure and the Fermi-Dirac distribution of electrons for a degenerately doped semiconductor are sketched in Figure 2.5. Due to high doping, the Fermi level E_F is located well above the conduction band edge E_C. Approximately $4k_BT$ below E_F all states in the conduction band are populated [31, pp. 291f], thus a transition from E_V to E_C at $k = 0$ is impossible due to the absence of unoccupied states in the conduction band. For parabolic bands, the energy of a direct optical transition is [31]:

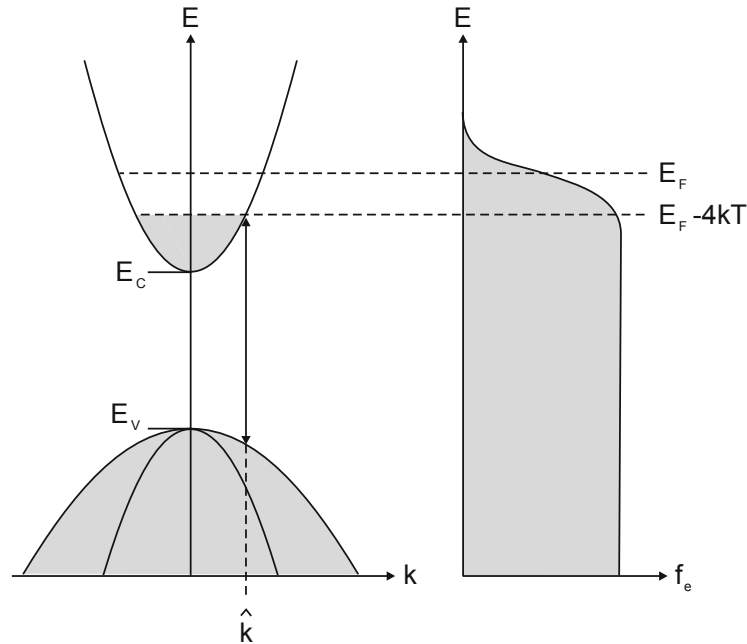$$E = E_g + \frac{\hbar^2 k^2}{2m_e^*} + \frac{\hbar^2 k^2}{2m_h^*}$$
(2.9)

Figure 2.5: Band structure (left) and Fermi-Dirac distribution of electrons (right) of a degenerately doped semiconductor [31, pp. 291].

with m_e^* and m_h^* the effective electron and hole masses, respectively. The energy difference ΔE_C of the lowest unoccupied state to E_C is

$$\Delta E_C = E_F - 4k_B T - E_C \equiv \frac{\hbar^2 k^2}{2m_e^*} \tag{2.10}$$

and thus the lowest k required for a transition is

$$\hat{k} = \sqrt{\frac{2m_e^*}{\hbar^2}\left(E_F - 4k_B T - E_C\right)}. \tag{2.11}$$

Additionally, the energy shift ΔE_V in the valence band has to be considered, which is

$$\Delta E_V = \frac{\hbar^2 \hat{k}^2}{2m_h^*} = \frac{m_e^*}{m_h^*}\left(E_F - 4k_B T - E_C\right). \tag{2.12}$$

The total Burstein-Moss shift (BMS) of the absorption edge is then [31]

$$\Delta E_{\text{BMS}} = \Delta E_V + \Delta E_C = \left(E_F - 4k_B T - E_C\right)\left(1 + \frac{m_e^*}{m_h^*}\right). \tag{2.13}$$

In the limit of extreme degeneracy the position of E_F depending on the free carrier concentration n is [44, p. 38]:

$$E_F - E_C = \frac{\hbar^2}{2m_e^*}\left(3\pi^2 n\right)^{2/3} \tag{2.14}$$

The **band gap renormalization (BGR)** refers to a reduction of the band gap due to many-body effects, that become relevant at high doping and/or free carrier concentrations [44, 48]. Coulomb interaction between electrons leads to a redistribution of carriers, when an electron is added to a highly doped, neutral semiconductor. This redistribution reduces the energy of the electron added [44, pp. 48ff]. Also spin causes interaction between electrons, as electrons with opposite spin attract each other and electrons with like spin are repulsive. This leads to a non-uniform distribution of electrons, which causes the total value of repulsive and attractive energy to be non-zero. The total energy of the electron system is thus reduced. The reduction of the electron energy leads to a lowering of the conduction band edge. Also interaction between electrons and ionized donors, which is attractive, causes a lowering of the conduction band edge [44]. Analogously, mutual interaction of holes and interaction between holes and ionized acceptors result in a net attractive energy, which rises the valence band edge [44]. The shift of both band edges leads to a narrowing of the band gap. A more detailed and mathematical description of this effect is given, e.g., in [49].

BMS and BGR are two effects that occur simultaneously and act against each other. As the BMS is inversely proportional to the effective carrier mass, it dominates over the BGR in highly n-doped semiconductors, while it is much weaker in p-type materials [44].

2.2.4 Doping of group III nitrides

There is a variety of elements that can act as dopants in GaN. Group VI elements like O, S, and Se on N sites can potentially act as shallow donors and Group II elements like Be, Mg, Ca, Zn, and Cd on Ga sites could form shallow acceptors [16, p. 1007]. Group IV elements as C, Si, Ge, Sn, and Pb are amphoteric. They can theoretically occupy both Ga or N sites, i.e. they could act both as donors and acceptors [44, p. 189]. It depends on the formation energy on which site they are actually incorporated. They could also incorporate on both sites at the same time, causing autocompensation, which reduces the free carrier density [44, p. 189]. The tendency for autocompensation rises at very high doping levels, which eventually leads to a saturation of the free carrier concentration when the doping is further increased [44, p. 189]. Calculations of formation energies in hexagonal GaN [50] carry out that O on the N site acts as a donor, and that Si and Ge are incorporated on Ga sites, where they also act as donors. The same holds for donors in cubic GaN [51–56]. Both Ge and Si are shallow donors here with binding energies around $30\,\text{meV}$ [56]. The best-performing acceptor in wurtzite GaN is Mg incorporated on a Ga site [50], featuring an ionization energy of $208\,\text{meV}$ [50]. C is found to show a high level of autocompensation in hexagonal GaN, leading to highly resistive layers [57]. In cubic GaN however C acts as an acceptor. Having an ionization energy of $215\,\text{meV}$ [58] it is the acceptor of choice in c-GaN, as its binding energy is $15\,\text{meV}$ lower than that of Mg [58]. Although these elements are called *shallow* acceptors, it has to be noted that their ionization energies are significantly higher than those of the aforementioned donors, making it difficult to achieve high hole concentrations, because only a small fraction of acceptors is ionized at room temperature.

The most commonly used donor in wurtzite GaN is Si. However, Si induces tensile strain, causing crack formation [7] and surface roughening [8] in highly-doped layers. This can be explained by the smaller atomic radius of Si compared to Ga. The atomic radius of Ge however is comparable to that of Ga, thus it can be expected that Ge is - from a structural point of view - the better suited donor. Doping experiments of wurtzite GaN reveal that the structural quality of highly Ge-doped GaN is actually significantly higher than with Si-doping [8, 10, 59, 60]. Fritze et al. report a maximum Ge donor concentration of $2.9 \times 10^{20}\,\text{cm}^{-3}$ for metal organic vapor phase epitaxy (MOVPE)-grown GaN, while three-dimensional growth begins at $1.9 \times 10^{19}\,\text{cm}^{-3}$ with Si doping [8]. Hageman et al. report smooth plasma-assisted molecular beam epitaxy (PAMBE)-grown GaN layers for Ge-concentrations up to $4 \times 10^{20}\,\text{cm}^{-3}$ [59]. They report even higher doping up to $2.6 \times 10^{21}\,\text{cm}^{-3}$, but this leads to the formation of secondary phases like Ge_3N_4 and crystalline Ge. Also Ajay et al. report no degradation of layers Ge-doped up to $6.7 \times 10^{20}\,\text{cm}^{-3}$ [60].

Doping of $Al_xGa_{1-x}N$ and AlN turns out to be more difficult compared to GaN. O forms a shallow donor in GaN, but in wurtzite $Al_xGa_{1-x}N$ it undergoes a transition to a DX-center at $x = 0.3$ [50, 61, 62] or, as reported more recently, at $x = 0.6$ [63]. It then behaves like a deep acceptor, which reduces the free electron concentration and strongly impairs the electrical properties of the layer [50]. Thus O is not suited for n-type doping of $Al_xGa_{1-x}N$ covering the entire range of x. Unfortunately, increasing Al mole fractions

favor the incorporation of O [64], leading to an unintentional and unfavorable doping by O of layers with high Al content. Theoretical calculations for cubic nitrides show that O does not form a DX center in c-Al$_x$Ga$_{1-x}$N for any x [61]. The electrical properties of Si as a n-type dopant in Al$_x$Ga$_{1-x}$N seem unclear up to now, as there are contradictory reports on the DX-formation. Park et al. calculate that Si forms a DX center for $x > 0.24$ [65]. Bogusławski et al. calculate a transition from shallow to DX for $x > 0.6$ [66]. Theoretical investigations of Gordon et al. predict a DX formation of Si for $x \geq 0.94$, with the DX center located relatively shallow (150 meV) below the conduction band, which still results in n-type conductivity at room temperature [63]. Van de Walle et al. however predict that Si is a shallow donor over the entire composition range [50, 61]. In the case of c-Al$_x$Ga$_{1-x}$N, authors agree that Si does not undergo a DX formation [61, 65]. Also experimental reports on the DX formation of Si in wurtzite GaN are inconsistent. Skierbiszewski et al. find that Si forms a DX center for $x > 0.5$ [67], while Trinh et al. report a transition at $x = 0.84$ [68]. Additionally to the (unclear) formation of deep states, Si induces tensile strain at high doping levels, affecting also the structural properties of layers [69, 70]. Also for the case of Ge the situation regarding the electrical behavior seems unclear. The theoretical work of Park et al. suggests that Ge does not form a DX center [65]. Bogusławski et al. calculate a transition at $x = 0.3$ [66] and Gordon et al. at $x = 0.52$ [63]. In both cases, the shallow-to-DX transition of Ge is stated to occur at lower x than predicted for Si. For c-Al$_x$Ga$_{1-x}$N no DX formation is predicted for Ge [65]. There is significantly less experimental data available on Ge-doping of Al$_x$Ga$_{1-x}$N compared to Si-doping. Zhang et al. report that Ge is a shallow donor in Al$_x$Ga$_{1-x}$N at least up to $x = 0.2$ [71]; they could not characterize layers with higher x. Blasco et al. report [11] that highly Ge-doped layers exhibit Ge segregation and clustering, and that the donor activation rate gradually decreases with increasing x. To the best of my knowledge, no experimental analysis of deep defects in c-Al$_x$Ga$_{1-x}$N is reported. There is some luminescence data of c-Al$_x$Ga$_{1-x}$N published [72–74], but the spectra shown in these works strongly differ and no consideration of deep defects is presented.

In Figure 2.6 donor binding energies in c-Al$_x$Ga$_{1-x}$N are calculated after equation 2.4. The effective electron mass m_e^* is linearly interpolated between $0.19m_0$ and $0.3m_0$ for c-GaN and c-AlN, respectively [75]. The relative permittivity ε_r is linearly interpolated between 9.44 for c-GaN [23] and 8.07 for c-AlN [24].
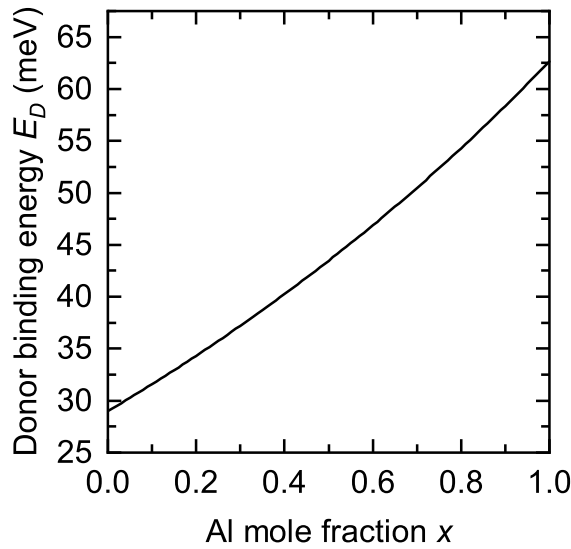
Figure 2.6: Donor binding energy in c-Al$_x$Ga$_{1-x}$N calculated after equation 2.4.

2.3 Epitaxy

2.3.1 Epitaxy methods

The almost exclusively used approaches to fabricate group III nitride layers are epitaxial methods. The term *epitaxy* refers to a crystal growth that occurs on a crystalline substrate, where the growing material is enabled to adopt crystallographic parameters of the substrate. The substrate can either be the same material as the growing layer (homoepitaxy), or foreign substrates with crystallographic parameters similar to the layer to be grown can be used (heteroepitaxy). The problem with heteroepitaxy is the formation of defects in the growing layer due to the mismatch of lattice constants. The lattice mismatch is defined as [76, p. 219]

$$f = \frac{a_{\text{substrate}} - a_{\text{layer}}}{a_{\text{layer}}}. \tag{2.15}$$

It is thus preferred to grow layers on native substrates or on those that have a small lattice mismatch to the grown layer. Unfortunately, the availability of bulk GaN substrates is very limited. This is due to the low solubility of N in Ga and the high vapor pressure of N over GaN [16, p. 232], which makes it impossible to use conventional growth techniques using melts like in the case of Si or GaAs. There are a few methods that allow growing bulk GaN in decent quality, namely the Na-flux method, the ammonothermal growth, and the hydride vapor phase epitaxy (HVPE), but bulk GaN substrates still are quite expensive [77]. The most commonly used substrate for wurtzite GaN is sapphire due to its low cost, although the lattice mismatch to GaN is relatively high ($\approx 13\%$) [16, pp. 324ff]. Also SiC is widely used, offering a lower lattice mismatch of about -3%, but being more expensive than sapphire [16]. For cubic GaN up to now no bulk substrates are available. There

Table 2.2: Basic parameters at $300\,\text{K}$ [31] of materials that already have been used as substrates for c-GaN epitaxy [12].

Substrate	Lattice constant a_0 (Å)	Lattice mismatch f to c-GaN (%)	Band gap E_g (eV)
3C-SiC	4.36	-3.2	2.4
GaAs	5.6533	25.5	1.42
Si	5.431	20.6	1.124
GaP	5.4506	21.0	2.26
InAs	6.0584	34.5	0.36
MgO	4.21	-6.5	7.3

are several materials that already have been used as substrates for cubic GaN, see Table 2.2. Substrates for c-GaN need to have a cubic crystal structure to induce growth of the metastable cubic phase. Due to the small lattice mismatch, 3C-SiC is the substrate of choice for c-GaN epitaxy, although the availability of high-quality 3C-SiC is low and prices are significantly higher than for more common substrates like Si or GaAs.

There are mainly three methods that are used for nitride epitaxy [16]: metal organic vapor phase epitaxy (MOVPE)[1], molecular beam epitaxy (MBE), and hydride vapor phase epitaxy (HVPE). HVPE is a method that features very high growth rates up to $800\,\mu\text{m/h}$ [16, pp. 385ff], which allows to grow thick layers, but is rather unsuited for fabrication of heterostructures consisting of thin, sharply separated layers. It is therefore used to grow thick (mostly wurtzite GaN) layers on foreign substrates (e.g., sapphire), that are then - as mentioned above - used as substrates for other epitaxial methods [16]. With MOVPE thin and sharply separated layers can be grown. It is the most widely used method to grow structures used for optoelectronic devices both in research and production [16]. Compared to MBE, low cost, higher growth rates, and higher throughput of MOVPE are advantageous, which makes MOVPE the method of choice for mass-production of devices like LEDs or high-power or high-frequency transistors [78, 79]. On the other hand, MBE offers a more precise control over layer thicknesses [78] and the possibility to precisely monitor the growth via reflection high-energy electron diffraction (RHEED). Furthermore, in MBE no hazardous metalorganic precursors are used. The problem that acceptors are passivated by H when using Mg for p-type doping in MOVPE does not exist for MBE-grown layers [80, p. 85].

2.3.2 Molecular beam epitaxy

In a MBE system the substrate is mounted on a heated, rotatable substrate holder and is facing towards the element sources. The MBE process needs to take place in vacuum

---

1   Also referred to as metal organic chemical vapor deposition (MOCVD) or organo-metallic vapor phase epitaxy (OMVPE).

for two reasons: First, the molecular beams emitted from the effusion cells need to retain their shapes when propagating towards the substrate. Since residual gas elements can cause scattering, the mean free path of the beams has to be larger than the distance from the effusion cells to the substrate. This condition is already fulfilled for high vaccum (HV) conditions around 10^{-3} mbar [76, pp. 3ff]. Second, due to the low growth rates unintentional incorporation of impurities from the residual gas is high. For achieving high-purity layers it is thus necessary to provide ultra high vaccum (UHV) conditions [76]. Typical base pressures of MBE systems are in the range of 10^{-9} mbar to 10^{-11} mbar. There is a variety of vacuum pumps that can be used to reach such pressures, e.g. turbomolecular pumps, cryopumps, ion pumps, or titanium sublimation pumps. A MBE chamber can basically be divided into three zones [76, p. 6]: The molecular beam generation zone, the beam mixing zone, and the substrate zone, where the crystal growth takes place. In the following, the molecular beam generation and the crystal growth are explained. In the beam mixing zone, no notable physical processes are expected to occur due to the long mean free path of the beam elements [76, p. 9].

Generation of molecular beams

The first zone is the molecular beam generation zone, where the elements are provided. The group III elements are thermally evaporated from Knudsen-type effusion cells. Such an effusion cell consists of a crucible[1] filled with the material to be evaporated, a resistive heater, and a thermocouple for temperature monitoring and controlling. When the temperature is increased, the vapor pressure over the material rises and an increasing number of molecules leaves the cell. The effusion rate Γ_e, i.e., the number of molecules leaving the cell per second, of an ideal Knudsen cell in UHV is [76, p. 31]

$$\Gamma_e = p A_e \sqrt{\frac{N_A}{2\pi M k_B T}} \tag{2.16}$$

with p the material's vapor pressure, M its molecular weight, and A_e the cell's orifice area. Vapor pressure curves of elements relevant to this work are printed in the appendix (Figure B.1 on page 127). The flux I_A, i.e., the rate of molecules per unit area, which impinges on the substrate in distance r_A from the cell's orifice, is [76, p. 34]

$$I_A = \frac{\Gamma_e}{\pi r_A^2} \tag{2.17}$$

in case the molecular beam hits the surface perpendicularly. Since not all effusion cells can be arranged perpendicular to the sample, the tilt angle ϕ needs to be considered [76, p. 35]:

$$I_A' = I_A \cos\phi \tag{2.18}$$

Each of the effusion cells is equipped with a shutter, which can block the molecular beams.

---

1 Due to its high thermal stability, mostly pyrolytic boron nitride, pBN, is used as crucible material.

Since nitrogen is present as N_2 molecules, which are little reactive due to their high binding energy of 9.8 eV [16, p. 410], measures must be taken to provide reactive nitrogen atoms. The two most common methods are providing nitrogen atoms from a plasma, which is called plasma-assisted MBE or PAMBE, or providing ammonia (NH_3), which thermally dissociates at the heated substrate surface above 600 °C (reactive MBE or RMBE) [16, p. 437]. In this work layers are grown by PAMBE, thus the principles of this method will be presented in more detail. Nitrogen is provided via a mass flow controller to the plasma source. Here, a plasma is ignited by applying a radio-frequency (typically 13.59 MHz [16, pp. 428ff]) electromagnetic field. There are several species of nitrogen present in the plasma [16]: N atoms, vibrationally or electronically excited N_2 molecules, and ionic N_2^+ and N^+ species. In common plasma sources, the cracking efficiency is about 1 % [16]. Atomic N can directly bond with group III elements without any potential barrier, and activated N_2 molecules can dissociate exothermically at surfaces [16]. Thus, atomic N and activated N_2 are the primary species involved in the growth process, and higher amounts of these species result in higher growth rates [16]. The ionic species on the other hand can cause different surface and lattice defects and thus should be hindered from reaching the growth front [16]. Mainly two parameters influence the amount of ionic species leaving the plasma source [81]: Higher temperatures of the cell walls and lower diameters of the aperture holes reduce the ionic flux. Appropriate precautions are made by plasma source manufacturers, such that modern plasma sources enable to grow nitride layers of higher quality at higher growth rates [81].

Growth process

The crystal growth takes place in the third of above mentioned zones of a MBE chamber, where the molecular beams impinge on the heated substrate. Several competing processes need to be considered in this stage [16, pp. 410ff]: adsorption and desorption of atoms or molecules, diffusion of atoms or molecules on the substrate surface, incorporation into the crystal, and decomposition of the crystal. Atoms or molecules can adsorb on the surface either by (weak) van der Waals interactions or by (strong) chemical binding. Depending on the substrate temperature T and the element specific desorption energy barrier E_{des}, the desorption rate rises proportionally to $\exp(-E_{des}/k_B T)$ [16, p. 412]. The *sticking coefficient* μ is defined as the ratio of atoms that adhere to the surface N_{ad} to the total number of impinging atoms N_{tot} [76, p. 10]:

$$\mu = \frac{N_{ad}}{N_{tot}} \tag{2.19}$$

Due to the elevated surface temperature during MBE growth, adsorbed atoms have sufficient energy to diffuse along the substrate surface. The average length of diffusion λ_s of an atom exponentially depends on the surface temperature [16, p. 413]. Depending on λ_s, crystal growth can take place in various ways [16, pp. 413f],[82, pp. 98ff]: If the crystal surface consists of large terraces delimited by steps of one or a few monolayers (i.e. a vicinal surface) and λ_s is larger than the terrace width, atoms move towards the step edges and are incorporated there (see Figure 2.7d). This is called the *step-flow growth* and results in smooth, two-dimensional surfaces. If λ_s is too low, atoms nucleate as new islands near
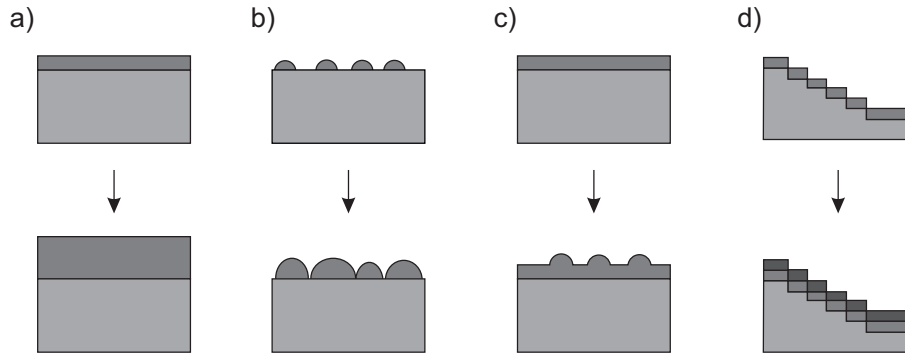
Figure 2.7: Basic modes of crystal growth. a) Frank–van der Merwe (2D); b) Volmer-Weber (3D); c) Stranski–Krastanov (3D); d) step-flow growth (2D). After [82, p. 100].

the spot where they impinged on the surface, and cannot move towards steps or already existing islands. This leads to a three-dimensional growth, resulting in a rough surface. The growth of islands is referred to as *Volmer-Weber* growth mode, see Figure 2.7b. For medium λ_s, island formation can occur, but atoms can diffuse towards island edges and incorporate there. In this way, the crystal can grow layer by layer, which also leads to a two-dimensional growth. This is called the *Frank-van der Merwe* growth, see Figure 2.7a. The last of the basic growth modes, the *Stranski-Krastanov* mode (see Figure 2.7c), can be induced by compressive strain, which relieves by formation of islands after growth of a few monolayers, the so-called wetting layer [83]. This mode can be utilized, e.g., to grow quantum dots [42, 84].

In the case of GaN growth, the mobility of Ga atoms on the surface is by orders of magnitude larger than that of N. Thus, for growth of smooth layers an excess of Ga is required, while N-rich growth conditions lead to surface roughening [16, pp. 414f.]. For the growth of cubic GaN, the presence of one monolayer of excess Ga results in smoothest surfaces [85]. N-rich conditions [86] and too high growth temperatures [55, 86] however favor the formation of the hexagonal phase.

The last of the processes to be considered during crystal growth is the decomposition of the crystal itself. It is reported [16, p. 416] that GaN begins to slowly decompose at temperatures around 800 °C, and decomposition increases significantly when temperatures rise further. At 850 °C the decomposition rate is stated to be $1\,\mu m\,h^{-1}$.

2.3.3 Antiphase domains

Antiphase domains (APDs) are a phenomenon connected to the growth of compound semiconductors on elemental substrates [87], such as 3C-SiC (001) grown on Si (001), which is used as a substrate for c-GaN growth. There are areas on the 3C-SiC surface that are Si-face, and other areas that are C-face [88]. These areas are surrounded by antiphase boundaries (APBs). The surface energies of both domains are different, resulting, e.g., in deviating growth rates [88], which is unfavorable for achieving smooth surfaces. The APDs are carried on when c-GaN is grown on a 3C-SiC substrate [88]. Boundaries can form deep levels in the band gap and act as scattering centers for carriers [87]. Furthermore, N-face domains of c-GaN favor the formation of hexagonal inclusions [88].

2.3.4 Growth monitoring via RHEED

Thanks to the UHV conditions and the geometry of MBE growth chambers, the reflection high-energy electron diffraction (RHEED) technique can be employed to monitor the crystal growth in great detail. An electron beam of typically 5 keV to 40 keV is directed to the sample surface at a shallow angle smaller than 3° [76, pp. 121ff]. The geometry is shown in Figure 3.1 on page 26. Due to this shallow angle, the penetration depth of the electrons into the surface amounts to a few monolayers, thus RHEED is a very surface-sensitive method. On the other hand, the beam spot on the surface extends to several mm [89], so the obtained information is an average over a large sample area. The electron beam is scattered at the sample surface and eventually hits a fluorescent screen, where a diffraction pattern becomes visible. The diffraction pattern can be explained with help of the *Ewald construction* [89]: The incident electron beam forms a sphere with radius $k_0 = 2\pi/\lambda$ in reciprocal space, where λ is the electron De Broglie-wavelength. The in two dimensions equidistantly arranged atoms of the sample surface are represented as rods in the reciprocal space, whose spacing is $2\pi/a$. Intersections of the sphere with the lattice rods in reciprocal space appear as diffraction spots on the screen. A more detailed discussion can be found in [76] or [89].

The two main information obtainable by RHEED are the surface morphology and the growth rate. Figure 2.8 shows different surface morphologies, their appearance in reciprocal space, and the resulting RHEED patterns. An ideal, flat and single-crystalline surface appears as diffraction spots located on the Laue-circle (a). A flat surface featuring domains (see Section 2.3.3) results in a streaky diffraction pattern (b). A vicinal surface also leads to a streaky diffraction pattern, with the streaks being inclined by the same angle as the surface miscut (e). A rough, three-dimensional surface eventually results in spots, that are not located on the Laue circle any more (f). Furthermore, surface reconstructions can be observed, which manifest themselves as reflections with reduced distance to each other.

The other important information that can be accessed by RHEED is the growth rate. When layer-by-layer (Frank-van der Merwe) growth occurs, the intensity of the reflected beam, called the *specular spot*, depends on the filling of the topmost layers. This is illustrated in Figure 2.9. When the surface is perfectly smooth, i.e. the last grown layer
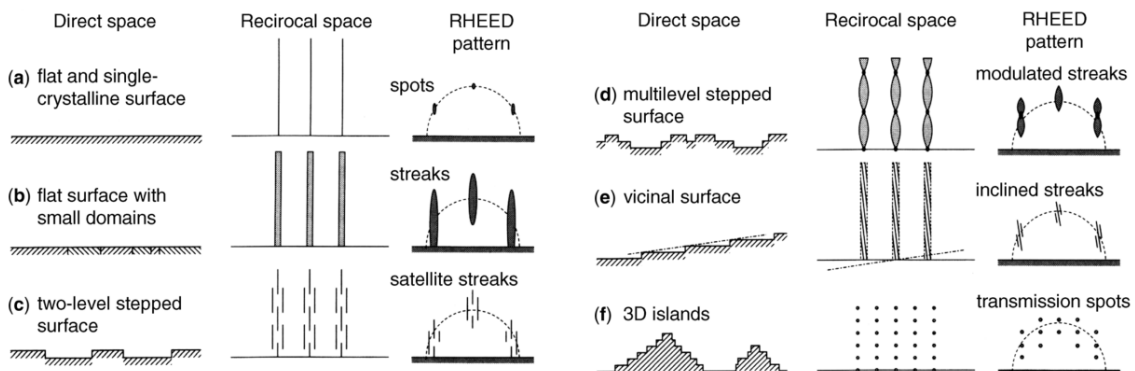

Figure 2.8: RHEED diffraction patterns of different surface morphologies [89].
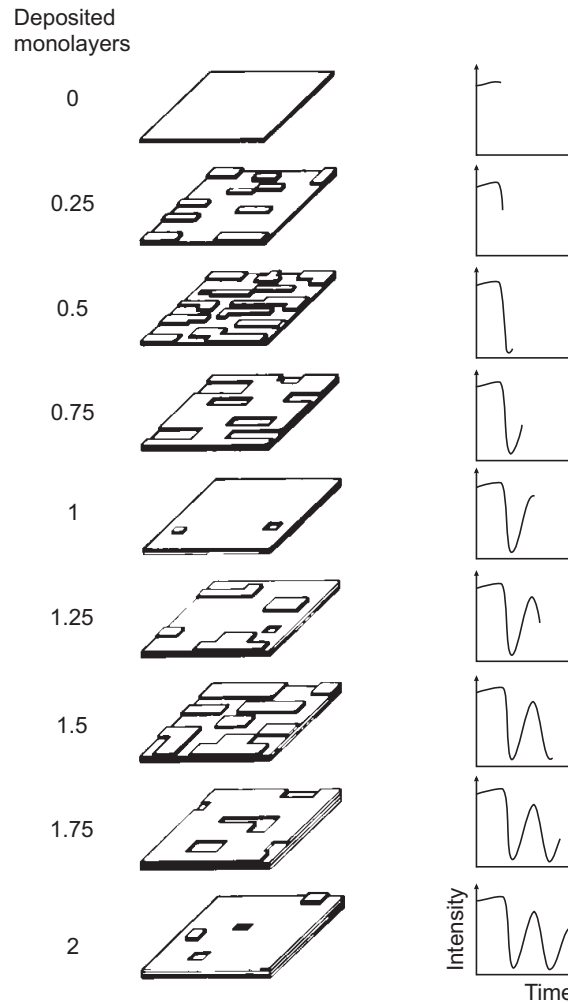
Figure 2.9: RHEED intensity oscillations during layer-by-layer growth. After [90].

is completely filled, the intensity is highest. In the following, new islands nucleate and begin to grow in lateral dimension. The surface becomes rougher and the specular intensity decreases. It reaches a minimum when the top layer is filled in half, and rises again as the layer is filled further. The intensity is back at maximum when the new layer is completely filled. From the knowledge of the monolayer thickness, which is half the lattice constant a, and the time required to grow one layer (i.e., the time required for one oscillation period), the growth rate can be calculated. Since the complete, smooth filling of layers is the ideal case and in reality the surface roughness increases with proceeding growth, a damping of intensity oscillations occurs. Not all growth conditions result in intensity oscillations. For example, during growth of c-GaN while maintaining a Ga excess of one monolayer no oscillations are visible due to attenuation and scattering effects.

2.4 Multiple quantum wells, superlattices and intersubband absorption

The contact between two semiconductors with different band gap is called a *heterojunction*. Both in the valence and conduction band a discontinuity arises. The offset in the conduction band ΔE_C is given by the difference in electron affinities χ of material 1 and material 2 [91, p. 13]:

$$\Delta E_C = \chi_2 - \chi_1 \tag{2.20}$$

Consequently, the valence band offset is

$$\Delta E_V = E_{g1} - E_{g2} - \Delta E_C. \tag{2.21}$$

When two semiconductors are arranged in a way such that the material with lower band gap (e.g., GaN) is surrounded by a higher band gap material (e.g., AlN), carriers in the valence and conduction band are trapped inside this so-called *double heterojunction (DHJ)*, as they cannot overcome the potential barriers on both faces of the low band gap material. If the width of the double heterojunction (DHJ) is comparable to the De Broglie wavelength of electrons and holes, quantization effects occur. The DHJ is called a *quantum well (QW)* in this case. Due to the restricted movement of carriers in one direction (typically the growth direction), carriers can only occupy discrete energy levels. While the energy levels in an infinitely deep potential well of width d can be easily calculated by [91, p. 5]

$$E_n = \frac{\pi^2 \hbar^2 N^2}{2m^* d^2}, \qquad N = 1, 2, ... \tag{2.22}$$

where m^* is the effective electron ore hole mass, there is no analytical solution giving the energy levels of a finite potential well. A detailed discussion on finite potential wells is given in [92, pp. 159ff]. There is a finite number of energy states, and always at least one bound state exists [91, p. 14]. Contrary to infinite potential wells, wave functions of carriers in finite potential wells penetrate the barriers with exponential decay. If carriers have enough energy to occupy levels higher than the band offset, they are not bound anymore and can escape the quantum well (QW). The band diagram of a finite QW is schematically drawn in Figure 2.10.

Incident light can be absorbed by a QW by exciting carriers to higher energy states. Two types of transition are possible: *interband* transitions describe excitation of an electron from a valence band state to a conduction band state, and *intraband* or *intersubband* transitions occur within one band, e.g., between two states in the conduction band. In every case the photon energy of the incident light has to be equal to or greater than the energy difference between the two involved states. However, not all transitions are allowed, which is described by some *selection rules*. In case of *interband* transitions from a valence band state E_M^h to a conduction band state E_N^e, only transitions with M and N having equal parity are allowed. In symmetrical QWs however all transitions with $M \neq N$ nearly vanish [91, p. 34], meaning essentially only $E_1^h \rightarrow E_1^e$, $E_2^h \rightarrow E_2^e$, ... transitions are allowed. Furthermore, transitions with participation of heavy holes are only allowed for TE-polarized light, while transitions originating from the light hole band are allowed for
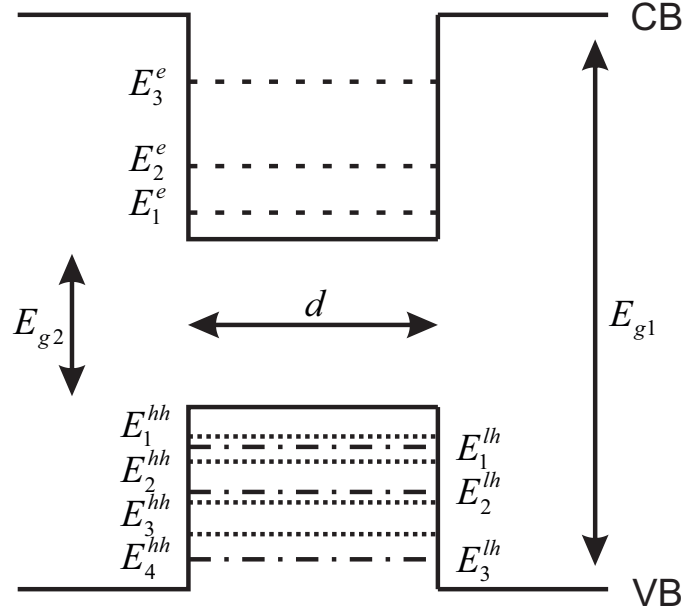
Figure 2.10: Band diagram of a QW of thickness d formed by the double heterojunction of a barrier material with band gap E_{g1} and a well material with band gap E_{g2}. Light hole (lh) and heavy hole (hh) states are not degenerate any more in a QW.

both TE- and TM-polarized light[1] [93]. Selection rules for *intersubband* transitions (still in symmetrical QWs), e.g., from conduction band state E_M^e to E_N^e are significantly different. Only transitions with opposite parity of M and N are allowed [91, pp. 36f]. For example $E_1^e \rightarrow E_2^e$ or $E_1^e \rightarrow E_4^e$ are allowed, while $E_1^e \rightarrow E_3^e$ is forbidden. Most importantly, the transition can only be induced by TM-polarized light [94, pp. 384ff]. In case of transitions within the conduction band, the n-type doping has to be high enough so that the E_1^e state is occupied in order to allow for light absorption.

To enhance, e.g., the optical gain or absorption of QW structures, a periodic arrangement of QWs can be grown. If the barrier thickness between individual QWs is large enough so that no overlap of adjacent wave functions occurs, this is called a *multiple quantum well (MQW)* structure. With sufficiently thin barriers however wave function of neighboring QWs overlap and tunneling of carriers from one QW to another can occur. The energy levels transform into so-called *minibands*. In this case one speaks of a *superlattice (SL)*.

Due to their large band gap, group III nitride heterostructures such as GaN/AlN MQWs or SLs can be used to fabricate devices emitting or absorbing light in the infrared spectral region, utilizing intersubband transitions within the conduction band. Devices operating based on only one carrier type, here electrons, are called unipolar. Due to the higher electron mobility compared to the hole mobility, n-type unipolar devices are very suitable for high-frequency applications. The wavelength of greatest interest is 1.55 μm,

---

1   TE (transversal electric) polarization means $\vec{E}$ is in the plane of the QW layer; TM (transversal magnetic) means $\vec{E}$ is perpendicular to the QW layer, i.e. $\vec{E}$ is parallel to the growth direction $\vec{e}_z$.

the commonly used wavelength for fiber-optic telecommunication. A detailed investigation of cubic GaN/AlN-based MQWs and SL structures can be found in [95].

2.4.1 Doping of quantum wells

There are different approaches to achieve a high free carrier density inside a QW by doping. Either the QW layer can be doped homogeneously, or by depositing a layer of the dopant with a thickness of one monolayer inside the QW layer. This technique is called δ-doping, and allows for achieving very high carrier densities. A discussion of δ-doping is given in [96, 97]. In Figure 2.11(a) the band structure of a homogeneously doped c-GaN/AlN QW simulated by nextnano[3] [98] is shown. Due to the high doping level, the bands are bent slightly and the Fermi level is located within the conduction band of the QW layer. A different approach is to apply the doping to the barrier layers instead of the QW layer. Free carriers will diffuse from the barriers to the QW layer, so that they are spatially separated from the ionized impurities. This leads to reduced scattering of the carriers at impurities, resulting in higher carrier mobilities. Further improvements of this modulation doping technique are the introduction of an undoped spacer layer between the QW layer and the dopants, and doping the barriers using a δ-like doping profile. In Figure 2.11(b) the simulated band structure of a c-GaN/AlN QW with homogeneously doped barriers is shown. Also in this case the high doping level leads to a bending of the bands, but here to the opposite direction compared to the doped QW layer.

When considering intersubband transitions, e.g., the $E_1^e \rightarrow E_2^e$ transition, the doping level of the QW structure plays an important role. A higher doping level provides more carriers in the E_1^e state that can be excited, resulting in a stronger intersubband absorption. If the doping level however is too high, the E_2^e target state will be populated, which makes
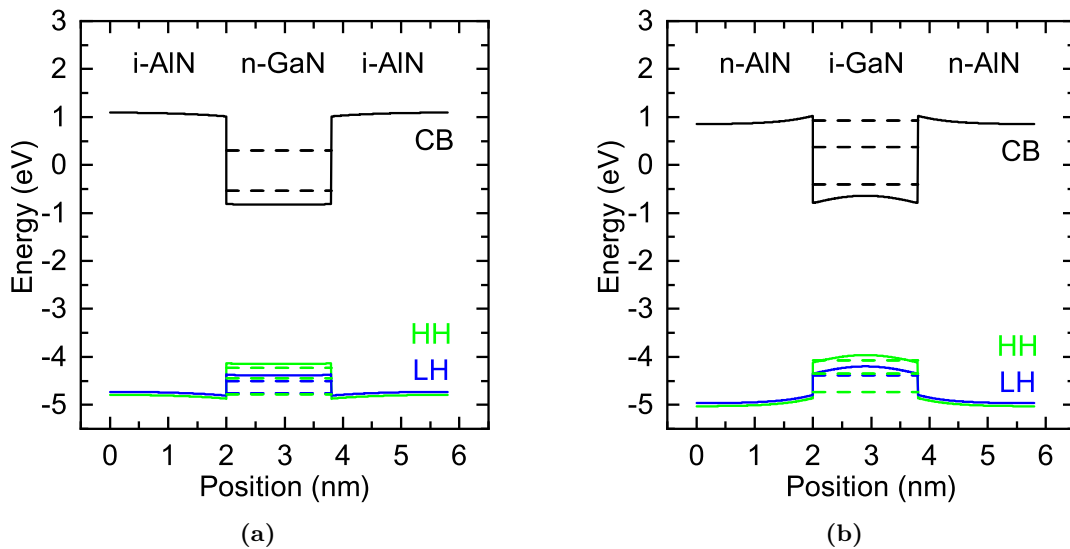

(a)   (b)

Figure 2.11: nextnano[3] simulations of a 1.8 nm c-GaN/AlN QW with homogeneous doping of **(a)** the QW layer, **(b)** the barriers (modulation doping). In both cases, the doping level is $3 \times 10^{20}\,\mathrm{cm}^{-3}$. Bound states are indicated by dashed lines.

the transition impossible. The Fermi level E_F is a measure up to which energy states are occupied in equilibrium, and it shifts to higher energies with increasing n-type doping. In a QW the Fermi level is given by [91, pp. 25f]:

$$E_F = E_1^e + k_B T \ln \left(1 + \exp \left(\frac{n_s}{N_C} \right) \right) \tag{2.23}$$

with n_s the sheet carrier concentration and N_C the effective density of states of a QW [91]:

$$N_C = \frac{m_e^* k_B T}{\pi \hbar^2} \tag{2.24}$$

In order for the E_2^e level to be unoccupied, the following relation needs to be fulfilled [91]:

$$n_s < \frac{m_e^*}{\pi \hbar^2} \left(E_2^e - E_1^e \right) \tag{2.25}$$

The values of n_s and N_C are sheet carrier densities and can be converted to 3D-equivalent carrier densities by dividing them by the QW layer thickness. Furthermore one has to consider, that the effective electron mass m_e^* increases when the QW becomes thinner. A model for effective electron mass calculation can be found in [99, pp. 62f].

CHAPTER 3

Experimental techniques

In this section, first the growth of cubic nitride layers is described. After that, the basics of the most important characterization methods used in this work are covered.

3.1 Growth of cubic nitrides

All (cubic) c-GaN and c-Al$_x$Ga$_{1-x}$N layers, and c-GaN/c-AlN heterostructures described in this work are grown by plasma-assisted molecular beam epitaxy (PAMBE). The basic principles of this epitaxial method are described in section 2.3 – in this section, the setup of the system used is described, followed by the explanation of the particular growth process for c-GaN, c-AlN, and c-Al$_x$Ga$_{1-x}$N.

3.1.1 Setup of the molecular beam epitaxy system

The cubic nitride layers are fabricated in a *Riber* 32 molecular beam epitaxy (MBE) system. The setup of the MBE system is schematically shown in Figure 3.1. The growth chamber consists of a UHV recipient, which is pumped to a base pressure of approximately 3×10^{-9} mbar by a combination of a rotary vane pump and a turbomolecular pump. A quadrupole mass spectrometer is equipped to the chamber for residual gas analysis. A typical residual gas spectrum of the growth chamber is shown in Figure B.3 in the appendix. The walls of the growth chamber are flowed by liquid nitrogen during layer growth, to further reduce the amount of impurities.

The substrate is mounted on a molybdenum sample holder, which is transferred via a transfer rod from the load lock chamber to the growth chamber. There the substrate holder is rotatably mounted in front of a heating element, which allows to achieve substrate temperatures up to approximately 950 °C. A thermocouple is mounted near the heating element to control and monitor the substrate temperature. However, the measured temperature is not the actual temperature at the substrate surface, thus a calibration is required at this point. This calibration process is described in the appendix in section A.1. The effusion cells are located opposite to the substrate. They consist of a pyrolytic boron nitride (PBN) crucible surrounded by a heating element, and a thermocouple for temperature monitoring. A PID controller allows to control the temperature with an accuracy of 0.1 °C. For a better thermal isolation of the cells from each other, the cells are surrounded by a water cooling shield. The system is equipped with effusion cells for Ga, Al, and In as group III-elements, and Si and Ge as n-type dopants. The purity of all source materials is 99.9999 %. The crucible orifices are 2.5 cm in diameter, and their distance to the substrate center is 12 cm. A Bayard–Alpert gauge can be positioned in place of the substrate to measure the beam equivalent pressure (BEP) of each effusion cell at a certain

cell temperature. To provide activated nitrogen atoms, an *Oxford Applied Research* HD25 inductively coupled radio frequency plasma source is mounted to the chamber. The flow of high purity N_2 is controlled by a mass flow controller in the range of $0\,sccm$ to $3\,sccm$ with an accuracy of $2\,\%$. A purifier is mounted to the N_2 supply to reduce remaining H_2O, O_2, and CO_2 contaminants to below $0.1\,ppb$. Each element source is equipped with a shutter, which allows to block the molecular beam emitting from the cells. A substrate shutter can be used to block all beams at the same time.

For monitoring and control of the growth process, a RHEED system consisting of an electron gun and a fluorescent screen is used (see section 2.3.4). The electron gun is operated at $16\,kV$ acceleration voltage and $1.6\,A$ filament current. The focused electron beam hits the sample surface at a shallow angle of incidence (approximately $3\,°$), and the diffraction pattern becomes visible on the fluorescent screen, from which it is recorded by a CCD camera and transferred to a PC for analysis.

3.1.2 Substrate preparation

As can be seen in Table 2.2, the substrate of choice for c-GaN epitaxy is 3C-SiC due to its relatively small lattice mismatch of $-3.2\,\%$. For c-$Al_xGa_{1-x}N$ and c-AlN, the lattice mismatch to 3C-SiC is even smaller. In this work, commercially available 3C-SiC substrates are used, which consist of a $10\,\mu m$ 3C-SiC(001) layer that is deposited by chemical vapor deposition (CVD) on a 4 in Si(001) wafer of $500\,\mu m$ thickness. From the wafers $10 \times 10\ mm^2$ pieces are cleaved, which are used as substrates. Prior to growth, the substrate pieces are cleaned from contamination and oxide layers. First, the substrates are cleaned subsequently
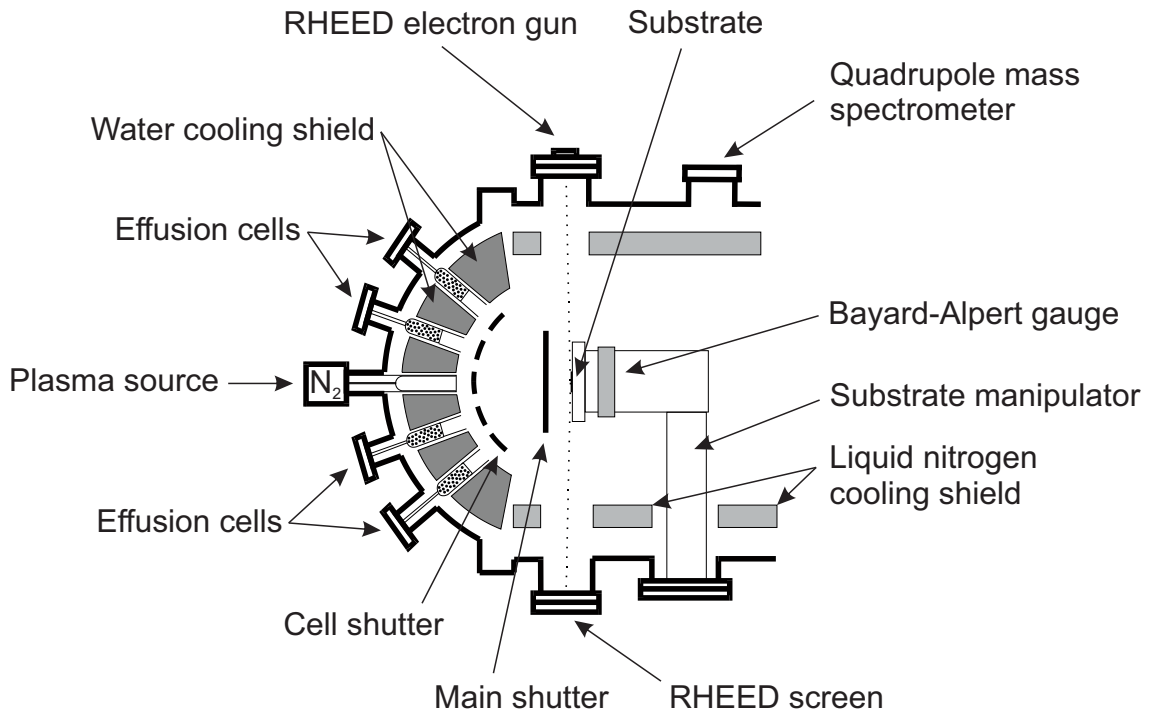

Figure 3.1: Schematic illustration of the MBE growth chamber. After [100].

using acetone and isopropyl alcohol in an ultrasonic bath to remove surface contaminations. After that, substrates are treated with buffered oxide etch in an ultrasonic bath to remove surface oxides. The last step of substrate preparation is performed in the growth chamber immediately before the growth process is started. The substrate is heated to $890\,°C$ and Al is evaporated to the surface for $5\,s$ at a flux of approximately $1 \times 10^{14}\,cm^{-2}\,s^{-1}$. When the shutter is closed, the Al re-evaporates from the surface. As the Al bonds with remaining O from the surface, the remaining oxides are removed by this process. The procedure of evaporation and re-evaporation is repeated ten times. It can be seen that the RHEED pattern transforms from diffuse reflections to clear ones, and additional lines from surface reconstructions become apparent (Figure 3.2). These are indications for a high surface purity.

| (a) | (b) |

Figure 3.2: RHEED diffraction pattern of a 3C-SiC substrate surface **(a)** before and **(b)** after the Al deoxidation procedure at $890\,°C$.

3.1.3 Growth of c-GaN

The growth of c-GaN is performed at a substrate temperature of $720\,°C$ and a Ga-flux of $3.2 \times 10^{14}\,cm^{-2}\,s^{-1}$. The sticking coefficient of Ga on 3C-SiC at this temperature is 0.5, thus the actually incorporated flux is $1.6 \times 10^{14}\,cm^{-2}\,s^{-1}$. The N_2 flow is around $0.21\,sccm$ and the plasma source is operated at a power of $260\,W$. The growth is performed in two steps. First, for the nucleation of c-GaN on the 3C-SiC substrate the growth is performed in cycles of $30\,s$ deposition and $30\,s$ growth interruption. This is repeated for ten periods. Based on the RHEED pattern, the nucleation of c-GaN on 3C-SiC occurs by growth of islands. The streaky pattern, which corresponds to a smooth 3C-SiC surface featuring APDs, rapidly transforms to a spot-like pattern, which corresponds to a three-dimensional surface. A typical diffraction pattern after $30\,s$ deposition of c-GaN is shown in Figure 3.3(a). With ongoing growth, the RHEED diffractions transform back streaks (indicating again a smooth surface featuring APDs), whose separation is now smaller than that of the 3C-SiC streaks, due to the larger lattice constant of c-GaN. A typical pattern after ten periods of the nucleation process is shown in Figure 3.3(b).

After a smooth surface is obtained by the nucleation process, c-GaN can be grown continuously. After Schörmann et al. [85] the optimum conditions for c-GaN growth are
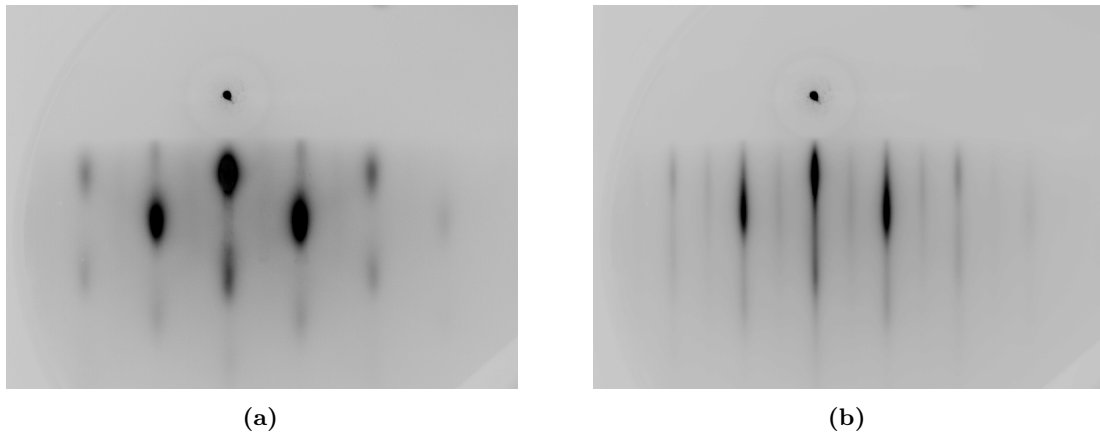
(a)   (b)

Figure 3.3: RHEED diffraction pattern after **(a)** the first cycle of the nucleation process, and **(b)** after ten cycles.
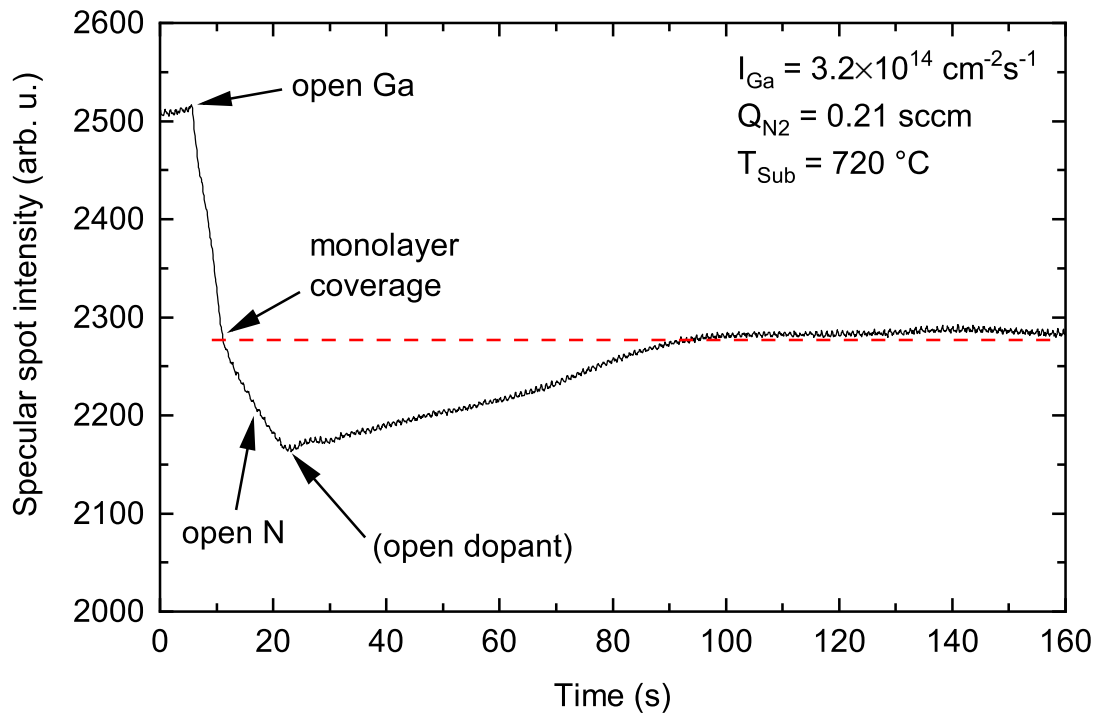

Figure 3.4: Course of the RHEED specular spot intensity when starting growth of c-GaN. The "kink" in the intensity drop after opening the Ga shutter indicates, that the surface is covered by exactly one monolayer of Ga at this point. After opening the N-shutter, the intensity rises again to this value, which means that the growth takes place under a Ga excess of one monolayer. ▱

slightly Ga-rich, with an excess of one monolayer of Ga. These conditions can exactly be established by monitoring the intensity progression of the specular spot of the RHEED pattern, see Figure 3.4. First, the Ga shutter is opened. Ga adsorbs on the sample surface and the RHEED intensity decreases with increasing Ga coverage. As soon as the surface is covered with exactly one monolayer of Ga, now Ga adsorbs to Ga and not to GaN any more. This causes a change in the sticking coefficient and thus a change in the adsorption rate, which expresses itself in a deviating slope of the RHEED intensity progression. Ga is still deposited for approximately the same time required to achieve the monolayer coverage, and then the N shutter is opened. The deposition of Ga beyond the monolayer coverage is required because when opening the N shutter, the N flux probably is elevated in the first place. An increase in intensity can be observed after a few seconds as the layer growth begins. Ga is incorporated into the layer and the Ga coverage decreases. If the layer is to be doped, the shutter of the dopant effusion cell is also opened at this time. In the following, the substrate temperature should be adjusted such that the RHEED intensity settles down to the value that corresponds to a coverage of exactly one monolayer of Ga (dashed line). If the substrate temperature is too high, too much Ga desorbs from the surface and the excess Ga is less than one monolayer, resulting in the intensity to rise above the dashed line. If even N-rich growth conditions are achieved, the formation of the hexagonal phase of GaN is favored [86]. If the temperature is too low, too little Ga desorbs from the surface and the excess Ga is more than one monolayer. In this case, the intensity stabilizes at a too low value, or it even decreases with ongoing growth. In case high dopant fluxes are present growth dynamics are changed, as the growth rate is reduced at high doping levels (see section 4.5) and the excess monolayer does not consist solely of Ga any more, but additionally consists of the dopant material. When the growth parameters are set correctly, the rotation of the substrate can be switched on to achieve more homogeneous growth. As mentioned in section 2.3.4, RHEED can in general be used to obtain the growth rate from intensity oscillations. However, with the presence of one excess monolayer of Ga these oscillations are dampened, such that the growth rate cannot be determined in this case.

3.1.4 Growth of c-AlN

Experience shows that growth of smooth c-AlN layers is much more difficult than that of c-GaN. When the optimum conditions are not met, the formation of islands or hexagonal inclusions is favored. Best results can be obtained, when c-AlN is grown in cycles of typically 20 s growth and 30 s interruption. Also here conditions need to be metal-rich, as N-rich conditions cause the formation of the hexagonal phase. Growth is performed at a substrate temperature of $720\,^{\circ}\mathrm{C}$, an Al flux of $1.6 \times 10^{14}\,\mathrm{cm}^{-2}\,\mathrm{s}^{-1}$, a N_2 flow of $0.21\,\mathrm{sccm}$, and the plasma source operating at $260\,\mathrm{W}$. As the sticking coefficient of Al is unity at this substrate temperature, the establishment of Al-rich conditions needs to be done carefully, because excess Al does not evaporate from the sample when shutters are closed. Prior to growth, one monolayer of Al is deposited on the sample. Then the N shutter is opened to start the growth process. To perform growth in cycles, the substrate shutter is opened and closed at intervals as mentioned above. Also here RHEED is utilized to monitor the growth. A typical intensity progression during c-AlN growth is shown in Figure 3.5.
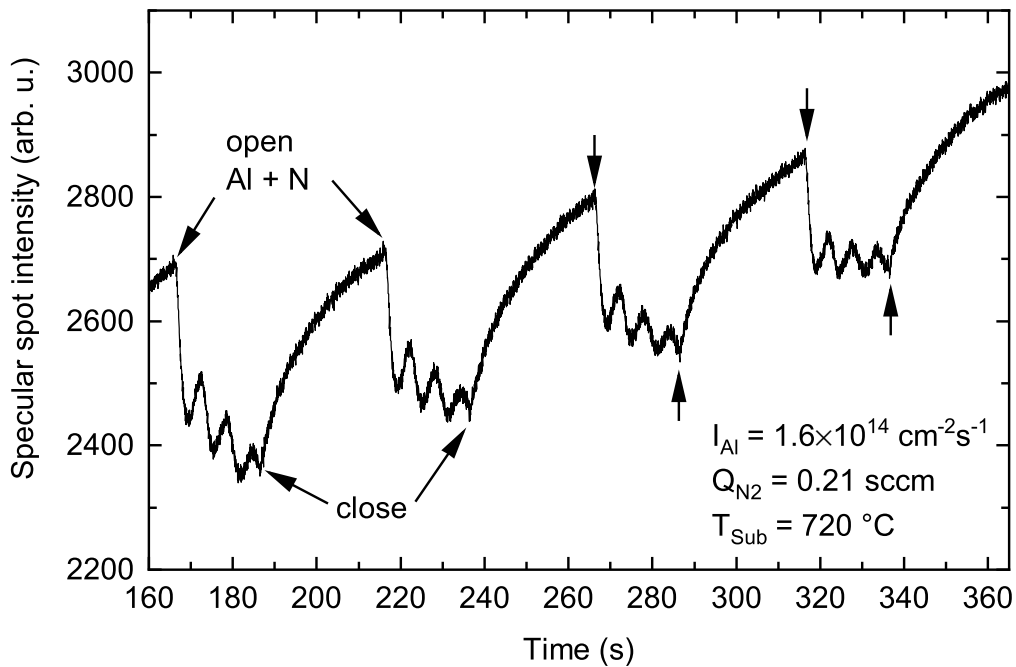
Figure 3.5: Course of the RHEED specular spot intensity during growth of c-AlN.

When the substrate shutter is opened, i.e., Al and N are deposited, the intensity first begins to drop and then to oscillate. While for c-GaN growth the excess metal suppresses intensity oscillations, they can be observed here. The time between two intensity maxima corresponds to the growth of one monolayer of c-AlN, which is 2.1865 Å. After closing the substrate shutter, the intensity rises again. This can be explained by a smoothing of the surface that occurs during growth interruptions. To establish optimum growth conditions, the Al flux needs to be adjusted such that over the course of several growth cycles the intensity in average runs at a constant level. In case of the example shown here, the intensity tends to rise with time, which means that the Al flux is too low and that the amount of excess Al decreases. If the intensity drops with time, the Al flux is too high and needs to be decreased.

In Figure 3.6 the growth rates of c-AlN obtained from RHEED oscillations for varying Al fluxes are plotted. In the range of low Al fluxes, the growth rates rise with rising flux. In this case, the conditions are N-rich, and the growth rate is limited by the supply of Al. As N-rich conditions favor hexagonal growth, this case should be avoided. With further increasing Al flux, at some point the supply of Al and N is exactly equal (stoichiometric growth). This is the desired case for c-AlN growth, because the excess Al monolayer deposited prior to growth is maintained under these conditions. When the Al flux is increased even further, the growth rate does not increase any more, due to limitation by the N supply. However, Al will accumulate on the surface in this case, which leads to the formation of islands on the sample surface.
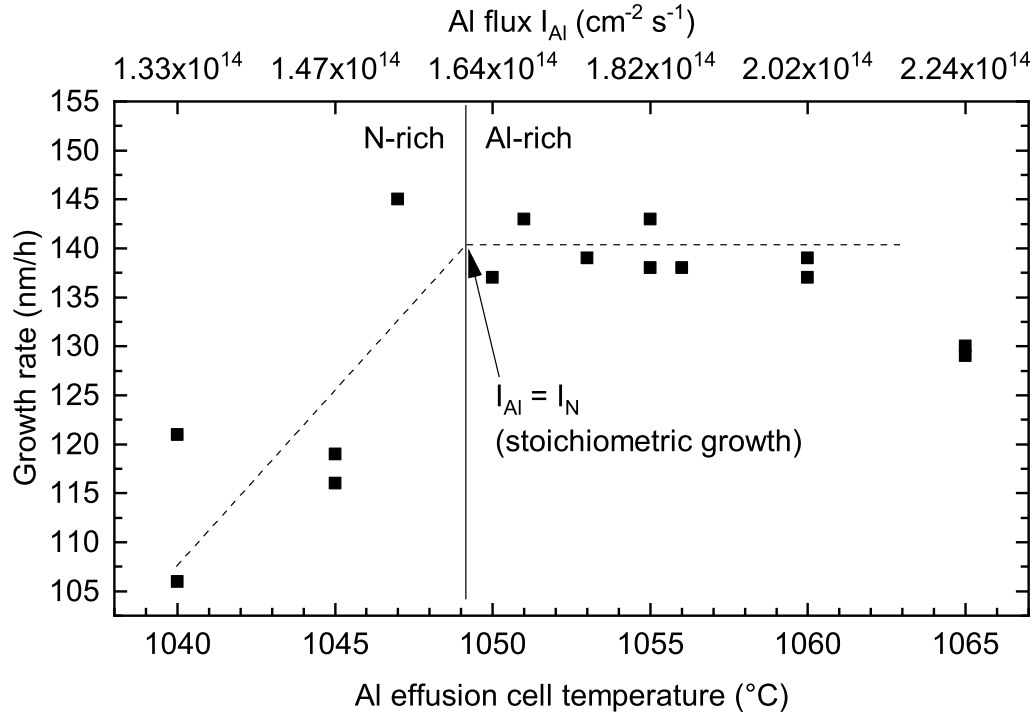
Figure 3.6: Growth rates of c-AlN at a substrate temperature of $720\,°C$ and N_2 flow of $0.21\,\text{sccm}$, depending on the Al flux. The dashed lines are a guide to the eye.

3.1.5 Growth of c-Al$_x$Ga$_{1-x}$N

For growth of c-Al$_x$Ga$_{1-x}$N, the Al and Ga fluxes need to be adjusted such that the amount of incorporated atoms is in the appropriate ratio. When the flux of Al required for c-AlN growth is $I_{Al,AlN}$, the following Al flux is required for growth of c-Al$_x$Ga$_{1-x}$N:

$$I_{Al,AlGaN} = xI_{Al,AlN} \tag{3.1}$$

Other than for Al, the sticking coefficient μ of Ga at growth temperature is lower than unity. Therefore, a larger Ga flux must be supplied ($I_{Ga,sup}$) than is actually incorporated ($I_{Ga,inc}$):

$$I_{Ga,inc} = \mu I_{Ga,sup} \tag{3.2}$$

With $I_{Ga,GaN,inc}$ the incorporated Ga flux at c-GaN growth, the incorporated Ga flux for c-Al$_x$Ga$_{1-x}$N growth needs to be:

$$I_{Ga,AlGaN,inc} = (1-x)I_{Ga,GaN,inc} \tag{3.3}$$

and thus the required supplied Ga flux is:

$$I_{Ga,AlGaN,sup} = (1-x)I_{Ga,GaN,sup} = \frac{1-x}{\mu}I_{Ga,GaN,inc} \tag{3.4}$$

All parameters other than the material fluxes, i.e., substrate temperature, N_2 flow, and plasma source power, are not changed for the growth of c-$Al_xGa_{1-x}N$.

The procedure for c-$Al_xGa_{1-x}N$ growth is almost identical to that of c-GaN. First, for nucleation growth is performed in ten cycles of 30 s deposition and 30 s interruption. After that, continuous growth is initiated as follows (see RHEED intensity diagram in Figure 3.7). The Ga shutter is opened, and the change in intensity drop indicates the surface coverage with one monolayer of Ga. After the same time, the N shutter is opened. The intensity begins to rise, and immediately Al is opened, which causes the intensity to drop in the first moment. After approximately 6 s, which corresponds to the growth time of one monolayer, the intensity begins to rise again and eventually plateaus at the intensity level of the monolayer coverage (dashed line). Very weak growth oscillations are superimposed to the intensity course.
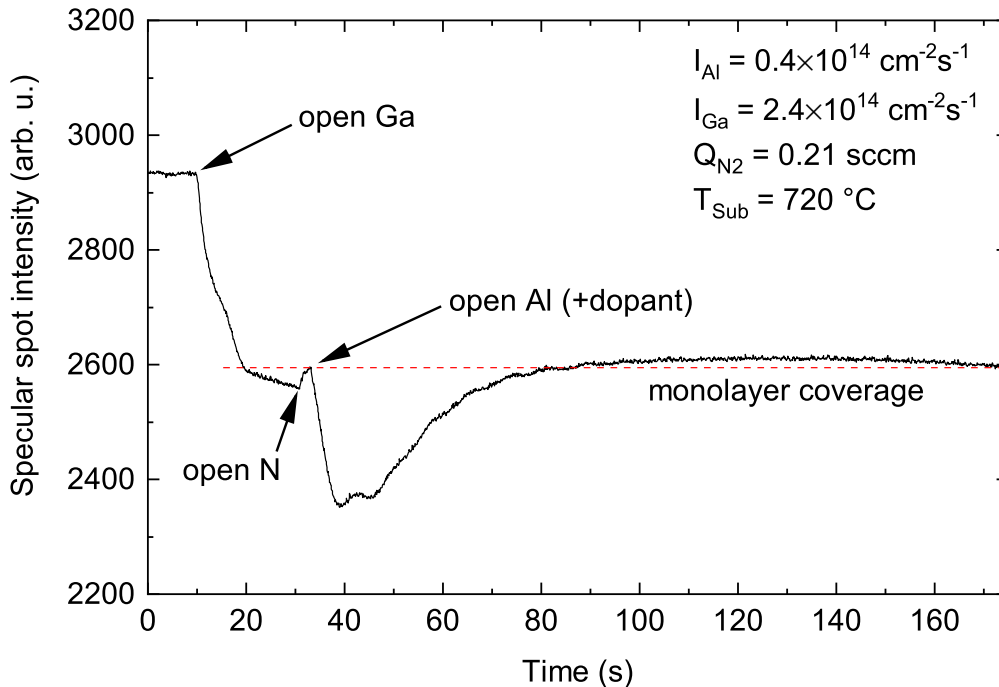

Figure 3.7: Course of the RHEED specular spot intensity when starting growth of c-$Al_{0.25}Ga_{0.75}N$.

3.2 Characterization methods

3.2.1 High-resolution x-ray diffraction

High resolution X-ray diffraction (HRXRD) is a technique, that can be used to examine the crystal structure of solids. It employs the diffraction of a monochromatic X-ray beam by the periodic alignment of atoms in the crystal. In this work a *Philips* X'Pert MRD diffractometer is used for high resolution X-ray diffraction (HRXRD) analysis. The setup is sketched in Figure 3.8 and it basically consists of three components [101, p. 69ff]:

a X-ray source combined with a monochromator to provide a focused beam of one single characteristic X-ray wavelength, here the Cu Kα_1 line ($\lambda = 1.54056$ Å); the sample mounted on an Euler cradle, which allows for sample positioning and alignment, such as X, Y, and Z translation, adjusting the angle of incidence ω, the azimuth angle φ, and the sample tilt Ψ; and lastly a movable detector located at an angle of 2θ with respect to the incident beam.

Figure 3.9 shows a sketch of the Bragg reflection of an X-ray hitting a set of crystal planes. Here a symmetric reflection is shown, i.e., the incident angle ω and the diffraction angle θ are equal. The path difference of two adjacent diffracted rays is $2d\sin\theta$, where d is the spacing between the crystal planes. Constructive interference occurs when the path difference is an integer multiple n of the X-ray wavelength λ. With this one obtains Bragg's law:

$$2d\sin\theta = n\lambda \tag{3.5}$$

Symmetric reflections only consider lattice planes parallel to the surface, which means that only the spacing between lattice planes d in growth direction can be observed. For asymmetric reflections there is an offset $\delta\theta$ between incident angle ω and diffraction angle θ, which corresponds to a tilt of the lattice planes with respect to the surface normal. The measured plane spacing d for this configuration has both an in-plane component and a component in growth direction, which is useful, e.g., for investigation of strained layers.
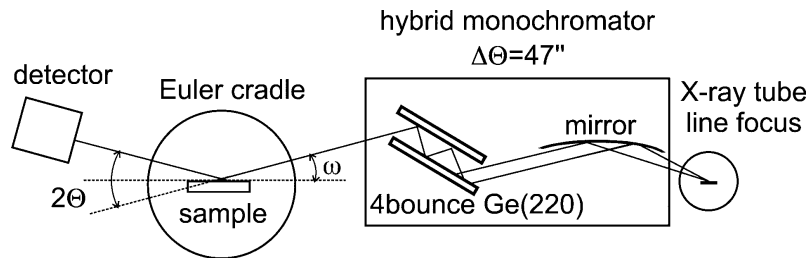

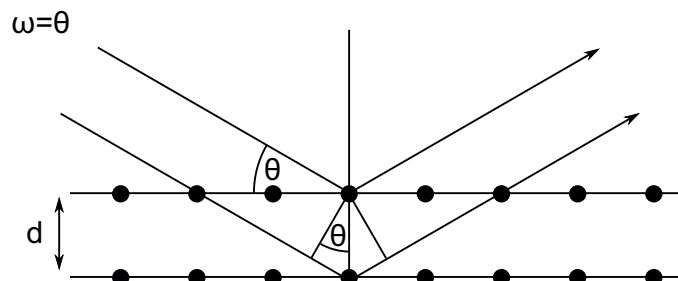**Figure 3.8:** Schematic illustration of the HRXRD setup [102].

Figure 3.9: Illustration of Bragg's law by means of a symmetric reflection.

The plane spacing depends on the lattice constant a, and for cubic crystal structure is calculated using the Miller indices h, k, and l of the lattice plane:

$$d = \frac{a}{\sqrt{h^2 + k^2 + l^2}} \tag{3.6}$$

There are several types of measurements that can be performed using a diffractometer. One important measurement performed in this work to estimate the dislocation density of a sample is the ω-scan or *rocking curve* measurement. First, the sample and detector are aligned such that the Bragg condition for a certain (hkl) reflection is fulfilled. Then the incident angle ω is varied over a range of typically $3°$ and the diffracted intensity is measured. A peak is obtained, whose full width at half maximum (FWHM) $\Delta\theta$ is a measure for the dislocation density of the crystal [103]. The other measurement that is performed in this work is the reciprocal space mapping. A reciprocal space map (RSM) is created by performing 2θ scans for a series of angles of incidence ω in the vicinity of a (hkl) reflection.[1] The in-plane reciprocal lattice parameter $q_\parallel$ is calculated from the ω and 2θ angles [101]

$$q_\parallel = \frac{2\pi}{\lambda} \left(\cos\omega - \cos(2\theta - \omega) \right) \tag{3.7}$$

and the reciprocal lattice parameter in growth direction $q_\perp$ is calculated by

$$q_\perp = \frac{2\pi}{\lambda} \left(\sin\omega + \sin(2\theta - \omega) \right). \tag{3.8}$$

3.2.2 Atomic force microscopy

The atomic force microscope (AFM) allows to investigate the topography of a sample surface with atomic resolution. The measuring principle is sketched in Figure 3.10. The cantilever with a tip curvature of a few nm is moved over the sample surface by a piezoelectric actuator. There are three basic modes of operation for topographic imaging: in *contact mode*, the tip touches the surface at every time, and due to changes in the height profile of the sample, it is deflected to different degrees. A laser beam is directed to the reflective backside of the cantilever and then detected by a four-segment photodiode. The deflection of the cantilever causes a displacement of the laser spot on the photodiode. The height of the cantilever above the surface is controlled in such a way that a constant deflection is maintained, so that the height profile of the surface can be reconstructed. The root mean square (RMS) roughness S_q of the surface is then calculated as follows [104, p. 223]:

$$S_q = \sqrt{\frac{1}{MN} \sum_{i=1}^{M} \sum_{j=1}^{N} (z(x_i, y_j) - \bar{z})^2} \tag{3.9}$$

---

1 Alternatively, $\omega - 2\theta$ scans can be performed for varying ω.

Here, M and N are the numbers of data points per line and the number of lines scanned, respectively, $z(x_i,y_j)$ is the height measured at one data point, and $\bar{z}$ is the mean height. The two other operating modes, which are not utilized in this work, are the *non-contact mode* and *tapping mode*. While the contact mode is only suited for rather smooth surfaces, these modes can be used to investigate surfaces with higher roughness, because the cantilever has no permanent contact to the surface, but oscillates at a certain height above the sample.
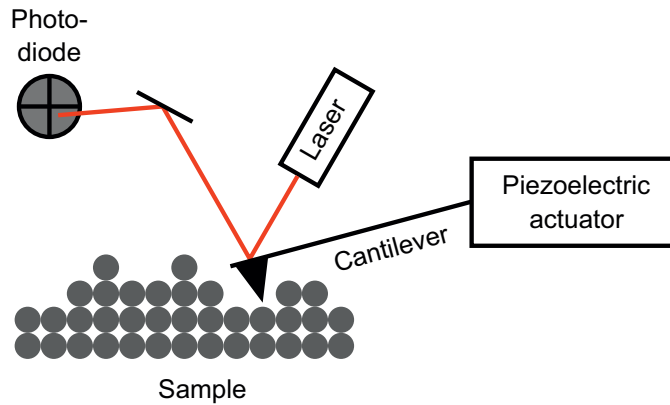

Figure 3.10: Schematic illustration of an atomic force microscope (AFM).

3.2.3 Secondary ion mass spectrometry

Secondary ion mass spectrometry (SIMS) is a very sensitive technique that allows to investigate the composition of a solid. A primary ion beam is directed onto the sample surface, where it penetrates into the material and transfers energy to the lattice by collisions. Near-surface particles can be removed from the sample, and a small percentage of them is ionized during this process. These particles are referred to as secondary ions. The secondary ion yield depends on several factors, for example the primary ion species or the sample composition [105]. Two basic modes of operation can be distinguished: static and dynamic SIMS. In static mode, the primary ion dose density is less than $10^{12}\,\mathrm{Ions/cm^2}$ [106], which means that the sputtering of one monolayer takes around $1\,\mathrm{h}$ or longer. This allows for a very precise analysis of the surface of a sample. In case of dynamic SIMS, the primary ion dose density is higher, or an additional sputter beam is used, such that the sputter rate is in the order of monolayers per second. Consequently, the secondary ions originate from continuously deeper layers of the solid. To detect the secondary ions mass-resolved, either a quadrupole mass spectrometer (QMS) can be used, or time-of-flight secondary ion mass spectrometry (TOF-SIMS) can be performed. The latter method exploits that ions of different masses m are accelerated to different velocities v in an electric field:

$$E = \frac{1}{2}mv^2 = qU \tag{3.10}$$

After accelerating the ions using a voltage U, they propagate through a field-free section of the length l and are eventually detected by, e.g., a Faraday cup or an electron multiplier.

Due to their different velocities, each secondary ion mass (or more specifically, each mass-to-charge ratio m/q) reaches the detector after a different time:

$$t = l\sqrt{\frac{m}{2qU}} \tag{3.11}$$

A pulsed primary ion beam is required for TOF-SIMS analysis.

The TOF-SIMS depth profile measurements presented in this work were performed at the Leibniz Institute of Surface Engineering (IOM), Leipzig, (thanks to Dr. Jürgen W. Gerlach) with an *ION-TOF* TOF-SIMS 5 instrument. A pulsed 15 keV ^{69}Ga$^+$ ion beam was used for analysis, and a pulsed 1.0 keV Cs$^+$ ion beam was used for sputtering. First, the Ga analysis beam was used to measure the mass spectrum. The beam therefore scanned an analysis area of 50×50 µm^2 in a grid of 128×128 pixels, and a complete negative ion mass spectrum was recorded for each individual pixel. The sample was then scanned with the sputter beam in an erosion area of 300×300 µm^2 for 1 s. Then a 100 ms long phase followed, in which the positive charge was compensated using a pulsed electron shower. This procedure is repeated, until the substrate of the sample is reached.

3.2.4 Hall effect measurements

Utilizing the Hall effect one can determine the carrier type (electrons or holes), carrier density, and carrier mobility of a semiconductor. Ohmic contacts need to be made to the sample, which is then placed in a magnetic field $\vec{B}$ perpendicular to the sample surface. When a current I is applied (perpendicular to the magnetic field), which causes the carriers to move with a velocity $\vec{v}$, the carriers are deflected by the magnetic component of the Lorentz force $\vec{F_B}$ perpendicular to the current flow and the magnetic field:

$$\vec{F_B} = q\vec{v} \times \vec{B}. \tag{3.12}$$

An electric field builds up, which is opposed to the Lorentz force and compensates it. Due to this field, a Hall voltage U_H can be measured. The Hall coefficient R_H is then given by [107]

$$R_H = \frac{dU_H}{BI}, \tag{3.13}$$

where d is the sample thickness in direction of the magnetic field. From the sign of R_H the carrier type is obtained. When the current flow is mainly based on electrons (i.e., n-type material), it has a negative sign. For p-type material, where current flow is mainly based on holes, R_H has a positive sign. In case the current flow is dominated by one carrier type, the carrier density can be calculated directly from R_H [107]:

$$p = \frac{1}{eR_H} \qquad\qquad n = -\frac{1}{eR_H} \tag{3.14}$$

The hall mobility μ_H is obtained by [107]

$$\mu_H = \frac{|R_H|}{\rho},\tag{3.15}$$

where ρ is the electrical resistivity of the sample.

While for classical Hall effect measurements the sample needs to be prepared in the so-called Hall bar geometry, the electrical resistivity and Hall coefficient can also be determined for arbitrarily shaped samples using the *van der Pauw* method [108]. The only requirements are, that the sample thickness d is homogeneous and small compared to the lateral dimensions, and it must not have holes. Four ohmic contacts are required, which need to be small compared to the lateral dimensions of the sample, and have to be located at the outermost edges of the sample. The samples prepared in this work are of quadratic shape, and the ohmic contacts are fabricated by alloying small In beads to the corners of the sample, see Figure 3.11.

The electrical resistivity is calculated by [108]

$$\rho = \frac{\pi d}{\ln 2} \frac{R_{12,34} + R_{23,41}}{2} f\left(\frac{R_{12,34}}{R_{23,41}}\right).\tag{3.16}$$

with $R_{12,34} = U_{34}/I_{12}$, where I_{12} is the current applied between contacts 1 and 2, and U_{34} is the voltage measured between contacts 3 and 4. Likewise applies $R_{23,41} = U_{41}/I_{23}$. The function f needs to fulfill the equation [108]

$$\frac{R_{12,34} - R_{23,41}}{R_{12,34} + R_{23,41}} = f \operatorname{arccosh}\left(\frac{\exp(\ln 2/f)}{2}\right),\tag{3.17}$$

which can be solved numerically. In case of symmetric samples $f = 1$ applies [107]. In a magnetic field B perpendicular to the sample surface, the Hall mobility is obtained by [108]

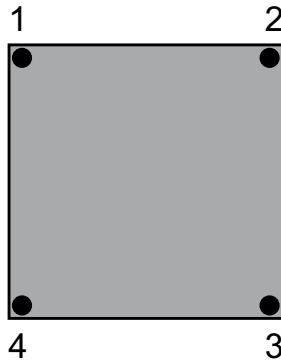$$\mu_H = \frac{d}{B} \frac{\Delta R_{24,13}}{\rho},\tag{3.18}$$

Figure 3.11: Sketch of the sample geometry used for van der Pauw measurements.

with $\Delta R_{24,13}$ the change of the resistance $R_{24,13}$ caused by applying the magnetic field. After eq. 3.15 the Hall coefficient is given by

$$R_H = \frac{d}{B} \Delta R_{24,13}. \tag{3.19}$$

3.2.5 Capacitance-voltage spectroscopy

Capacitance-voltage (CV) spectroscopy measurements were performed by Tobias Henksmeier at Paderborn University, to electrically determine the donor concentration in doped c-$Al_x Ga_{1-x}N$ layers. An extensive description of the measurement setup and procedure can be found in [109]. CV measurements require a gate contact and an ohmic contact to the epitaxial layer. Gates are fabricated by depositing circular Au contacts with diameters between $200\,\mu m$ to $800\,\mu m$ on top of $100\,nm$ thick SiO_2, which acts as an isolation layer. Ohmic contacts are fabricated by alloying In onto the sample corners.

An AC signal with frequency of $f = 1\,MHz$ and peak voltage of $5\,mV$ was superimposed to a DC voltage U_g sweeping from $-1\,V$ to $4\,V$. The capacitance C is then measured by an *Agilent* E4980A LCR meter. The donor concentration N_D can be calculated by [110]

$$N_D = \frac{2}{e\varepsilon\varepsilon_0 S^2} \left[-\frac{1}{\mathrm{d}\left(\frac{1}{C^2}\right)/\mathrm{d}U_g} \right] \tag{3.20}$$

where S is the gate area.

3.2.6 Photoluminescence spectroscopy

Fundamentals of photoluminescence spectroscopy

Photoluminescence (PL) spectroscopy is a method to optically characterize semiconductors regarding intrinsic properties as their band gap or excitonic effects, as well as extrinsic properties like crystal defects or impurities [111]. It is possible to identify shallow and deep impurities if they recombine radiatively. However, the determination of the impurity density is not easily possible [107]. Photoluminescence (PL) spectroscopy requires the optical excitation of the semiconductor (typically by a laser) with photon energy $\hbar\omega_{exc}$ higher than the band gap energy E_g of the material. Electron-hole pairs are generated by absorption of the photons. In case the photon energy is larger than the band gap, the excess energy of the electron-hole pairs is released to the crystal lattice by thermalization, which causes the electrons and holes to relax towards the conduction and valence band edge, respectively. From there, different recombination processes can occur, which can be radiative or non-radiative processes. Non-radiative processes however cannot be accessed directly by PL spectroscopy, but they lower the total emission intensity. Figure 3.12 schematically shows the generation, thermalization and recombination process using the example of a band-band transition. A spectrometer measures the intensity of the emitted light depending on the wavelength.

Emitted photons can have different energies, depending on the recombination process involved. A selection of recombination processes is displayed in Figure 3.13 and described in the following. In case of a direct interband transition (e,h), an electron from the conduction
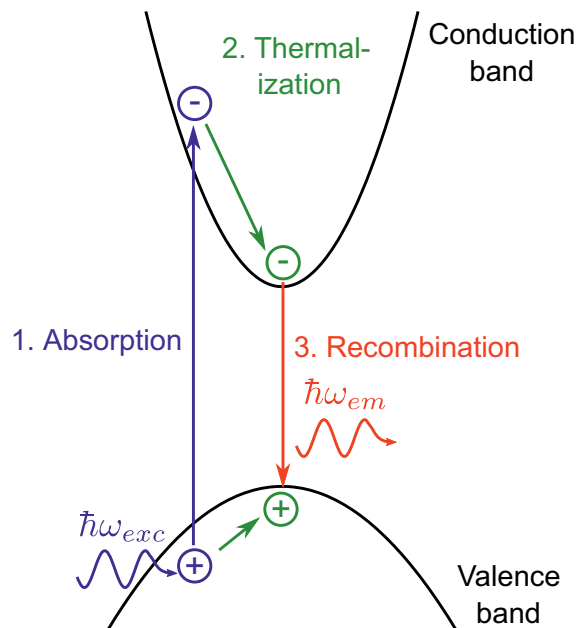
Figure 3.12: Illustration of the basic processes in PL spectroscopy. Electron-hole pairs are excited by absorption of exciting photons with energy $\hbar\omega_{exc}$, thermalize towards the band edges, and then recombine by emitting a photon with energy $\hbar\omega_{em}$. Here a band-band-transition is shown.
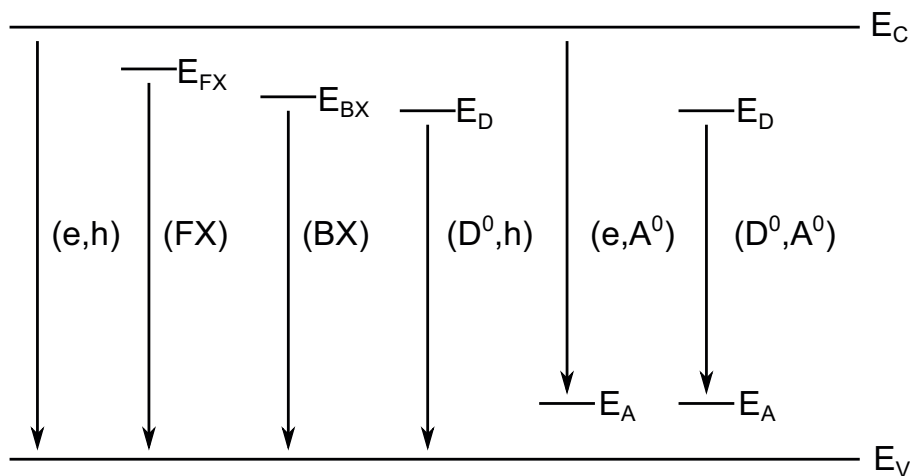

Figure 3.13: Selection of possible radiative recombination processes of electron-hole pairs in a semiconductor.

band recombines with a hole in the valence band. The photon energy depends on the band gap energy E_g and the thermal energy $k_B T$ [112]:

$$\hbar\omega_{e,h} = E_g + \frac{1}{2}k_B T \tag{3.21}$$

An electron-hole pair can also form an exciton, which means electron and hole form a hydrogen-like bond due to Coulomb interaction. An exciton, which can move through the crystal, is called a free exciton (FX). The energy E_X of the exciton bound states can be calculated as follows [112]:

$$E_X = \frac{1}{n^2}\frac{\mu^* e^4}{2\hbar^2\varepsilon_0^2\varepsilon_r^2} \tag{3.22}$$

Here e is the elementary charge, ε_0 the vacuum permittivity, ε_r the relative permittivity of the semiconductor, and n the principal quantum number ($n \geq 1$). Usually, only the ground state $n = 1$ can be observed by PL, because the luminescence intensity drops with the third power of n [113]. The exciton reduced mass μ^* is calculated from the effective electron and hole masses m_e^* and m_h^*, respectively [112]:

$$\mu^* = \frac{m_e^* m_h^*}{m_e^* + m_h^*} \tag{3.23}$$

The photon which is emitted during the recombination of an exciton has an energy, which is reduced by the exciton binding energy E_X [112]:

$$\hbar\omega_{FX} = E_g - E_X \tag{3.24}$$

Excitons can furthermore be bound to impurities, in which case they are called bound excitons (BX). There are excitons bound to neutral ($D^0 X$) or ionized donors ($D^+ X$), as well as excitons bound to neutral ($A^0 X$) or ionized acceptors($A^+ X$). The photon energy is additionally reduced by the localization energy E_{BX} [112]:

$$\hbar\omega_{BX} = E_g - E_X - E_{BX} \tag{3.25}$$

Another recombination process, which is mostly observed at low temperatures, is the donor-acceptor pair recombination (D^0, A^0). After an electron-hole pair is generated, an ionized donor can capture the electron and an ionized acceptor can capture the hole, after which the donor and acceptor are in a neutral state. In the following, the electron bound to the donor may recombine with the hole bound to the acceptor, given that the distance between donor and acceptor is sufficiently small. In the final state of the transition, the donor and acceptor are ionized again, and a Coulomb force resulting in a binding energy of $e^2/\varepsilon_0\varepsilon_r r$ acts between them, which depends on their distance r to each other [112]. This energy is additionally available to the emitted photon, so that its energy is [107]:

$$\hbar\omega_{DAP} = E_g - (E_A + E_D) + \frac{e^2}{\varepsilon_0\varepsilon_r r} \tag{3.26}$$

E_A and E_D are the donor and acceptor binding energies, respectively. At higher temperatures, the (D^0,A^0) transition cannot be observed, because the impurities can be ionized thermally. As the donor ionization energy is typically lower than the acceptor ionization energy, at medium temperatures the recombination of free electrons with holes bound to acceptors can be observed (e,A^0) [112].

Experimental setup

Figure 3.14 outlines the PL spectroscopy setup. The sample is positioned in a cryostat on a cooling finger which can be cooled down to approximately 12 K by means of a He closed cycle cryocooler. The temperature can be adjusted between 12 K and 300 K by means of a heating element attached to the cooling finger. A frequency-quadrupled *CryLaS* FQCW266 Nd:YAG-laser emitting at $\lambda = 266$ nm with an optical power of 5 mW to 50 mW (typically operated at 5 mW) is used for excitation of the sample. The laser beam is focused by a lens and directed onto the sample surface via a mirror. The laser spot diameter on the sample is approximately 140 µm. The luminescence light emitted by the sample is collected by a lens, which is adjusted so that its focal point is at the location of the laser spot. An additional lens focuses the beam on the input slit of a *SPEX* 270M monochromator. An edge filter is positioned in front of the input slit to prevent high intensity reflections of the laser spot from damaging the detector. The monochromator is in Czerny-Turner design with asymmetrical focal lengths of the two mirrors. The asymmetrical setup is used to suppress stray light. The collimating mirror has a focal length of 220 mm and directs the incoming light as a parallel beam onto the reflective diffraction grating. Most commonly a $g = 1/300$ mm grating is used, but if a higher resolution is required it can be exchanged by a $g = 1/1200$ mm grating. The blaze wavelength of both gratings is 500 nm. Depending on the wavelength λ, the grating constant g, and the order of diffraction n (usually $n = 1$), the intensity maximum for the certain wavelength is located at an angle of φ:

$$g \sin \varphi = n\lambda \tag{3.27}$$

The diffracted light is then imaged by a focusing mirror ($f = 270$ mm) onto a *Andor* iDus 420 CCD camera. Due to different diffraction angles, each wavelength hits the CCD array at a different position. For each pixel, the corresponding wavelength can be calculated. The spectral resolution is limited by the pixel size, which is 26×26 µm. When using the 1/1200 mm grating, the resolution is 0.07 nm and the maximum spectral range that can be observed with one grating position is 65 nm. With the 1/300 mm grating, the resolution is 0.3 nm and the maximum spectral range is 260 nm.

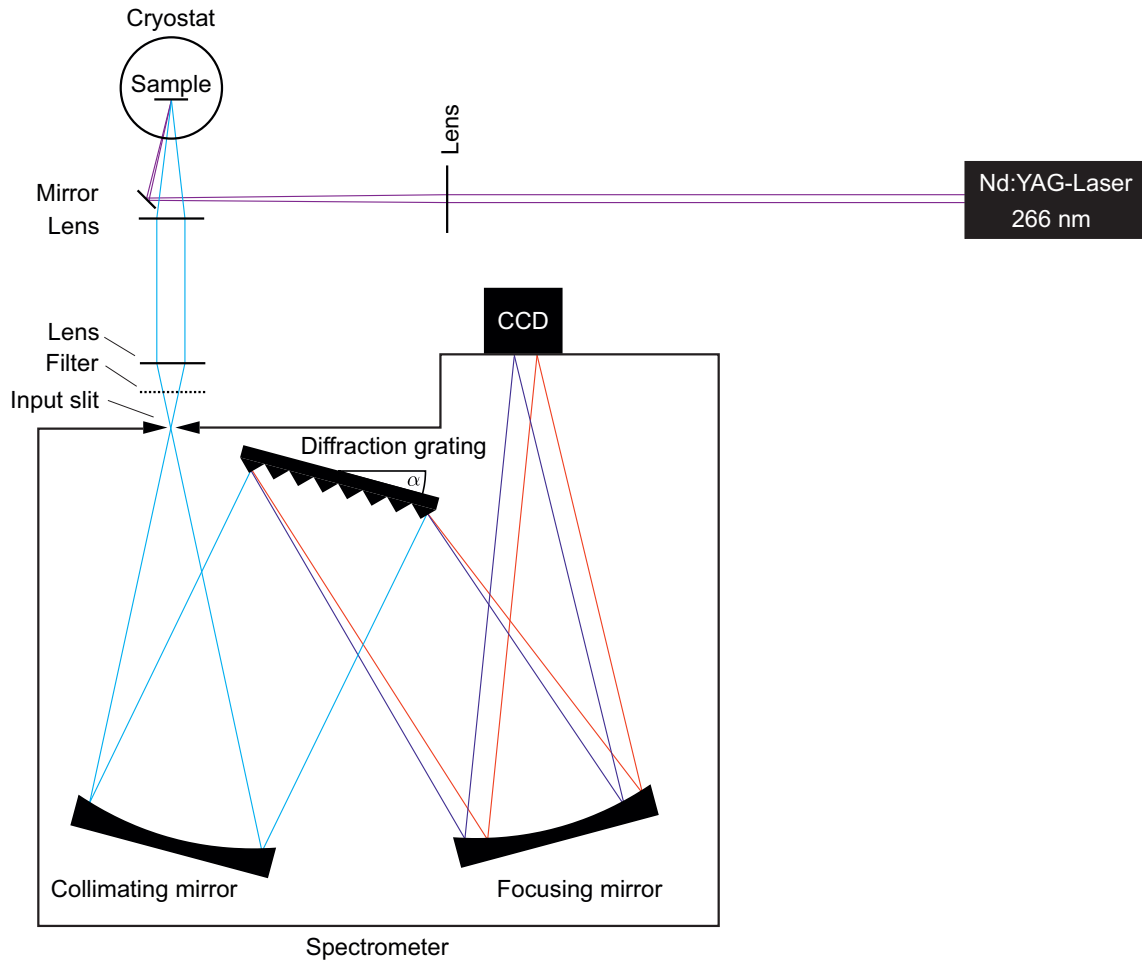**Figure 3.14:** Schematic illustration of the photoluminescence spectroscopy setup.

3.3 Intersubband absorption

Absorption measurements are performed to investigate the intersubband transitions of c-GaN/AlN superlattice (SL) structures. As mentioned in section 2.4, intersubband transitions can only be induced by TM-polarized light, i.e., the electric field is parallel to the QW growth direction. Thus, absorption measurements cannot be performed with light under normal incidence to the sample surface, but the light has to be coupled into the sample sideways. A waveguide structure as sketched in Figure 3.15 is fabricated, which on the one side ensures that part of the light fulfills the polarization requirement, and on the other side effects multiple passes of the light through the SL structure by total reflection at the sample surfaces. For the typical sample geometry, i.e., a sample length of approximately 10 mm, height of 0.5 mm, and facet angle of 30°, the light passes the SL structure around 30 times. For the chosen angle of 30° total reflection occurs at the interfaces Si/Air and AlN/Air, but not at other interfaces as Si/SiC [114].
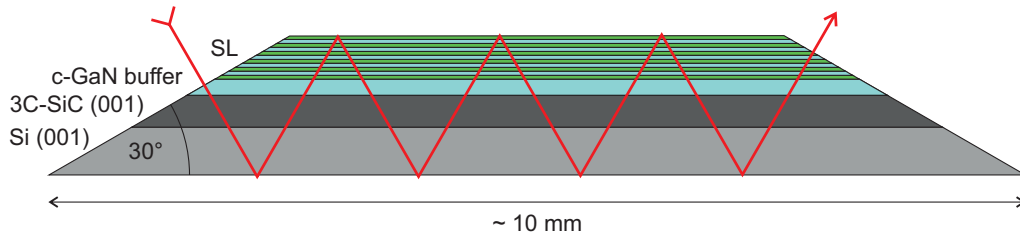
Figure 3.15: Waveguide structure for intersubband absorption measurements of SL samples. Dimensions are not to scale.

3.3.1 Sample preparation

After growth, two opposing sample edges are ground, so that facets of 30° with respect to the surface plane are created. A sample holder is used for grinding, which allows fabrication of the facets at the exact angle. Facets are initially ground roughly using a P80 sandpaper, and then subsequentially polished using P1200 and P2400 SiC sandpapers. Also the backside of the substrate needs to be polished to avoid loss of light due to scattering. A photo of a prepared waveguide sample is shown in Figure 3.16.
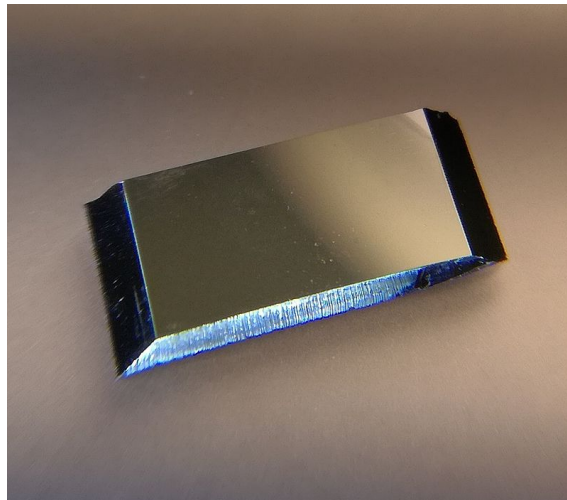

Figure 3.16: Waveguide sample. Photo by Jan Mundry, TU Dortmund University.

3.3.2 Measurement setup and procedure

There are two similar measurement setups for the investigation of intersubband absorption: one is located at Paderborn University and the other one at TU Dortmund University. Samples are measured at both setups, but in this work only measurements from TU Dortmund University (measured by Jan Mundry) are shown due to higher sensitivity. A sketch of the setups is shown in Figure 3.17. The broadband infrared light emitted by a stabilized tungsten light source passes a linear polarization filter and is then directed onto one of the sample's facets. At the other facet, the exiting light beam is collected by a fiber. After exiting the fiber, the light beam passes a chopper, which modulates the signal. The beam is then coupled into a spectrometer and detected by an InGaAs photodiode located
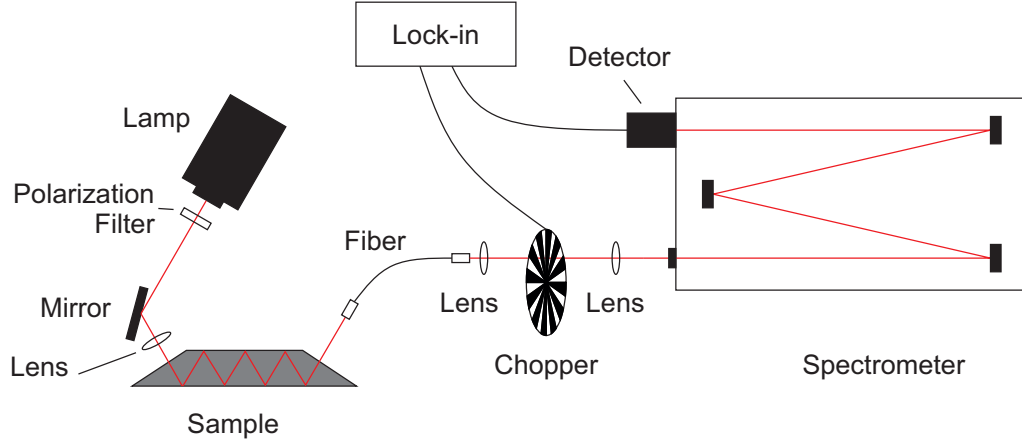
Figure 3.17: Sketch of the intersubband absorption measurement setup at Paderborn University. See also [114].

at the exit of the spectrometer. With help of a lock-in amplifier the modulated signal is amplified while suppressing noise signals, and afterwards measured by a digital voltmeter.

The measurement procedure is as follows. The spectrum transmitted through the sample is measured both with TE and TM polarization of the incident light, by rotating the polarization filter by 90° between the two measurements. Furthermore, for both polarizations the transmission spectrum of a reference sample is measured. This reference sample is grown on the same substrate as the SL samples, but only consists of a c-GaN layer. The measured spectra of the SL sample are then normalized by dividing them by the reference spectra measured using the respective polarization ($I(\lambda)$ are the intensities measured at a certain wavelength λ):

$$I_{\text{TE,norm}}(\lambda) = \frac{I_{\text{TE,SL}}(\lambda)}{I_{\text{TE,ref}}(\lambda)} \qquad\qquad I_{\text{TM,norm}}(\lambda) = \frac{I_{\text{TM,SL}}(\lambda)}{I_{\text{TM,ref}}(\lambda)} \tag{3.28}$$

Finally, the absorption $\alpha(\lambda)$ of the SL sample is obtained by calculating the difference between the TM and TE spectrum and normalizing it to the TE spectrum, as intersubband absorption is only allowed for TM polarization:

$$\alpha(\lambda) = \frac{I_{\text{TM,norm}}(\lambda) - I_{\text{TE,norm}}(\lambda)}{I_{\text{TE,norm}}(\lambda)} \tag{3.29}$$

CHAPTER 4

Results and discussion

In this chapter the experimental results are presented and discussed. First, the influence of the layer thickness of c-GaN on the structural properties is discussed. Next a calibration procedure for TOF-SIMS is presented, which allows to quantify the amount of Ge in doped c-GaN layers. Afterwards a comparison of Ge- and Si-doping of c-GaN is given, followed by an extensive discussion of Ge as a dopant in c-Al$_x$Ga$_{1-x}$N. The reduction of the growth rate, which is observed at high dopant fluxes, is covered in a separate section. Finally, the analysis of Ge-doped SL structures, which are fabricated with the aim to obtain intersubband absorption in the infrared spectral range, is presented.

4.1 Influence of layer thickness on structural properties

The thickness of epitaxial layers is a parameter, that can critically influence other properties of the layer such as the dislocation density or the surface roughness. The heteroepitaxial growth of layers that have a lattice mismatch to the substrate causes the emergence of dislocations. Dislocations are formed to reduce the stress that is induced due to the growth of strained layers. According to the *glide model* introduced by Ayers [115], the dislocation density is reduced with increasing layer thickness due to the coalescence of dislocations that occurs when two dislocation lines meet. An inverse proportional relation between dislocation density D and layer thickness d is predicted: $D \propto d^{-1}$. For c-GaN layers on free-standing 3C-SiC substrates, this relation could be verified experimentally [14]. However, in this work 3C-SiC/Si substrates are used. The dislocation densities of numerous c-GaN layers of different thickness on 3C-SiC/Si substrates are determined. HRXRD rocking curves of the (002) reflections were measured, which can be used to estimate the dislocation densities of epitaxial layers. From the full width at half maximum (FWHM) $\Delta\theta$ of these curves the dislocation density D is estimated by [103]

$$D = \frac{\Delta\theta^2}{9b^2}, \tag{4.1}$$

where b is the length of the Burgers vector. For 60° dislocations in c-GaN the length of the Burgers vector is $b = a/\sqrt{2}$ [116]. Layer thicknesses are measured by reflectometric interference spectrometry (see Figure B.5 on page 131). The obtained dislocation densities are plotted versus the layer thickness on a double-logarithmic scale in Figure 4.1(a). A $D \propto d^{-1}$ function fitted to the data (red line), but it does not reflect the values well. Instead, a $D \propto d^{-0.5}$ relation is found here (blue line).

Assuming that layer-by-layer growth occurs, one would expect that layers feature

extremely smooth surfaces. In reality however, subsequent layers will begin to nucleate before the present layer is fully closed. Thus, with increasing layer thickness the number of unfinished layers increases, which manifests itself in an increasing surface roughness. The root mean square (RMS) surface roughness S_q of c-GaN layers is determined from atomic force microscope (AFM) scans performed in 10×10 µm^2 and 5×5 µm^2 areas. The roughness values are plotted versus the layer thickness in Figure 4.1(b). A linear dependence is found (dashed lines), and values in general don't differ between the scans performed in different area sizes. A roughness of $1.5\,\mathrm{nm}$ is measured for the thinnest investigated layer ($d = 74\,\mathrm{nm}$), and a value of $12\,\mathrm{nm}$ is measured for a $1\,\mathrm{µm}$ thick layer. For comparison, the 3C-SiC substrates have typical roughness values around $0.5\,\mathrm{nm}$ to $1\,\mathrm{nm}$. Additionally, the substrate roughness also influences the roughness of the grown layer. Some layers deviate from the linear trend, because Ga droplets, which are formed due to too high Ga fluxes, drastically increase the roughness.
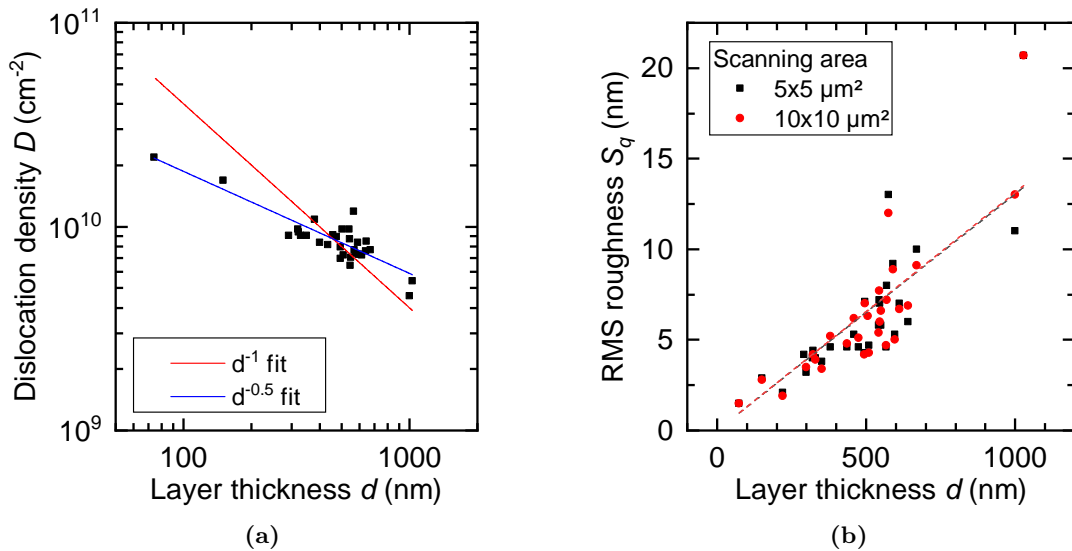

Figure 4.1: Layer thickness dependence of **(a)** the dislocation density determined by HRXRD and **(b)** the surface roughness measured by AFM of c-GaN layers grown on 3C-SiC/Si (001) substrates. Part of the data is taken from samples from [117].

4.2 Calibration of the TOF-SIMS Ge-signal

Parts of this section have been published in Ref. 52.

TOF-SIMS provides depth-resolved analysis of the composition of epitaxial layers. The obtained information is the signal intensity output of the detector for a given ion mass. The signal intensity depends on a variety of factors, e.g., the element-specific ion yield, the surrounding matrix of a lattice atom (e.g., Ge in c-GaN), and parameters influenced by the TOF-SIMS instrument itself. In order to obtain quantitative information on the layer composition, a calibration of the signal intensities needs to be performed. The calibration is only valid for the respective ion species and for the instrument in use. In this work there is particular interest in quantifying the Ge distribution within c-GaN and c-Al$_x$Ga$_{1-x}$N

layers, thus a calibration of the Ge signal was performed. Therefore one needs to provide layers, whose Ge concentration is well known. This can for example be achieved by ion implantation. Two different ion implanters at the RUBION at Ruhr-University of Bochum were used to implant Ge ions into not intentionally doped (n.i.d.) 580 nm thick c-GaN layers (Sample number GND2669). A 100 kV ion accelerator was used to implant ^{72}Ge at low energies of 95 keV to achieve shallow implantation. A 4 MV tandem accelerator was used to implant ^{74}Ge at higher energies of 750 keV to achieve deep implantation profiles. Additionally, the ion fluence was varied. Thus it is possible to achieve Ge concentrations over several orders of magnitude, and different Ge isotopes can be used for analysis. Samples are tilted slightly for implantation to avoid channeling effects. The implantation parameters are summarized in Table 4.1. The distribution of implanted ions within the layers is simulated using the SRIM-2013 software [118].

Figure 4.2 shows the implantation profiles obtained for ion energies of 95 keV and 750 keV. The calculated quantity is the density of Ge ions per fluence. Thus, to obtain values for the Ge concentration the y-axis values have to be multiplied by the respective ion fluence Φ.

After ion implantation the TOF-SIMS depth profiles are measured. In Figure 4.3 the depth profiles of implantation samples A (left panel) and B (right panel) are shown. The graphs represent the signal intensity of different secondary ions versus sputter time. The sputter time is linearly proportional to the distance from the sample surface. For better clarity only the GaN$^-$ and the Ge$^-$ and GeN$^-$ signals of the respective Ge isotope are displayed. The GaN$^-$ signal is constant throughout the entire c-GaN layer and begins to

Table 4.1: Parameters for Ge ion implantation into c-GaN.

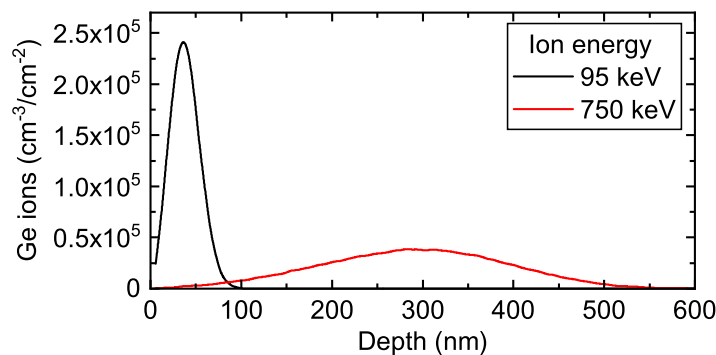| Implantation sample	Isotope	Ion energy (keV)	Fluence Φ (cm^{-2})	Angle of incidence
A	^{72}Ge	95	1.6×10^{15}	$7\,^\circ$
B	^{74}Ge	750	1.0×10^{15}	$7\,^\circ$
C	^{74}Ge	750	1.0×10^{14}	$7\,^\circ$

Figure 4.2: Implantation profiles (Ge ions per fluence) of Ge in cubic GaN simulated by SRIM-2013 [118] for an angle of incidence of $7\,^\circ$ and ion energies of 95 keV and 750 keV.
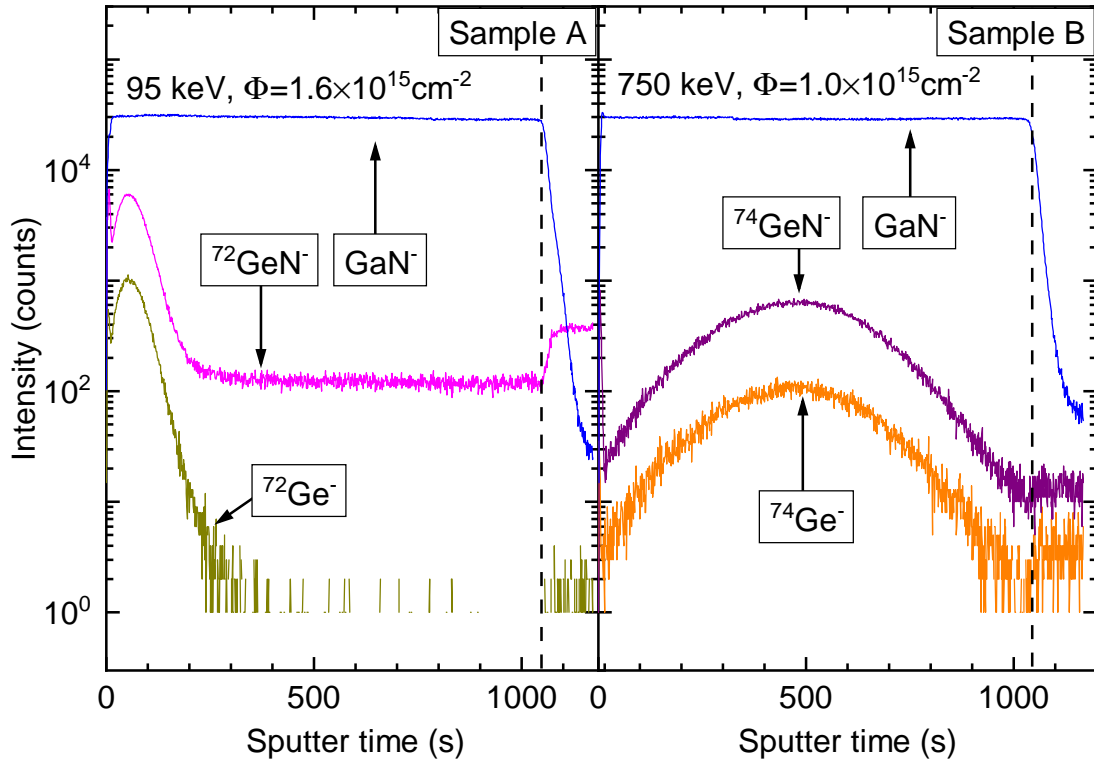
Figure 4.3: TOF-SIMS depth profiles of ion-implanted c-GaN layers.

drop at approximately 1050 s, when the transition between c-GaN and 3C-SiC is reached. The ^{72}Ge$^-$ and ^{74}Ge$^-$ signals recorded for samples A and B, respectively, directly resemble the simulated ion distribution as seen in Figure 4.2. The ^{74}GeN$^-$ signal from sample B runs proportional to the ^{74}Ge$^-$ signal, but features an approximately six times higher sensitivity and thus is preferably taken for evaluation. This in principle also holds for the relation between the ^{72}Ge$^-$ and ^{72}GeN$^-$ signals from sample A, but here the ^{72}GeN$^-$ signal is overlapped by a GaN-related signal, resulting in the ^{72}GeN$^-$ signal not dropping to zero like the ^{72}Ge$^-$ signal does.[1] However, the constant GaN-related contribution can be subtracted from the ^{72}GeN$^-$ signal, which enables to use the higher-sensitivity GeN$^-$ signal for evaluation also in this case.

To perform the calibration, the maximum of the GeN$^-$ signals is determined by performing a peak fit. The ^{72}GeN$^-$ intensity from sample A is corrected by the constant background and furthermore corrected by the natural abundance of Ge isotopes (see Table 4.2) to obtain an intensity equivalent to ^{74}GeN$^-$ from samples B and C. To account for slightly varying sputter parameters, the signal are normalized to the respective ^{69}GaN$^-$ intensity.

---

1   In the appendix on page 128 the depth profile of a n.i.d. c-GaN layer is shown with focus on Ge-related signals to further illustrate this phenomenon.

Table 4.2: Naturally occuring isotopes of Germanium. All but ^{76}Ge, which has a half-life of over 10^{21} years, are stable. [119]

Isotope	Atomic mass (u)	Natural abundance
^{70}Ge	69.924252	21.2 %
^{72}Ge	71.922082	27.7 %
^{73}Ge	72.923462	7.7 %
^{74}Ge	73.921181	35.9 %
^{76}Ge	75.921405	7.4 %

The normalized intensities are then correlated with the maximal ^{74}Ge concentrations, which are obtained from the SRIM-2013 simulations, see Figure 4.4. By performing a linear fit a proportionality factor of $k = 1.5695 \times 10^{21}\,\mathrm{cm}^{-3}$ is obtained. This factor must be corrected by the natural abundance of ^{74}Ge to get the total Ge concentration.

In summary, the following steps are necessary to extract the actual Ge concentration from a TOF-SIMS depth profile: Calculate the ^{74}GeN^{-}/^{69}GaN^{-} intensity ratio, multiply the ratio by the calibration factor $k = 1.5695 \times 10^{21}\,\mathrm{cm}^{-3}$, and multiply by the abundance correction factor $1/0.359 \approx 2.79$.
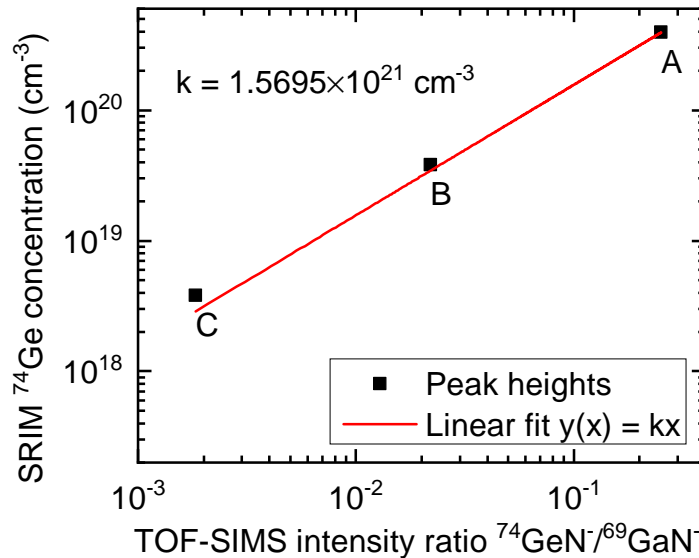

Figure 4.4: Correlation of SRIM-simulated maximal ^{74}Ge concentrations and ^{74}GeN^{-} to ^{69}GaN^{-} signal intensity ratios from TOF-SIMS measurements.

4.3 Ge- and Si-doping of c-GaN

Parts of this section have been published in Refs. 51, 52, and 53.

The properties of Ge and Si as n-type dopants in c-GaN are in part already discussed in my Master's thesis [120], thus only a short summary of topics covered there is given at this point. Extended TOF-SIMS measurements and doping of layers with Ge and Si near the doping limit however are completely new and will be covered in greater detail. Also effects of high doping on the growth rate are discussed here considerably more extensive, see section 4.5.

Two series of c-GaN samples were grown. Ge-doped layers were grown with the Ge effusion cell temperature T_{Ge} varying from 600 °C to 1000 °C, which resulted in nominal Ge concentrations in the range 10^{14} cm^{-3} to 10^{20} cm^{-3}. For comparison, highly Si-doped layers were grown utilizing effusion cell temperatures T_{Si} from 950 °C to 1100 °C. The resulting donor concentrations are expected to be in the range from 10^{17} cm^{-3} to 10^{19} cm^{-3}. Layers with even higher doping levels are discussed in section 4.3.5. Furthermore, a n.i.d. layer was grown. Basic sample parameters are listed in Table 4.3. The Ge- and Si-fluxes given there were calculated based on eq. 2.17 and the vapor pressure curves printed in the appendix (Figure B.1 on page 127). The estimated donor concentrations are given as follows: The values for the two highest Ge-doped samples and the highest Si-doped sample (printed in bold) were determined by room temperature Hall effect measurements. For this purpose it is assumed that all donors are ionized in these layers, which means that the measured free electron concentration is equal to the donor concentration. Donor concentrations of lower doped samples (printed in italics) were extrapolated based on the dopants vapor pressure curves. TOF-SIMS donor concentrations are determined using the

Table 4.3: Basic sample parameters and characterization results of Ge- and Si-doped c-GaN layers. Bold values for estimated donor concentrations are measured by Hall effect, values in italics are extrapolated from vapor pressure curves. Donor concentrations determined by infrared spectroscopic ellipsometry (IRSE) from [121].

Sample number	Dopant	Cell temp. (°C)	Flux (cm^{-2} s^{-1})	Estimated donor concentration (cm^{-3})	TOF-SIMS donor concentration (cm^{-3})	IRSE donor concentration (cm^{-3})	Hall mobility (cm^2 V^{-1} s^{-1})	Thickness (nm)
2518	n.i.d.							612
2521	Ge	600	1.8×10^6	*1.7×10^{14}*	1.5×10^{18}			588
2536	Ge	650	3.1×10^7	*3.0×10^{15}*				552
2520	Ge	700	3.4×10^8	*3.2×10^{16}*	3.6×10^{18}			556
2535	Ge	750	3.3×10^9	*3.1×10^{17}*				558
2522	Ge	800	2.9×10^{10}	*2.7×10^{18}*	6.0×10^{18}	2.3×10^{18}	105	543
2523	Ge	900	9.3×10^{11}	**8.7×10^{19}**	7.7×10^{19}	5.6×10^{19}	90	460
2524	Ge	1000	8.9×10^{12}	**3.7×10^{20}**	3.2×10^{20}	1.8×10^{20}	63	363
2513	Si	950	1.1×10^{10}	*3.0×10^{17}*				607
2510	Si	1000	6.2×10^{10}	*1.7×10^{18}*			84	647
2511	Si	1050	2.8×10^{11}	*7.6×10^{18}*		7.8×10^{18}	74	611
2512	Si	1100	1.4×10^{12}	**3.8×10^{19}**		2.8×10^{19}	77	564

calibration presented in section 4.2. Layer thicknesses given in the table are determined by reflectometric interference spectroscopy. Due to reduced growth rates at high Ge fluxes, the thickness of highly Ge-doped layers is reduced. This effect is covered in section 4.5.

4.3.1 TOF-SIMS depth profiles

TOF-SIMS depth profiles of c-GaN:Ge layers were recorded to verify the incorporation of Ge into the layers and to get information on unintentionally incorporated elements. First, the focus is put on the Ge incorporation. In Figure 4.5 the TOF-SIMS depth profile of the highest Ge-doped sample of this series is shown ($n_{Ge} = 3.7 \times 10^{20}\,\mathrm{cm}^{-3}$). For better clarity, only signals related to Ge are displayed. Additionally, the $^{69}\mathrm{GaN}^-$ signal is plotted serving as a reference, and the $\mathrm{Si}_2\mathrm{C}_2{}^-$ signal is plotted representing the 3C-SiC substrate. The dashed line indicates the epilayer-to-substrate transition. Secondary ion signals of all five naturally occurring Ge isotopes are found (cf. Table 4.2), which on the one hand proves the incorporation of Ge into the layer, and on the other hand can be utilized to analyze the composition of the Ge source material used for epitaxy. Therefore, it is assumed that the sensitivity for all isotopes is equal. The signals are averaged over the entire c-GaN layer and the ratio of the signal intensities is calculated.
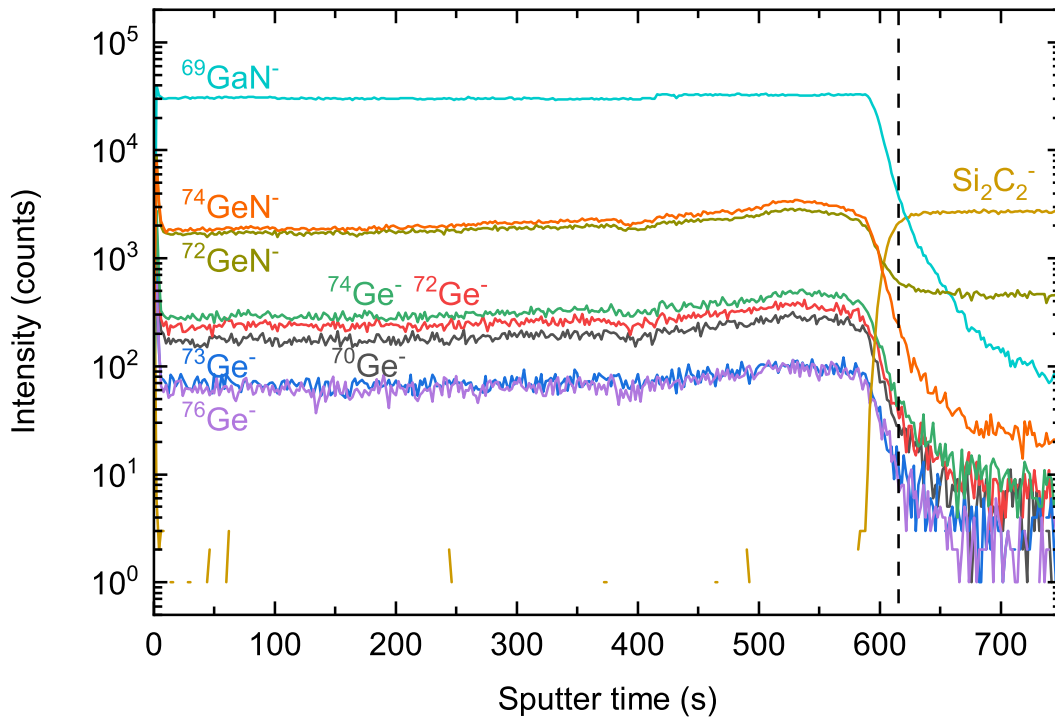

Figure 4.5: TOF-SIMS depth profile of sample GND2524 with focus on the Ge-related signals.
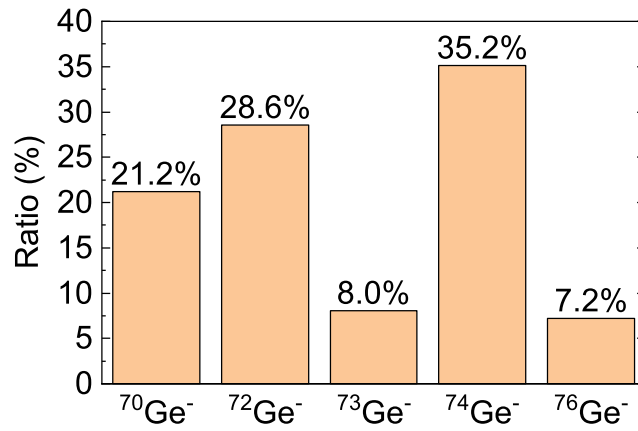
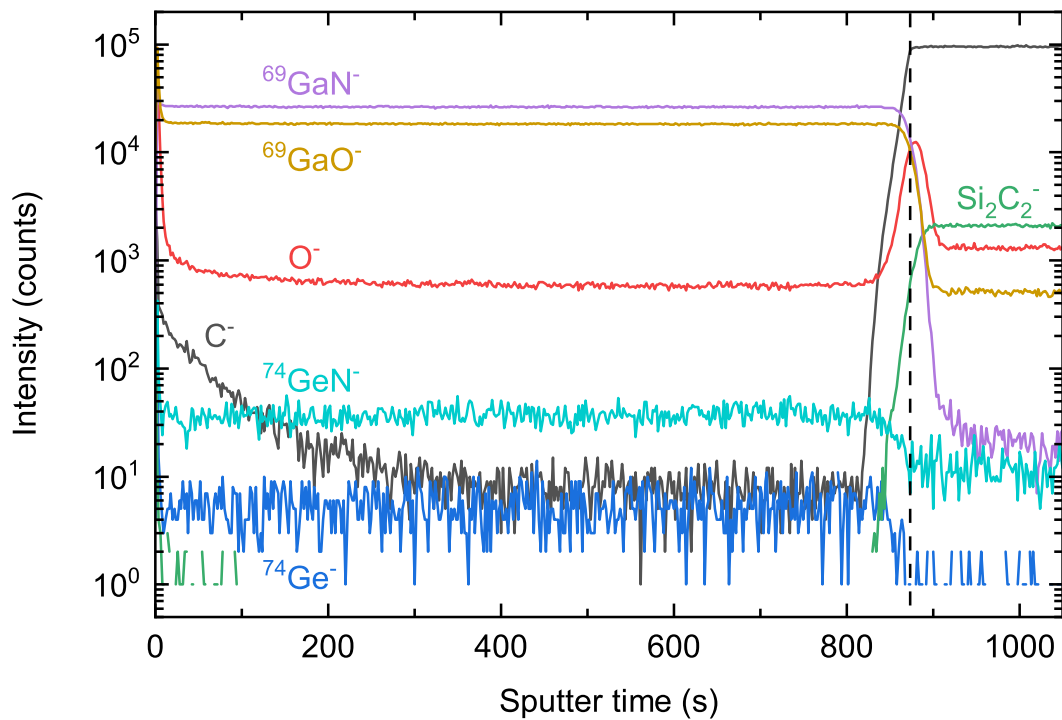**Figure 4.6:** Ratio of Ge isotopes extracted from the TOF-SIMS depth profile of sample GND2524.

Figure 4.7: TOF-SIMS depth profile of sample GND2522 with focus on the impurity-related signals.

As it is displayed in Figure 4.6, the isotopic ratio of Ge in this layer is almost identical to the natural abundance given in Table 4.2. Furthermore it can be seen that the sensitivity of $^{74}GeN^-$ is about six times higher than that of $^{74}Ge^-$, as it has been described in section 4.2.

Now focus is put on impurity-related secondary ion signals in c-GaN layers. In Figure 4.7 the depth profile of a medium doped sample ($n_{Ge} = 2.7 \times 10^{18}\,cm^{-3}$) is displayed. Also here the $^{69}GaN^-$ signal is plotted as a reference to account for deviating sputter parameters and the $Si_2C_2^-$ signal representing the 3C-SiC substrate. Signals from $^{74}Ge^-$ and $^{74}GeN^-$ again prove the incorporation of Ge. $^{69}GaO^-$ and O^- signals clearly indicate the incorporation of O into the layer, which causes an unintentional n-type doping [50]. Furthermore, a signal of C^- secondary ions is observed. The signal rises in intensity towards the sample surface, possibly caused by surface contamination, but drops to a constant level well above the noise level after a while. C acts as an acceptor in c-GaN and causes an unintentional p-type doping [50, 54]. A quadrupole mass spectrum of the growth chamber during c-GaN growth is attached in the appendix on page 129, Figure B.3. It shows that O and C impurities could be incorporated from the residual gas. Also the N plasma source is an origin for unwanted O, which can be seen in Figure B.4 (page 130), where the residual gas analysis during operation of the plasma source is shown. It should be noted that when comparing secondary ion signals corresponding to different elements, higher signal intensities do not imply higher element concentrations, because signal intensities depend on the element-specific ion yield.

By using the calibration of the $^{74}GeN^-$ signal presented in section 4.2, the Ge concentrations can be determined from the TOF-SIMS depth profiles. The results are listed in Table 4.3.

4.3.2 Structural properties

HRXRD and AFM measurements were performed to investigate the structural properties of the Ge- and Si-doped c-GaN layers. HRXRD rocking curves of the (002) reflections were recorded to estimate the dislocation densities after eq. 4.1. Dislocation densities of the undoped layer, and Ge-doped as well as Si-doped layers up to donor concentrations $1 \times 10^{19}\,cm^{-3}$, are in the range of 7 to $9 \times 10^9\,cm^{-2}$. With further increased doping, dislocation densities begin to rise. The $3.8 \times 10^{19}\,cm^{-3}$ Si-doped sample has a dislocation density of $1.2 \times 10^{10}\,cm^{-2}$, and the dislocation densities of the $8.7 \times 10^{19}\,cm^{-3}$ and $3.7 \times 10^{20}\,cm^{-3}$ Ge-doped samples are $1.4 \times 10^{10}\,cm^{-2}$ and $3.0 \times 10^{10}\,cm^{-2}$, respectively. No significant difference between Ge- and Si-doped layers is found here. Reciprocal space maps (RSMs) around the (002) reflexes are gathered to evaluate the amount of hexagonal inclusions in c-GaN layers. Hexagonal inclusions mainly grow on (111) facets of c-GaN [14], and their ($\bar{1}011$) and ($10\bar{1}1$) reflections appear in the vicinity of the c-GaN (002) reflection. As an example, the (002) RSM of the highest Ge-doped layer is shown in Figure 4.8. The areas, where hexagonal reflections would appear, are indicated by red ellipses. No intensity is recorded in these areas, which means the amount of hexagonal GaN in this layer is below the detection limit of $< 1\,\%$. No hexagonal inclusions could be found in any of the other Ge- and Si-doped layers either.

AFM was performed to image the surface topography and determine the surface roughness of the layers. Measurements were performed in contact mode in an area of $10 \times 10\,\mu m^2$

and the RMS roughness S_q was calculated from the obtained surface height profiles. The surface roughnesses are plotted over the respective Ge and Si donor concentration in Figure 4.9(a). Values for the n.i.d. and Ge-doped samples range between 4 nm and 6 nm, which are commonly measured for c-GaN layers of comparable thickness. For comparison, the 3C-SiC substrate roughness is (0.75 ± 0.25) nm. A reduction of surface roughness is observed for the 8.7×10^{19} cm^{-3} Ge-doped layer (2.4 nm) and Si-doped layers in the doping range of 10^{19} cm^{-3}. In Figure 4.9(b) the surface topography of the highest Ge-doped layer (3.7×10^{20} cm^{-3}) is shown. An accumulation of material in shape of droplets can be seen along distinct lines. These are most likely antiphase boundaries (APBs), which are commonly observed on c-GaN layers (see section 2.3.3). The droplets are only present on the two highest Ge-doped layers, but not on Si-doped, lower Ge-doped, or n.i.d. layers of this series. They are however also present when Si-doping near the doping limit is applied (see section 4.3.5). Thus it is assumed that the excess material is dopant-related. Unfortunately, this assumption could not yet be confirmed using energy-dispersive X-ray spectroscopy (EDX) equipped to either a scanning electron microscope (SEM) or a transmission electron microscope (TEM).

4.3.3 Electrical properties

For the electrical characterization of doped c-GaN, room temperature Hall effect measurements in van der Pauw geometry were performed. The 3C-SiC substrate exhibits n-type conductivity with a free carrier concentration of 1.6×10^{16} cm^{-3}, and the underlying Si is highly resistive. As the 3C-SiC thickness is over one order of magnitude larger than the c-GaN thickness, it is expected that only for highly doped c-GaN the current flow is dominated by the c-GaN layer. By using a two-layer model, for the n.i.d. c-GaN layer p-type conductivity with a free hole concentration of 4.7×10^{16} cm^{-3} is found. P-type conductivity is caused by 60° dislocations, which are electrically active by acting as electron traps [116, 122], and by C incorporated as an acceptor. The two highest Ge-doped and the highest Si-doped layers are expected to be degenerately doped (see optical measurements), and thus the measured free electron concentration of these layers is equal to the donor concentration. The respective values are printed in Table 4.3 (bold values in *estimated donor concentration* column). Furthermore, electron mobilities of highly doped layers were determined, see Table 4.3. The highest electron mobility measured for Ge-doped layers is 105 cm^2 V^{-1} s^{-1} at $n_{Ge} = 2.7 \times 10^{18}$ cm^{-3}, whereas the mobility of a comparably high Si-doped layer ($n_{Si} = 1.7 \times 10^{18}$ cm^{-3}) is only 84 cm^2 V^{-1} s^{-1}. With increased doping, electron mobilities begin to drop due to scattering at impurities [123]. The electron mobility at highest Ge doping (3.7×10^{20} cm^{-3}) is reduced to 63 cm^2 V^{-1} s^{-1}, and at highest Si doping (3.8×10^{19} cm^{-3}) it is reduced to 77 cm^2 V^{-1} s^{-1}. Overall, mobilities of Ge-doped layer are approximately 20 % higher than those of Si-doped layers with comparable doping level.

4.3.4 Optical properties

Photoluminescence (PL) spectra of Ge- and Si-doped layers are recorded at 13 K. Figure 4.10(a) shows the spectra of Ge-doped layers and the n.i.d. sample. Spectra are normalized and shifted vertically. The c-GaN band gap $E_g = 3.2928$ eV [23, 33] is indicated

by a dashed line. As it can be seen best on the basis of the n.i.d. layer, the main emission consists of three peaks (see also Figure 4.10(b)). The near band edge peak is attributed to the recombination of bound excitons (BX) [124, 125]. The next peak at lower energies is related to a donor-acceptor pair recombination (D^0,A^0) [124], and a second donor-acceptor pair recombination $(D^0,A^{0'})$ is visible at even lower energies [54, 58]. Weak defect-related luminescence is observed below 3 eV. With increasing doping up to 10^{18} cm^{-3}, the (D^0,A^0) transition shifts to higher energies due to coulomb interaction between donors and acceptors [107, p. 606], while the (BX) peak does not shift. The (D^0,A^0) energy of the n.i.d. layer is drawn as a dotted line as a guide to the eye. The (D^0,A^0) transition energy is given by eq. 3.26 with $E_D = 30$ meV and $E_A = 130$ meV the donor and acceptor binding energy, respectively, $\varepsilon_r = 9.44$ the relative permittivity of c-GaN, and r the mean distance between donors and acceptors [23]

$$r = \sqrt[3]{\frac{3}{4\pi N_D}}.$$ (4.2)

When the Ge flux is further increased, samples become degenerately doped, resulting in a blue-shift of the emission and spectral broadening. As stated in section 2.2.3 there are two competing effects that become relevant at high doping levels: band gap renormalization (BGR) and Burstein-Moss shift (BMS). In c-GaN, these effects begin to occur at free electron concentrations of around 10^{18} cm^{-3} (see Figure 4.11), with BMS being the dominant effect, resulting in the observed blue shift of emission.

Figure 4.10(b) compares the 13 K PL spectra of a Ge-doped and a Si-doped layer with comparable donor concentrations. Emission intensities and intensity ratios of the peaks are almost identical for both layers. The spectral width of the individual peaks however is slightly smaller in case of the Si-doped layer. The FWHM of the (D^0,A^0) emission from the Ge-doped layer is 62 meV, whereas it is 50 meV for the Si-doped layers. Possible reasons for the narrower linewidth are the greater thickness and slightly smaller dislocation density of the Si-doped layer.

Temperature dependent PL measurements were performed for the 3.2×10^{16} cm^{-3} Ge-doped layer in the range of 13 K to 300 K. The spectra are plotted in Figure 4.12. With rising temperature, the overall emission intensity drops, with the intensities of the donor-acceptor peaks dropping stronger than the intensity of the exciton peak. Also the spectra move to lower energies with rising temperature. Figure 4.13(a) is an Arrhenius plot of the integral peak intensities. Intensities are plotted logarithmically over the reciprocal temperature. For processes with a single non-radiative recombination mechanism the temperature-dependent intensity can be calculated after [126]

$$I(T) = \frac{I_0}{1 + a \exp\left(\frac{-E_a}{k_B T}\right)}$$ (4.3)

where I_0 and a are constants, k_B is Boltzmann's constant and E_a is the activation energy of the respective process. By fitting this function to the measured integral intensities, activation energies of 23.9 meV and 24.2 meV are obtained for the (D^0,A^0) and $(D^0,A^{0'})$

transitions, respectively. At low temperatures an activation energy of $E_{BX} = 7.7\,\text{meV}$ is obtained for the (X) transition, which is ascribed to the transition of donor-bound to free excitons. At higher temperatures a second activation energy of $E_X = 24\,\text{meV}$ is found (not shown here), which is the exciton binding energy. After Haynes' rule the correlation between exciton-to-donor binding energy E_{BX} and the donor binding energy E_D is [127, 128]

$$E_{BX} = a_1 + a_2 E_D \tag{4.4}$$

where $a_1 = 0$ and $a_2 = 0.214$ for GaN [129]. From this a binding energy of $E_{Ge} = 36\,\text{meV}$ is estimated for the Ge donor.

Figure 4.13(b) shows the temperature-dependent peak energies of the (X) and (D^0,A^0) transitions. Energies of the exciton peaks are represented by blue triangles and energies of the donor-acceptor peak by red circles. The dotted blue curve displays the temperature dependence of the free exciton transition measured by photo-reflectivity [23]. At high temperatures, the exciton peak energies observed by PL are in accordance with this curve. In the range of temperatures below approximately $100\,\text{K}$ however the PL peak energies are lower than the free exciton transition energy, due to binding of the excitons to donors with a binding energy of $E_{BX} = 13\,\text{meV}$. This value deviates from the localization energy of excitons determined from Figure 4.13(a) for reasons not yet clarified. By adding the exciton binding energy of $E_X = 24\,\text{meV}$ to the free exciton energies, the temperature-dependent band gap of c-GaN is obtained (solid black curve). By shifting the band gap curve towards the donor-acceptor peak energies it becomes clear that in the range of $100\,\text{K}$ a transition between a donor-acceptor pair recombination (D^0,A^0) towards a band-acceptor recombination (e,A^0) occurs. An acceptor binding energy of $E_A = 97\,\text{meV}$ is determined, and considering a Coulomb interaction between donors and acceptors at a doping level of $3.2 \times 10^{16}\,\text{cm}^{-3}$ of about $10\,\text{meV}$ a binding energy of $36\,\text{meV}$ is determined for the Ge donor. This value is in excellent agreement to the value determined from the Arrhenius plot in Figure 4.13(a).

4.3.5 Limit of doping

A further set of layers was grown to approach the limit of doping using Ge or Si as dopants. Due to temporal distance and changed growth conditions compared to the sample series described above, the relation between dopant cell temperature and resulting donor concentration has slightly changed. Layer thicknesses are around $400\,\text{nm}$. A list of basic layer properties is given in Table 4.4.

The highest Ge effusion cell temperature of the first sample series, $T_{Ge} = 1000\,^\circ\text{C}$, resulted in a free electron concentration (measured by Hall effect at room temperature) of $3.7 \times 10^{20}\,\text{cm}^{-3}$. The reproduction of this layer in this second series resulted in a comparable free electron concentration of $3.1 \times 10^{20}\,\text{cm}^{-3}$. When T_{Ge} is further raised in steps up to $1030\,^\circ\text{C}$, there is hardly any effect on the free electron concentration within measurement inaccuracy. At even higher T_{Ge} of $1050\,^\circ\text{C}$ however no c-GaN growth is possible any more. According to the RHEED pattern polycrystalline growth occurs, and Hall effect measurements reveal *p-type* conductivity with a carrier density of $1.7 \times 10^{17}\,\text{cm}^{-3}$.
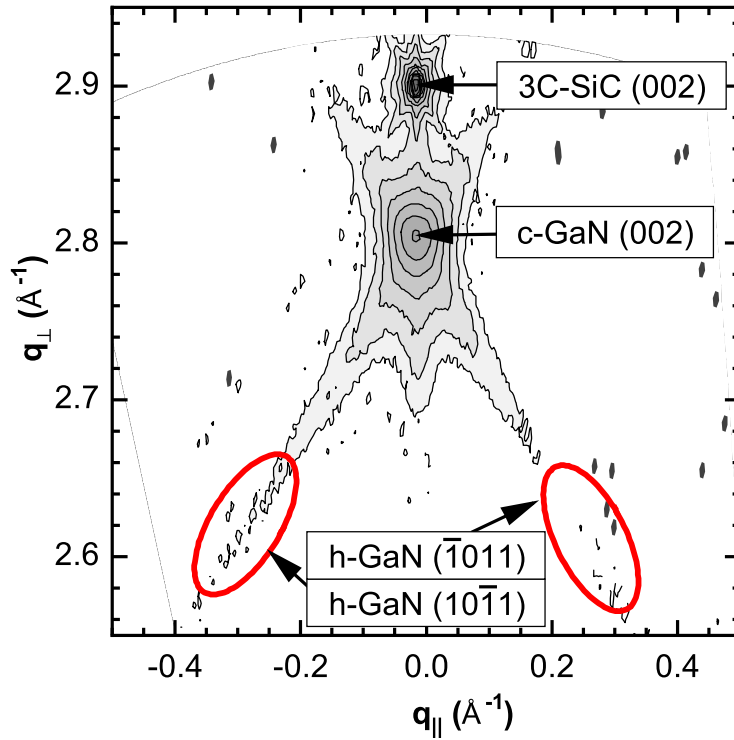
Figure 4.8: RSM around the c-GaN (002) reflection of the $3.7 \times 10^{20}\,\mathrm{cm}^{-3}$ Ge-doped layer (sample GND2524). Ellipses mark the spots where reflections of hexagonal inclusions would appear, if there are any. Hexagonal inclusions in this layer are below the detection limit of $1\,\%$.

Table 4.4: Basic sample parameters and characterization results of highly Ge- and Si-doped c-GaN layers.

Sample number	Dopant	Cell temp. (°C)	Flux (cm^{-2} s^{-1})	Hall carrier density (cm^{-3})	Hall mobility (cm^2 V^{-1} s^{-1})	PL Fermi level (eV)
2975	Ge	1000	8.9×10^{12}	3.1×10^{20}	66	3.80
2996	Ge	1010	1.5×10^{13}	3.3×10^{20}	61	3.85
2999	Ge	1020	2.7×10^{13}	3.2×10^{20}	63	3.80
3000	Ge	1030	3.8×10^{13}	2.9×10^{20}	55	3.78
2974	Ge	1050	5.8×10^{13}	1.7×10^{17a}		
2949	Si	1050	2.8×10^{11}	1.6×10^{19}	104	
2951	Si	1150	6.8×10^{12}	4.3×10^{20}	68	3.57
2946	Si	1200	1.8×10^{13}	4.3×10^{20}	73	3.73

---

a p-type conductivity

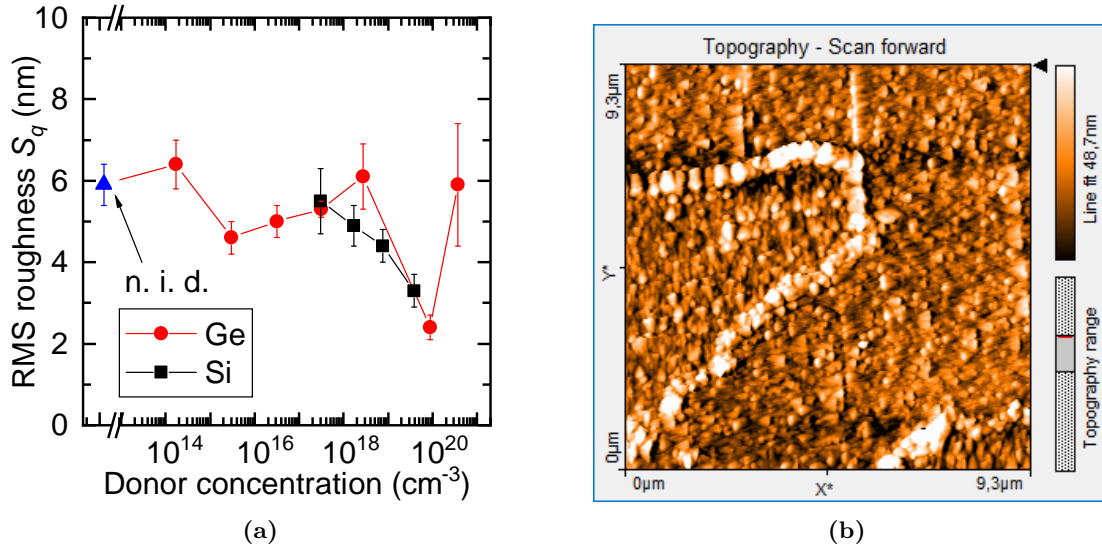(a)   (b)

Figure 4.9: **(a)** Root mean square roughness of Ge- and Si-doped c-GaN layers measured by AFM in a $10 \times 10\,\mathrm{\mu m^2}$ area. **(b)** AFM surface topography of the highest Ge-doped layer ($n_{Ge} = 3.7 \times 10^{20}\,\mathrm{cm^{-3}}$, sample GND2524). ⬜

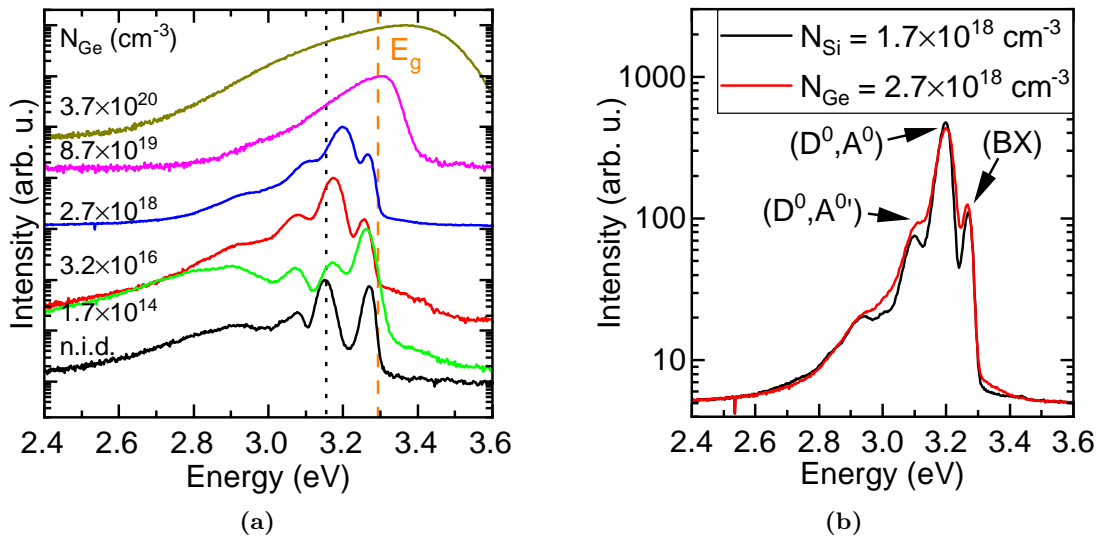(a)   (b)

Figure 4.10: **(a)** PL spectra of n.i.d. and Ge-doped c-GaN layers at $T = 13\,\mathrm{K}$. Intensities are normalized and spectra are shifted. The dashed line indicates the c-GaN band gap and the dotted line is the (D^0,A^0) transition energy of the n.i.d. layer. **(b)** Comparison of $13\,\mathrm{K}$ PL spectra of comparably Ge- and Si-doped layers. Intensities are *not* normalized here. ⬜
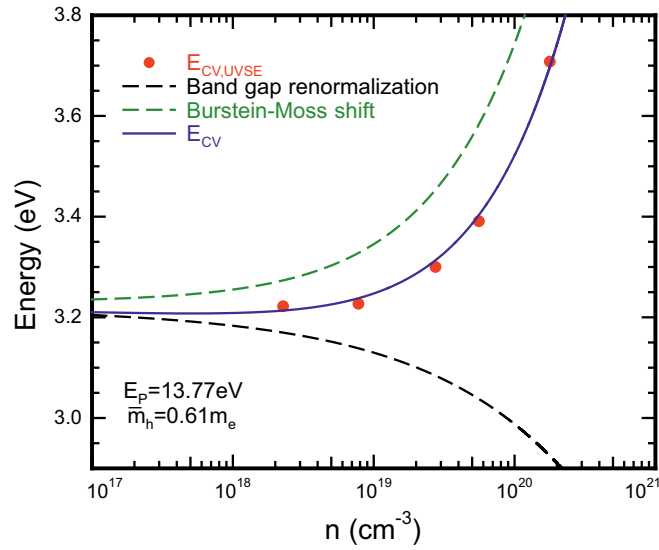
Figure 4.11: Contribution of band gap renormalization (BGR) and Burstein-Moss shift (BMS) to the conduction-to-valence band transition energy E_{CV} depending on the free electron concentration n in c-GaN. Transition energies obtained by ultraviolet spectroscopic ellipsometry are plotted as circles. [121]
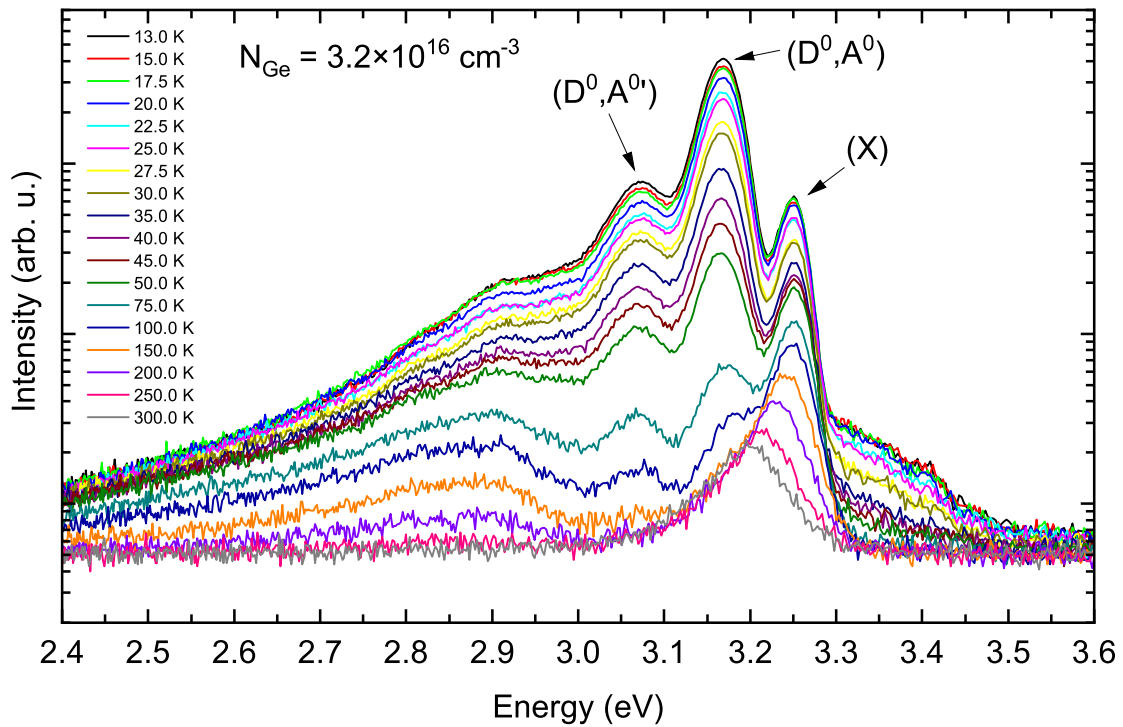

Figure 4.12: Temperature-dependent PL spectra of the $3.2 \times 10^{16}\,\mathrm{cm}^{-3}$ Ge-doped c-GaN layer.

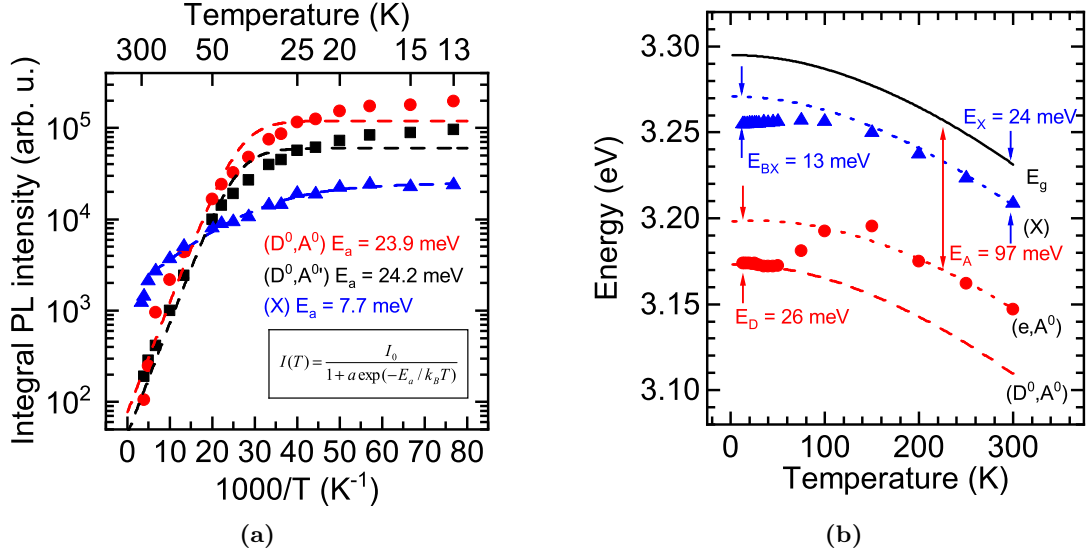**Figure 4.13:** **(a)** Arrhenius plot of the temperature-dependent integral PL peak intensities of the $3.2 \times 10^{16}\,\mathrm{cm^{-3}}$ Ge-doped c-GaN layer. **(b)** Temperature dependence of the PL peak energies.

As mentioned above, p-type conductivity in c-GaN is caused by $60°$ dislocations [116, 122]. Concerning Si-doping, effusion cell temperatures were also increased compared to the first sample series. Doping with effusion cell temperatures of $T_{Si} = 1150\,°\mathrm{C}$ and $T_{Si} = 1200\,°\mathrm{C}$ both result in the same free electron concentration of $4.3 \times 10^{20}\,\mathrm{cm^{-3}}$. This is thus assumed to be the maximum doping level achievable with Si. The reason why both for doping by Si and Ge the free electron concentration cannot be increased any more by raising the dopant flux is assumed to be autocompensation (see section 2.2.4). The tendency of amphoteric donors like Si and Ge to occupy the other lattice site (here the N site instead of Ga) rises at very high doping levels [44, p. 189]. Thus, they not only act as donors but also as acceptors, which compensate each other.

Layer quality is examined by HRXRD and AFM. In Figure 4.14(a) FWHMs of (002) rocking curves and the corresponding dislocation densities D calculated after eq. 4.1 are plotted over the free electron concentration measured by Hall effect. Circles represent Ge-doped layers and squares Si-doped layers. The respective dopant effusion cell temperatures are denoted next to the data points. Values from highly doped layers of the first series are also included here. In the regime $< 10^{20}\,\mathrm{cm^{-3}}$, dislocation densities are in the range of $1 \times 10^{10}\,\mathrm{cm^{-2}}$ and below, as described above, with a tendency of D rising with increased doping. For the layers doped near the limit, no general trend is visible. Concerning the Si-doped layers, the layer doped with highest T_{Si} has a two times higher dislocation density than the $T_{Si} = 1150\,°\mathrm{C}$ layer, while both feature the same free electron concentration. It is thus not useful to apply higher Si fluxes than required to achieve the maximum doping level. Dislocation densities of layers doped with Ge near the limit have no dependency on T_{Ge}. Values of D are spread over a wide range with no regularity concerning the doping concentration. It seems that there is another growth-related parameter, that is not
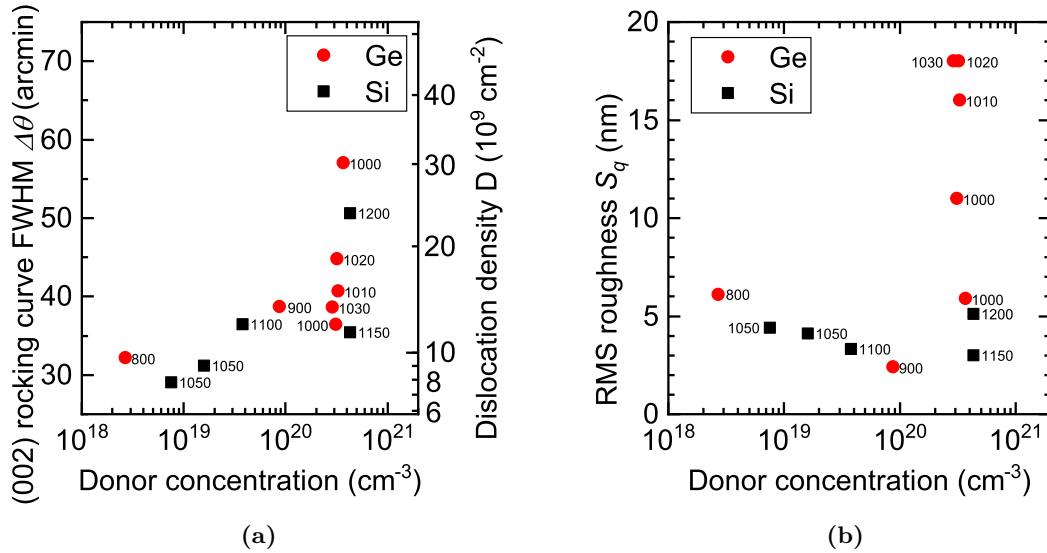
Figure 4.14: **(a)** Full width at half maximum (FWHM) of (002) HRXRD rocking curves measured for highly Ge- and Si-doped c-GaN layers. Corresponding dislocation densities are plotted on the right axis and are calculated after eq. 4.1. **(b)** Root mean square (RMS) surface roughness of highly doped layers measured by AFM. In both diagrams the respective dopant effusion cell temperatures are denoted next to the data points.
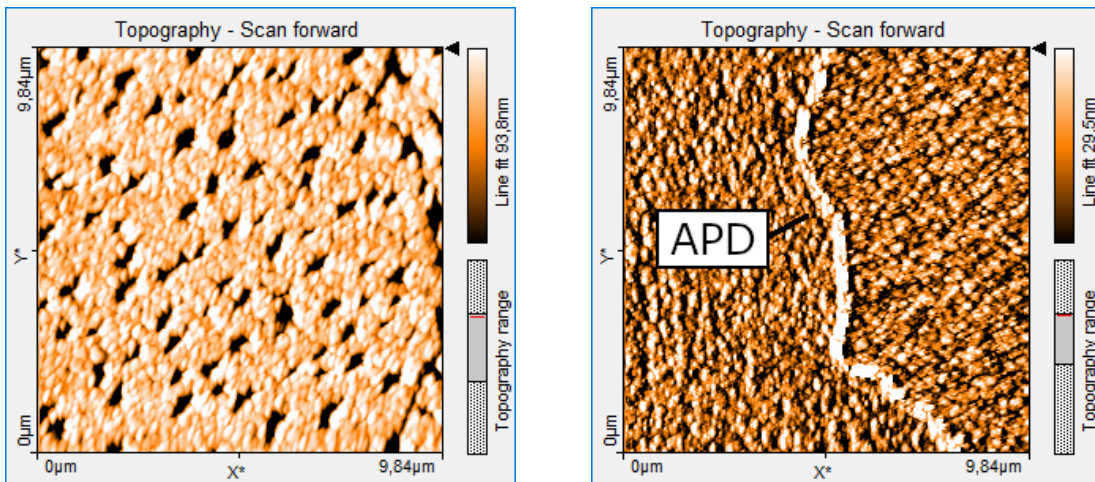
(a) Sample 3000 – $T_{Ge} = 1030\,^{\circ}\mathrm{C}$

(b) Sample 2946 – $T_{Si} = 1200\,^{\circ}\mathrm{C}$

Figure 4.15: AFM images of highly **(a)** Ge-doped and **(b)** highly Si-doped layers.

apparent here, which critically influences the layer quality. However, with both dopants the highest free electron concentration in each case resulted in comparable dislocation densities. RSMs were recorded additionally to the (002) rocking curves to account for hexagonal inclusions. No hexagonal phase could be found in any of the layers (except the polycrystalline sample 2974).

AFM was carried out to determine the surface roughness of the layers. Obtained values are plotted versus the free electron concentration in Figure 4.14(b). As already described in section 4.3.2, there is a downward trend of roughnesses in the 10^{18} to $10^{19}\,\mathrm{cm}^{-3}$ doping range. The situation in the high doping range ($> 10^{20}\,\mathrm{cm}^{-3}$) is similar to that of the HRXRD measurements. The roughness of the $T_{Si} = 1200\,°\mathrm{C}$ layer is higher than that of the $T_{Si} = 1150\,°\mathrm{C}$ layer, so raising T_{Si} although the doping maximum is reached is not useful in this regard either. Roughnesses of Ge-doped layers increase as T_{Ge} is raised. Due to the fact that higher T_{Ge} does not further increase the free electron concentration in this doping range, T_{Ge} should be as low as possible to achieve the required doping concentration. In contrast to the $T_{Ge} = 1000\,°\mathrm{C}$ layer of the first series, where the surface was closed and had material accumulated along the APBs, the surfaces of higher Ge-doped layers have holes (see Figure 4.15(a)), which causes the high roughness. The highest Si-doped layer of the present series however has a closed surface, but also features material accumulated along the APBs (see Figure 4.15(b)). The reliability of van der Pauw-Hall effect measurements is expected to decrease at high surface roughnesses, as this measurement principle relies on the presence of closed surfaces.

Figure 4.16 shows the electron mobilities of highly doped layers measured by Hall effect at room temperature. The trend is, that in the doping range below $10^{20}\,\mathrm{cm}^{-3}$ mobilities
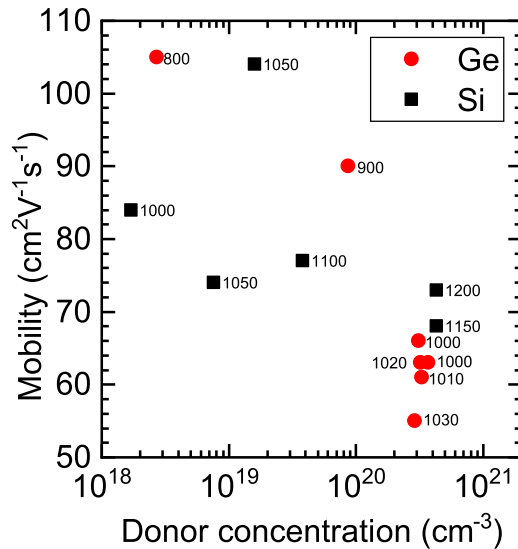

Figure 4.16: Electron mobilities of highly Ge- and Si-doped c-GaN layers depending on the donor concentration. The respective dopant effusion cell temperatures are denoted next to the data points.

of Ge-doped layers are higher than those of Si-doped layers (see section 4.3.3). The $T_{Si} = 1050\,°C$ layer grown in the second sample series however has a significantly higher mobility than the comparably doped layer from the first series, almost as high as that of the Ge-doped layers. Concerning AFM and HRXRD measurements of these layers, there is no obvious reason for this behavior, probably it is caused by the deviating growth conditions. Relations change in the doping range of $10^{20}\,cm^{-3}$. Here the highest mobility of Si-doped layers is approximately $10\,\%$ higher than that of the Ge-doped layer with highest mobility and comparable donor concentration. While the roughness and dislocation density of the Si-doped layer grown at $T_{Si} = 1200\,°C$ were worse than those values of the $T_{Si} = 1150\,°C$ layer, the mobility of the layer grown at higher T_{Si} unexpectedly is higher. On the other side, mobilities of Ge-doped layers drop as T_{Ge} is increased. As a comparison with literature, Kim et al. [130] report for MBE-grown Si-doped c-GaN on 3C-SiC a maximum free carrier concentration of $3.0 \times 10^{20}\,cm^{-3}$ and measure a room temperature mobility of $68\,cm^2\,V^{-1}\,s^{-1}$. In this work a mobility of $73\,cm^2\,V^{-1}\,s^{-1}$ is measured for an even higher maximum free carrier concentration of $4.3 \times 10^{20}\,cm^{-3}$. However, as mentioned above, due to the poor surface quality of the highly doped layers the Hall effect measurements are expected to have a decreased reliability.
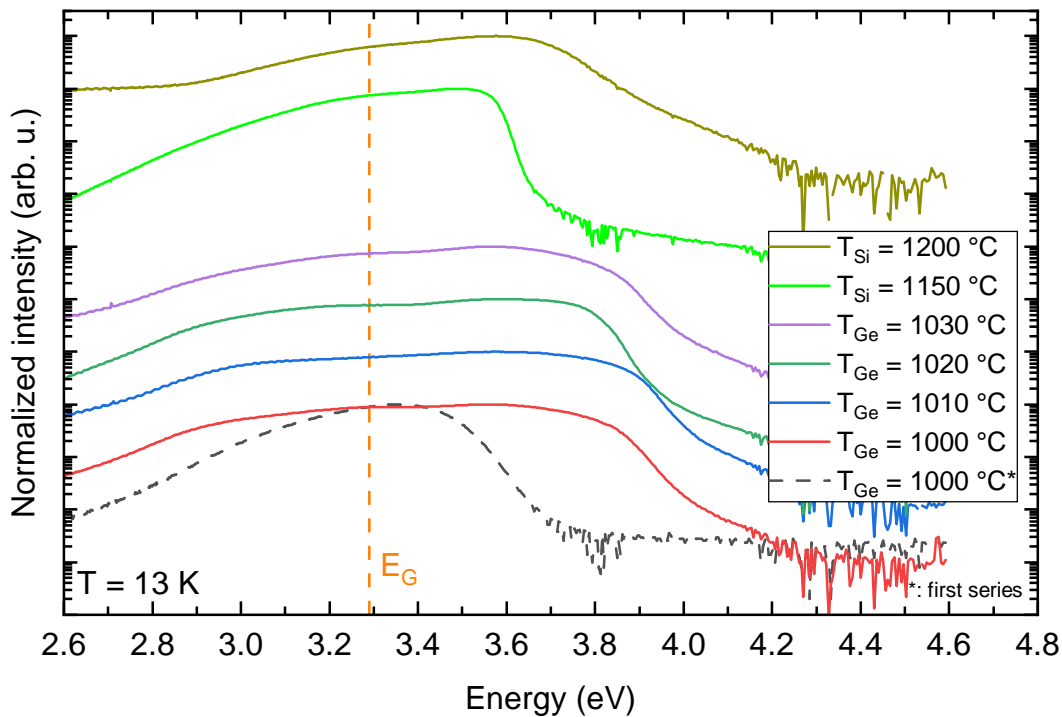

Figure 4.17: PL spectra of highly Ge- and Si-doped layers measured at $13\,K$. Spectra are normalized and shifted for better clarity. E_G denotes the $13\,K$ band gap of c-GaN. The spectrum of the highest Ge-doped layer from the first series is plotted dashed as a reference (marked by an asterisk in the legend).

PL spectra of the highly doped layers were measured at $13\,\text{K}$ and are displayed in Figure 4.17. The spectra are normalized and shifted for better visibility. All spectra are extremely broadened and emission extends highly above the band gap of c-GaN, which indicates strong degenerate doping. The position of the Fermi level E_F, which depends on the free electron concentration (see eq. 2.14), is extracted from the spectra by determining the energy, where the intensity drops to half on the high-energy edge of each spectrum. Values for E_F are listed in Table 4.4. In case of Ge-doping, E_F is consistently at higher energies for those layers with higher carrier density. The two Si-doped layers, whose carrier density determined by Hall effect is identical, however strongly differ regarding their emission energy. E_F is significantly lower for the $T_{Si} = 1150\,°\text{C}$ layer ($3.57\,\text{eV}$ versus $3.73\,\text{eV}$), indicating a lower free electron concentration. Furthermore, the emission of every single Ge-doped layer with Hall carrier density around $3 \times 10^{20}\,\text{cm}^{-3}$ is at higher energy than the two Si-doped layers, although based on the Hall effect measurements the Si-doped layers should be doped slightly higher. For comparison, the spectrum of the highest Ge-doped layer of the first sample series ($T_{Ge} = 1000\,°\text{C}$) is plotted as a dashed curve. Although a nearly equal free electron concentration is measured for this layer and for the Ge-doped layers of the present sample series, the emission energies strongly deviate. Emission energies of Ge-doped layers of the second sample series are higher by several $100\,\text{meV}$, indicating considerably higher doping levels. Based on the slightly lower growth rates of the second sample series it is expected that doping levels are slightly higher when applying the same dopant element flux, but this would not explain the deviation between optical and electrical measurements. TOF-SIMS measurements on these highly doped layers would be helpful to get more reliable information on the actual dopant incorporation.

4.3.6 Discussion

The Ge donor concentrations obtained by the different methods described above are summarized in Figure 4.18. From TOF-SIMS depth profiles Ge concentrations are determined by using the calibration presented in section 4.2. PL spectroscopy allows to calculate the donor concentration from the shift of the (D^0,A^0) transition due to Coulomb interaction. As can be seen from equations 3.26 and 4.2, the (D^0,A^0) transition shifts to higher energies with increasing donor concentration. Conversely, the donor concentration can be calculated from the energy shift. Room temperature Hall effect measurements were performed to determine the free electron concentrations of the layers, which are equal to the respective donor concentrations in case all donors are ionized. This is assumed to be valid for the degenerately doped layers.

In the medium doping regime the measured donor concentrations are in good agreement with the trend of the vapor pressure curve. At higher doping levels there is however a deviation towards lower donor concentrations observed by all of the measurement methods. The BEP of the Ge effusion source was measured to examine the actual amount of Ge supplied during growth. The measured BEP is displayed by diamonds in Figure 4.18 and is fitted by an exponential function, which is then shifted vertically for better comparability to the measured values. There is a perfect agreement of the trend of the BEP to the measured Ge concentrations, which means that the Ge incorporation is actually determined by the supplied Ge. On the other hand, this also means that the Ge BEP does not comply
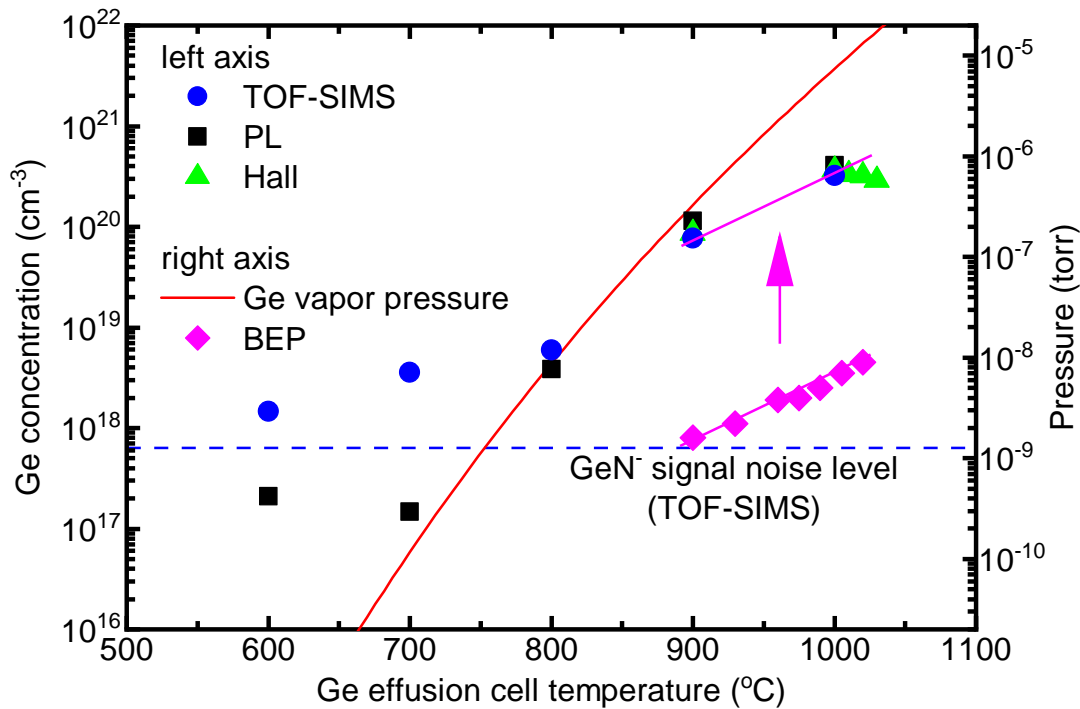
Figure 4.18: Overview of Ge donor concentrations determined by different methods. TOF-SIMS values are determined based on the calibration presented in section 4.2. PL values are calculated from the (D^0, A^0) transition energy using eq. 3.26. Free electron concentrations measured by Hall effect at room temperature are assumed to be identical to the respective donor concentration. The Ge vapor pressure curve is overlaid to fit to the data points. The BEP of the Ge effusion source is measured, fitted by a line, and shifted upwards as a guide to the eye.

with the vapor pressure curve in this temperature range. No statement can be made for temperatures below 900 °C, since the BEP is too low to be measured at these cell temperatures.

As the Ge concentrations measured by TOF-SIMS and the measured free electron densities agree within the measurement error, nearly all of the incorporated Ge atoms are electrically active donors up to Ge concentrations around $3.7 \times 10^{20}\,\text{cm}^{-3}$. When trying to further increase the doping level by raising the Ge effusion cell temperature, the free electron concentration measured by Hall effect however does not increase any more, probably due to autocompensation effects.

In the regime of low doping, there is a significant deviation of donor concentrations measured by TOF-SIMS and PL, and the values also deviate from the trend of the Ge vapor pressure curve. The Ge concentrations obtained from PL measurements are nearly equal for the two lowest doped layers. Either the Ge doping is in the range of or lower than the residual doping, or this method for determining the donor concentration is not sensitive enough at low donor concentrations. TOF-SIMS measurements reveal considerably higher

Ge concentrations for the two lowest doped layers, that also are by orders of magnitude higher than expected based on the vapor pressure curve. The TOF-SIMS values however are assumed to be accurate, as the GeN$^-$ signal is well above the noise level (dashed line) and thus above the detection limit.

In conclusion, the maximum free electron concentrations measured by Hall effect are $3.7 \times 10^{20}\,\mathrm{cm}^{-3}$ and $4.3 \times 10^{20}\,\mathrm{cm}^{-3}$ for Ge- and Si-doping, respectively. When using Ge as a donor, the free electron concentration cannot be increased further and when supplying more Ge, the structural quality deteriorates. With Si as a donor, a similar effect is observed, but the deterioration is slightly less pronounced. Still, the structural quality of Ge- and Si-doped layers is comparable when achieving the doping limit using the lowest possible effusion cell temperature. The electron mobilities of Ge-doped layers are about $20\,\%$ higher than those of Si-doped layers at donor concentrations below $10^{20}\,\mathrm{cm}^{-3}$. Mobilities are comparable within the margin of error when the doping limit is approached.

4.4 Ge-doping of c-Al$_x$Ga$_{1-x}$N

Parts of this section have been published in Ref. 131.

The ternary alloy c-Al$_x$Ga$_{1-x}$N allows to extend the optical emission of nitrides further into the UV spectral region, and can also be employed as a barrier material for fabrication of low-dimensional structures such as quantum wells. Doping of barriers instead of the active layers (called *modulation doping*) is of special interest, as carriers are scattered at ionized dopant impurities, resulting in lower electron mobilities. Scattering effects are reduced if carriers and impurities are separated spatially.

Ge-doping of c-Al$_x$Ga$_{1-x}$N is investigated by means of two sample series. In the first series, the Al mole fraction x is varied from 0 to 0.6. For each x a n.i.d. and a layer doped using a Ge effusion cell temperature of $T_{Ge} = 800\,°\mathrm{C}$ are grown. In the second series, the Al mole fraction is kept constant at $x = 0.25$ and T_{Ge} is varied between $700\,°\mathrm{C}$ and $1000\,°\mathrm{C}$. A list of samples and their basic properties is given in Table 4.5. Al mole fractions x are determined by EDX and HRXRD. Results of both methods are in good agreement, but as EDX has a higher accuracy, the values obtained by this method are used to refer to the samples in the following. Layer thicknesses given in the table are determined by reflectometric interference spectroscopy. For the first series, a growth time of $4.5\,\mathrm{h}$ was targeted. At higher x however after time hexagonal inclusions became apparent in the RHEED patterns during growth. At that point growth was stopped to obtain purely cubic layers. For this reason, the four layers with highest x were too thin to accurately measure their thickness. The thickness of these layers is estimated based on the growth rate instead. The growth time for all layers of the second series was $5\,\mathrm{h}$. Donor concentrations given in the table are obtained from CV spectroscopy measurements.

Structural characterization (except TOF-SIMS), PL spectroscopy and Hall effect measurements of the *first* sample series have already been described in the Master's thesis of Fabian Tacken [132] and will be summarized here briefly. The *second* sample series and their investigations, as well as CV and TOF-SIMS measurements of both series, have not been covered so far and will be discussed here in detail.

Table 4.5: Overview of Ge-doped c-Al$_x$Ga$_{1-x}$N layers and their basic properties. In sample series 1, the Al mole fraction x was varied from 0 to 0.6 and for each x a n.i.d. and a Ge-doped layer were grown. In the second series x was kept constant at 0.25 and the Ge concentration was varied.

Series	Sample number	Al mole fraction (EDX)	Al mole fraction (HRXRD)	Cell temp. (°C)	Flux (cm^{-2} s^{-1})	Thick- ness (nm)	CV donor conc. (cm^{-3})
	2701	0	0	-	-	506	2.4×10^{17}
	2692	0	0	800	2.9×10^{10}	427	1.4×10^{19}
	2703	0.08	0.09	-	-	484	7.3×10^{17}
	2706	0.09	0.10	800	2.9×10^{10}	480	9.6×10^{18}
	2707	0.25	0.23	-	-	487	4.9×10^{18}
1	2708	0.24	0.26	800	2.9×10^{10}	456	1.6×10^{19}
	2709	0.33	0.37	-	-	430	1.4×10^{19}
	2710	0.39	0.38	800	2.9×10^{10}	336	2.5×10^{19}
	2712	0.49	0.46	-	-	$\approx$ 230 [a]	1.8×10^{17}
	2714	0.50	0.48	800	2.9×10^{10}	$\approx$ 170 [a]	1.9×10^{19}
	2716	0.60	0.59	-	-	$\approx$ 150 [a]	1.8×10^{19}
	2720	0.63	0.62	800	2.9×10^{10}	$\approx$ 140 [a]	1.8×10^{19}
	2932	0.23	0.23	-	-	497	4.2×10^{18}
	2934	0.23	0.23	700	3.4×10^{8}	455	5.3×10^{18}
	2936	0.26	0.27	800	2.9×10^{10}	437	1.5×10^{19}
2	2939	0.28	0.24	850	1.9×10^{11}	409	1.3×10^{19}
	2940	0.26	0.22	900	9.3×10^{11}	438	7.5×10^{19}
	2964	0.28	0.24	950	4.6×10^{12}	475	7.7×10^{19}
	2942	0.22	0.22	1000	8.9×10^{12}	467	1.4×10^{20}

[a] too small for accurate measurement – estimated thickness based on growth rate and time

4.4.1 TOF-SIMS depth profiles

TOF-SIMS depth profiles are measured for all layers of both sample series. As an example, the depth profile of the c-Al$_{0.25}$Ga$_{0.75}$N layer doped at $T_{Ge} = 900\,$°C is shown in Figure 4.19(a). The transition between c-Al$_{0.25}$Ga$_{0.75}$N layer and 3C-SiC substrate occurs at approximately 770 s and is indicated by a vertical dashed line. At this point, the Si$_2$C$_2^-$ and C$^-$ signals rise strongly, with the latter being so strong that the detector saturates. From the c-Al$_{0.25}$Ga$_{0.75}$N layer, several high-intensity signals are recorded. AlN$^-$, AlGaN$^-$, GaN$^-$, and Al$^-$ for example run at constant intensity within the layer. The ^{74}Ge$^-$ and ^{74}GeN$^-$ signals prove the incorporation of Ge into the layer. While for c-GaN layers a constant ratio of approximately six could be observed between these two signals, this does

not hold anymore for c-$Al_xGa_{1-x}N$ layers. As this ratio depends on x, and furthermore the signal calibration presented in section 4.2 is only valid for c-GaN layers, the two signals cannot be used to determine the Ge concentration in c-$Al_xGa_{1-x}N$. Like in the case of c-GaN layers, also here C and O impurities are present, which can cause unintentional doping [50, 54].

Figure 4.19(b) shows the $^{74}Ge^-$ and O^- signals from n.i.d. and Ge-doped layers ($T_{Ge} = 800\,°C$) of the first sample series depending on the Al mole fraction x. Both signals are normalized to the $^{29}Si^-$ signal from the 3C-SiC substrate to account for varying sputter conditions. The $^{74}Ge^-$ signal rises slightly with increasing x. Possibly the Ge incorporation is actually enhanced with increasing Al content, but as there is also ambiguity concerning the $^{74}GeN^-$ signal, it is unclear if the Ge-related signals reliably reflect the Ge concentration in c-$Al_xGa_{1-x}N$ with varying x. For example, TOF-SIMS related matrix effects could affect the Ge-related signals. The O^- signal is found to linearly rise with increasing x both for n.i.d. and Ge-doped layers. This can be explained by two effects: First, the incorporation of O is enhanced by the presence of Al [64]; second, the incorporation of impurities in general is increased with rising dislocation densities [133], which are observed for layers with higher Al content (see section 4.4.2). The n.i.d. $x = 0.49$ layer deviates from this trend – here a significantly lower than expected O incorporation is observed. This behavior is unclear up to now, as growth conditions were comparable for all samples. $^{74}Ge^-$ and O^- signal intensities from layers of the second series (c-$Al_{0.25}Ga_{0.75}N$ with varying Ge-doping) are shown in Figure 4.19(c). The $^{74}Ge^-$ signal exponentially rises with increasing Ge effusion cell temperature, which in good approximation resembles the course of the Ge vapor pressure curve [134] in small temperature ranges. The intensity of the O^- signal does not depend on the doping level, thus the presence of Ge does not affect the unintentional incorporation of O.

4.4.2 Structural properties

Concerning structural properties, first selected RHEED patterns are shown to discuss the crystal structure as observed during growth. EDX was performed to measure the Al mole fraction x of the layers. From HRXRD measurements dislocation densities are estimated from the (002) rocking curves, hexagonal inclusions are detected by recording RSMs around the (002) reflections, and the Al mole fractions are extracted from RSMs around the asymmetric ($\bar{1}\bar{1}3$) reflections. Lastly, the layer surface is imaged by AFM.

RHEED patterns

RHEED has been performed to monitor the evolution of the crystal structure during growth. As mentioned above, in the first sample series (varying x) growth has been stopped as soon as hexagonal reflexes appeared in the RHEED patterns. The growth time for the second sample series with fixed x and varying doping level was fixed at 5 h for better comparability, regardless of any structural degradation observed by RHEED. The RHEED patterns of layers grown with Ge temperatures up to $900\,°C$ are line-shaped, corresponding to a smooth, single crystalline surface with APDs. During growth of the $T_{Ge} = 950\,°C$ layer, after approximately 3 h satellite streaks began to appear. Figure 4.20(a) shows the RHEED pattern of this layer recorded after growth. According to Figure 2.8, this
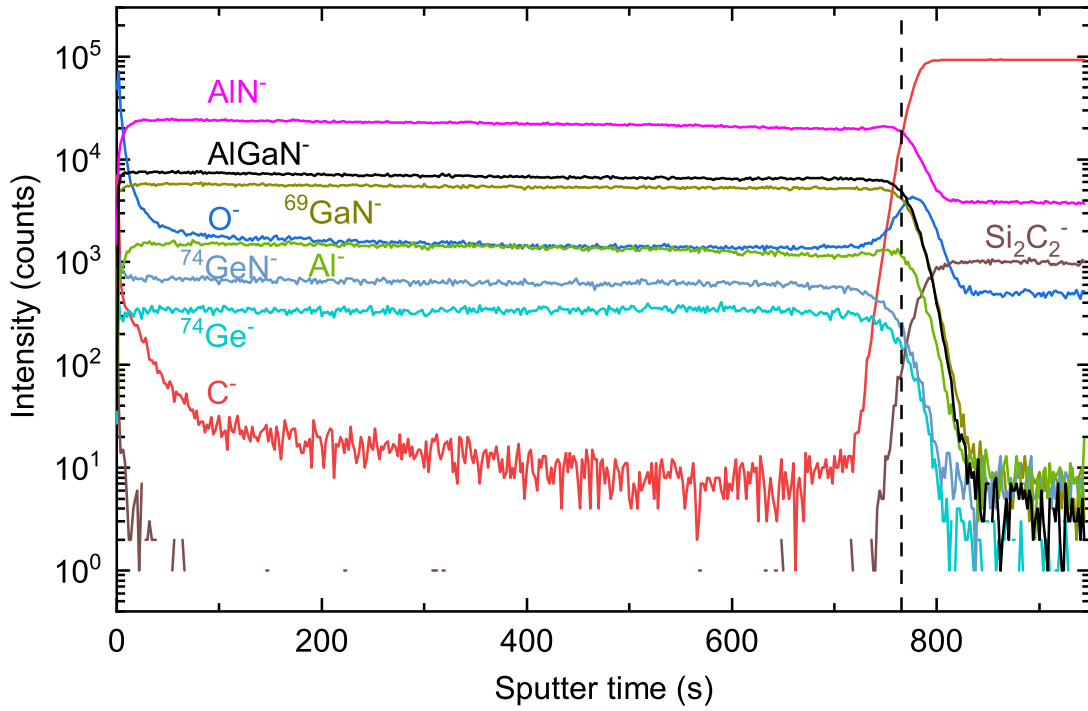
(a)
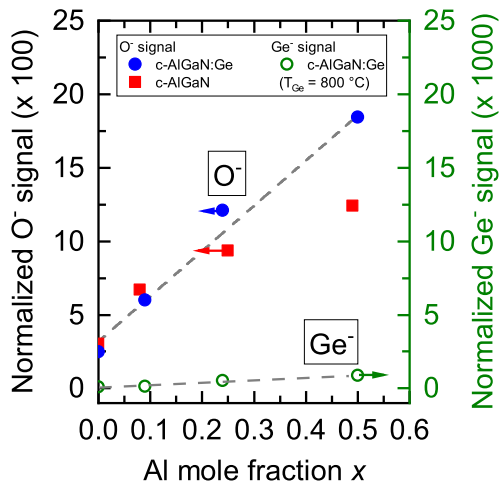
(b)
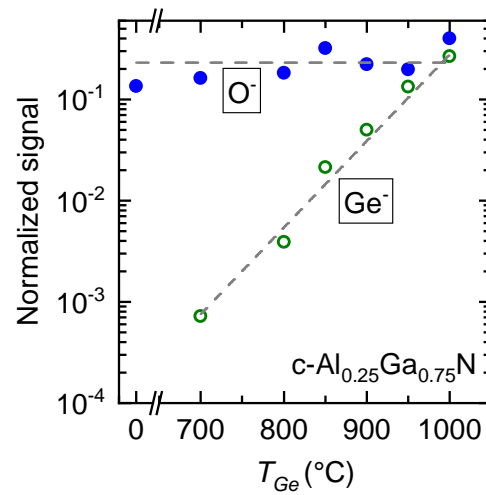
(c)

Figure 4.19: **(a)** TOF-SIMS depth profile of the c-Al$_{0.25}$Ga$_{0.75}$N layer doped at $T_{Ge} = 900\,°C$ (sample 2940). The vertical dashed line indicates the transition between epitaxial layer and 3C-SiC substrate. **(b)** O$^-$ and ^{74}Ge$^-$ secondary ion signals measured from n.i.d. and Ge-doped ($T_{Ge} = 800\,°C$) c-Al$_x$Ga$_{1-x}$N layers depending on x (series 1). **(c)** O$^-$ and ^{74}Ge$^-$ secondary ion signals measured from c-Al$_x$Ga$_{1-x}$N depending on the Ge effusion cell temperature T_{Ge} (series 2). In (b) and (c) the signals are normalized to the ^{29}Si$^-$ signal from the 3C-SiC substrate to account for varying sputter conditions.

(a) Sample 2964 ($T_{Ge} = 950\,°\text{C}$)   **(b)** Sample 2942 ($T_{Ge} = 1000\,°\text{C}$)
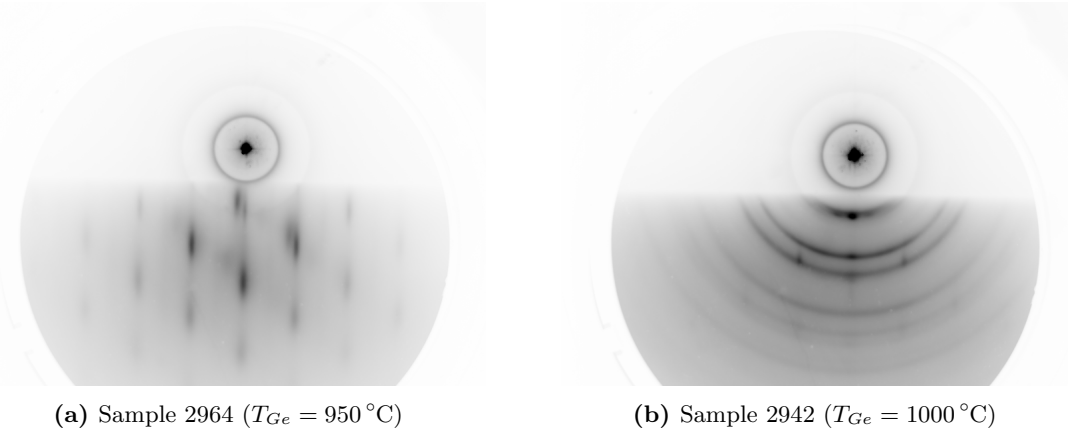
Figure 4.20: RHEED patterns of Ge-doped c-$\text{Al}_{0.25}\text{Ga}_{0.75}\text{N}$ layers after $5\,\text{h}$ of growth.

pattern corresponds to a stepped surface. The RHEED pattern of the $T_{Ge} = 1000\,°\text{C}$ layer indicated polycrystalline growth already after one hour of growth, which intensified as growth continued. In Figure 4.20(b) the pattern after growth is shown, which exhibits a strong polycrystalline reflection. The growth of these two layers was reproduced using optimized parameters, but results were the same.

EDX analysis

The EDX spectrum of the highest doped $x = 0.25$ layer from the second series is shown in Figure 4.21 as an example. The spectrum is recorded using an acceleration voltage of $5\,\text{keV}$ and scanning an area of approximately $25 \times 20\,\text{µm}^2$ (magnification 5000X). An integration time of $500\,\text{s}$ was chosen to achieve a sufficient signal-to-noise ratio. The peaks are automatically fitted by the measurement software *EDAX TEAM*, which also does the quantification and outputs the layer composition. Peaks can also be identified using an appropriate table of characteristic X-ray lines [135]. The lowest energy peak in the spectrum is assigned to the C $\text{K}\alpha_1$ line and stems from the 3C-SiC substrate. The Si $\text{K}\alpha_1$ line of the substrate should appear at $1.740\,\text{keV}$, but it is overexposed by the background caused by *bremsstrahlung*. From the c-$\text{Al}_{0.25}\text{Ga}_{0.75}\text{N}$ layer, the N $\text{K}\alpha_1$ line is visible at $0.392\,\text{keV}$, and the $\text{K}\alpha_1$ and $\text{K}\beta_1$ lines of Al at $1.486\,\text{keV}$ and $1.557\,\text{keV}$, respectively. From Ga, due to the acceleration voltage only the $\text{L}\alpha_1$ and $\text{L}\beta_1$ lines at $1.098\,\text{keV}$ and $1.125\,\text{keV}$, respectively, can be observed. There is also evidence of Ge $\text{L}\alpha_1$ ($1.188\,\text{keV}$) and $\text{L}\beta_1$ ($1.218\,\text{keV}$) lines, but they are overlapped by the Ga-related peaks and thus are too weak to be used for quantification. The separation of the K-lines of Ga and Ge would be high enough that no overlap occurs, but the acceleration voltage required to excite these lines ($\approx 15\,\text{keV}$) is so high that mainly the substrate would be excited. Thus, even for the highest doped layer the Ge concentration cannot be determined using EDX. From quantification results, an actual Al mole fraction of $x = 0.22$ is calculated for this layer. Results for all of the other c-$\text{Al}_x\text{Ga}_{1-x}\text{N}$ layers are summarized in Table 4.5.
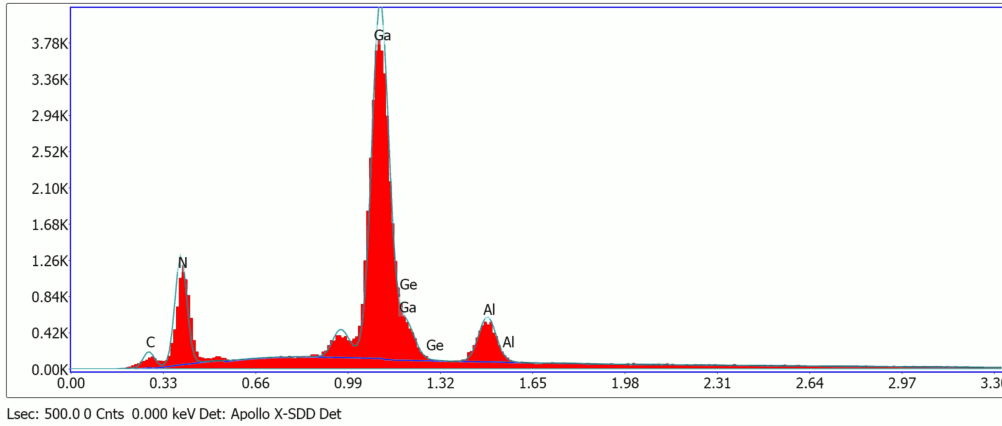
Figure 4.21: EDX spectrum of the highest Ge-doped c-Al$_{0.25}$Ga$_{0.75}$N layer (sample number 2942). The intensity (in counts) is plotted over the X-ray energy (in keV). Peaks are identified and fitted by the measurement software *EDAX TEAM*.

HRXRD measurements

Dislocation densities D are estimated from the FWHM $\Delta\theta$ of (002) rocking curves by using eq. 4.1. As the Burgers vector b depends on the lattice constant a, which in turn depends on the Al mole fraction x, the respective lattice constant for each layer is calculated after eq. 2.1 using the Al mole fraction determined by EDX. In Figure 4.22(a) the dislocation densities of the layers with varying x are displayed. Based on the n.i.d. layers (red squares) it is evident that the dislocation density rises with increasing x. To a small portion, this effect is due to the smaller layer thickness of layers with higher x (see also section 4.1), but mainly the degradation of the structural quality can be ascribed to the higher Al content itself. Dislocation densities of the Ge-doped layers (blue circles) are nearly equal to those of n.i.d. layers with comparable Al content. Figure 4.22(b) shows the dislocation densities of the c-Al$_{0.25}$Ga$_{0.75}$N layers depending on the Ge doping. As the layer thickness of all samples from this series is comparable, no significant influence of the layer thickness on comparing dislocation densities is expected here. Up to $T_{Ge} = 800\,°\mathrm{C}$ (according to the CV measurements presented in section 4.4.3 this corresponds to donor concentrations around $1 \times 10^{19}\,\mathrm{cm}^{-3}$) values are nearly constant at around $3 \times 10^{10}\,\mathrm{cm}^{-2}$. A sharp rise by a factor of two is observed when doping is further increased.

RSMs around the (002) reflections are measured to detect hexagonal inclusions (see section 4.3.2). The amount of the hexagonal phase in the first sample series is below 10 % for Al mole fractions up to $x = 0.36$. At higher x, hexagonal inclusions rise up to around 30 %. Within uncertainty of measurement there is however no difference between n.i.d. and Ge-doped layers ($T_{Ge} = 800\,°\mathrm{C}$). Regarding the second series with fixed $x = 0.25$, no hexagonal inclusions are apparent up to $T_{Ge} = 850\,°\mathrm{C}$. With increasing doping level, hexagonal inclusions rise to around 5 % to 15 %. In Figure 4.23(a) the (002) RSM of the c-Al$_{0.25}$Ga$_{0.75}$N layer doped with $T_{Ge} = 950\,°\mathrm{C}$ is exemplarily shown. ($\bar{1}011$) reflections from the hexagonal phase are highlighted by a red ellipse. The intensity of the hexagonal reflection in this case sums up to 28 % of the cubic intensity. For each layer, the (002)
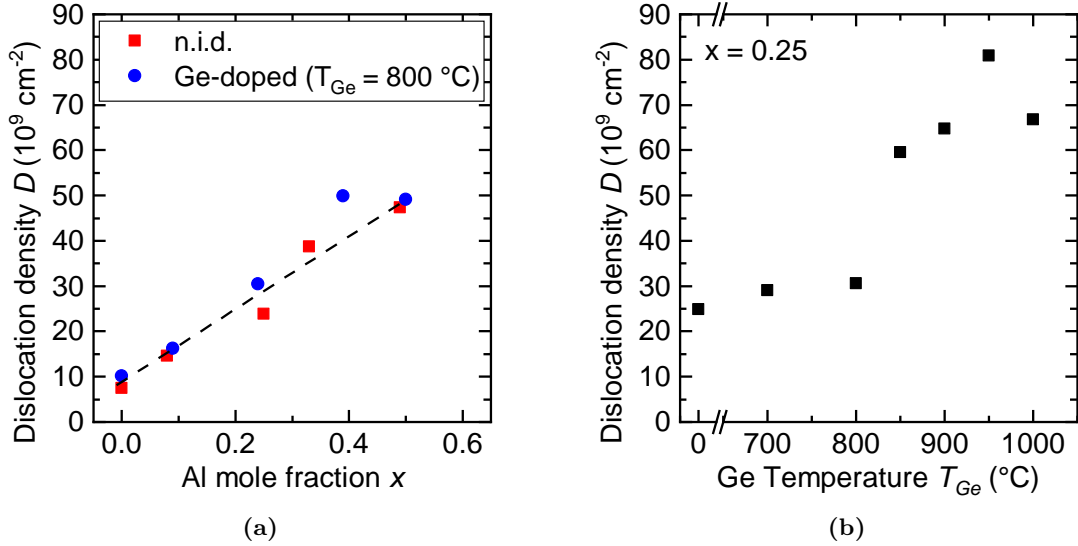
(a)   (b)

Figure 4.22: Dislocation densities calculated from the HRXRD (002) reflection FWHMs after eq. 4.1. **(a)** n.i.d. and Ge-doped layers ($T_{Ge} = 800\,°C$) with varying Al mole fraction x (series 1) **(b)** Layers with fixed $x = 0.25$ and varying Ge doping (series 2).

(a)   (b)
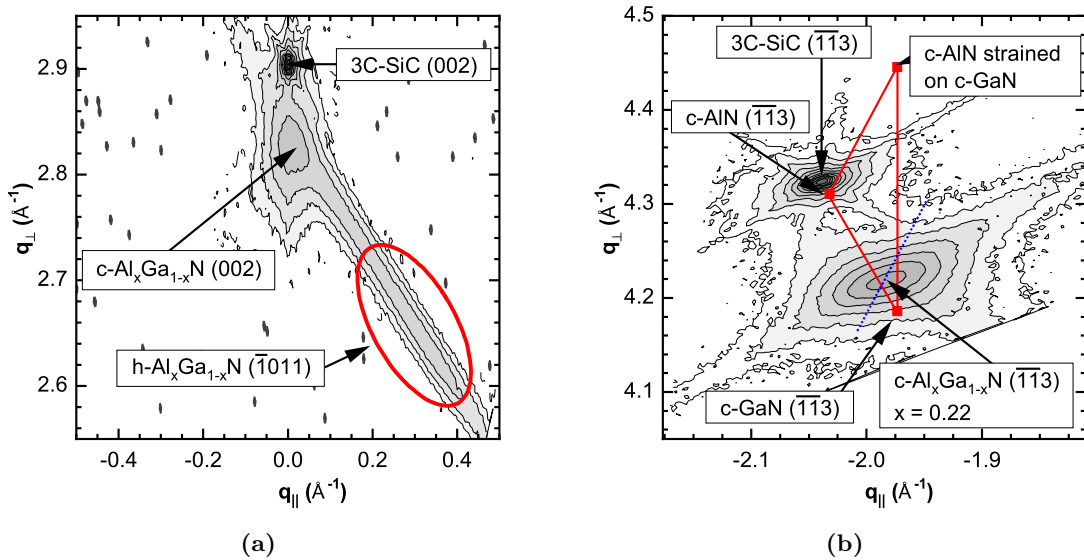
Figure 4.23: **(a)** RSM around the (002) reflection of c-Al$_{0.25}$Ga$_{0.75}$N doped at $T_{Ge} = 1000\,°C$ (sample 2964) to detect hexagonal inclusions. **(b)** RSM around the ($\bar{1}\bar{1}3$) reflection of n.i.d. c-Al$_{0.25}$Ga$_{0.75}$N (sample 2932) to obtain the actual Al mole fraction.

RSM is measured for two perpendicular sample orientations and the hexagonal amount is averaged over both measurements. Thus, for this layer the total amount of hexagonal inclusions is 16.5 %.

From RSMs around the asymmetrical $(\bar{1}\bar{1}3)$ reflection of c-Al$_x$Ga$_{1-x}$N, Al mole fractions x can be extracted. This is shown in Figure 4.23(b) on example of the n.i.d. c-Al$_x$Ga$_{1-x}$N layer with nominal $x = 0.25$. In this diagram, the $(\bar{1}\bar{1}3)$ reflections of the 3C-SiC substrate and the c-Al$_x$Ga$_{1-x}$N layer are visible and labeled accordingly. Additionally, the positions where the $(\bar{1}\bar{1}3)$ reflections of relaxed c-GaN and c-AlN, and of c-AlN fully strained on c-GaN would appear are marked by red squares. When shifting the connecting line between relaxed and strained c-AlN over the c-Al$_x$Ga$_{1-x}$N peak (dashed blue line), the intersection with the connection between relaxed c-GaN and c-AlN marks the position of fully relaxed c-Al$_x$Ga$_{1-x}$N with equal x. Due to Vegard's law, the ratio of the distance between the intersection and the c-GaN reflection to the total distance between c-GaN and relaxed c-AlN reflections is equal to the Al mole fraction x. In this case, a value of $x = 0.22$ is obtained. Again, RSMs are measured for two perpendicular sample orientations and values of x are averaged. The results are listed in Table 4.5.

AFM measurements

AFM was performed to image the surface topography of the c-Al$_x$Ga$_{1-x}$N layers, and to calculate the RMS surface roughness S_q. In Figure 4.24(a) the roughness values S_q of n.i.d. and Ge-doped ($T_{Ge} = 800\,^\circ$C) layers are plotted versus the Al mole fraction x. As not all layers of this sample series are of equal thickness, roughness values are not necessarily comparable if there is a large deviation in layer thickness. This is due to the fact that the roughness becomes higher with increasing layer thickness, see section 4.1. However, the thicknesses of layers with comparable x are nearly equal, and from this it can be seen that the roughness is reduced by up to 50 % by the Ge-doping at $T_{Ge} = 800\,^\circ$C. The calculated roughness values S_q of c-Al$_{0.25}$Ga$_{0.75}$N layers with varying doping are plotted in Figure 4.24(b). The roughness of these layers is reduced from 5.5 nm (n.i.d. sample) down to 1.9 nm when the Ge effusion cell temperature is raised up to $T_{Ge} = 800\,^\circ$C. Figure 4.24(c) shows the surface topography of this layer with the smallest roughness. With T_{Ge} further increasing, the surface roughness begins to climb again. The highest doped layer ($T_{Ge} = 1000\,^\circ$C) features the highest roughness of 11 nm. The surface of this layer (Figure 4.24(d)) exhibits droplets and line-shaped hills, which probably are deposits of the group III elements or Ge. From both sample series it is apparent that the doping by Ge – at least at $T_{Ge} = 800\,^\circ$C – is smoothing the c-Al$_x$Ga$_{1-x}$N surface. Such a surfactant behavior of Ge has also been reported for the MOVPE growth of wurtzite GaN [136].

4.4.3 Electrical properties

In order to determine the donor concentrations of the c-Al$_x$Ga$_{1-x}$N layers by electrical measurements, capacitance-voltage (CV) spectroscopy was performed. All obtained values are listed in Table 4.5. The donor concentrations N_D obtained for the sample series with varying Al mole fraction x are displayed in Figure 4.25(a). For the n.i.d. layers (red squares) a linear rise of the donor concentration with increasing x is measured. A linear function (red line) is fitted to the data for better clarity. While the donor concentration is 2.4×10^{17} cm^{-3}
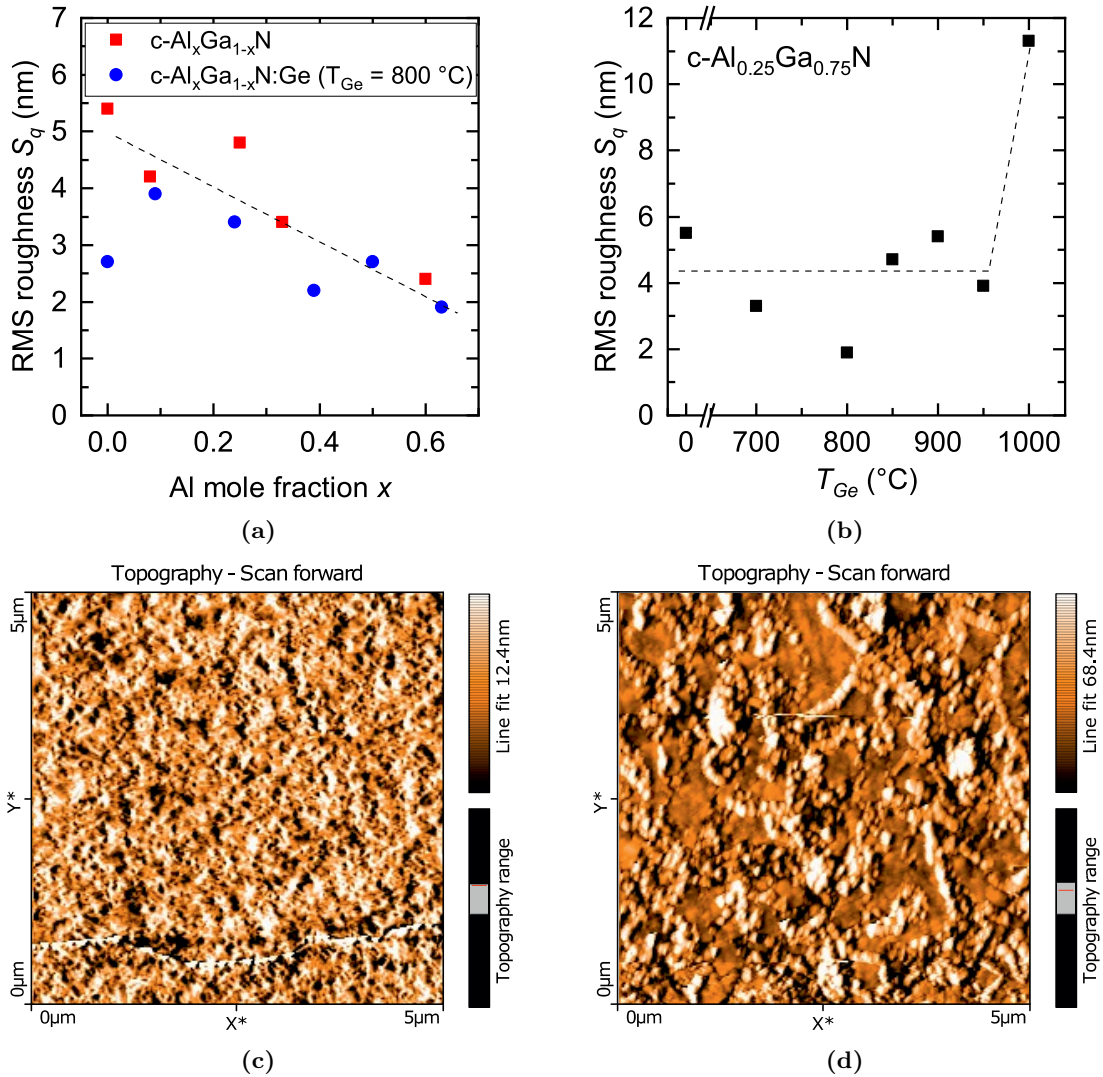
(a)

(b)

(c)

(d)

Figure 4.24: **(a)** AFM roughness S_q of n.i.d. and Ge-doped layers depending on the Al mole fraction x (series 1). **(b)** Roughness of c-Al$_{0.25}$Ga$_{0.75}$N layers depending on the Ge effusion cell temperature T_{Ge} (series 2). Dashed lines are a guide to the eye. **(c)** Surface topography of c-Al$_{0.25}$Ga$_{0.75}$N doped at $T_{Ge} = 800\,°$C. **(d)** Surface topography of c-Al$_{0.25}$Ga$_{0.75}$N doped at $T_{Ge} = 1000\,°$C. All measurements were performed in an area of $5 \times 5\,\mu$m^2.
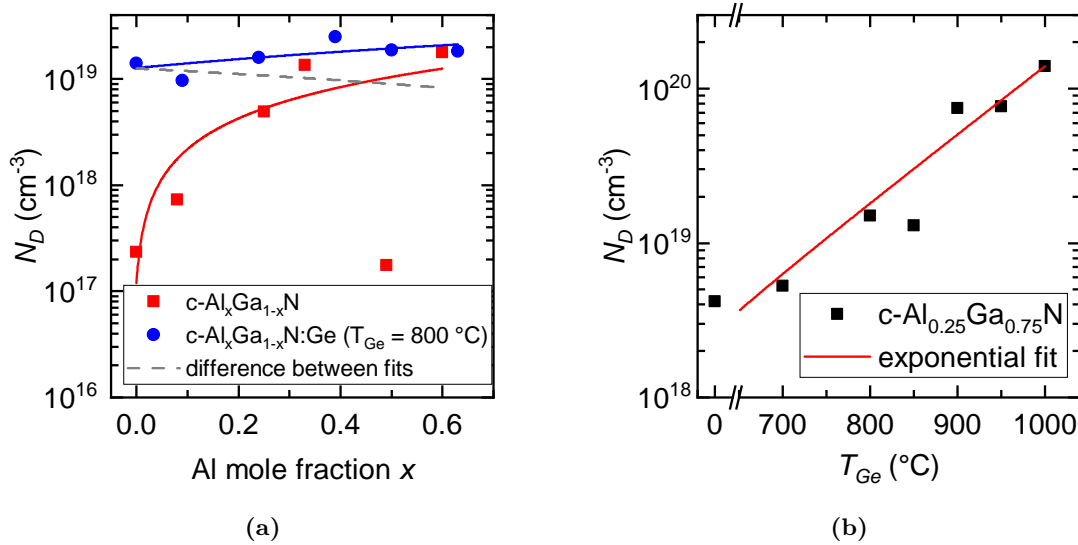
Figure 4.25: Donor concentrations N_D measured by CV spectroscopy. **(a)** n.i.d. and Ge-doped layers ($T_{Ge} = 800\,°\mathrm{C}$) with varying Al mole fraction x (series 1); **(b)** Layers with fixed $x = 0.25$ and varying Ge doping (series 2).

for the $x = 0$ layer, it rises up to $1.8 \times 10^{19}\,\mathrm{cm}^{-3}$ at $x = 0.60$. This unintentional doping can be put in relation to the incorporation of O, which has also found to linearly increase with rising Al content x (see TOF-SIMS measurements in Figure 4.19(b)). This correlation is further emphasized considering the n.i.d. layer with $x = 0.49$, which has an unexpectedly low O concentration compared to the rest of the layers. The donor concentration measured for this layer also is significantly lower than expected based on the linear fit.

For the Ge-doped layers ($T_{Ge} = 800\,°\mathrm{C}$) the donor concentration (blue circles) slightly increases with higher x. Also here a linear relationship is found (blue line). On the one hand, this fits to the slightly linearly increasing ^{74}Ge$^-$ signal measured by TOF-SIMS. On the other hand, the unintentional doping by O needs to be considered. This is done by subtracting the linear fit to N_D for the n.i.d. layers from that of the Ge-doped ones. The resulting line (dashed gray line) is expected to represent the doping caused only by Ge, and is found to slightly decrease with increasing x. Overall, the effect of a rising Al content on the Ge incorporation is not particularly large, but due to the inconclusive behavior of Ge-related TOF-SIMS signals and the uncertainties of the CV measurements, it is not clear whether the Ge incorporation is dropping or rising. Additional to the CV measurements, donor concentrations were exemplarily verified by Hall-effect measurements at room temperature for the two $x \approx 0.1$ layers. Free electron concentrations of $7.7 \times 10^{17}\,\mathrm{cm}^{-3}$ and $5.4 \times 10^{18}\,\mathrm{cm}^{-3}$ are measured for the n.i.d. and Ge-doped layer, respectively, which is in good agreement to the values determined by CV. Figure 4.25(b) shows the donor concentrations in c-Al$_{0.25}$Ga$_{0.75}$N depending on the Ge effusion cell temperature (series 2). Donor concentrations rise exponentially with increasing T_{Ge}, exactly like the ^{74}Ge$^-$ signals from TOF-SIMS measurements (Figure 4.19(c)). The maximum achieved donor concentration is $1.4 \times 10^{20}\,\mathrm{cm}^{-3}$ at $T_{Ge} = 1000\,°\mathrm{C}$, but it is

accomplished to the disadvantage of the structural quality of the layer (see section 4.4.2). Up to $T_{Ge} = 800\,^\circ\mathrm{C}$ dislocation densities did not rise, which according to the CV measurements corresponds to a donor concentration of $1.5 \times 10^{19}\,\mathrm{cm}^{-3}$.

4.4.4 Optical properties

PL spectroscopy was performed at $13\,\mathrm{K}$ to investigate the optical properties of all c-$\mathrm{Al}_x\mathrm{Ga}_{1-x}\mathrm{N}$ samples of the two series. In Figure 4.26(a) for comparison first the spectra of n.i.d. (dashed line) and Ge-doped ($T_{Ge} = 800\,^\circ\mathrm{C}$, solid line) c-GaN are shown. The emission mainly arises from three recombination mechanisms: the recombination of donor-bound excitons (BX) at $3.262\,\mathrm{eV}$, and two donor-acceptor pair recombinations $(\mathrm{D}^0,\mathrm{A}^0)$ and $(\mathrm{D}^0,\mathrm{A}^0{}')$ at $3.137\,\mathrm{eV}$ and $3.068\,\mathrm{eV}$, respectively (cf. section 4.3.4). Two distinct changes can be observed that are related to the doping. First, the overall emission intensity rises strongly, with the $(\mathrm{D}^0,\mathrm{A}^0)$ emission rising significantly stronger in intensity than the (BX) emission. Second, a blue-shift of the $(\mathrm{D}^0,\mathrm{A}^0)$ transition by $52\,\mathrm{meV}$ occurs due to Coulomb interaction between donors and acceptors (see section 4.3.4). After eq. 3.26 a donor concentration of $4 \times 10^{18}\,\mathrm{cm}^{-3}$ is calculated for the doped layer, which complies with the Ge concentration of $6 \times 10^{18}\,\mathrm{cm}^{-3}$ measured by TOF-SIMS. Figure 4.26(b) shows the PL spectra of the two c-$\mathrm{Al}_x\mathrm{Ga}_{1-x}\mathrm{N}$ layers with $x \approx 0.1$. The n.i.d. layer is displayed as a dotted line and the Ge-doped layer ($T_{Ge} = 800\,^\circ\mathrm{C}$) as a solid line. The emission intensity from both layers is nearly equal, thus the spectrum of the doped layer is shifted upwards by one order of magnitude for better clarity. While in the c-GaN spectra the near band-edge emission peaks were clearly separable, here the peaks have merged to a broad emission band. However, by performing multi-peak fits the individual (BX) and $(\mathrm{D}^0,\mathrm{A}^0)$ peaks can be identified. Due to the slightly deviating Al mole fraction of both layers, the (BX) peak of the n.i.d. c-$\mathrm{Al}_{0.08}\mathrm{Ga}_{0.92}\mathrm{N}$ layer is located at $3.426\,\mathrm{eV}$, and that of the Ge-doped c-$\mathrm{Al}_{0.09}\mathrm{Ga}_{0.91}\mathrm{N}$ layer at $3.440\,\mathrm{eV}$. The separation of the (BX) and $(\mathrm{D}^0,\mathrm{A}^0)$ peaks was $125\,\mathrm{meV}$ in case of the n.i.d. c-GaN sample, but the higher unintentional doping by O in the n.i.d. c-$\mathrm{Al}_{0.08}\mathrm{Ga}_{0.92}\mathrm{N}$ layer causes a blue-shift of the $(\mathrm{D}^0,\mathrm{A}^0)$ peak, due to which this separation is reduced to $51\,\mathrm{meV}$. With additional Ge-doping, a further blue-shift of the $(\mathrm{D}^0,\mathrm{A}^0)$ transition is observed, and the separation between (BX) and $(\mathrm{D}^0,\mathrm{A}^0)$ peaks is reduced to $40\,\mathrm{meV}$. Furthermore, the intensity of the $(\mathrm{D}^0,\mathrm{A}^0)$ peak rises to the disadvantage of the (BX) peak, which is also an indication for the higher doping level in the Ge-doped layer.

The spectra of all n.i.d. and Ge-doped layers with varying x are shown in Figure 4.26(c). N.i.d. layers are plotted as dotted lines and layers doped using $T_{Ge} = 800\,^\circ\mathrm{C}$ as solid lines. Spectra are normalized and shifted vertically. The respective Al mole fraction x is denoted besides the spectra. The spectra shift to higher energies and become broader with increasing x. Barely no effect of the doping on the spectra can be made out for $x \geq 0.2$ due to the high unintentional doping by O. Based on the CV measurements (see Figure 4.25(a)) this is an expected result, because the unintentional doping is nearly as high as the Ge-doping for elevated Al concentrations. The high doping level causes merging of the (BX) and $(\mathrm{D}^0,\mathrm{A}^0)$ emission peaks, such that the peak energies of the separate transitions cannot be obtained by multi-peak fits any more. In the diagram arrows indicate
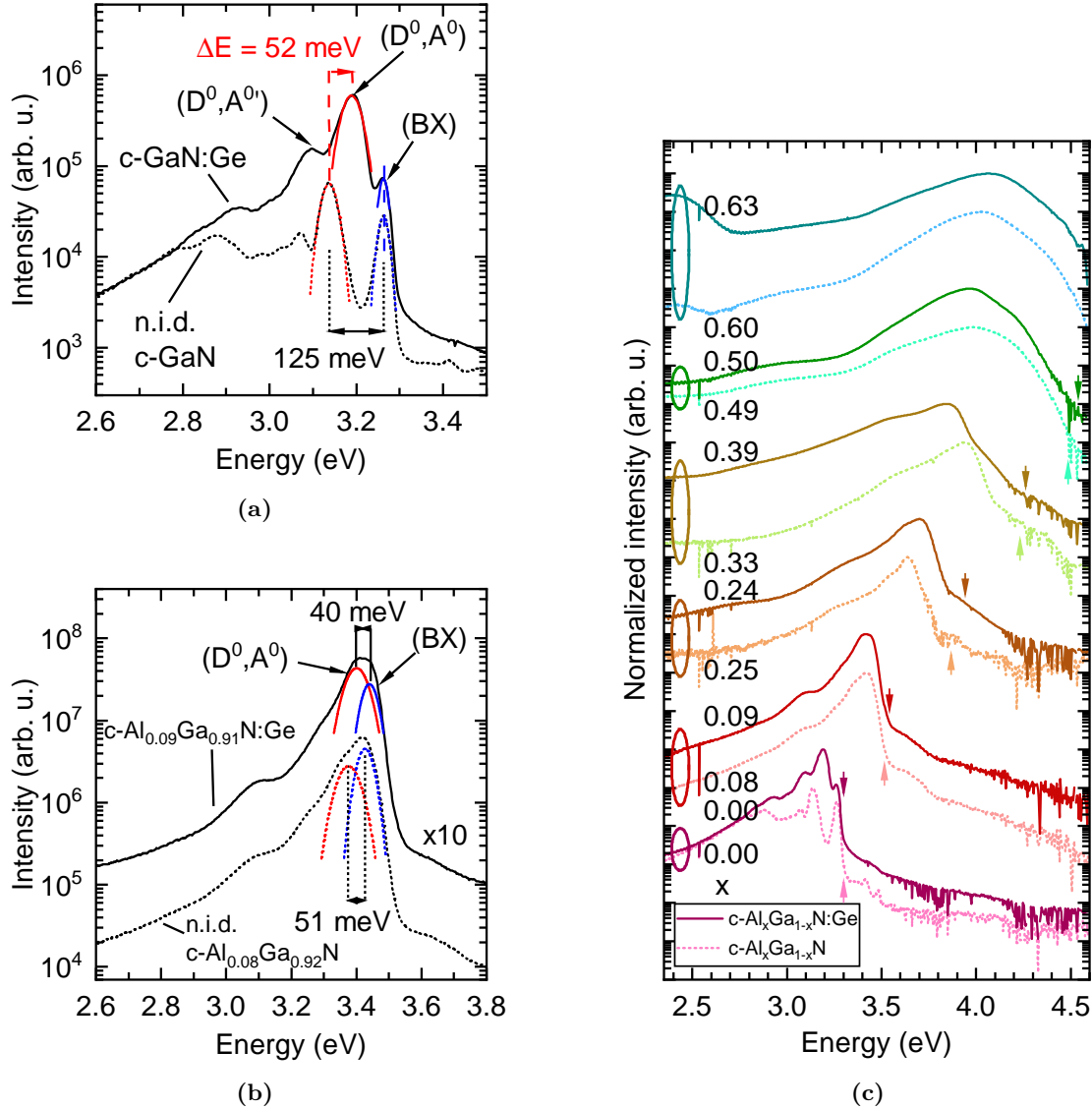
Figure 4.26: **(a)** PL spectra at 13 K of n.i.d. (dotted) and Ge-doped ($T_{Ge} = 800$ °C, full) c-GaN. Peaks are fitted by Gaussian functions to obtain the peak energies. (Samples 2701 and 2692) **(b)** PL spectra at 13 K of n.i.d. (dotted) and Ge-doped ($T_{Ge} = 800$ °C, full) c-Al$_{0.10}$Ga$_{0.90}$N. Multi-peak fits illustrate that the near band-edge emission consists of two transitions. The spectrum of the doped sample is shifted vertically for better clarity. (Samples 2703 and 2706) **(c)** PL spectra at 13 K of all n.i.d. (dotted) and Ge-doped ($T_{Ge} = 800$ °C, full) c-Al$_x$Ga$_{1-x}$N layers with varying x. Spectra are normalized to the respective maximum intensity and shifted vertically. Al mole fractions x are denoted besides the spectra and arrows indicate the direct band gap for the respective x [25].

the calculated direct band gap [25] of c-$Al_xGa_{1-x}N$ for the respective x. With increasing x the peak emission more and more deviates from the band gap towards lower energies.

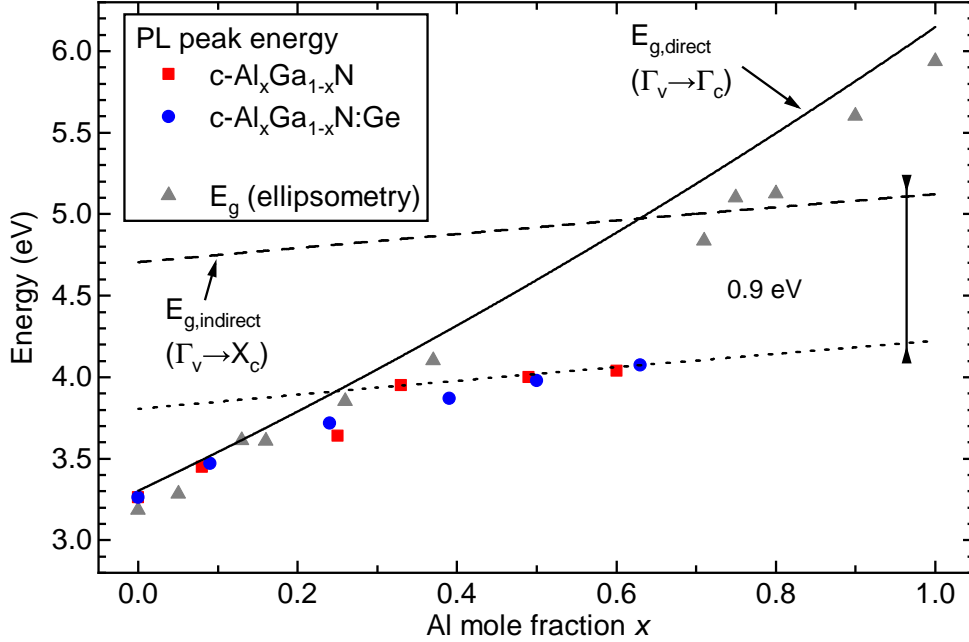**Figure 4.27:** Peak energies of the PL emission at $13\,K$ of n.i.d. (red squares) and Ge-doped ($T_{Ge} = 800\,°C$, blue circles) c-$Al_xGa_{1-x}N$ layers depending on x. The calculated low-temperature direct band gap is plotted as a solid line and the indirect band gap as a dashed line [25]. The band gap experimentally determined by ellipsometry at $300\,K$ is plotted as triangles [25]. To visualize that the PL emission is related to a defect level located $0.9\,eV$ below the indirect band gap, this level is drawn as a dotted line.

To investigate this behavior, the peak energies of the spectra are plotted versus the Al mole fraction x together with the calculated low temperature direct (solid line) and indirect band gap (dashed line) [25] of c-$Al_xGa_{1-x}N$ in Figure 4.27. Peak energies of spectra of n.i.d. layers are displayed as red squares, and those of doped layers as blue circles. Additionally, values for the direct band gap experimentally determined by ellipsometry (at $300\,K$) [25] are plotted as triangles. The emission follows the direct band gap in excellent agreement up to $x \approx 0.1$, but for $x \geq 0.37$ it is related to a deep defect level (dotted line) situated $0.9\,eV$ below the indirect band gap of c-$Al_xGa_{1-x}N$. The emission of the $x = 0.23$ and $x = 0.26$ layers is related to neither the band gap nor the defect level. The crossing of direct band gap and deep defect level occurs at $x = 0.25$. This deep defect possibly could be a DX center formed by O. It is known for wurtzite $Al_xGa_{1-x}N$ that O forms a DX center at $x > 0.3$ [50, 61, 62], however theoretical calculations carry out that O should not form a DX center in cubic $Al_xGa_{1-x}N$ [61]. Since DX centers cause persistent photoconductivity, the presence of such a defect can be verified by an appropriate experiment. This is presented in the appendix (section A.2) and carries out, that the defect is very likely *not* a DX center. Further investigation is required at this point to identify the origin of this defect. However,

it seems not to be related to the incorporation of Ge, because the emission of both n.i.d. and Ge-doped layers sticks to this defect level.

The PL spectra of the second sample series, where c-Al$_{0.25}$Ga$_{0.75}$N was doped using different Ge effusion cell temperatures T_{Ge}, are shown in Figure 4.28(a). The spectra are normalized and shifted vertically; a dashed line at 3.92 eV indicates the low temperature band gap of c-Al$_{0.25}$Ga$_{0.75}$N [25]. The Ge effusion cell temperature T_{Ge} used for doping is denoted next to each spectrum. Up to $T_{Ge} = 800\,°$C the emission stems from below the band gap. As described above, for this Al mole fraction x it is neither related to the band gap nor to the deep defect level. Performing multi-peak fits (not shown here) indicates that the near band-edge emission consists of two peaks. These are most likely, like in the case of c-GaN, an excitonic and a donor-acceptor pair recombination. When the Ge effusion cell temperature is raised to $T_{Ge} = 850\,°$C and above, the spectra become broader and shift to energies above the band edge. As in the case of highly doped c-GaN (cf. section 4.3.4) this blue-shift is expected to occur due to the Burstein-Moss effect and is an indication for degenerate doping. Up to $T_{Ge} = 950\,°$C the emission energy rises monotonously, but it decreases again in case of the highest doped layer ($T_{Ge} = 1000\,°$C). This layer is partially polycrystalline (cf. section 4.4.2), thus the emission from this layer is expected to be defect-related. In Figure 4.28(b) the integral intensities of the PL spectra are plotted versus T_{Ge}. With T_{Ge} being increased up to 800 °C, the emission intensity rises by one order of magnitude compared to the n.i.d. layer. The emission intensity of the $T_{Ge} = 850\,°$C layer drops slightly, but is still higher than that of the n.i.d. layer. When the doping is further increased, emission intensities rapidly drop by several orders of magnitude. This observation partially coincides with the sharp rise of dislocation densities, that occurs at $T_{Ge} = 850\,°$C (see section 4.4.2), as dislocations act as non-radiative recombination centers. Also, the incorporation of high Ge concentrations seems to lead to the formation of additional non-radiative recombination centers, that are not related to dislocations.

4.4.5 Conclusion

The incorporation of Ge into c-Al$_x$Ga$_{1-x}$N layers could be verified by TOF-SIMS. For layers doped using $T_{Ge} = 800\,°$C, the incorporation of Ge is almost independent on the Al mole fraction x, and as a result the donor concentration measured by CV spectroscopy is almost constant over the whole range $0 \leq x \leq 0.6$. The incorporation of O, which causes unintentional n-type doping, however rises linearly with x and results in an increasing donor concentration in n.i.d. layers. PL spectroscopy reveals that the optical emission of c-Al$_x$Ga$_{1-x}$N layers is related to a deep defect level 0.9 eV below the indirect band gap, when the Al mole fraction exceeds $x = 0.25$. This defect level is however present in both Ge-doped and n.i.d. layers and is thus not related to the incorporation of Ge. For c-Al$_{0.25}$Ga$_{0.75}$N layers grown with varying Ge effusion cell temperature T_{Ge}, the Ge incorporation measured by TOF-SIMS and the donor concentration measured by CV spectroscopy proceed proportionally to the Ge vapor pressure curve. However, structural degradation of the layers occurs when the doping level exceeds approximately $3 \times 10^{19}\,$cm^{-3}. This also manifests in the PL spectra of these layers, as the emission intensity rapidly drops when doping exceeds the low $10^{19}\,$cm^{-3} range. Overall, Ge is well suited for n-type doping of c-Al$_x$Ga$_{1-x}$N within the investigated range of parameters. The maximum achieved
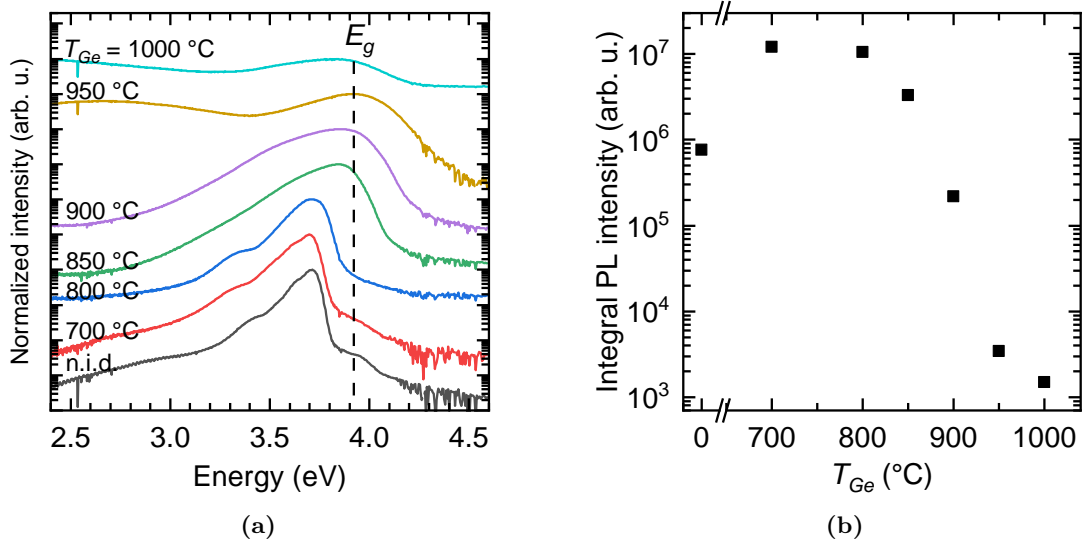
Figure 4.28: (a) PL spectra at 13 K of differently doped c-Al$_{0.25}$Ga$_{0.75}$N layers. Spectra are normalized and shifted vertically. The dashed line corresponds to the low temperature band gap of c-Al$_{0.25}$Ga$_{0.75}$N $E_g = 3.92$ eV [25]. **(b)** Integral intensity of the PL spectra shown in (a).

donor concentration is 1.4×10^{20} cm^{-3}, but considering the poor structural and optical properties of highly doped layers, the maximum reasonable donor concentration is around 3×10^{19} cm^{-3}.

4.5 Reduction of growth rates at high doping levels

It has been noticed (see section 4.3), that the growth rate of c-GaN is significantly reduced when high Ge or Si dopant fluxes are applied. From literature it is known, that Si acts as an anti-surfactant in wurtzite GaN growth, by forming a SiGaN$_3$ layer below the surface that inhibits further growth [137]. Reduced growth rates are reported for highly doped layers [138]. Possibly this is also the case for zinc blende GaN, and similar effects could occur with Ge. In this chapter, first a summary of growth rate reduction of Si- and Ge-doped c-GaN and Ge-doped c-Al$_x$Ga$_{1-x}$N layers is given. After that, the origin of this effect is investigated.

Growth rates are obtained by dividing the measured layer thickness by the growth time of the respective layer. Layer thicknesses of Ge-doped c-GaN and c-Al$_{0.25}$Ga$_{0.75}$N layers are determined by reflectometric interference spectroscopy (see Figure B.5 in the appendix on page 131) and TOF-SIMS measurements (Figure B.6, page 132), and layer thicknesses of Si-doped c-GaN layers are determined by reflectometry only.

In Figure 4.29(a) the growth rates of Ge-doped c-GaN layers (samples listed in Table 4.3) are shown depending on the doping level. Within the accuracy of measurement, values determined by both methods are consistent. Up to the mid 10^{18} cm^{-3} doping range the growth rates are nearly constant, but begin to drop with further increased doping. At the highest achieved doping level of 3.7×10^{20} cm^{-3} the growth rate is reduced by 40 %.
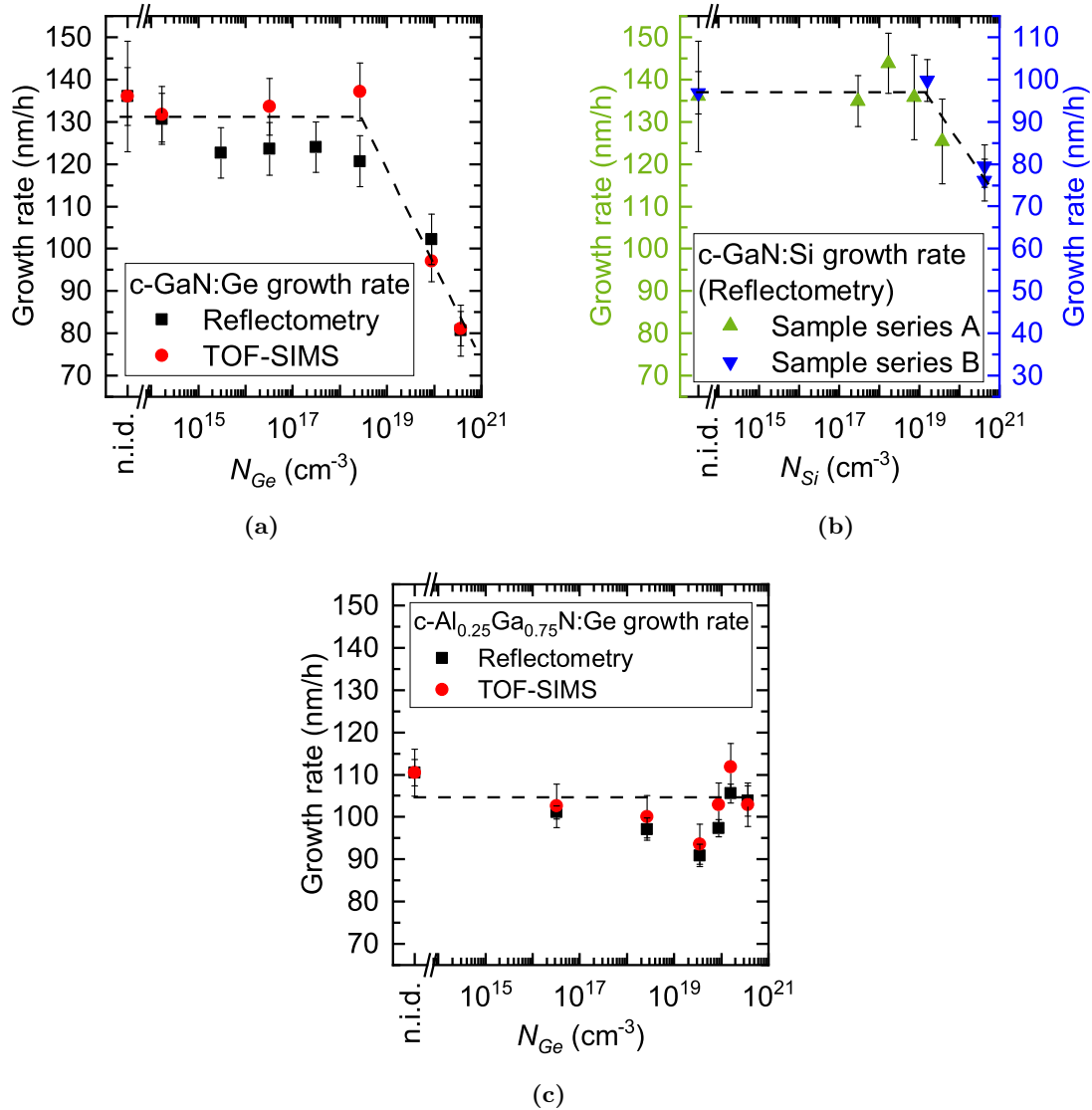
(a)

(b)

(c)

Figure 4.29: Growth rates of **(a)** Ge-doped, **(b)** Si-doped c-GaN and **(c)** Ge-doped c-$Al_{0.25}Ga_{0.75}N$ depending on the doping level. Values are obtained by dividing the measured layer thickness by the growth duration.

Figure 4.29(b) shows the growth rates of Si-doped c-GaN layers. Here, two sample series are investigated. The Si-doped layers listed in Table 4.3 are referred to as series A, and the highly Si-doped layers from Table 4.4 are referred to as series B. As the growth rates during the growth of series B were lower in general, the growth rates of this series are plotted on the right axis, which is shifted so that the growth rates of the respective n.i.d. layers of both series match. Up to a doping concentration around $10^{19}\,\text{cm}^{-3}$ the growth rates of the Si-doped layer are constant, and they drop with further increased doping. At the highest achieved free electron concentration of $4.3 \times 10^{20}\,\text{cm}^{-3}$ the growth rate is reduced by 20 %. Figure 4.29(c) displays the growth rates of Ge-doped c-Al$_{0.25}$Ga$_{0.75}$N layers (sample series 2 from Table 4.5). No clear trend is recognizable here; the growth rates are nearly independent on the doping level.

The reason for the growth rate reduction of highly doped c-GaN layers is probably an accumulation of the dopant material during growth. As described in section 3.1.3, when growing n.i.d. layers a Ga excess of exactly one monolayer is maintained to obtain highest-quality layers. If now for example additionally Ge is supplied, the excess monolayer consists of both Ga and Ge atoms. The accumulation of Ge in this layer can be explained by considering the bond dissociation energies of the Ge–Ge and Ga–Ga bonds given in Table 4.6. The Ge–Ge bond has a higher dissociation energy than the Ga–Ga bond, thus it is expected that the evaporation of Ga from the excess layer is stronger than the evaporation of Ge. Therefore, an increasing amount of Ge can accumulate on the surface during growth. Impinging Ga atoms could then be hindered by the Ge adlayer to reach growth front. Also considering the bond dissociation energies, the Ge–N bond is more likely to be formed than the Ga–N bond. The same relations also apply to Si-containing bonds. Turning towards the Al-containing layers, for which no growth rate reduction is observed, the dissociation energy of Al–N is higher than for Ge–N and Ga–N. Therefore, it is expected that Al is directly built into the crystal without accumulating in an adlayer, and it is not expected to be hindered from incorporation by the accumulated Ge and/or Ga. It is however unclear, why the growth rates are not reduced at all, even at low Al mole fractions of $x = 0.25$. It is expected more likely that the presence of low Al mole fractions only weakens the effect of growth rate reduction rather than eliminating it.

There are several measurements that support the assumption of dopant material accumulation. In surface topography images measured by AFM both for highly Ge-doped (Figure 4.9(b)) and Si-doped (Figure 4.15(b)) layers accumulation of material is observed along APBs. This material is possibly Ge or Si, because it is not present on lower doped layers.

Accumulation of Ge is also observed in the TOF-SIMS depth profiles of samples that consist of several differently doped layers separated by n.i.d. layers. In Figure 4.30 the depth profile (only Ga- and Ge-related signals) of such a sample is plotted. The layer structure is indicated by different colors in the background of the diagram: First, a 100 nm n.i.d. c-GaN layer is grown. After that, a 70 nm thick Ge-doped layer is grown followed by a 70 nm n.i.d. layer. This sequence is repeated with increasing Ge effusion cell temperatures from $T_{Ge} = 600\,°\text{C}$ up to $1000\,°\text{C}$ in steps of $100\,°\text{C}$. Lastly, a 100 nm layer of n.i.d. c-GaN is grown. The ^{69}GaN$^-$ signal (blue line) is constant throughout the whole structure and drops as soon as the 3C-SiC substrate is reached. Violet and orange lines correspond to the

Table 4.6: Bond dissociation energies ΔH for bonds containing Si, Ge, Ga, Al, and N.

Bond	ΔH (kcal/mol)	Reference
Ga – Ga	33.0	[139, p. 4.45]
Al – Al	44.5	[139, p. 4.41]
Ge – Ge	45	[140, p. 159]
	65.5	[139, p. 4.45]
Si – Si	78.2	[139, p. 4.50]
	54	[140, p. 159]
Ga – N	37.7	[141, p. 76]
	48.5	[16, p. 6]
Al – N	71.0	[139, p. 4.41]
	63.5	[16, p. 6]
Ge – N	61	[140, p. 159]
	55	[142, p. 202]
Si – N	104.9	[139, p. 4.50]
	80	[140, p. 159]
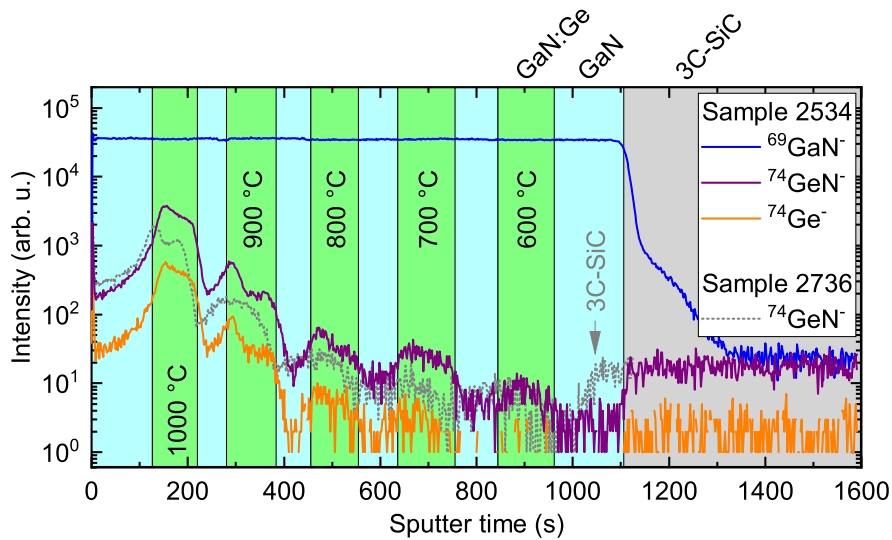
Figure 4.30: TOF-SIMS depth profile of a sample consisting of several differently Ge-doped layers separated by n.i.d. layers. The layer structure is indicated by colors in the background (cyan: n.i.d., green: Ge-doped). Temperatures given for the Ge-doped layers refer to the Ge effusion cell temperature. The profile of a second sample with the same layer sequence is plotted as a dotted line.

^{74}GeN$^-$ and ^{74}Ge$^-$ signals, respectively. Both signals proceed proportionally to each other, but the ^{74}GeN$^-$ signal features a six times higher sensitivity. It is immediately visible that the Ge-related signals are not constant within the Ge-doped layers. To confirm this, a second sample with the same layer sequence was grown and investigated by TOF-SIMS. The ^{74}GeN$^-$ signal from this sample is plotted as a dotted line. Due to deviating growth conditions, the thickness of this sample is slightly smaller, but however the depth profile shows exactly the same behavior as mentioned above. The interfaces between doped and n.i.d. layers cannot be made out exactly, because the Ge-signals rise and fall gradually at the interfaces. When sputtering the sample, some Ge atoms of doped layers are taken along into the n.i.d. layers by recoil implantation, which explains the gradual decrease of the Ge concentration at the bottom boundaries of doped layers (seen in sputtering direction). The decrease of the Ge-signals is however more gradual at the boundaries facing the surface of the structure. If one assumes an accumulation of Ge during growth of the Ge-doped layers, there is still excess Ge present when growing the following n.i.d. layer, which results in a gradually decreasing incorporation of this excess Ge into the n.i.d. layer. The Ge accumulation also explains that the Ge-related signals rise monotonously with ongoing growth of the doped layers. A deviation from this behavior is observed for the $T_{Ge} = 900\,°C$ layer of sample 2534 and the $T_{Ge} = 1000\,°C$ layer of sample 2736. Here, the increase of the Ge-concentration is rather step-like, which is probably caused by a fluctuation of the Ge-flux. Similar multilayer-structures of wurtzite GaN grown by MOVPE exhibit constant doping profiles [143], which means that the observed effect is very likely related to the growth process employed here. Furthermore, depth profiles of the 600 nm thick Ge-doped c-GaN layers (cf. section 4.3) exhibit homogeneous doping profiles. It is assumed that due to the longer growth time of those layers at some point a saturation of Ge at the surface occurs.

Transmission electron microscope (TEM) images were taken of a $3.1 \times 10^{20}\,cm^{-3}$ Ge-doped c-GaN layer (sample 2975). EDX was performed near the surface to investigate the layer composition. In Figure 4.31(a) the near-surface TEM image is shown. The c-GaN layer is visible in the upper part of the image. The yellow line indicates where the EDX analysis is performed. Along this line, in steps of 1 nm EDX spectra are recorded, and for each step the ratio between Ga and Ge atoms is calculated from the respective Kα line intensities (Figure 4.31(b)). The obtained Ge content is constant up to 4 nm below the surface, but rises by a factor of six in the area close to the surface. This is a further indication, that Ge accumulates during growth, and the excess Ge remains on the surface when growth is stopped. To investigate if the high Ge concentration near the surface distorts the crystal structure, a high resolution TEM image is taken (Figure 4.32). In the left part of the image, residues of the adhesive are visible; the c-GaN layer is located in the right part of the image. Apart from dislocation lines, that proceed diagonally through the c-GaN layer, there are no distortions of the lattice apparent. Also near the surface, where the Ge concentration is increased, no defects are visible.
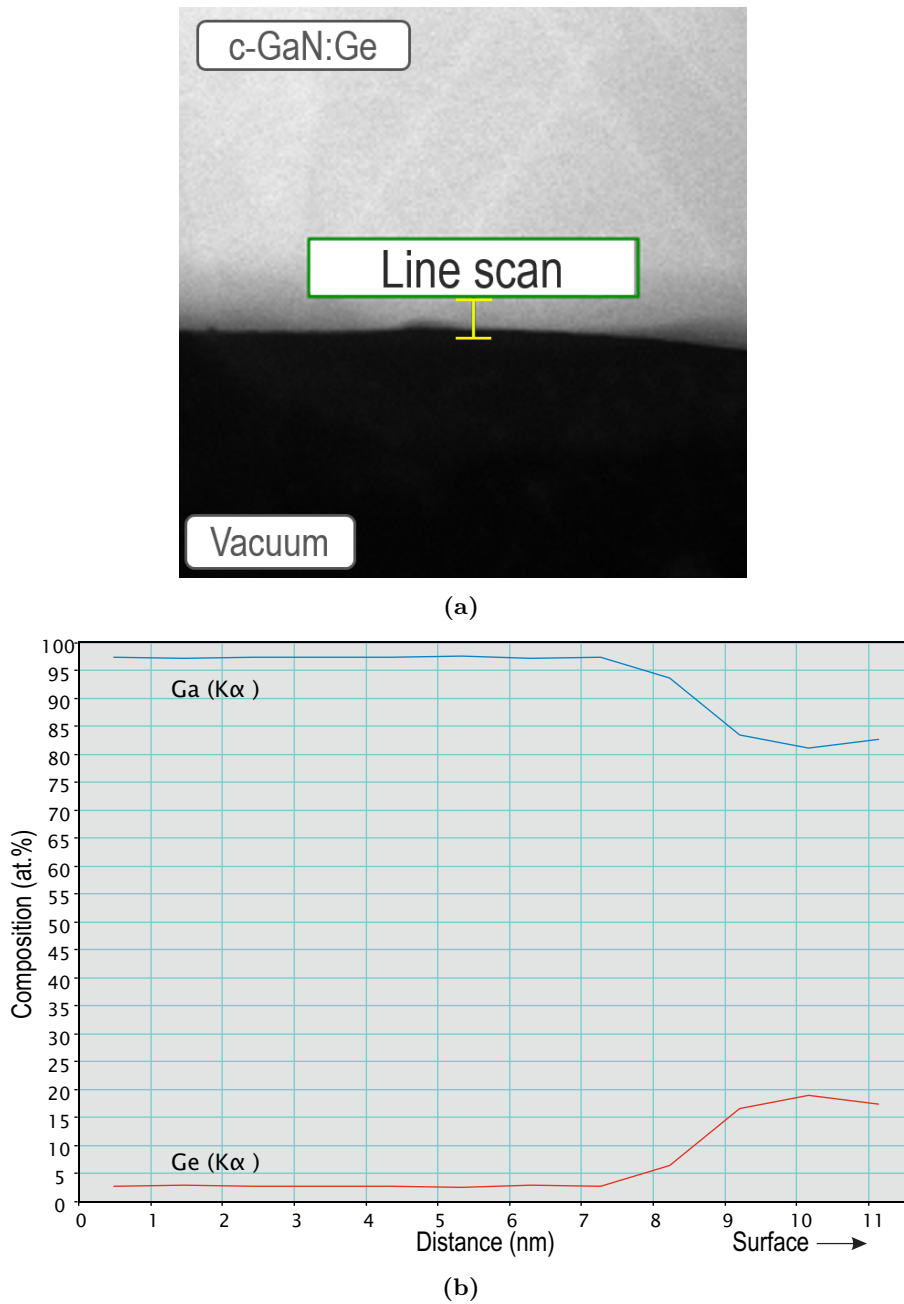
(a)

(b)

Figure 4.31: (a) Near-surface TEM image of a highly Ge-doped layer (sample 2975). **(b)** EDX analysis is performed along the yellow line drawn in (a). The material composition is calculated for several positions based on the Ga and Ge Kα line intensities. Other signals such as N are discarded, thus the denoted compositions only refer to the ratio between Ga and Ge atoms, and not to the actual layer composition. The distance axis proceeds from top to bottom of the yellow line in (a).

Figure 4.32: High resolution TEM image of a highly Ge-doped layer (sample 2975). The c-GaN layer is visible in the right part of the image; in the left part residual adhesive can be seen.

4.6 Ge-doping of GaN/AlN superlattices

In the previous sections, the doping of single c-GaN and c-Al$_x$Ga$_{1-x}$N layers was investigated. In this section now the doping of GaN/AlN superlattices (SLs) is covered. These structures are fabricated with the aim to obtain intersubband absorption around the telecommunication wavelength 1.55 µm. While intersubband absorption is also possible for a single QW, it is enhanced in a SL structure with numerous periods. Structural properties of layers with different doping levels and doping profiles are investigated, and PL spectroscopy is performed to investigate the optical properties. Furthermore, intersubband absorption of SL structures is measured.

The general layer structure is sketched in Figure 4.33. First, a 90 nm thick buffer layer of n.i.d. c-GaN is grown. Thereafter the SL structure follows, which consists of 40 periods of 2 nm c-AlN barriers and 1.8 nm c-GaN quantum wells. The structure is terminated again by a c-AlN barrier layer. In Table 4.7 the samples and their doping characteristics are listed. One sample is grown without intentional doping (2991). A series of samples (2986-2990) is grown with differently Ge-doped QW layers, where the Ge flux was enabled during growth of the entire QW layers. Decreasing growth rates at high doping levels were considered to obtain comparable QW thicknesses at all doping levels. A bunch of other samples, which are not listed here, were grown at $T_{Ge} = 900\,°C$ on different 3C-SiC substrates. In three samples (3003-3005) the QWs were doped, but δ-doping was applied. This means, that each time first only half of a QW layer was grown without doping, then growth was interrupted and the Ge shutter was opened. The Ge shutter was closed again after 6 s, which corresponds to a deposition of one monolayer Ge at $T_{Ge} = 770\,°C$, and corresponds to a higher Ge amount for the other two samples where T_{Ge} was higher. After that, the second half of the QW layer was grown. And finally, one sample (3002) was grown with doping of the c-AlN barriers instead of the c-GaN QWs (modulation doping).
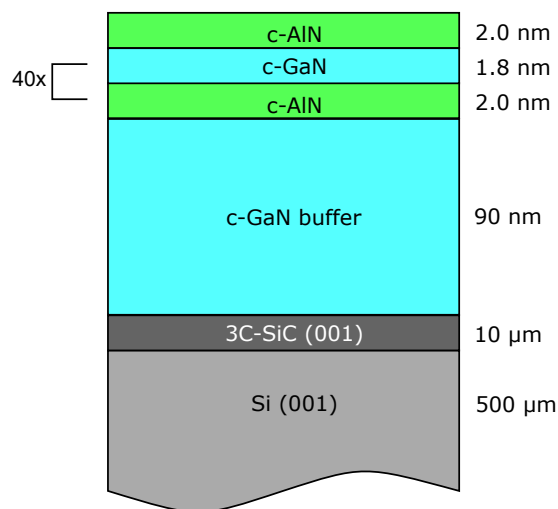

Figure 4.33: General stacking sequence of the superlattice samples. (Not to scale)

Table 4.7: List of superlattice samples with different Ge doping profiles. General sample structure see Figure 4.33. All layers are grown on substrate 16CO126.

Sample	Doping profile	Ge cell temp. T_{Ge} (°C)	Surface roughness (nm)
2991	not intentionally doped (n.i.d.)	-	2.5
2988	c-GaN QWs (conventional doping)	800	2.3
2987	c-GaN QWs (conventional doping)	850	3.2
2986	c-GaN QWs (conventional doping)	900	3.5
2989	c-GaN QWs (conventional doping)	950	3.7
2990	c-GaN QWs (conventional doping)	1000	19
3002	c-AlN Barriers (conventional doping)	900	2.1
3003	c-GaN QWs (δ-doping)	770	2.1
3005	c-GaN QWs (δ-doping)	900	5.0
3004	c-GaN QWs (δ-doping)	1000	7.0

4.6.1 nextnano³ simulations

The commercially available software nextnano³ [98] was used to simulate the band structures and energy levels of the investigated sample structures. nextnano³ is a self-consistent Schrödinger-Poisson-Current solver, which calculates the electronic structure of 3D, 2D, and 1D devices quantum mechanically.

The purpose of the SL structures is to obtain intersubband transitions at the telecommunication wavelength 1.55 μm, which corresponds to a photon energy of 800 meV. To determine the QW thickness that is required to achieve a $E_1^e \to E_2^e$ transition energy of 800 meV, as a good approximation a single c-GaN/c-AlN QW is simulated with c-AlN barrier thicknesses of 2 nm and the c-GaN QW thickness varying from 0.1 nm to 5 nm in steps of 0.05 nm. The donor concentration of the QW layer is set to 7.8×10^{19} cm^{-3} in these simulations (see next section). The nextnano³ input file used for this simulation is printed in Appendix C. In the example given there, the QW thickness is set to 1.8 nm. A separate simulation is performed for each thickness step. The obtained $E_1^e \to E_2^e$ intersubband transition energies and also the $E_1^e \to E_1^{hh}$ interband transition energies are plotted versus the QW thickness d in Figure 4.34. The interband transition energies can be employed to estimate the QW thickness from PL measurements. Based on the simulations, a QW thickness of 1.85 nm is required to obtain the intersubband transition energy of 800 meV. However, the layer thickness is limited to be an integer multiple of the monolayer thickness 0.22515 nm. The nearest possible thickness is eight monolayers or 1.8 nm. The simulated intersubband transition energy for this thickness is 835 meV, which is sufficiently close to the intended value. A $E_1^e \to E_1^{hh}$ interband transition energy of 3.685 eV is simulated for
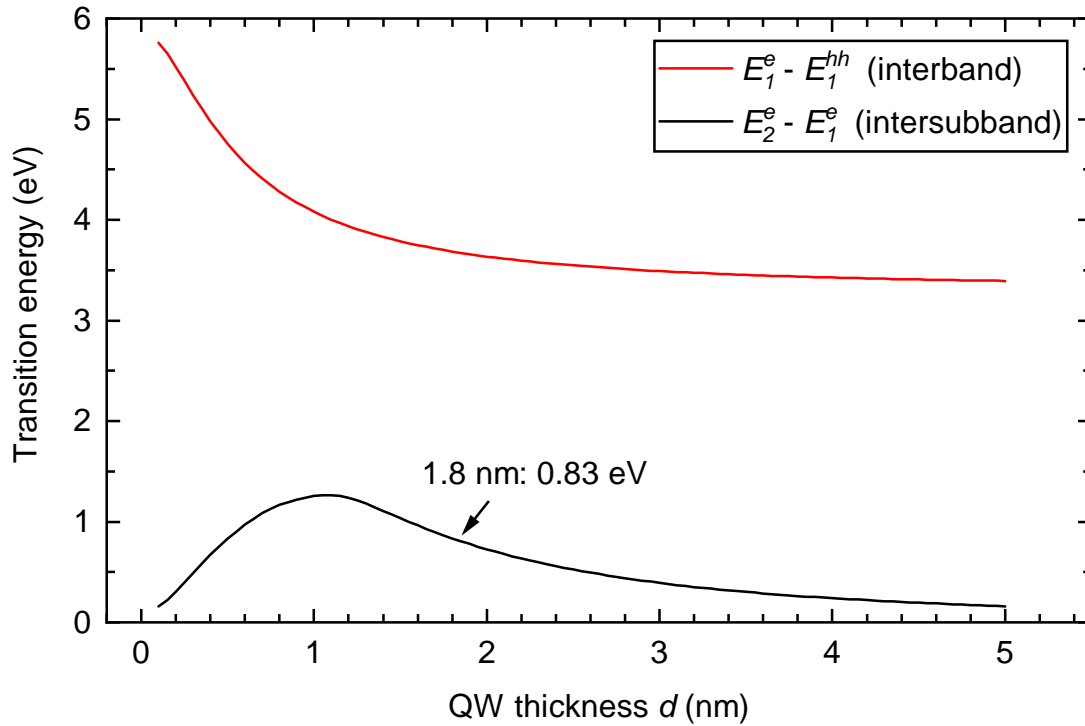
Figure 4.34: nextnano^3 simulation of a single c-GaN/AlN quantum well with n-type doping of 7.8×10^{19} cm^{-3}. The c-AlN barriers are 2 nm thick and the c-GaN quantum well thickness d is varied from 0.1 nm to 5 nm. The simulated $E_1^e \rightarrow E_1^{hh}$ and $E_2^e \rightarrow E_1^e$ transition energies are plotted versus d.

this QW thickness. It is important to keep in mind that nextnano^3 simulations do not incorporate exciton binding energies, which need to be considered when evaluating e.g. PL spectra. As the contribution of the exciton binding energy to the PL transition energy is in the range of a few percent, it is neglected here for the sake of simplicity.

4.6.2 Quantum well doping level

In order to achieve strong $E_1^e \rightarrow E_2^e$ intersubband absorption, the E_1^e state should be highly occupied by applying high n-type doping. On the other hand, if the doping is too high, the E_2^e state will be occupied as well, which would reduce the availability of free target states and result in a weaker absorption. To determine an appropriate doping level, the Fermi level E_F in a 1.8 nm thick QW is calculated depending on the doping level after equation 2.23. As mentioned in section 2.4.1, the effective electron mass m_e^* depends on the QW thickness. After [99, pp. 62f], the effective electron mass in bulk c-GaN of $0.19m_e$ [75] increases to $0.207m_e$ in a 1.8 nm thick QW. Calculated Fermi levels are plotted in Figure 4.35; energies are given with respect to the conduction band edge. The E_1^e level (lower dashed red line) is occupied in any case, but up to a donor concentration of around 1×10^{19} cm^{-3} the position of the Fermi level does not significantly rise, and then
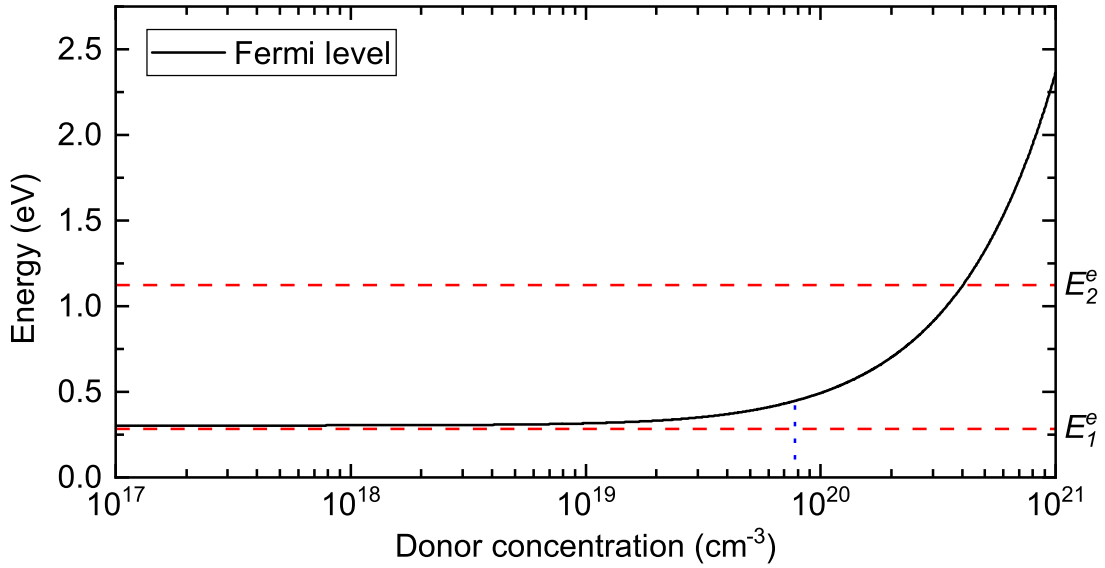
Figure 4.35: Position of the Fermi level in a 1.8 nm thick c-GaN/c-AlN QW depending on the free carrier concentration within the QW. Energies are given with respect to the conduction band edge. The first two energy states are indicated by dashed red lines and the actually employed doping level of 7.8×10^{19} cm^{-3} is indicated by a dotted blue line.

begins to exponentially increase. As it can be seen from the diagram and calculated from equation 2.25, a donor concentration of 4×10^{20} cm^{-3} is required to occupy the second energy level (upper dashed red line). For most of the samples that were fabricated for investigation of intersubband absorption, a donor concentration of 7.8×10^{19} cm^{-3} was chosen, which corresponds to a Ge effusion cell temperature of $T_{Ge} = 900\,°C$. This ensures a high population of the E_1^e level, but is also low enough that the upper doping limit is not exceeded even if the actual doping level deviates from the targeted one.

4.6.3 Structural properties

The surface topography of the SL layers is investigated by AFM. The RMS roughnesses determined from 5×5 µm^2 AFM images are denoted in Table 4.7. For the conventionally doped samples and the n.i.d. sample (samples 2986-2991) the values are plotted versus the Ge effusion cell temperature T_{Ge} in Figure 4.36. Smooth surfaces with a roughness between 2 nm and 4 nm are obtained up to $T_{Ge} = 950\,°C$. These values are comparable to the roughness expected for similarly thick bulk c-GaN layers (cf. section 4.1). The surface at highest doping however features islands with a diameter of over 1 µm, which cause the roughness to climb up tp 19 nm. Also the roughnesses of the δ-doped layers with the two highest doping levels are larger than the average. This result is unexpected to some extent, because the surface of the thick c-GaN layers doped at $T_{Ge} = 1000\,°C$ featured a three times lower roughness. However, this high doping level led to polycrystalline growth and a rough surface of c-Al$_{0.25}$Ga$_{0.75}$N (see section 4.4.2), which means that even the presence of low Al mole fractions deteriorates the layer quality at high doping levels. Thus, the high
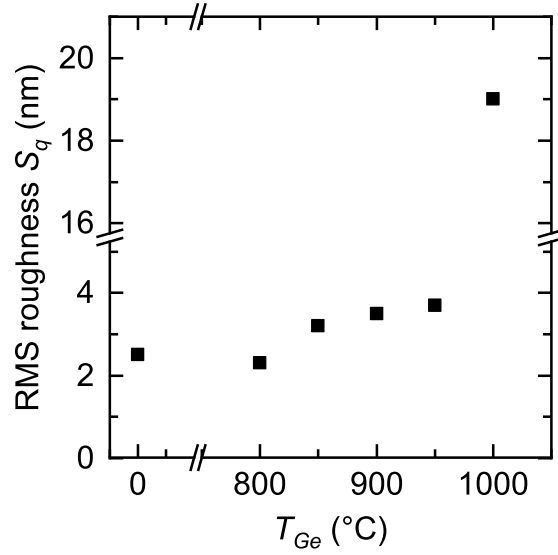
Figure 4.36: RMS roughness determined from $5 \times 5 \, \mu m^2$ AFM measurements of the n.i.d. and conventionally Ge-doped SL samples. ▭
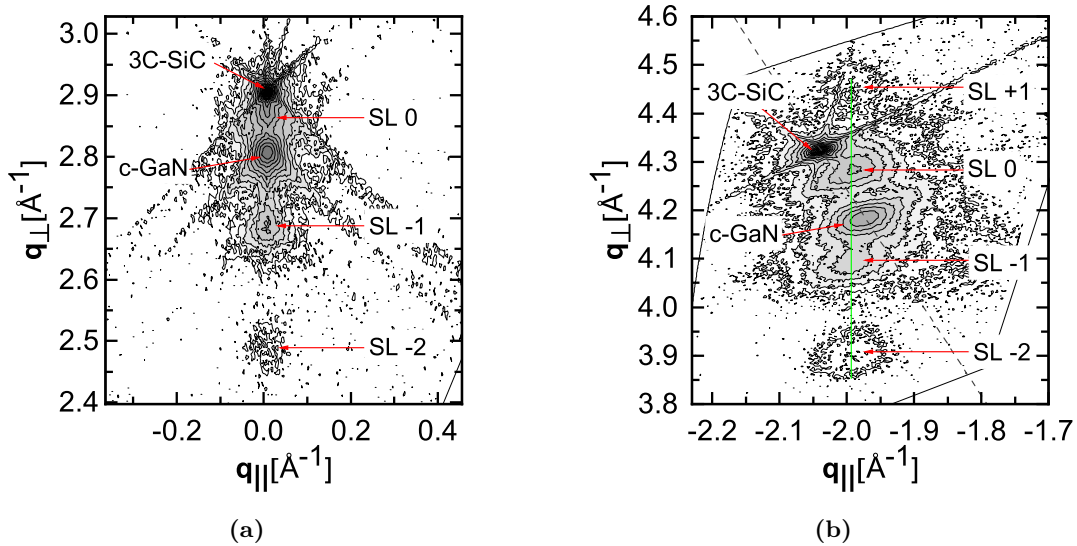

(a)

(b)

Figure 4.37: **(a)** (002) RSM measured by HRXRD of a Ge-doped SL sample ($T_{Ge} = 900\,°C$, sample 2986). **(b)** ($\bar{1}\bar{1}3$) RSM measured by HRXRD of the same sample. The dashed line indicates expected positions of fully relaxed layers. ▭ ▭

surface roughness in this case is expected to be caused by the c-AlN barriers, whose growth is distorted by the high amount of residual Ge present after growth of the c-GaN:Ge layers.

Further structural properties of the layers are investigated by HRXRD. From RSMs around the (002) reflexes the amount of hexagonal inclusions in the layers is estimated. No hexagonal inclusions could be found in any of the SL samples, see for example Figure 4.37(a). RSMs around the asymmetric ($\bar{1}\bar{1}3$) reflexes are recorded to detect the different layers of the structure and to evaluate their strain status. Figure 4.37(b) shows a ($\bar{1}\bar{1}3$) RSM on example of sample 2986. The 3C-SiC substrate peak appears with highest intensity. A dashed connecting line from the 3C-SiC peak to the origin of the coordinate system indicates, where peaks of fully relaxed layers are expected to appear. The c-GaN buffer layer peak is visible exactly on this line, which means that the buffer layer is grown fully relaxed on the 3C-SiC substrate. There are four further peaks visible that correspond to different orders of diffraction of the SL structure. All peaks appear at the same $q_\parallel$ coordinate as indicated by the green vertical line. If the SL structure was grown fully strained on the c-GaN buffer, the SL peaks would appear at the same $q_\parallel$ coordinate as the c-GaN peak. They appear however at lower $q_\parallel$, which means that the SL structure is grown partially strained on the buffer layer. This finding is considered in the nextnano^3 simulations. SL peaks are visible in RSMs of all samples listed in Table 4.7, except the δ-doped layer with highest Ge doping (sample 3004). This sample does not exhibit any SL reflex, not even of the first order. The sample with highest conventional Ge doping (Sample 2990) however exhibits pronounced SL peaks up to the second order. This observation coincides with the RHEED patterns of the samples recorded after growth (see Figure B.7 in the appendix). The pattern of the conventionally doped sample is spotty, which corresponds to the high surface roughness, but still indicates a cubic crystal structure of reasonable quality. The pattern of the δ-doped layer however exhibits strong reflections from polycrystalline material.

TEM images are taken to further investigate the structural quality of the SL structures. In Figure 4.38(a) a TEM image of sample 2986 is shown. At the bottom the 3C-SiC substrate is visible. Within the field of view, no dislocations are apparent, and the surface of the substrate is very smooth. On top the c-GaN buffer layer is visible. It exhibits a number of dislocation lines, which start at the interface to the 3C-SiC substrate and proceed diagonally to the growth direction. Next follows the SL structure, which is also crossed by the dislocation lines, which continue from the c-GaN buffer into the SL structure. A high resolution TEM image of the SL structure is shown in Figure 4.38(b). Please note that the perspective is rotated here, thus the c-GaN buffer layer is located in the upper part of the image. There is a high contrast between the c-AlN barriers (bright) and the c-GaN QWs (dark). Despite the waviness of the structure, the individual layers are sharply separated from each other. Based on rough estimation, the observed layer thicknesses fit to the intended values of 2 nm for c-AlN and 1.8 nm for c-GaN. Also the dislocation lines are visible in this image. The SL structure is disturbed in areas where the dislocation lines proceed, but it is unimpaired in dislocation-free areas. The SL structure hardly generates any new dislocations, but also does not reduce the dislocation density.
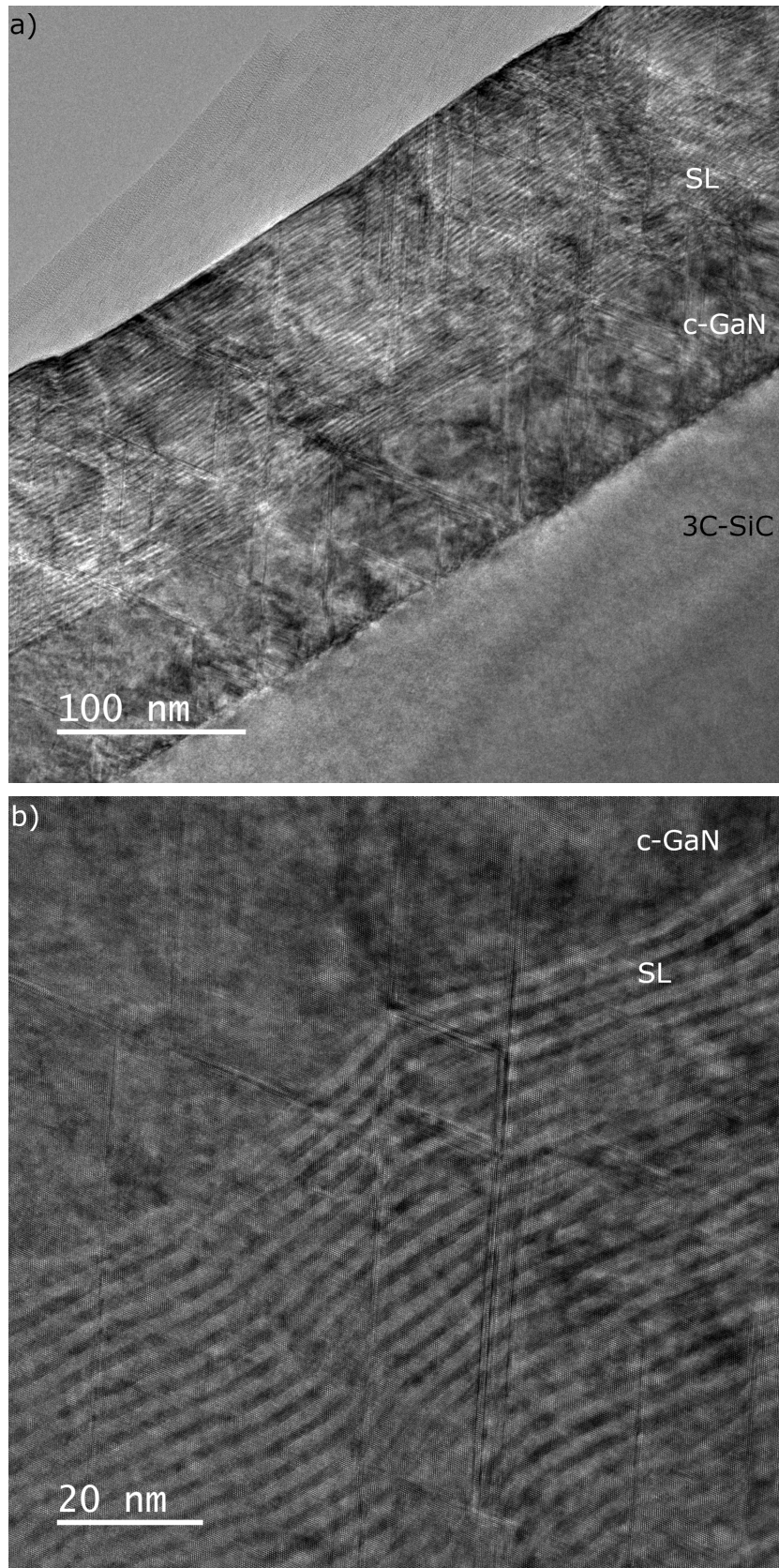
Figure 4.38: **(a)** TEM and **(b)** high resolution TEM image of a Ge-doped SL structure (sample 2986). Please note that the view is rotated in **(b)**.

4.6.4 Photoluminescence spectroscopy

Optical properties of the samples are investigated by PL spectroscopy performed at room temperature. The spectra of the conventionally doped samples with varying Ge doping level as well as the spectrum of the n.i.d. layer are plotted in Figure 4.39(a). In all spectra an emission band at 3.23 eV is visible, which corresponds to the band gap of the c-GaN buffer layer (dashed line). At higher energies the emission from the QWs is visible. For the n.i.d. layer, the peak emission is located at 3.60 eV. With doping up to $T_{Ge} = 850\,°C$ the emission does not shift, but rises in intensity by a factor of five; the FWHM of the emission is not affected. With further increasing doping, the peak emission shifts to higher energies, the emission becomes broader, and the intensity begins to drop. This process is indicated by arrows in the diagram. This behavior is an indication that the structural quality begins to drop if Ge-doping exceeds $8 \times 10^{19}\,cm^{-3}$ ($T_{Ge} = 900\,°C$). The peak emission of the $T_{Ge} = 900\,°C$ sample is at 3.65 eV. Based on the nextnano³ simulation in Figure 4.34, this interband transition energy corresponds to a QW layer thickness of 1.9 nm, which is close to the intended 1.8 nm.

In Figure 4.39(b) the PL spectra of further samples with other doping profiles are shown. The spectrum of the $T_{Ge} = 900\,°C$ sample from the figure above is plotted for comparison (black curve). The peak emission of the barrier-doped layer (red curve) is shifted to 3.77 eV. The FWHM of the peak is comparable to the reference, but the peak intensity has halved. Due to the higher emission energy, the QW thickness is expected to be too low. Possibly the growth rate of the c-GaN layer was reduced, even if the doping was applied to the c-AlN barrier and not to the c-GaN QW. For all of the layers with doping applied to the QW layer, the growth rate reduction was taken into account, but not for this particular layer. Concerning the δ-doped layers, the spectra have some special characteristics. In the spectrum of the $T_{Ge} = 770\,°C$ sample (blue curve) there is besides the QW emission at 3.54 eV an emission band around 3.1 eV. This emission lies 130 meV below the c-GaN band gap and thus cannot be related to a band-to-band or excitonic transition. The δ-doping layer must have introduced further states, that are located within the band gap. A detailed analysis of the influence of δ-doping layers on the band structure is presented in [97]. According to the simulation from Figure 4.34, the QW emission energy of 3.54 eV corresponds to a QW thickness of 2.5 nm. This means that the reduction of growth rate was overestimated in this case. Experience values from conventionally doped layers were taken, but these are apparently not valid when δ-doping is applied. The QW peak emission of the $T_{Ge} = 900\,°C$ δ-doped layer (purple line) is located at 3.72 eV, which is only slightly higher compared to the reference sample. The FWHM of the peak is 15 % lower for the δ-doped layer, but the integral intensity is lower by one third. Besides the QW and c-GaN buffer layer emission, there is a further emission between 3.3 eV and 3.4 eV. This is probably caused by hexagonal inclusions, or additional states have been introduced by the δ-doping layer. Due to the poor quality of the $T_{Ge} = 1000\,°C$ δ-doped sample, the PL emission is very weak. Also, the peak emission energy is far too high, indicating that the QW layer thickness is significantly smaller than intended. Overall, based on the PL spectra, δ-doping of the QW layers is a promising alternative to doping of the entire layer, as a reduction of the peak FWHM could be achieved. However, the growth rate reduction
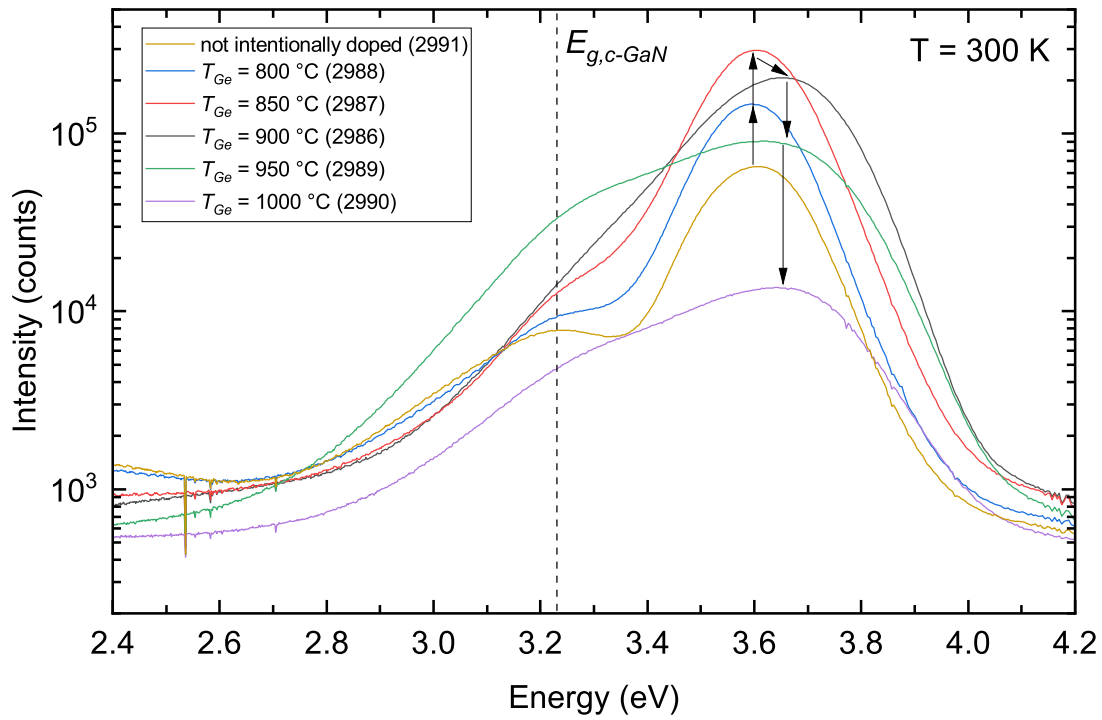
(a)
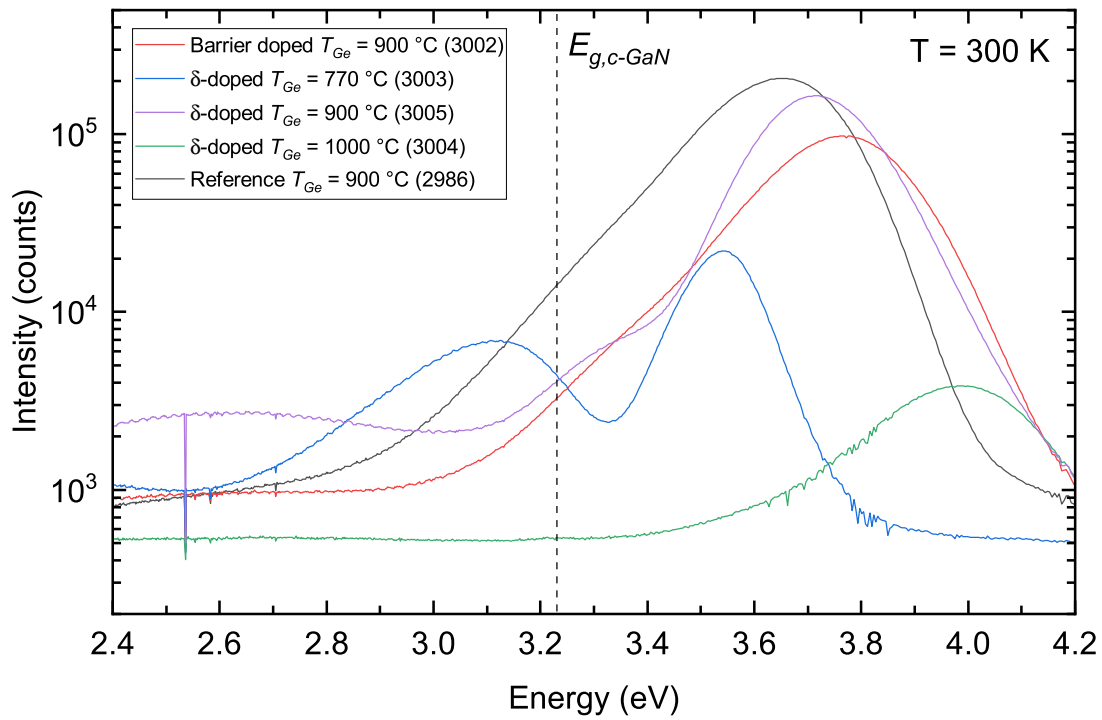
(b)

Figure 4.39: PL spectra at room temperature of SL samples with different doping profiles. **(a)** N.i.d. and conventionally doped SL samples with different doping levels. **(b)** δ-doped samples and sample with doped barriers. The spectrum of the $T_{Ge} = 900\,^{\circ}\text{C}$ sample from (a) is plotted for comparison.

caused by Ge needs to be investigated further, to accurately control the QW thickness, and further investigation regarding energy states introduced by the δ-doping layer needs to be done. No significant impact could be observed for doping of the barriers instead of the QW layer so far. However, only one such sample was grown and there is a lot of room for improvement of the growth process.

4.6.5 Intersubband absorption measurements

Intersubband transitions of SL samples are investigated by performing absorption measurements in the infrared spectral range. The process of sample preparation, measurement, and analysis is described in section 3.3. In Figure 4.40(a) and (b) absorption spectra of two SL samples consisting of 40 periods of 1.8 nm c-GaN QWs with Ge doping at $T_{Ge} = 900\,°C$ and 2 nm c-AlN barriers are plotted. These are some of the first Ge-doped c-GaN/AlN SL samples; prior to this work doping was done using Si. Both samples exhibit strong but broad intersubband absorption. The center of the absorption is at 0.93 eV and 0.96 eV for samples 2863 and 2891, respectively. According to the nextnano³ simulations (see Figure 4.34) these intersubband transition energies correspond to QW thicknesses of 1.65 nm and 1.60 nm, respectively, which are slightly smaller than intended. Also from PL spectra of these samples the QW thickness is estimated based on the simulations, which results in values 0.1 nm smaller than those estimated from the absorption measurements. Figure 4.40(c) shows the absorption spectrum of a similar sample, but with a barrier thickness of 2.5 nm. Also in this case the peak energy of 0.91 eV is slightly too high, but the absorption spectrum is comparable to the previous ones. For comparison, in Figure 4.40(d) the spectrum of a sample with Si-doped QWs and a barrier thickness of 1 nm is shown. The absorption is narrower than that of the other samples, and the peak energy is at slightly too low energy (0.76 eV). However, the absorption is weaker compared to the Ge-doped QWs. The substrate used for all these layers, which clearly exhibit absorption, is *16CO174*. Unfortunately, none of the layers with varying doping profiles, that were described in the previous section, show intersubband absorption. These were grown on a different substrate *16CO126*. Also layers grown on a further substrate by another vendor don't show intersubband absorption. Thus, in the following section the influence of the layer quality and the substrate properties on the absorption are discussed in detail.

4.6.6 Impact of layer quality and substrate properties on absorption

As described in the previous section, SL samples grown on some substrates show absorption, and samples on other substrates don't. In this section, three nominally identical samples grown on three different substrates are compared, and also the substrates are investigated in more detail. All samples consist of a 90 nm c-GaN buffer layer, followed by the SL structure of 40 periods 1.8 nm c-GaN QWs doped by Ge ($T_{Ge} = 900\,°C$, $N_{Ge} \approx 8 \times 10^{19}\,\mathrm{cm^{-3}}$) and 2 nm c-AlN barriers (see Figure 4.33). In Table 4.8 the samples and substrates investigated in this section are listed. All substrates consist of 500 µm Si(001) and approximately 10 µm 3C-SiC(001). Substrate *TYN-B-06* is miscut by 4° towards the (110) direction, the other two are exactly in (001) direction. Substrates *16CO174* and *16CO126* are obtained from the same vendor and substrate *TYN-B-06* from another one.
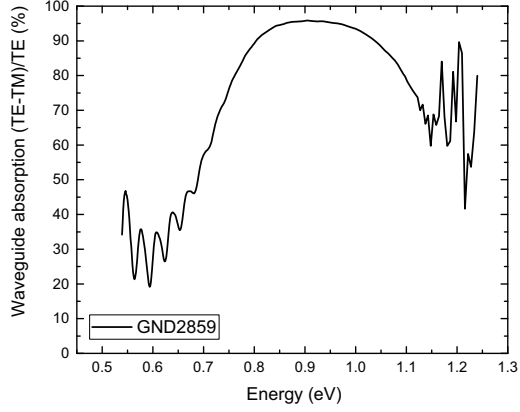
The structural quality of the grown layers is compared by means of HRXRD and AFM
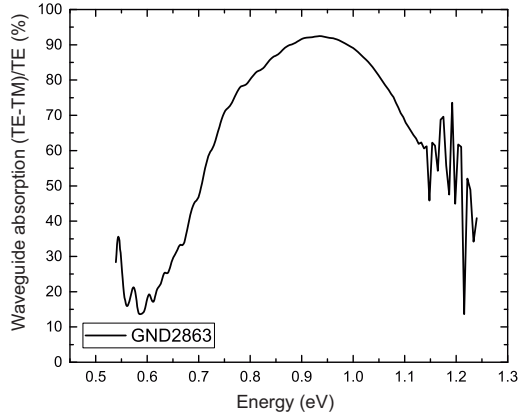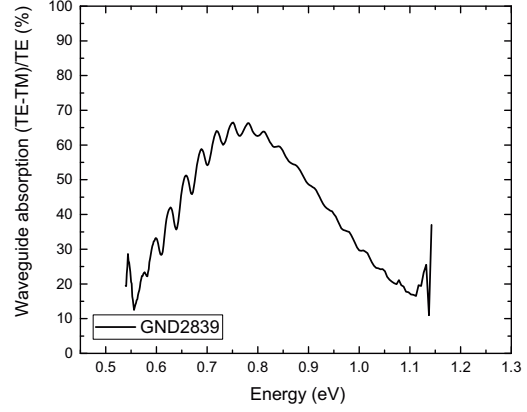
(a) Sample 2863:
40x 1.8 nm c-GaN:Ge / 2 nm c-AlN
$T_{Ge} = 900\,°C$
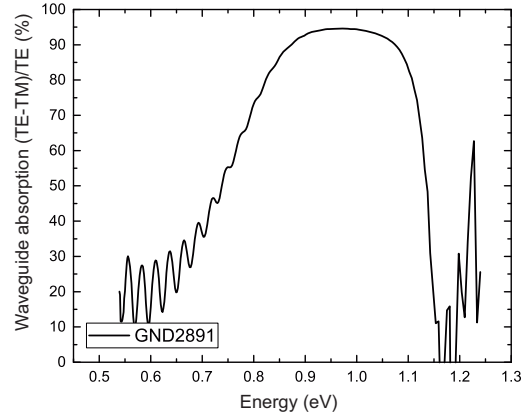
(b) Sample 2891:
40x 1.8 nm c-GaN:Ge / 2 nm c-AlN
$T_{Ge} = 900\,°C$

(c) Sample 2859:
40x 1.8 nm c-GaN:Ge / 2.5 nm c-AlN
$T_{Ge} = 900\,°C$

(d) Sample 2839:
40x 1.8 nm c-GaN:Si / 1 nm c-AlN
$T_{Si} = 970\,°C$

Figure 4.40: Intersubband absorption spectra of SL samples with QW doping levels in the upper $10^{19}\,\mathrm{cm}^{-3}$ range.

Table 4.8: List of superlattice samples grown on three different substrates. Sample structure see Figure 4.33.

Sample	Substrate	Intersubband absorption	c-GaN (002) rocking curve FWHM	AFM roughness $(5 \times 5\ \mathrm{µm}^2)$
2891	16CO174	yes	50.5′	5.9 nm
2986	16CO126	no	50.3′	3.5 nm
3043	TYN-B-06	no	48.2′	3.2 nm

measurements. With HRXRD the (002) rocking curves of the c-GaN buffer layers are measured. The obtained FWHM is proportional to the dislocation density. The measured values are nearly equal; the FWHM of the buffer layer on the miscut substrate is a little smaller. RSMs around the (002) reflections were measured to look for hexagonal inclusions. None of the layers features detectable hexagonal inclusions. Both in (002) and ($\bar{1}\bar{1}3$) RSMs superlattice reflections up to the second order can be observed for all samples. The RMS surface roughness of the samples was determined from 5×5 µm^2 AFM images. The roughness of sample 2891 is almost twice as big as the roughness of the other two samples. The surface of sample 2891 is characterized by small droplets, which are typically formed when growth conditions are too metal-rich. This however seems not to affect the absorption of the SL structure, because this sample shows absorption and the other two samples with smoother surfaces don't.

In Figure 4.38 the SL structure of sample 2986, which has no intersubband absorption, was investigated by TEM. The single layers of the structure are wavy, but clearly separated. Also from sample 2891, which shows intersubband absorption, TEM images are recorded, see Figure 4.41. Unfortunately, the sample could not be prepared exactly in zone axis, but still the SL structure is well visible. Also in this sample, the single layers are wavy, but well separated, and dislocation lines proceed through the whole structure. Also from the TEM measurements there is no reason apparent why one sample shows intersubband absorption and the other does not.

PL spectra at room temperature of the three samples are compared in Figure 4.42. Apart from the difference in peak energy of the QW emission, which is due to slightly deviating c-GaN thicknesses, a strong difference in emission intensity becomes obvious. The emission intensity of sample 2891, which shows intersubband absorption, is the lowest of the three samples. The peak intensity of samples 3043 and 2986 is higher by a factor of 3 and 30, respectively. It is unclear why the emission intensities differ that strongly. Probably the doping of the *16CO126* and *TYN-B-06* substrates is significantly higher than that of the *16CO174* substrate, but according to the data sheets the resistivity of the Si layers is comparable and the 3C-SiC layers are stated to be not intentionally doped.

The substrate surfaces are furthermore investigated using a laser confocal microscope. The images at $100\times$ magnification of substrates *16CO174* and *16CO126* are shown in Figure 4.43. The image of substrate *16CO126* clearly shows the presence of antiphase boundaries (APBs), which is significantly less pronounced for substrate *16CO174*. It has been found that the growth rate of c-GaN can differ up to $10\,\%$ between the two domain orientations [88, 144]. This could result in a broken SL structure at APBs, which is expected to impair the intersubband absorption.

The formation of antiphase domains (APDs) is suppressed when substrates are used whose surface normal is tilted with respect to the (001) direction, as it is the case for the substrate *TYN-B-06*. In Figure 4.44 the confocal laser microscope images of $600\,\text{nm}$ c-GaN on the $4\,°$ miscut *TYN-B-06* substrate (bottom) and a non-miscut 3C-SiC(001) substrate (top) are shown. As indicated by black lines, the APDs, which are already present on the substrate, are carried on to the c-GaN layer. On the miscut substrate there are no APBs present (not shown here), and neither are they on the c-GaN layer. The use of miscut substrates is thus promising for fabricating higher-quality quantum
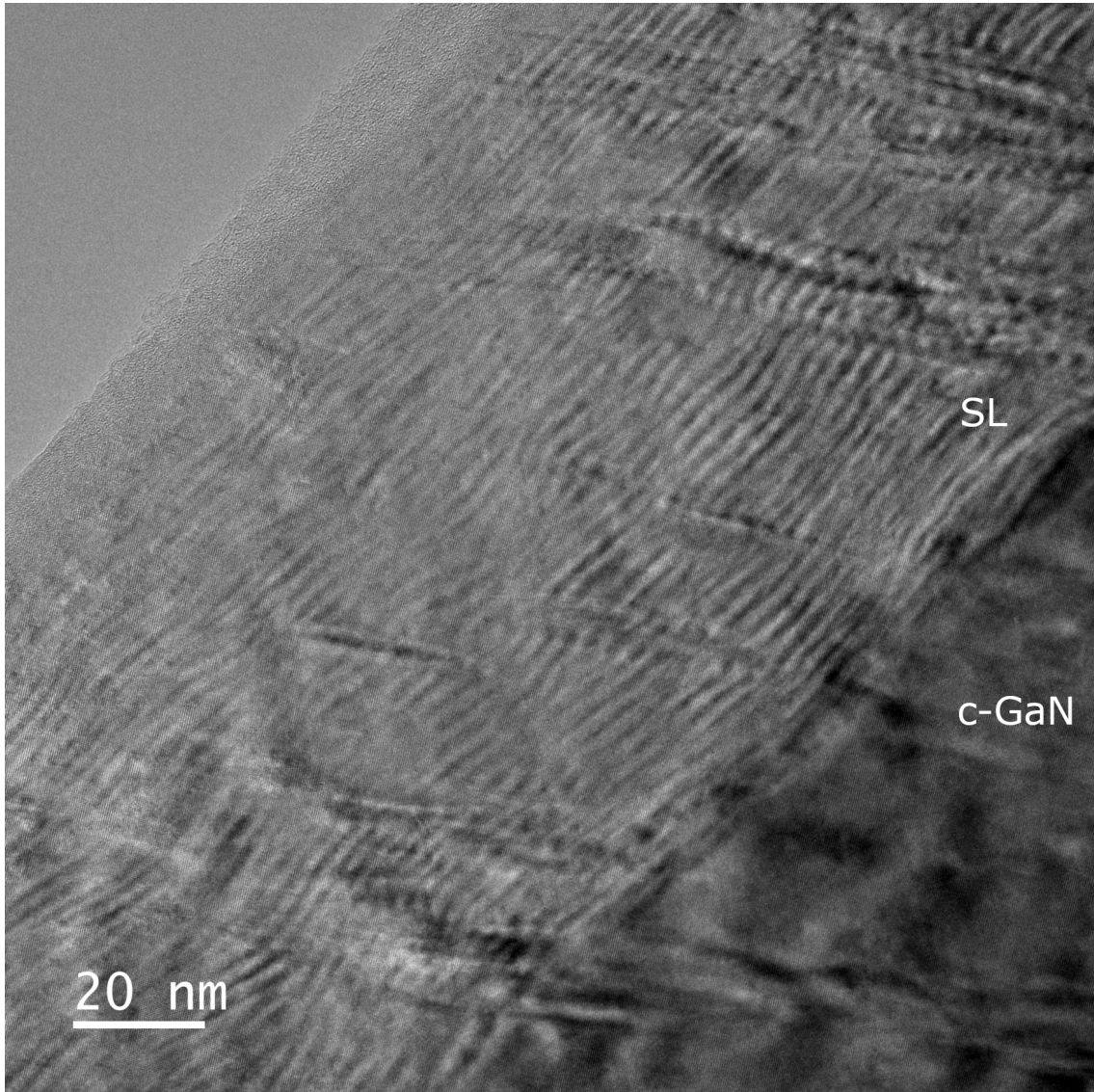
Figure 4.41: High resolution TEM image of a Ge-doped SL structure that shows intersubband absorption (sample 2891: 40x 1.8 nm c-GaN:Ge / 2 nm c-AlN, $T_{Ge} = 900\,°C$).

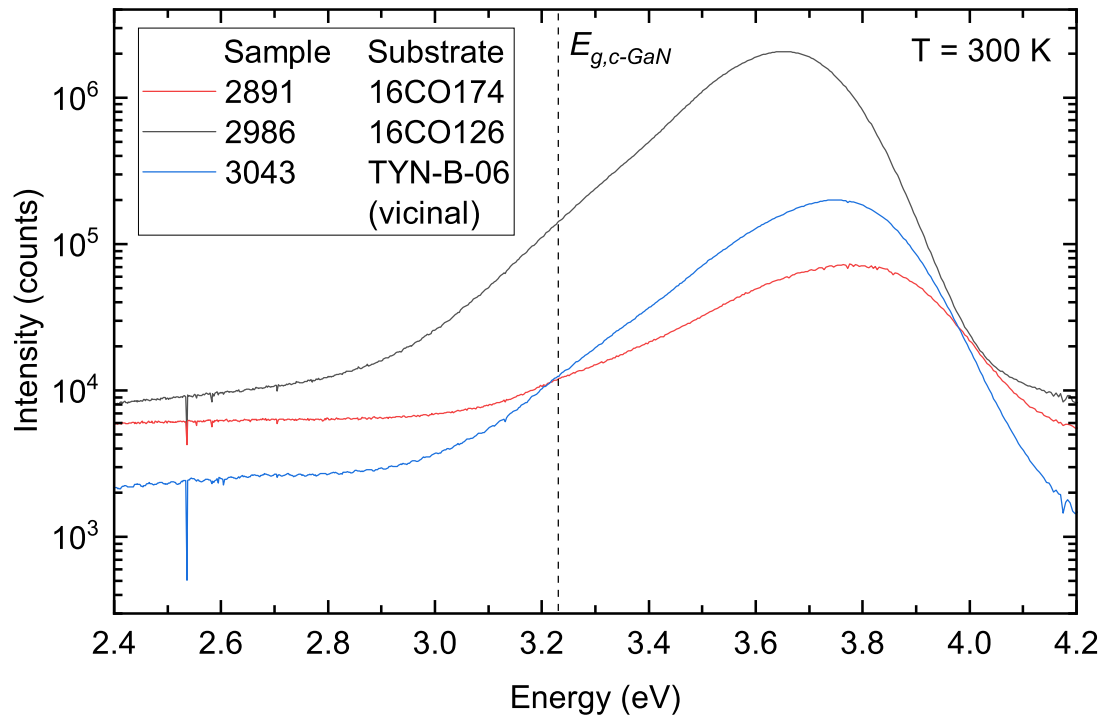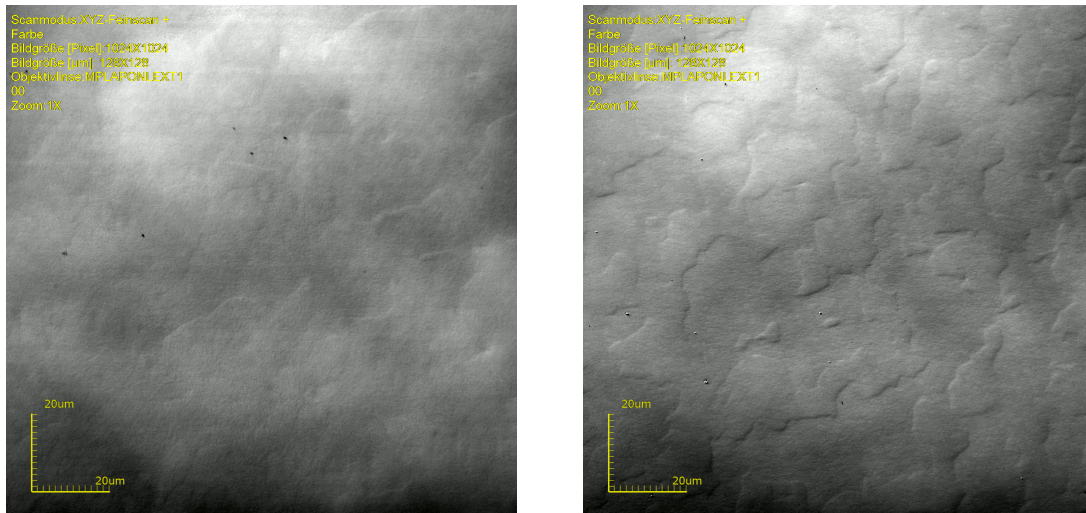**Figure 4.42:** PL spectra at room temperature of SL samples grown on three different substrates.

(a) 16CO174   **(b)** 16CO126

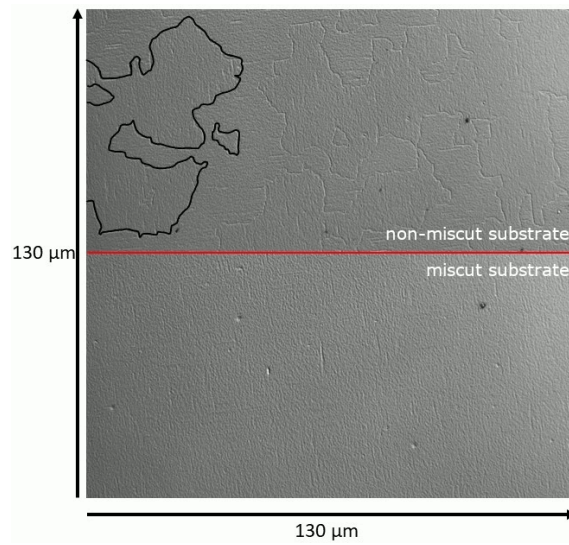**Figure 4.43:** Confocal laser microscope images at $100\times$ magnification of two different 3C-SiC substrates.

Figure 4.44: Confocal laser microscope images at $100\times$ magnification of $600\,\mathrm{nm}$ c-GaN on a non-miscut (top) and $4\,°$ miscut (bottom) 3C-SiC substrate. [145]

structures. Unfortunately, the SL structure grown on the miscut substrate still didn't exhibit intersubband absorption. It seems that the particular miscut substrate that was used here is not suitable for structures operating in the infrared spectral range. The transmission spectrum of the bare substrate was investigated, and it was found that the transmission begins to drop above approximately $1300\,\mathrm{nm}$ (see Figure B.8 in the appendix). A non-miscut substrate by the same vendor shows the same behavior. Further work is required at this point to investigate which effect causes the absorption by the substrate. One possible reason is the high doping level of the Si substrate underneath the 3C-SiC layer, which disturbs measurements in the infrared spectral range.

In summary, the structural quality of the investigated layers is comparable, thus the reason for the lack of absorption is assumed to be related to the substrate. One big difference between the substrates is how strongly the APDs are pronounced. The other difference is the absorption of the substrate itself.

CHAPTER 5

Summary and outlook

In this work an extensive study of Ge as an n-type dopant in c-GaN and c-Al$_x$Ga$_{1-x}$N up to $x = 0.6$ was presented. Besides optical, electrical, and structural properties of doped layers also the influence of the dopant on the growth rate was investigated. Ge-doped SL structures were fabricated and characterized with the aim to achieve intersubband transitions in the range of the telecommunication wavelength $1.55\,\mu$m.

Concerning c-GaN layers, properties of Ge and Si as n-type dopants were compared in a doping range spanning over several orders of magnitude. The incorporation of Ge into the layers was verified by TOF-SIMS. Calibration of the Ge-related TOF-SIMS signals in c-GaN was done by preparing ion-implanted calibration samples, which enables to quantify the amount of Ge actually incorporated into the layers. The maximum free electron concentrations measured by Hall effect are $3.7 \times 10^{20}\,\text{cm}^{-3}$ and $4.3 \times 10^{20}\,\text{cm}^{-3}$ for Ge- and Si-doping, respectively. With increasing dopant effusion cell temperature the free electron concentration cannot be increased any more, probably due to autocompensation effects. The structural quality of Ge- and Si-doped layers is comparable in the range of the doping limit. In this range, electron mobilities with Si doping are around $10\,\%$ higher than those achieved with Ge doping. For lower doped layers however mobilities of Ge-doped layers are about $20\,\%$ higher than those of Si-doped layers.

To investigate properties of Ge as an n-type dopant in c-Al$_x$Ga$_{1-x}$N, two sample series were prepared. In the first series, a constant Ge flux is employed and the Al mole fraction is varied in the range of $0 \leq x \leq 0.6$. In the second series, x is kept constant at 0.25 and the Ge flux is varied over several orders of magnitude. The incorporation of Ge is found to be almost independent on x, and as a result the donor concentration measured by CV spectroscopy is almost constant over the whole investigated range of Al mole fractions. However, the unintentional incorporation of O, which acts as a donor as well, is enhanced with rising x, causing the donor concentration of n.i.d. layers to linearly rise with increasing x. When varying the Ge effusion cell temperature, the Ge incorporation measured by TOF-SIMS and the donor concentration measured by CV spectroscopy proceed proportionally to the vapor pressure curve of Ge. The maximum achieved donor concentration is $1.4 \times 10^{20}\,\text{cm}^{-3}$, but structural quality of the layers degrades when the doping level exceeds $3 \times 10^{19}\,\text{cm}^{-3}$. Also the emission intensity in PL spectroscopy drops rapidly when doping is increased above this threshold. Furthermore, the PL emission of layers with $x \geq 0.25$ is found to originate from a deep defect level $0.9\,\text{eV}$ below the indirect band gap. The origin of this defect is unclear up to now, but it is not related to the incorporation of Ge, and is not a DX center.

It has been found that growth rates of c-GaN drop at high doping levels. With Ge doping the growth rate is reduced by $40\,\%$, and with Si doping it is reduced by $20\,\%$ at the highest investigated dopant flux. The origin of this effect is most probably the accumulation of Ge or Si at the sample surface during growth. The growth rate reduction is not observed for the growth of c-Al$_x$Ga$_{1-x}$N layers.

Ge-doped GaN/AlN SL structures were grown in order to investigate optical absorption related to intersubband transitions. SLs are of high structural quality and intersubband absorption around $1.55\,\mu$m could be observed. However, the substrate quality and properties seem to have a critical influence on the absorption capabilities of the structures. Despite comparable structural quality of the SL samples, layers grown on some of the different substrates do not exhibit intersubband absorption. It is assumed that the presence of APDs impairs the intersubband absorption, and also some of the substrates themselves exhibit absorption in the relevant spectral range.

To improve the reproducibility of SL structures for intersubband absorption and to improve the strength of absorption, first of all it is of utmost importance to investigate the role of the substrate. When this is done, further experiments on different doping profiles of the structures should be performed, e.g., doping of the c-AlN barriers or δ-doping. Concerning doping of the barriers, so far Ge-doping has only been investigated in detail for c-Al$_x$Ga$_{1-x}$N up to $x = 0.6$, thus further work is also required to investigate Ge as a dopant for higher Al mole fractions up to $x = 1$.

Bibliography

1. I. Ho and G. B. Stringfellow: 'Solid phase immiscibility in GaInN'. *Applied Physics Letters* **69**, 2701 (1996).

2. L. K. Teles, L. G. Ferreira, J. R. Leite, L. M. R. Scolfaro, A. Kharchenko, O. Husberg, D. J. As, D. Schikora, and K. Lischka: 'Strain-induced ordering in In[x]Ga[1-x]N alloys'. *Applied Physics Letters* **82**, 4274 (2003).

3. H. Naoi, M. Kurouchi, D. Muto, T. Araki, T. Miyajima, and Y. Nanishi: 'Growth of high-quality In-rich InGaN alloys by RF–MBE for the fabrication of InN-based quantum well structures'. *Journal of Crystal Growth* **288**, 283 (2006).

4. B. Mirzaei, A. Rostami, and H. Baghban: 'Terahertz dual-wavelength quantum cascade laser based on GaN active region'. *Optics and Laser Technology* **44**, 378 (2012).

5. S. Fujikawa, T. Ishiguro, K. Wang, W. Terashima, H. Fujishiro, and H. Hirayama: 'Evaluation of GaN/AlGaN THz quantum-cascade laser epi-layers grown on AlGaN/Si templates by MOCVD'. *Journal of Crystal Growth* **510**, 47 (2019).

6. F. R. Giorgetta, E. Baumann, F. Guillot, E. Monroy, and D. Hofstetter: 'High frequency (f=2.37 GHz) room temperature operation of 1.55 µm AlN/GaN-based intersubband detector'. *Electronics Letters* **43**, 185 (2007).

7. L. T. Romano, C. G. Van De Walle, B. S. Krusor, R. Lau, J. Ho, T. Schmidt, J. W. Ager III, W. Götz, and R. S. Kern: 'Effect of Si doping on the strain and defect structure of GaN thin films'. *Physica B: Condensed Matter* **273-274**, 50 (1999).

8. S. Fritze, A. Dadgar, H. Witte, M. Bügler, A. Rohrbeck, J. Bläsing, A. Hoffmann, and A. Krost: 'High Si and Ge n-type doping of GaN doping - Limits and impact on stress'. *Applied Physics Letters* **100**, 122104 (2012).

9. Armin Dadgar, Jürgen Bläsing, Annette Diez, and Alois Krost: 'Crack-free, highly conducting GaN layers on Si substrates by Ge doping'. *Applied Physics Express* **4**, 011001 (2011).

10. M. N. Fireman, G. L'Heureux, F. Wu, T. Mates, E. C. Young, and J. S. Speck: 'High germanium doping of GaN films by ammonia molecular beam epitaxy'. *Journal of Crystal Growth* **508**, 19 (2019).

11. R. Blasco, A. Ajay, E. Robin, C. Bougerol, K. Lorentz, L. C. Alves, I. Mouton, L. Amichi, A. Grenier, and E. Monroy: 'Electrical and optical properties of heavily Ge-doped AlGaN'. *Journal of Physics D: Applied Physics* **52**, 125101 (2019).

12. D. Schikora, D. J. As, and K. Lischka: 'The molecular beam epitaxy of cubic III-nitrides'. *Vacuum Science and Technology: Nitrides as seen by the technology.* Ed. by T. Paskova and B. Monemar. Kerala, India, 2002. Chap. 15.

13. D. J. As: 'Growth and Characterization of MBE-Grown Cubic GaN, InGaN and AlGaN'. *III-nitride semiconductor growth.* Ed. by M. O. Manasreh and I. T. Ferguson. New York: Taylor & Francis, 2003. Chap. Chapter 9.

14. D. J. As and K. Lischka: 'Nonpolar cubic III-nitrides : from the basics of growth to device applications'. *Molecular Beam Epitaxy: From research to mass production.* Ed. by M Henini. Elsevier, 2013. Chap. 11, pp. 203–215.

15. F. Shi: 'GaN Nanowires Fabricated by Magnetron Sputtering Deposition'. *Nanowires - Fundamental Research.* Ed. by A. Hashim. InTech, 2011, p. 225.

16. H. Morkoç: *Handbook of Nitride Semiconductors and Devices Vol. 1: Materials Properties, Physics and Growth.* Weinheim: WILEY-VCH, 2008.

17. W. R. L. Lambrecht and B. Segall: 'General remarks and notations on the band structure of pure group III nitrides'. *Properties of group III nitrides.* Ed. by J. H. Edgar. London: INSPEC, 1994. Chap. 4.1, p. 125.

18. L. Vegard: 'Die Konstitution der Mischkristalle und die Raumfüllung der Atome'. *Zeitschrift für Physik* **5**, 17 (1921).

19. A. R. Denton and N. W. Ashcroft: 'Vegards law'. *Physical Review A* **43**, 3161 (1991).

20. P. Schley, R. Goldhahn, C. Napierala, G. Gobsch, J. Schörmann, D. J. As, K. Lischka, M. Feneberg, and K. Thonke: 'Dielectric function of cubic InN from the mid-infrared to the visible spectral range'. *Semiconductor Science and Technology* **23**, 055001 (2008).

21. I. Akasaki and H. Amano: 'Crystal structure, mechanical properties and thermal properties of GaN'. *Properties of group III nitrides.* Ed. by J. H. Edgar. London: INSPEC, 1994. Chap. 1.4.

22. T. Schupp, K. Lischka, and D. J. As: 'MBE growth of atomically smooth non-polar cubic AlN'. *Journal of Crystal Growth* **312**, 1500 (2010).

23. M. Feneberg, M. Röppischer, C. Cobet, N. Esser, J. Schörmann, T. Schupp, D. J. As, F. Hörich, J. Bläsing, A. Krost, and R. Goldhahn: 'Optical properties of cubic GaN from 1 to 20 eV'. *Physical Review B* **85**, 155207 (2012).

24. M. Röppischer, R. Goldhahn, G. Rossbach, P. Schley, C. Cobet, N. Esser, T. Schupp, K. Lischka, and D. J. As: 'Dielectric function of zinc-blende AlN from 1 to 20 eV: Band gap and van Hove singularities'. *Journal of Applied Physics* **106**, 076104 (2009).

25. M. Landmann, E. Rauls, W. G. Schmidt, M. Röppischer, C. Cobet, N. Esser, T. Schupp, D. J. As, M. Feneberg, and R. Goldhahn: 'Transition energies and direct-indirect band gap crossing in zinc-blende AlxGa1-xN'. *Physical Review B* **87**, 195210 (2013).

26. V. Yu. Davydov, A. A. Klochikhin, V. V. Emtsev, D. A. Kurdyukov, S. V. Ivanov, V. A. Vekshin, F. Bechstedt, J. Furthmüller, J. Aderhold, J. Graul, A. V. Mudryi, H. Harma, A. Hashimoto, A. Yamamoto, and E. E. Haller: 'Band gap of hexagonal InN and InGaN alloys'. *Physica Status Solidi B* **234**, 787 (2002).

27. W. W. Lin, Y. K. Kuo, and B. T. Liou: 'Band-Gap Bowing Parameters of the Zincblende Ternary III-Nitrides Derived from Theoretical Simulation'. *Japanese Journal of Applied Physics* **43**, 113 (2004).

28. S. Berrah, A. Boukortt, and H. Abid: 'The composition effect on the bowing parameter in the cubic InGaN, AlGaN and AlInN alloys'. *Semiconductor Physics, Quantum Electronics & Optoelectronics* **11**, 59 (2008).

29. M. A. Caro Bayo: 'Theory of elasticity and electric polarization effects in the group-III nitrides'. PhD Thesis. University College Cork, 2013.

30. S. Li: 'Growth and Characterization of Cubic InGaN and InGaN / GaN Quantum Wells'. Dissertation. Universität Paderborn, 2005.

31. M. Grundmann: *The Physics of Semiconductors*. Second ed. Berlin, Heidelberg: Springer-Verlag, 2010.

32. Y. P. Varshni: 'Temperature dependence of the energy gap in semiconductors'. *Physica* **34**, 149 (1967).

33. G. Ramirez-Flores, H. Navarro-Contreras, A. Lastras-Martinez, R. C. Powell, and J. E. Greene: 'Temperature-dependent optical band gap of the metastable zinc-blende structure β-GaN'. *Physical Review B* **50**, 8433 (1994).

34. E. T. Yu, X. Z. Dang, P. M. Asbeck, S. S. Lau, and G. J. Sullivan: 'Spontaneous and piezoelectric polarization effects in III-V nitride heterostructures'. *J. Vac. Sci. Technol. B* **17**, 1742 (1999).

35. T. Wang: 'Topical Review: Development of overgrown semi-polar GaN for high efficiency green/yellow emission'. *Semiconductor Science and Technology* **31**, 093003 (2016).

36. M. T. Durniak, A. S. Bross, D. Elsaesser, A. Chaudhuri, M. L. Smith, A. A. Allerman, S. C. Lee, S. R. J. Brueck, and C. Wetzel: 'Green Emitting Cubic GaInN/GaN Quantum Well Stripes on Micropatterned Si(001) and Their Strain Analysis'. *Adv. Electron. Mater.* **2**, 1500327 (2016).

37. S. Li, J. Schörmann, D. J. As, and K. Lischka: 'Room temperature green light emission from nonpolar cubic InGaN/GaN multi-quantum-wells'. *Appl. Phys. Lett* **90**, 071903 (2007).

38. S.-H. Park and S.-L. Chuang: 'Comparison of zinc-blende and wurtzite GaN semiconductors with spontaneous polarization and piezoelectric field effects'. *Journal of Applied Physics* **87**, 353 (2000).

39.   D. Jena, S. P. Alpay, and J. V. Mantese: 'Functionally Graded Polar Heterostructures'. *Polarization Effects in Semiconductors*. Ed. by C. Wood and D. Jena. Springer-Verlag, 2008.

40.   U. K. Mishra and J. Singh: *Semiconductor Device Physics and Design*. Dordrecht, The Netherlands: Springer, 2008.

41.   F. Bechstedt, U. Grossner, and J. Furthmüller: 'Dynamics and polarization of group-III nitride lattices: A first-principles study'. *Physical Review B* **62**, 8003 (2000).

42.   T. Schupp, T. Meisch, B. Neuschl, M. Feneberg, K. Thonke, K. Lischka, and D. J. As: 'Molecular beam epitaxy based growth of cubic GaN quantum dots'. *Physica Status Solidi (C)* **8**, 1495 (2011).

43.   J. Simon, N. T. Pelekanos, C. Adelmann, E. Martinez-Guerrero, R. André, B. Daudin, L. S. Dang, and H. Mariette: 'Direct comparison of recombination dynamics in cubic and hexagonal GaN/AlN quantum dots'. *Physical Review B* **68**, 035312 (2003).

44.   E. F. Schubert: *Doping in III-V semiconductors*. Cambridge: Cambridge Univ. Press, 1993.

45.   L. Nevou, F. H. Julien, Colombellim R., F. Guillot, and E. Monroy: 'Room-temperature intersubband emission of GaN/AlN quantum wells at 2.3 µm'. *Electronics Letters* **42**, 1308 (2006).

46.   E. Burstein: 'Anomalous Optical Absorption Limit in InSb'. *Physical Review* **93**, 632 (1954).

47.   T. S. Moss: 'The Interpretation of the Properties of Indium Antimonide'. *Proceedings of the Physical Society B* **67**, 775 (1954).

48.   K.-F. Berggren and B. E. Sernelius: 'Band-gap narrowing in heavily doped many-valley semiconductors'. *Physical Review B* **24**, 1971 (1981).

49.   Martin Feneberg, Sarah Osterburg, Karsten Lange, Christian Lidig, Bernd Garke, Rüdiger Goldhahn, Eberhard Richter, Carsten Netzel, Maciej D. Neumann, Norbert Esser, Stephanie Fritze, Hartmut Witte, Jürgen Bläsing, Armin Dadgar, and Alois Krost: 'Band gap renormalization and Burstein-Moss effect in silicon- and germanium-doped wurtzite GaN up to 10ˆ20 cmˆ-3'. *Physical Review B* **90**, 075203 (2014).

50.   C. G. Van De Walle and J. Neugebauer: 'First-principles calculations for defects and impurities: Applications to III-nitrides'. *Journal of Applied Physics* **95**, 3851 (2004).

51.   M. Deppe, J. W. Gerlach, D. Reuter, and D. J. As: 'Incorporation of germanium for n-type doping of cubic GaN'. *physica status solidi (b)* **254**, 1600700 (2017).

52.   M. Deppe, J. W. Gerlach, S. Shvarkov, D. Rogalla, H.-W. Becker, D. Reuter, and D. J. As: 'Germanium doping of cubic GaN grown by molecular beam epitaxy'. *Journal of Applied Physics* **125**, 095703 (2019).

53. D. J. As, M. Deppe, J. W. Gerlach, and D. Reuter: 'Optical Properties of Germanium Doped Cubic GaN'. *MRS Advances* **2**, 283 (2017).

54. D. J. As: 'n- and p-Type Doping of Cubic GaN'. *Defect and Diffusion Forum* **206-207**, 87 (2002).

55. D. J. As, D. Schikora, and K. Lischka: 'Molecular beam epitaxy of cubic III-nitrides on GaAs substrates'. *Physica Status Solidi C* **0**, 1607 (2003).

56. H. Wang and a.-B. Chen: 'Calculation of shallow donor levels in GaN'. *Journal of Applied Physics* **87**, 7859 (2000).

57. D. S. Green, U. K. Mishra, and J. S. Speck: 'Carbon doping of GaN with in radio-frequency plasma-assisted molecular beam epitaxy'. *Journal of Applied Physics* **95**, 8456 (2004).

58. D. J. As, U. Köhler, M. Lübbers, J. Mimkes, and K. Lischka: 'p-Type Doping of Cubic GaN by Carbon'. *Physica Status Solidi (A)* **188**, 699 (2001).

59. P. R. Hageman, W. J. Schaff, J. Janinski, and Z. Liliental-Weber: 'n-type doping of wurtzite GaN with germanium grown with plasma-assisted molecular beam epitaxy'. *Journal of Crystal Growth* **267**, 123 (2004).

60. A. Ajay, J. Schörmann, M. Jiménez-Rodriguez, C. B. Lim, F. Walther, M. Rohnke, I. Mouton, L. Amichi, C. Bougerol, M. I. Den Hertog, M. Eickhoff, and E. Monroy: 'Ge doping of GaN beyond the Mott transition'. *Journal of Physics D: Applied Physics* **49**, 445301 (2016).

61. C. G. Van de Walle: 'DX-center formation in wurtzite and zinc-blende AlxGa1-xN'. *Physical Review B* **57**, R2033 (1998).

62. M. McCluskey, N. Johnson, C. Van de Walle, D. Bour, M. Kneissl, and W. Walukiewicz: 'Metastability of Oxygen Donors in AlGaN'. *Physical Review Letters* **80**, 4008 (1998).

63. L. Gordon, J. L. Lyons, A. Janotti, and C. G. Van de Walle: 'Hybrid functional calculations of DX centers in AlN and GaN'. *Physical Review B* **89**, 085204 (2014).

64. H. Kim, F. J. Fälth, and T. G. Andersson: 'Unintentional incorporation of B, As, and O impurities in GaN grown by molecular beam epitaxy'. *Journal of electronic materials* **30**, 1343 (2001).

65. C. H. Park and D. J. Chadi: 'Stability of deep donor and acceptor centers in GaN, AlN, and BN'. *Physical Review B* **55**, 55 (1997).

66. P. Bogusławski and J. Bernholc: 'Doping properties of C, Si, and Ge impurities in GaN and AlN'. *Physical Review B* **56**, 9496 (1997).

67. C. Skierbiszewski, T. Suski, M. Leszczynski, M. Shin, M. Skowronski, M. D. Bremser, and R. F. Davis: 'Evidence for localized Si-donor state and its metastable properties in AlGaN'. *Applied Physics Letters* **74**, 3833 (1999).

68. X. T. TRINH, D. NILSSON, I. G. IVANOV, E. JANZÉN, A. KAKANAKOVA-GEORGIEVA, and N. T. SON: 'Stable and metastable Si negative-U centers in AlGaN and AlN'. *Applied Physics Letters* **105**, 162106 (2014).

69. I. C. MANNING, X. WENG, J. D. ACORD, M. A. FANTON, D. W. SNYDER, and J. M. REDWING: 'Tensile stress generation and dislocation reduction in Si-doped AlxGa1-xN films'. *Journal of Applied Physics* **106**, 023506 (2009).

70. F. BRUNNER, A. MOGILATENKO, V. KUELLER, A. KNAUER, and M. WEYERS: 'Stress evolution during AlxGa1-xN/AlN growth on sapphire'. *Journal of Crystal Growth* **376**, 54 (2013).

71. X. ZHANG, P. KUNG, A. SAXLER, D. WALKER, T. C. WANG, and M. RAZEGHI: 'Growth of AlxGa1-xN:Ge on sapphire and silicon substrates'. *Applied Physics Letters* **67**, 1745 (1995).

72. T. KOIZUMI, H. OKUMURA, K. BALAKRISHNAN, H. HARIMA, T. INOUE, Y. ISHIDA, T. NAGATOMO, S. NAKASHIMA, and S. YOSHIDA: 'Growth and characterization of cubic AlGaN and AlN epilayers by RF-plasma assisted MBE'. *Journal of Crystal Growth* **201/202**, 341 (1999).

73. S. FANGET, C. BRU-CHEVALLIER, G. GUILLOT, E. MARTINEZ-GUERRERO, D. JALABERT, B. DAUDIN, H. MARIETTE, L. S. DANG, G. FERRO, and Y. MONTEIL: 'Optical properties of cubic AlGaN'. *MRS Proceedings* **693**, I6.44 (2001).

74. R. E. L. POWELL, S. V. NOVIKOV, F. LUCKERT, P. R. EDWARDS, A. V. AKIMOV, C. T. FOXON, R. W. MARTIN, and A. J. KENT: 'Carrier localization and related photoluminescence in cubic AlGaN epilayers'. *Journal of Applied Physics* **110**, 063517 (2011).

75. L. C. de CARVALHO, A. SCHLEIFE, and F. BECHSTEDT: 'Influence of exchange and correlation on structural and electronic properties of AlN, GaN, and InN polytypes'. *Physical Review B* **84**, 195105 (2011).

76. M. A. HERMAN and H. SITTER: *Molecular Beam Epitaxy.* Berlin: Springer-Verlag, 1989.

77. K. XU, J.-F. WANG, and G.-Q. REN: 'Progress in bulk GaN growth'. *Chinese Physics B* **24**, 066105 (2015).

78. N. M. NASSER, Z. YE, J. LI, and Y. XU: 'GaN Heteroepitaxial Growth Techniques'. *Journal of Microwaves and Optoelectronics* **2**, 22 (2001).

79. U. K. MISHRA, L. SHEN, T. E. KAZIOR, and Y.-F. WU: 'GaN-based RF power devices and amplifiers'. *Proceedings of the IEEE* **96**, 287 (2008).

80. M. N. FIREMAN and J. S. SPECK: 'Ammonia Molecular Beam Epitaxy of III-Nitrides'. *Molecular beam epitaxy: materials and applications for electronics and optoelectronics.* Ed. by H. ASAHI and Y. HORIKOSHI. John Wiley & Sons, 2019. Chap. 5.

81. A. V. BLANT, O. H. HUGHES, T. S. CHENG, S. V. NOVIKOV, and C. T. FOXON: 'Nitrogen species from radio frequency plasma sources used for molecular beam epitaxy growth of GaN'. *Plasma Sources Science and Technology* **9**, 12 (2000).

82. C. W. SCHNEIDER and T. LIPPERT: 'Laser Ablation and Thin Film Deposition'. *Laser Processing of Materials.* Ed. by P. SCHAAF. Berlin, Heidelberg: Springer-Verlag, 2010. Chap. 5.

83. H. BRUNE: 'Growth Modes'. *Encyclopedia of Materials: Science and Technology*, 3683 (2001).

84. M. BÜRGER, M. RUTH, S. DECLAIR, J. FÖRSTNER, C. MEIER, and D. J. AS: 'Whispering gallery modes in zinc-blende AlN microdisks containing non-polar GaN quantum dots'. *Applied Physics Letters* **102**, 081105 (2013).

85. J. SCHÖRMANN, S. POTTHAST, D. J. AS, and K. LISCHKA: 'In situ growth regime characterization of cubic GaN using reflection high energy electron diffraction'. *Applied Physics Letters* **90**, 041918 (2007).

86. D. SCHIKORA, M. HANKELN, D. J. AS, K. LISCHKA, T. LITZ, A. WAAG, T. BUHROW, and F. HENNEBERGER: 'Epitaxial growth and optical transitions of cubic GaN films.' *Physical Review B* **54**, R8381 (1996).

87. Y. ISHIDA, T. TAKAHASHI, H. OKUMURA, and S. YOSHIDA: 'Investigation of antiphase domain annihilation mechanism in 3C-SiC on Si substrates'. *Journal of Applied Physics* **94**, 4676 (2003).

88. R. M. KEMPER, T. SCHUPP, M. HÄBERLEN, T. NIENDORF, H.-J. MAIER, A. DEMPEWOLF, F. BERTRAM, J. CHRISTEN, R. KIRSTE, A. HOFFMANN, J. LINDNER, and D. J. AS: 'Anti-phase domains in cubic GaN'. *Journal of Applied Physics* **110**, 123512 (2011).

89. S. HASEGAWA: 'Reflection High-Energy Electron Diffraction'. *Characterization of Materials.* Ed. by ELTON N. KAUFMANN. John Wiley & Sons, Inc., 2012, pp. 1925–1938.

90. B. A. JOYCE, P. J. DOBSON, J. H. NEAVE, K. WOODBRIDGE, J. ZHANG, P. K. LARSEN, and B. BÔLGER: 'RHEED studies of heterojunction and quantum well formation during MBE growth - from multiple scattering to band offsets'. *Surface Science* **168**, 423 (1986).

91. A. Y. SHIK: *Quantum wells: physics and electronics of two-dimensional systems.* Singapore: World Scientific, 1997.

92. S. FLÜGGE: *Practical Quantum Mechanics.* Berlin, Heidelberg: Springer, 1971.

93. D. A. B. MILLER: 'Optical Physics of Quantum Wells'. *Quantum Dynamics of Simple Systems.* Ed. by G. L. OPPO, S. M. BARNETT, E. RIIS, and M. WILKINSON. London: Institute of Physics Publishing, 1997, pp. 239ff.

94. S. L. CHUANG: *Physics of photonic devices.* Second ed. Hoboken, New Jersey: John Wiley & Sons Inc., 2009.

95. T. WECKER: 'Inter- and Intraband Carrier Dynamics in Cubic GaN/AlxGa1-xN Heterostructures Grown by MBE'. Dissertation. Universität Paderborn, 2017.

96. E. F. SCHUBERT: 'Delta doping of III-V compound semiconductors: Fundamentals and device applications'. *J. Vac. Sci. Technol. A* **8**, 2980 (1990).

97. V. AKIMOV, V. TULUPENKO, C. A. DUQUE, A. L. MORALES, R. DEMEDIUK, A. TIUTIUNNYK, D. LAROZE, V. KOVALOV, and D. SUSHCHENKO: 'Background impurities and a delta-doped QW. Part I: Center doping'. *Semiconductor Science and Technology* **34**, 125009 (2019).

98. S BIRNER, T ZIBOLD, T ANDLAUER, T KUBIS, M SABATHIL, A TRELLAKIS, and P VOGL: 'nextnano: General Purpose 3-D Simulations'. *IEEE Transactions on Electron Devices* **54**, 2137 (2007).

99. C. MIETZE: 'Cubic AlN/GaN multi-quantum-wells for unipolar device applications'. Dissertation. Paderborn University, 2013.

100. B. SCHÖTTKER: 'Molecular Beam Epitaxy and characterization of doped and undoped cubic GaN layers'. Dissertation. Universität-GH Paderborn, 1999.

101. P. KIDD: *XRD of gallium nitride and related compounds: strain, composition and layer thickness.*

102. U. KÖHLER: 'A Study of Growth and Doping of cubic Group III Nitride Structures'. Dissertation. Universität Paderborn, 2003.

103. P. GAY, P. B. HIRSCH, and A. KELLY: 'The estimation of dislocation densities in metals from X-ray data'. *Acta Metallurgica* **1**, 315 (1953).

104. E. P. DEGARMO, J. BLACK, and R. A. KOHSER: *Materials and Processes in Manufacturing.* 9th ed. Wiley, 2003.

105. H. DÜSTERHÖFT, M. RIEDEL, and B. K. DÜSTERHÖFT: *Einführung in die Sekundärionenmassenspektrometrie -SIMS-*. Stuttgart: Teubner, 1999.

106. Y.-P. KIM, H. K. SHON, S. K. SHIN, and T. G. LEE: 'Probing nanoparticles and nanoparticle-conjugated biomolecules using time-of-flight secondary ion mass spectrometry'. *Mass Spectrometry Reviews* **34**, 237 (2015).

107. D. K. SCHRODER: *Semiconductor Material and Device Characterization.* 3rd ed. Hoboken, New Jersey: John Wiley & Sons, Inc., 2006.

108. L. J. van der PAUW: 'A method of measuring specific resistivity and hall effect of discs of arbitrary shape'. *Philips Research Reports* **13**, 1 (1958).

109. T. HENKSMEIER: 'Electrical and optical investigation of III-V heterostructures'. Master's Thesis. Paderborn University, 2018.

110. N. ARORA: *MOSFET Modeling For VLSI Simulation.* Singapore: World Scientific, 2007.

111. P. J. DEAN: 'Photoluminescence as a diagnostic of semiconductors'. *Progress in Crystal Growth and Characterization* **5**, 89 (1982).

112. L. Pavesi and M. Guzzi: 'Photoluminescence of AlxGa1-xAs alloys'. *Journal of Applied Physics* **75**, 4779 (1994).

113. J. I. Pankove: *Optical Processes in Semiconductors*. New York: Dover, 1975.

114. J. Saatz: 'Intersubband Übergänge in kubischen Gruppe-III-Nitrid-Heterostrukturen'. Master's Thesis. Paderborn University, 2017.

115. J. E. Ayers: 'New model for the thickness and mismatch dependencies of threading dislocation densities in mismatched heteroepitaxial layers'. *Journal of Applied Physics* **78**, 3724 (1995).

116. A. T. Blumenau, J. Elsner, R. Jones, M. I. Heggie, S. Öberg, T. Frauenheim, and P. R. Briddon: 'Dislocations in hexagonal and cubic GaN'. *Journal of Physics: Condensed Matter* **12**, 10223 (2000).

117. M. Rüsing, T. Wecker, G. Berth, D. J. As, and A. Zrenner: 'Joint Raman spectroscopy and HRXRD investigation of cubic gallium nitride layers grown on 3C-SiC'. *Physica Status Solidi (B)* **253**, 778 (2016).

118. J. Ziegler, J. Biersack, and M. Ziegler: *SRIM, the Stopping and Range of Ions in Matter*. 2013.

119. H. Kuchling: *Taschenbuch der Physik*. 19th ed. Carl Hanser Verlag, 2007.

120. M. Deppe: 'Ge-Dotierung von kubischen Gruppe III-Nitriden'. Master's Thesis. University of Paderborn, 2015.

121. E. Baron, R. Goldhahn, M. Deppe, D. J. As, and M. Feneberg: 'Influence of the free-electron concentration on the optical properties of zincblende GaN up to 1x10^20 cm-3'. *Physical Review Materials* **3**, 104603 (2019).

122. A. F. Wright and U. Grossner: 'The effect of doping and growth stoichiometry on the core structure of a threading edge dislocation in GaN'. *Applied Physics Letters* **73**, 2751 (1998).

123. S. Dhar and S. Ghosh: 'Low field electron mobility in GaN'. *Journal of Applied Physics* **86**, 2668 (1999).

124. D. J. As, F. Schmilgus, C. Wang, B. Schöttker, D. Schikora, and K. Lischka: 'The near band edge photoluminescence of cubic GaN epilayers'. *Applied Physics Letters* **70**, 1311 (1997).

125. J. Menniger, U. Jahn, O. Brandt, H. Yang, and K. Ploog: 'Identification of optical transitions in cubic and hexagonal GaN by spatially resolved cathodoluminescence'. *Physical Review B* **53**, 1881 (1996).

126. M. Leroux, N. Grandjean, B. Beaumont, G. Nataf, F. Semond, J. Massies, and P. Gibart: 'Temperature quenching of photoluminescence intensities in undoped and doped GaN'. *Journal of Applied Physics* **86**, 3721 (1999).

127. J. R. Haynes: 'Experimental Proof of the Existence of a New Electronic Complex in Silicon'. *Phys. Rev. Lett.* **4**, 361 (1960).

128. R. E. Halsted and M. Aven: 'Photoluminescence of Defect-Exciton Complexes in II-VI Compounds'. *Phys. Rev. Lett.* **14**, 64 (1965).

129. J. A. Freitas, W. J. Moore, B. V. Shanabrook, G. C. B. Braga, S. K. Lee, S. S. Park, and J. Y. Han: 'Donor-related recombination processes in hydride-vapor-phase epitaxial GaN'. *Physical Review B* **66**, 233311 (2002).

130. J. G. Kim, A. C. Frenkel, H. Liu, and R. M. Park: 'Growth by molecular beam epitaxy and electrical characterization of Si-doped zinc blende GaN films deposited on β-SiC coated (001) Si substrates'. *Applied Physics Letters* **65**, 91 (1994).

131. M. Deppe, T. Henksmeier, J. W. Gerlach, D. Reuter, and D. J. As: 'Molecular Beam Epitaxy Growth and Characterization of Germanium-Doped Cubic AlxGa1-xN'. *physica status solidi (b)* **257**, 1900532 (2020).

132. F. Tacken: 'Ge-Dotierung von kubischem AlGaN'. Master's Thesis. University of Paderborn, 2017.

133. G. Popovici, W. Kim, A. Botchkarev, H. Tang, H. Morkoç, and J. Solomon: 'Impurity contamination of GaN epitaxial films from the sapphire, SiC and ZnO substrates'. *Applied Physics Letters* **71**, 3385 (1997).

134. 'Germanium (Ge), heats of fusion and sublimation, enthalpy and entropy, vapor pressure'. *Group IV Elements, IV-IV and III-V Compounds. Part b - Electronic, Transport, Optical and Other Properties.* Ed. by O. Madelung, U. Rössler, and M. Schulz. Berlin/Heidelberg: Springer-Verlag, 2002, pp. 1–4.

135. Bruker: *Periodic Table of Elements and X-ray Energies.* (www.bruker.com/hhxrf).

136. M. Wieneke, H. Witte, K. Lange, M. Feneberg, A. Dadgar, J. Bläsing, R. Goldhahn, and A. Krost: 'Ge as a surfactant in metal-organic vapor phase epitaxy growth of a-plane GaN exceeding carrier concentrations of 1020cm-3'. *Applied Physics Letters* **103**, 012103 (2013).

137. T. Markurt, L. Lymperakis, J. Neugebauer, P. Drechsel, P. Stauss, T. Schulz, T. Remmele, V. Grillo, E. Rotunno, and M. Albrecht: 'Blocking growth by an electrically active subsurface layer: The effect of si as an antisurfactant in the growth of GaN'. *Physical Review Letters* **110**, 036103 (2013).

138. S. Li, C. Mo, L. Wang, C. Xiong, X. Peng, F. Jiang, Z. Deng, and D. Gong: 'The influence of Si-doping to the growth rate and yellow luminescence of GaN grown by MOCVD'. *Journal of Luminescence* **93**, 321 (2001).

139. J. A. Dean: *Lange's Handbook of Chemistry.* 15th ed. New York: McGraw-Hill, 1999.

140. D. A. Johnson: *Some thermodynamic aspects of inorganic chemistry.* Cambridge: Cambridge Univ. Press, 1976.

141. S. Porowski and I. Grzegory: 'Phase diagram of GaN'. *Properties of group III nitrides.* Ed. by J. H. Edgar. London: INSPEC, 1994.

142. F. P. Pruchnik: *Organometallic Chemistry of the Transition Elements.* New York: Springer, 1990.

143. C. Berger, A. Lesnik, T. Zettler, G. Schmidt, P. Veit, A. Dadgar, J. Bläsing, J. Christen, and A. Strittmatter: 'Metalorganic chemical vapor phase epitaxy of narrow-band distributed Bragg reflectors realized by GaN:Ge modulation doping'. *Journal of Crystal Growth* **440**, 6 (2016).

144. M. Littmann: 'Epitaxie von c-GaN auf vorstrukturierten 3C-SiC Substraten'. Master's Thesis. Paderborn University, 2019.

145. M. Littmann: 'Vergleich von kubischen Galliumnitrid-Schichten auf Siliciumcarbid-Substraten von verschiedenen Herstellern'. Bachelor's Thesis. Paderborn University, 2017.

146. D. R. Lide: *CRC Handbook of Chemistry and Physics*. 84th Ed. Boca Raton, FL: CRC Press, 2003.

147. M. T. Hirsch, J. A. Wolk, W. Walukiewicz, and E. E. Haller: 'Persistent photoconductivity in n- type GaN Persistent photoconductivity in n -type GaN'. *Applied Physics Letters* **71**, 1098 (1997).

148. J. Z. Li, J. Y. Lin, H. X. Jiang, M. Asif Khan, and Q. Chen: 'Persistent photoconductivity in a two-dimensional electron gas system formed by an AlGaN/GaN heterostructure'. *Journal of Applied Physics* **82**, 1227 (1997).

149. R. Zeisel, M. Bayerl, S. Goennenwein, R. Dimitrov, O. Ambacher, M. Brandt, and M. Stutzmann: 'DX-Behavior of Si in AlN'. *Physical Review B* **61**, R16283 (2000).

150. P. D. Desai: 'Thermodynamic Properties of Iron and Silicon'. *J. Phys. Chem. Ref. Data* **15**, 967 (1986).

List of Figures

List of Tables

A Appendix A

A.1 Calibration of substrate temperature

Exact knowledge of the substrate temperature is essential for precise control and reproducibility of MBE growth. The substrate temperature is monitored by means of a thermocouple, which is located near the substrate heater. The temperature measured in this way, however, is not the real temperature of the sample surface. To determine the offset between measured and real temperature, a calibration is performed. Several elements, whose melting points are well known, are evaporated onto a 3C-SiC substrate at temperatures below the melting point. The list of elements used is given in Table A.1. When the substrate is then heated slowly, the RHEED pattern is monitored. It changes significantly, as the respective metal melts. In Figure A.1 this is shown on the example of Al. Figure (a) displays the RHEED pattern of the 3C-SiC substrate at $500\,^{\circ}$C. It is line-shaped, indicating a smooth surface with APDs. Al is then evaporated for $10\,$s using a flux of around $3 \times 10^{14}\,\mathrm{cm^{-2}\,s^{-1}}$. The RHEED pattern becomes spot-shaped, which corresponds to a surface featuring islands. The substrate temperature is ramped up by $2\,^{\circ}\mathrm{C\,min^{-1}}$ and the RHEED intensity of one of the spots is monitored continuously. A distinct change of the pattern occurs when the melting point is reached, and the pattern is line-shaped again after the Al is melted (Figure (c)). In Figure A.2(a) the measured RHEED intensity is plotted versus the substrate temperature measured by the thermocouple. The center of the intensity transition is assumed to be the melting point of Al. By fitting a sigmoidal function (red curve) the center value is determined to be $678\,^{\circ}$C. The same procedure is performed using In and Ge. The elements are actually evaporated with ascending melting point, so that the previously evaporated element has re-evaporated from the substrate when the next element is evaporated onto the substrate. In Figure A.2(b) the measured melting points are plotted versus the actual melting points of the elements and a (arbitrarily chosen) function is fitted to the data to obtain a calibration curve for the substrate temperature.

Table A.1: Actual and measured melting points of elements used for calibration of the substrate temperature. Data for melting points from [146].

Element	Melting point (°C)	Measured melting point (°C)
In	157	138
Al	660	678
Ge	938	932
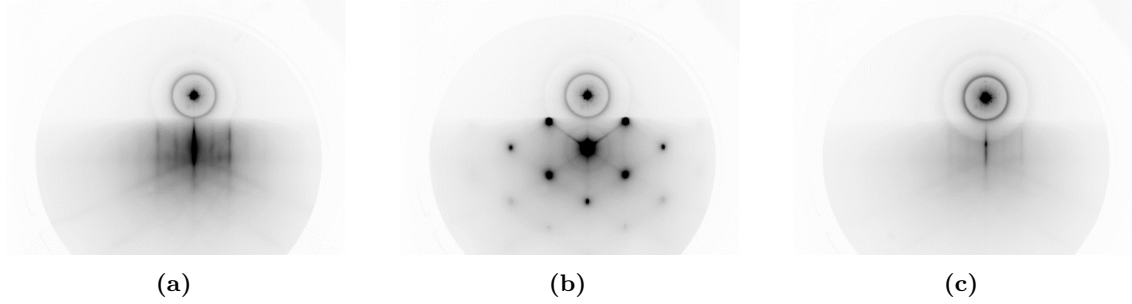
Figure A.1: RHEED pattern of 3C-SiC at 500 °C (a) before and (b) after evaporation of Al. (c) Pattern after melting of Al at 678 °C.
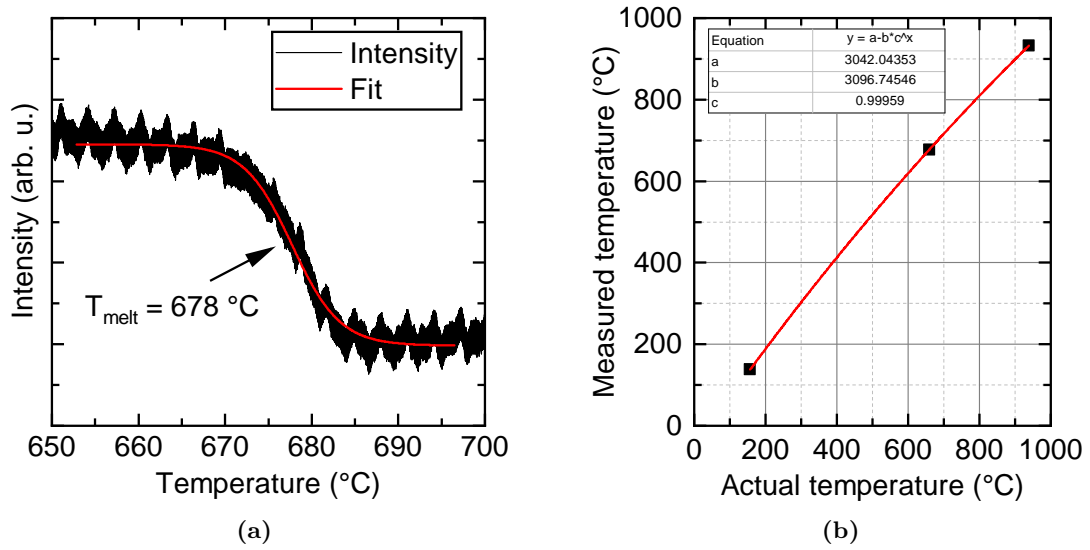
Figure A.2: (a) RHEED intensity of a island-type reflection of Al during substrate heat-up. A sigmoidal function is fitted to obtain the melting point. (b) Substrate temperature calibration curve obtained from three melting point measurements.

A.2 Deep defect level in c-Al$_x$Ga$_{1-x}$N – persistent photoconductivity measurements

In section 4.4.4 it was carried out that the PL emission of c-Al$_x$Ga$_{1-x}$N layers with Al mole fractions above $x = 0.25$ is related to a deep defect level situated 0.9 eV below the indirect band gap of c-Al$_x$Ga$_{1-x}$N. A possible explanation is, that a DX center is formed by oxygen. In this section, first DX centers are explained briefly, and then measurements to verify if a DX center is present in this case are presented.

When a DX center is present, the lattice in the vicinity of a donor relaxes, as soon as an electron is captured [31, p. 225]. This can be explained using a configuration coordinate diagram as shown in Figure A.3. The left parabola at the configuration coordinate q_0 is related to the conduction band and represents the case that the defect is not filled with an electron and the lattice is undistorted. The parabola at q_t represents the case that the defect filled with an electron and the lattice is relaxed. The lattice relaxation causes a
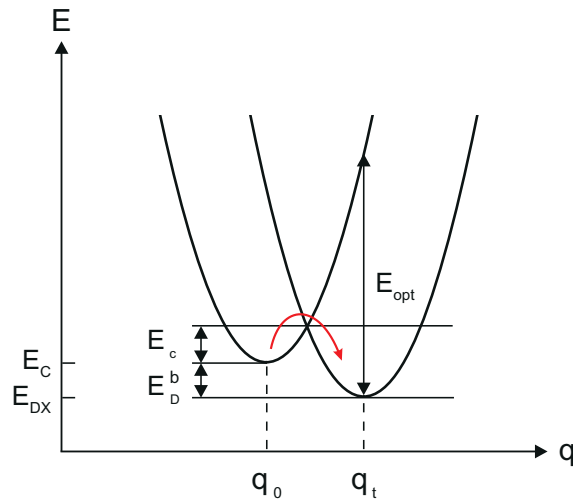
Figure A.3: Configuration coordinate diagram of a DX-center. E_C is the conduction band energy and E_{DX} the energy of the DX center. After [31, p. 225].

reduction of the total energy, because it is energetically more favorable. When an electron arrives at an unfilled DX center, it is situated at the minimum of the left parabola. When the electron energy is higher than E_c it will overcome the barrier towards the DX state (red arrow). Usually thermal energy at room temperature is sufficiently high to activate the capturing process. Although the energy difference between DX state and conduction band is only the donor binding energy E_D^b, due to the reduced lattice energy the electron cannot be excited back to the conduction band when this energy is provided. Only by optical excitation (E_{opt}) the captured electron can be transferred back to the conduction band. If temperatures are sufficiently low, electrons can be excited from the DX centers to the conduction band by illumination, but thermal energy is not high enough to activate the capturing process, so that electrons will not be bound to the DX centers again. The electrons remain in the conduction band even if the illumination is stopped. This effect is called persistent photoconductivity (PPC), because by illumination the conductivity is strongly enhanced, and it will not drop again unless the temperature is raised.

To check for persistent photoconductivity (PPC) in c-Al$_x$Ga$_{1-x}$N, the sheet resistance of n.i.d. c-GaN (green dots) and c-Al$_{0.37}$Ga$_{0.63}$N (black squares) is measured at 7.2 K with and without illumination, see Figure A.4. The sheet resistance of the c-GaN layer is $1.1 \times 10^6 \, \Omega$ and that of the c-Al$_{0.37}$Ga$_{0.63}$N layer is $9.6 \times 10^5 \, \Omega$ after cooling down and before illumination. Then a LED emitting at 950 nm (1.3 eV) is mounted in front of the sample and operated at an optical power of 7 mW. The resistance drops to approximately $7 \times 10^5 \, \Omega$ in case of both samples. After turning off the illumination, the resistivities of the c-GaN and c-Al$_{0.37}$Ga$_{0.63}$N layers rise to 90 % and 95 % of their original values, respectively. With further increasing optical power, the resistivities go down to smaller values during illumination, but the resistivities in the following dark phases do not drop further considerably. After the last illumination period at an optical power of 108 mW
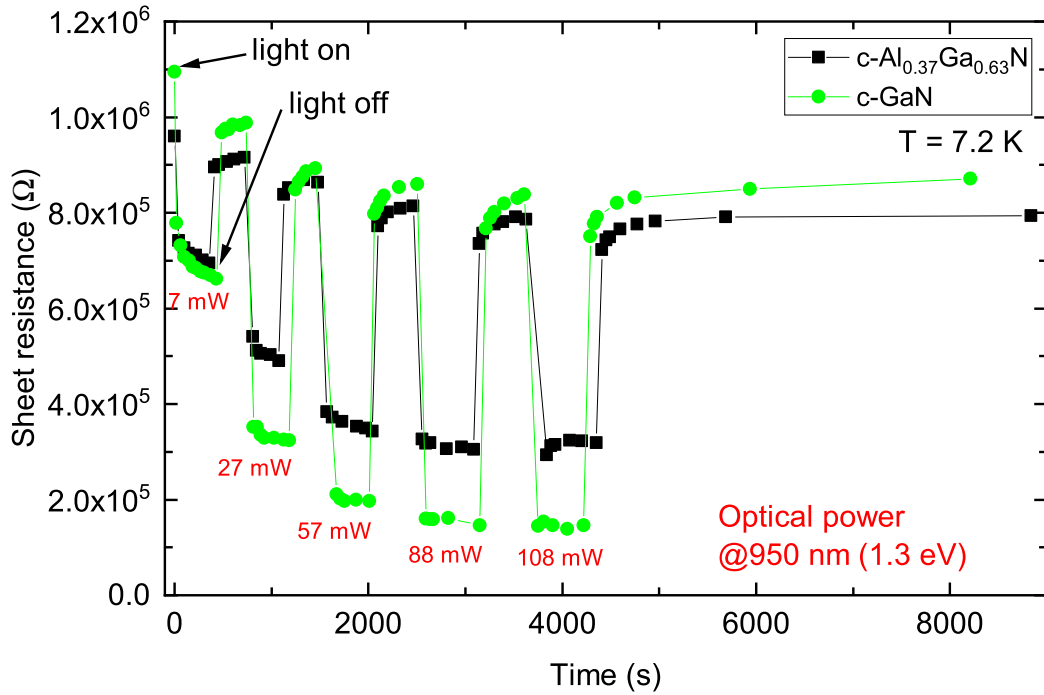
Figure A.4: The sheet resistance of n.i.d. c-GaN (sample 2701) and c-Al$_{0.37}$Ga$_{0.63}$N (sample 2709) measured at 7.2 K in van der Pauw geometry. The layers were illuminated at 950 nm with successively increasing optical power, with a dark interval between two illumination periods.

the samples are kept in the dark at low temperature for over an hour and the resistivity is measured again. The resistivity of c-GaN is at 80 % of its original value before the measurements, and that of c-Al$_{0.37}$Ga$_{0.63}$N at 83 %. There are two findings gained from these measurements. The first is, that both c-GaN and c-Al$_{0.37}$Ga$_{0.63}$N feature PPC. In the literature this is already reported for wurtzite GaN [147] and Al$_{0.1}$Ga$_{0.9}$N [148]. The existence of PPC alone is no safe indication for the presence of a DX center, and other methods like electron paramagnetic resonance (EPR) need to be performed to identify the type of defect [149]. Second, if O had formed a DX center, one would expect a more pronounced PPC effect compared to the c-GaN reference sample. Since this is not the case, it cannot be confirmed that O forms a DX center in c-Al$_x$Ga$_{1-x}$N.

B Appendix B - supporting figures
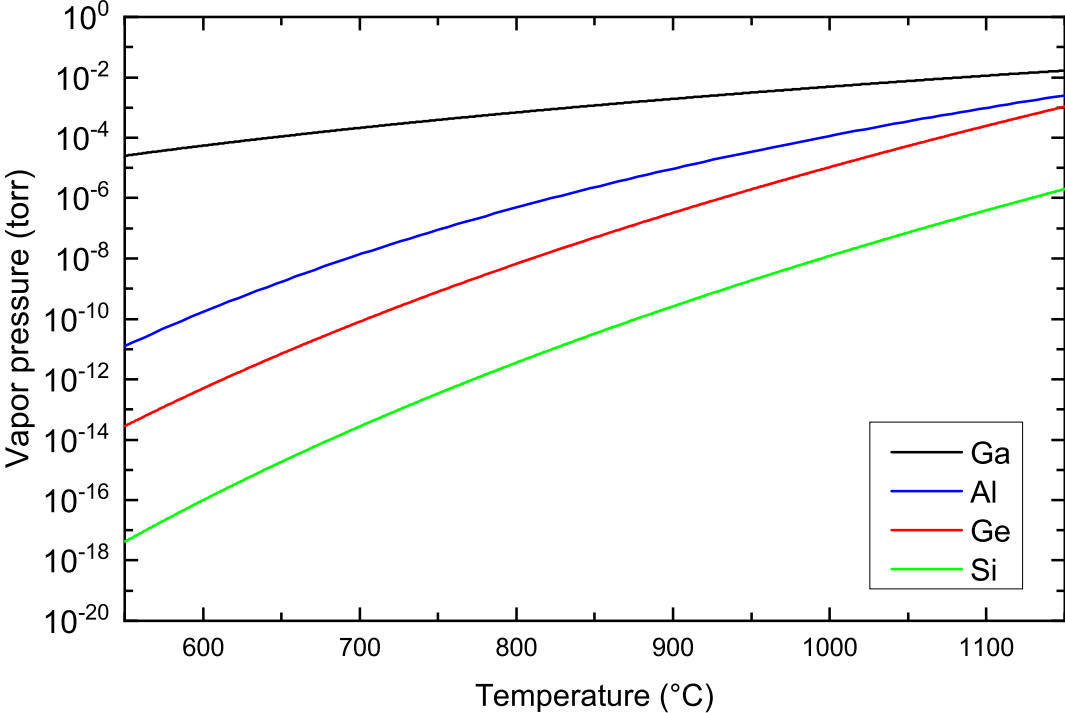
Figure B.1: Vapor pressure curves of Ga [146], Al [146], Ge [134], and Si [150].
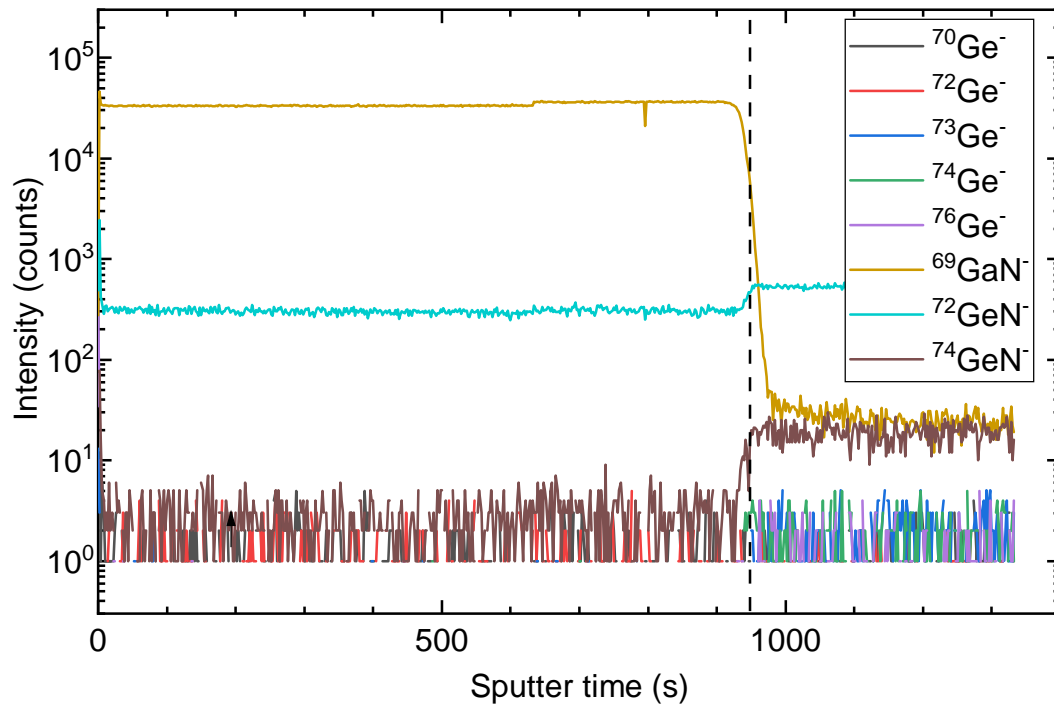
Figure B.2: TOF-SIMS depth profile of a n.i.d. 600 nm thick c-GaN layer (sample number GND2518) with focus on the Ge isotopes. Signals of all naturally occuring Ge isotopes are at noise level, as well as the ^{74}GeN^{-} signal. The ^{72}GeN^{-} signal however runs at rather high intensity, meaning it is overlapped by a contribution stemming from GaN.
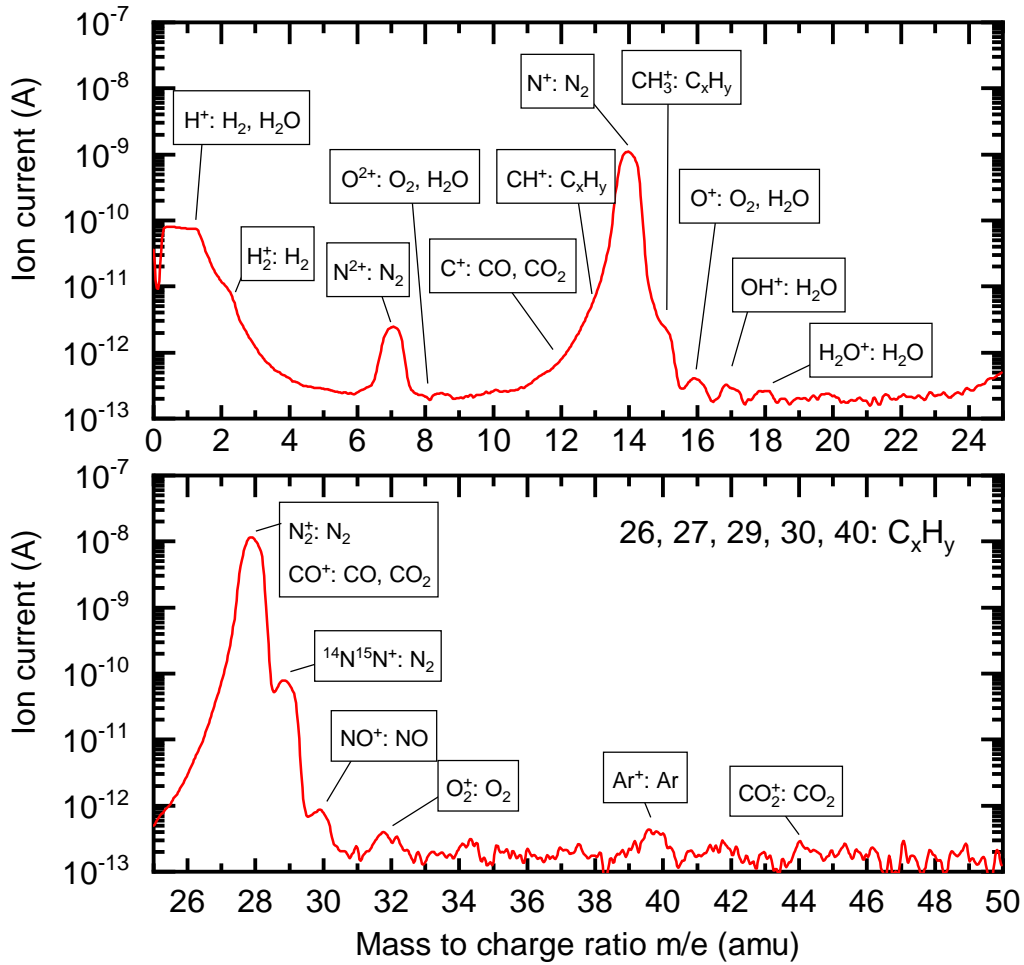
Figure B.3: Quadrupole mass spectrum of the growth chamber during c-GaN-growth. Labels denote the most probable elements that contribute to the respective peak.
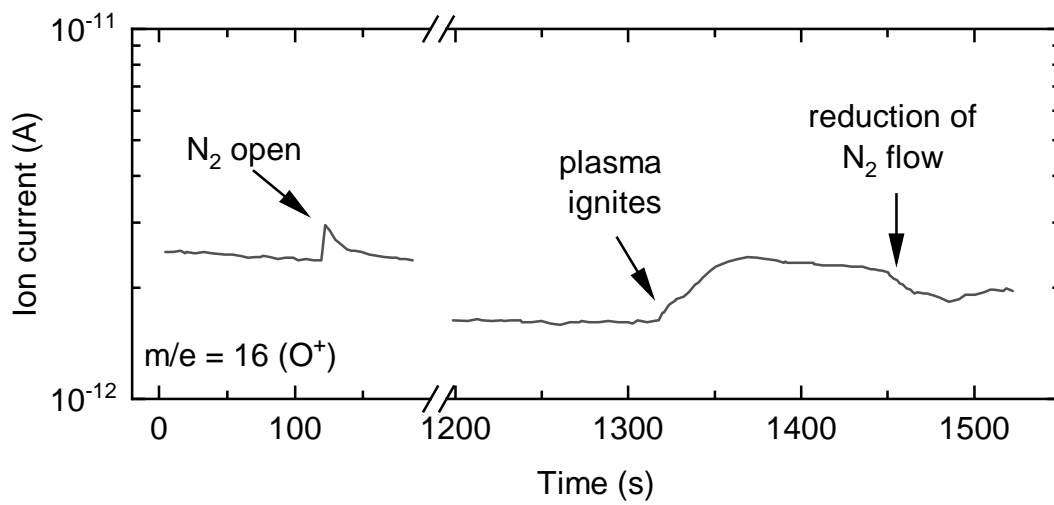
Figure B.4: Quadrupole mass spectrometer signal at $m/e = 16$ amu (mostly O^+ ions) during operation of the nitrogen plasma source of the MBE. Different stages of plasma source operation are labeled in the diagram. First, the N_2 flow is started, which results in a climb of the O^+ signal. The ion current drop that is noticed in the following minutes is most probably due to instrument warm-up. A further rise of the O^+ signal occurs when the plasma is ignited. After subsequent reduction of the N_2 flow, also the O^+ signal decreases. Thus, it can be seen that O is introduced into the growth chamber by the nitrogen plasma source. However, the signal intensity of O^+ is by orders of magnitudes lower than that of N^+ (see Fig. B.3).
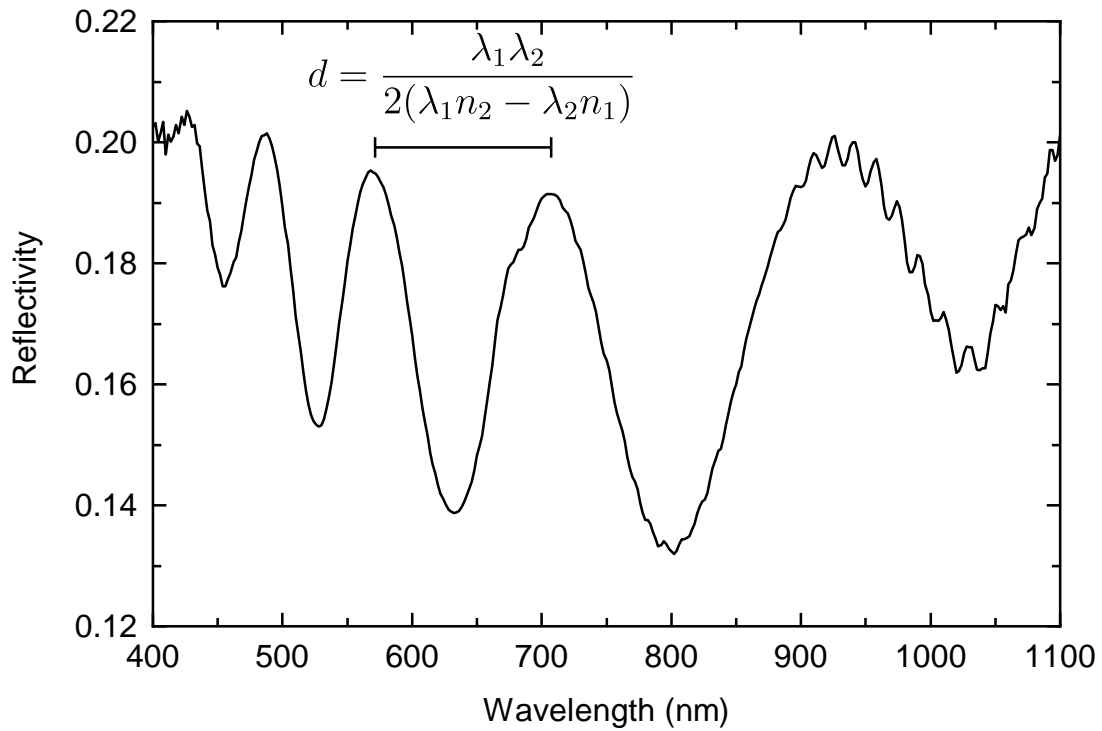
Figure B.5: The thickness of a layer is determined by reflectometric interference spectroscopy, by measuring the sample reflectivity over a wide spectral range. Therefore, light of an incandescent lamp is directed onto the sample in (nearly) normal incidence, and the reflected beam is analyzed by a spectrometer. By dividing the spectrum by the lamp's reference spectrum, the reflectivity is obtained. The layer thickness can be calculated by evaluating the distance between two adjacent interference maxima or minima (equation in the diagram). The layer thickness is calculated for each pair of adjacent maxima and minima and is averaged over all obtained values. (Here sample 2518 is used as an example.)
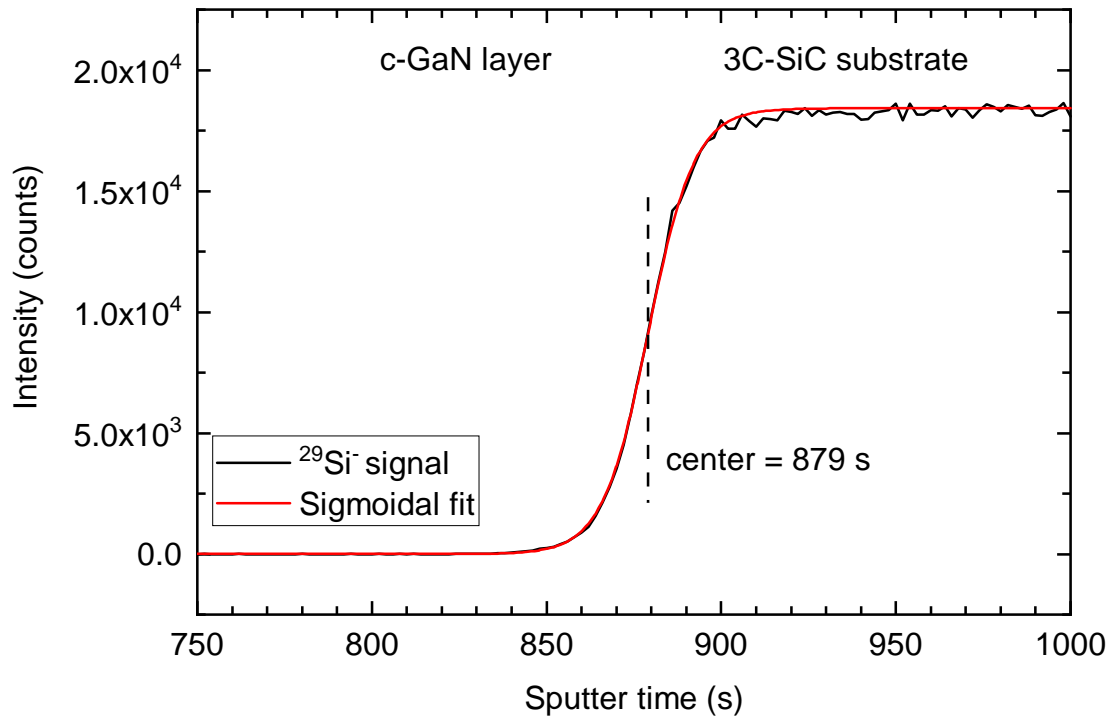
Figure B.6: A sigmoidal function is fitted to the $^{29}Si^-$ signal measured by TOF-SIMS to obtain the sputter time where the transition from c-GaN layer to 3C-SiC substrate occurs. The sputter rate is determined using the layer thickness of a thick, n.i.d. layer measured by reflectometry. The layer thickness is obtained by multiplying the sputter time with the sputter rate. (Here sample 2522 is used as an example.)
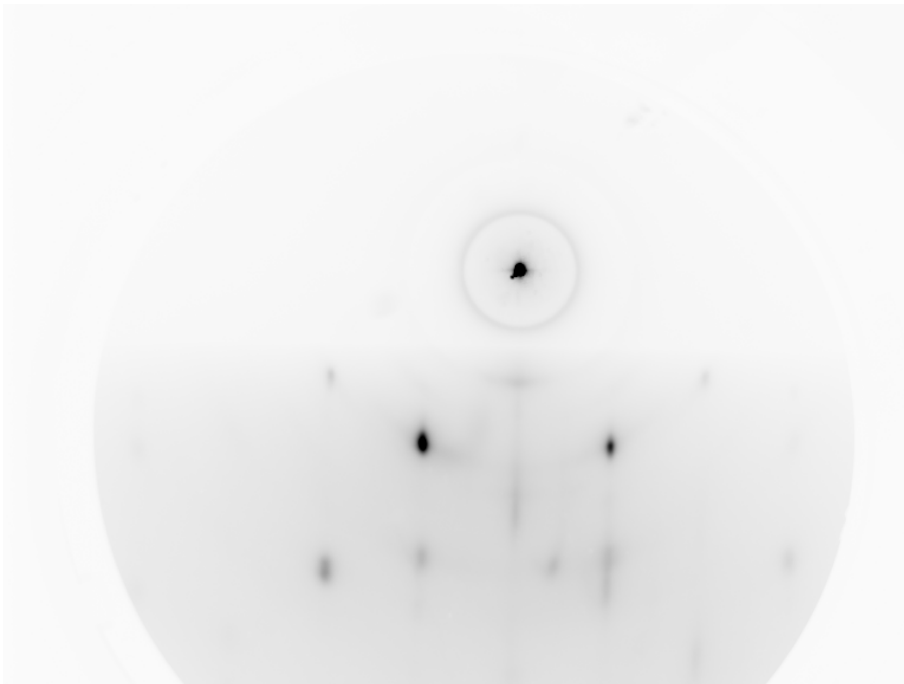
(a) Sample 2990 – conventionally doped
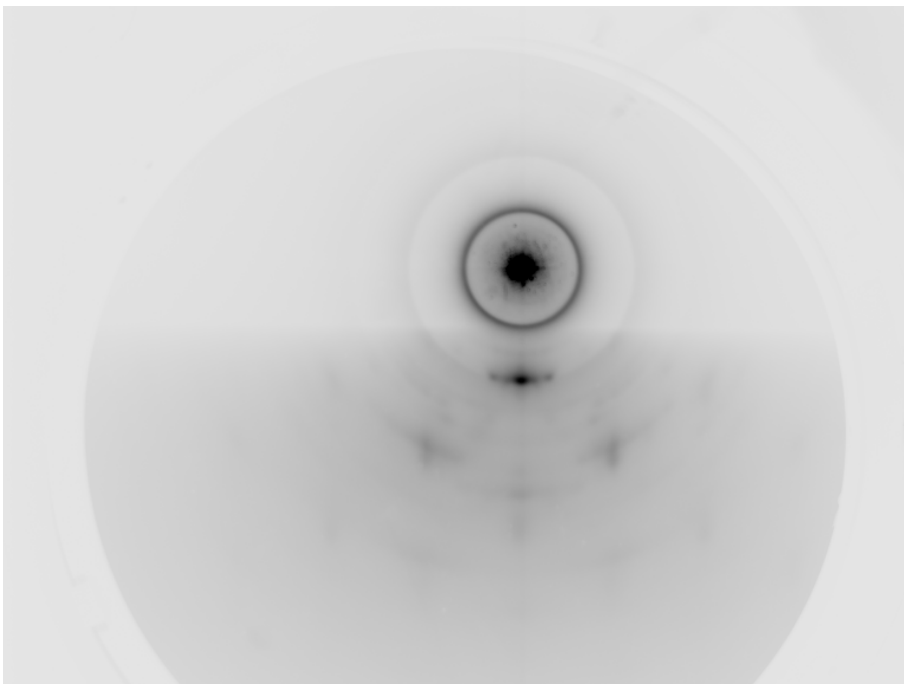
(b) Sample 3004 – δ-doped

Figure B.7: RHEED patterns of SL samples with highest Ge-doping of the QW layers ($T_{Ge} = 1000\,^{\circ}$C).
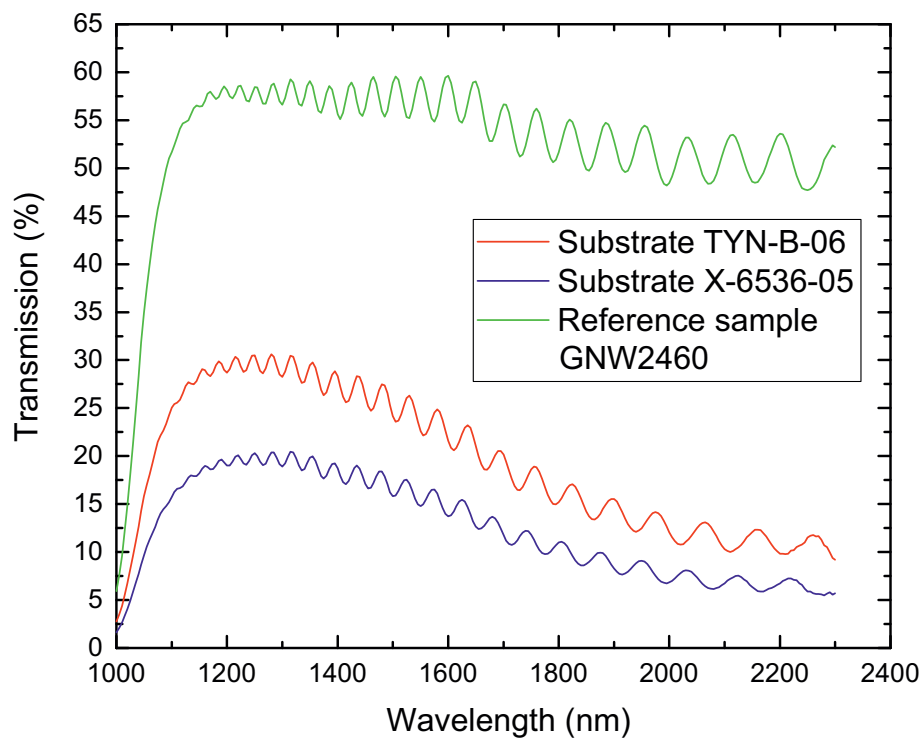
Figure B.8: Transmission spectra of two 3C-SiC substrates and a reference SL sample, which shows intersubband absorption.

C Appendix C - nextnano³ input file

On the following pages, the nextnano³ [98] input file for simulation of a single c-GaN/c-AlN or c-GaN/c-Al$_x$Ga$_{1-x}$N quantum well is printed. The Al mole fraction can be adjusted and the parameters for c-Al$_x$Ga$_{1-x}$N are interpolated between c-GaN and c-AlN.

```
!****** OVERALL SIMULATION PARAMETERS ***************************************!
!This input file simulates a single GaN/Al(Ga)N quantum well
!&macro filename = 'macro.in'
%FunctionParser = yes

!Layer thicknesses
%Barrier1 = 2d0 !AlN Barrier (nm)
%QW = 1.8d0 !GaN QW (nm)

%piezo_AlGaN = 0d0
%piezo = 0d0

!Simulation areas
%region1 = %Barrier1 + %QW
%domain = %Barrier1 + %QW + %Barrier1

%AlGehalt = 1 !Al content

%Temperatur = 300E0
%Strain_status = 0.25E0 ! 1= pseudomorph
%Strain_qw = 1-%Strain_status

!Lattice constants
%g_AlN = 0.4373E0
%g_GaN = 0.4503E0

!Doping properties
%dopingConcentration = 78d0     !78 * 10^18 cm^-3 = 7.8 * 10^19 cm^-3 : Doping in GaN QW
%donorBindingEnergy = -1000d0  !all ionized

%g_rel_AlGaN = %g_AlN*%AlGehalt +%g_GaN*(1-%AlGehalt) !AlGaN lattice constant
%g_AlGaN = %g_rel_AlGaN
%g_Buffer = (1-%Strain_qw) * %g_GaN+ (%Strain_qw)* %g_rel_AlGaN

!Band energies and alignment
%CBO = 74  !Conduction band offset
%VBO = 100-%CBO  !Valence band offset
%E_GaN = 3.24+0.006 !c-GaN band gap @300K
%E_AlN = 5.93 !c-AlN band gap @300K
%b = -0.85 !Bowing Parameter for AlGaN
%GaN_VB = -0.726
%GaN_LB = %E_GaN+%GaN_VB
%E_AlGaN = %E_GaN*(1-%AlGehalt) + %E_AlN*%AlGehalt + %b*%AlGehalt *(1-%AlGehalt) !AlGaN band gap
%DeltaE = %E_AlGaN - %E_GaN
%Leitunsgband_AlGaN = %DeltaE *%CBO/100 +%GaN_LB
%Valenzband_AlGaN = -%DeltaE *%VBO/100+%GaN_VB

!effective masses
%mass_eGaN = 0.19E0 !Carvalho Phys Rev B 84, 195105 (2011)
%mass_eAlN = 0.30E0 !Carvalho Phys Rev B 84, 195105 (2011)
%mass_hhGaN = 0.83E0 !Carvalho Phys Rev B 84, 195105 (2011)
%mass_hhAlN = 1.32E0 !Carvalho Phys Rev B 84, 195105 (2011)
%mass_lhGaN = 0.28E0 !Carvalho Phys Rev B 84, 195105 (2011)
%mass_lhAlN = 0.44E0 !Carvalho Phys Rev B 84, 195105 (2011)
%mass_SOGaN = 0.34E0 !Carvalho Phys Rev B 84, 195105 (2011)
%mass_SOAlN = 0.55E0 !Carvalho Phys Rev B 84, 195105 (2011)

!GaN Parameters
%c11_GaN = 293d0 !Elasticity coefficients
%c12_GaN = 159d0
%c44_GaN = 155d0
%GaN_splitt_off = 0.015d0 !Split off energy (eV)
%av_GaN = 2d0 !deformation potential VB (eV)
%ac_GaN = -6d0 !deformation potential CB (eV)
%uniaxial_GaN = -1.7d0 !deformation potential uniaxial strain VB (eV)

!Linear interpolation of parameters for AlGaN
%lb_mass1 = %mass_eAlN*%AlGehalt + %mass_eGaN*(1 - %AlGehalt) !e mass
%vb_mass1 = %mass_hhAlN*%AlGehalt + %mass_hhGaN*(1 - %AlGehalt) !hh mass
%vb_mass2 = %mass_lhAlN*%AlGehalt + %mass_lhGaN *(1 - %AlGehalt)!lh mass
%vb_mass3 = %mass_SOAlN*%AlGehalt + %mass_SOGaN*(1 - %AlGehalt) !so mass
%c11_AlGaN = 304*%AlGehalt +%c11_GaN*(1-%AlGehalt) !elasticity coefficers
%c12_AlGaN = 160*%AlGehalt +%c12_GaN*(1-%AlGehalt)
%c44_AlGaN = 193*%AlGehalt +%c44_GaN*(1-%AlGehalt)
%splitt_off = 0.019*%AlGehalt +%GaN_splitt_off*(1-%AlGehalt) !split off energy (eV)
%av_AlGaN = 2.3*%AlGehalt +%av_GaN*(1-%AlGehalt) !deformation potential VB (eV)
%ac_AlGaN = -6.8*%AlGehalt +%ac_GaN*(1-%AlGehalt)!deformation potential CB (eV)
%uniaxial_AlGaN = -1.5 *%AlGehalt -%uniaxial_GaN*(1-%AlGehalt) !deformation potential uniaxial strain VB (eV)

$numeric-control
 simulation-dimension           = 1                     ! only simulate directions in which charge carriers are bound, therefore 1D
simulation for a quantum well
 zero-potential                 = no                    ! don't consider charge redistribution
 varshni-parameters-on          = no                    ! don't consider temperature dependence of band gap
 lattice-constants-temp-coeff-on     = no               ! temperature dependent lattice constants
 nonlinear-poisson-cg-lin-eq-solv    = lapack-full
 schroedinger-1band-ev-solv          = lapack           ! 'lapack', 'laband', 'arpack', 'davids', 'it_jam',
'chearn'
 8x8kp-params-from-6x6kp-params      = yes              !
 8x8kp-params-rescale-S-to           = no               ! no, ONE, ZERO
 varshni-parameters-on = no                             ! Temperature dependent energy gaps
 lattice-constants-temp-coeff-on = no                   ! Lattice constants independent of temperature. Absolute
values from database are taken.
```

```
$end_numeric-control
$simulation-dimension
 dimension    = 1                                                          ! 1D simulation
 orientation = 0 0 1                                                       ! along z axis (as defined below)
$end_simulation-dimension                                                  !

$global-parameters                                                         !
 lattice-temperature = %Temperatur                                         ! 300 Kelvin
$end_global-parameters                                                     !

$simulation-flow-control
 flow-scheme        = 2                                                    ! 2 = self-consistent Schroedinger-Poisson
 strain-calculation = homogeneous-strain                                  ! homogeneous-strain  or  strain-minimization  or  zero-
strain-amorphous
$end_simulation-flow-control                                               !

$domain-coordinates                                                        !
 domain-type            = 0 0 1                                            ! again: along z axis
 z-coordinates          = 0d0 %domain                                     ! beginning and end of simulated region in nm
 growth-coordinate-axis = 0 0 1                                           ! needed if pseudomorphic strain is to be calculated
 pseudomorphic-on       = GaN(zb)                                         ! needed if pseudomorphic strain is to be calculated
 lattice-constants      = %g_Buffer %g_Buffer %g_Buffer
 lattice-constants-temp-coeff = 5.59d-6    5.59d-6    5.59d-6             ! [nm/K] http://www.ioffe.ru/SVA/NSM/
$end_domain-coordinates                                                    !
!****** REGIONS AND CLUSTERS ****************************************!
$regions                                                                   !
region-number = 1    base-geometry = line    region-priority = 2    z-coordinates = 0d0       %Barrier1 !Material: Barrier
region-number = 2    base-geometry = line    region-priority = 2    z-coordinates = %Barrier1 %region1  !Material: QW
region-number = 3    base-geometry = line    region-priority = 2    z-coordinates = %region1  %domain   !Material: Barrier
$end_regions                                                               !

$grid-specification                                                        ! for every boundary between regions, there has to exist a
grid line
 grid-type       =    0 0 1                                               ! again: along z axis
 z-grid-lines    =    0d0      %Barrier1    %region1    %domain           ! explicity specified grid lines
 z-nodes         =    300      300          300                          ! number of additional grid lines between those
 z-grid-factors  =    1d0      1d0          1d0                          ! can be used for inhomogeneous grids
$end_grid-specification                                                    !
! You specified n regions in the simulation area. If they do not           !
! completely fill the simulation area, the resulting rest area is          !
! automatically assigned as region number n+1.                            !

$region-cluster                           ! regions can be grouped into clusters
 cluster-number = 1    region-numbers = 1 3 4    ! Barriers
 cluster-number = 2    region-numbers = 2        ! Quantum Well
$end_region-cluster
!****** MATERIALS AND ALLOY PROFILES ****************************************
$material

 material-number = 1
 material-name   = AlN(zb)                        ! here overwritten by AlGaN
 cluster-numbers = 1
 crystal-type    = zincblende

 material-number = 2
 material-name   = GaN(zb)                        ! QW material
 cluster-numbers = 2
$end_material

! Here we are overwriting the database entries for GaAs.                   !
!****** DOPING AND IMPURITIES ****************************************!

$doping-function                                                           !
 doping-function-number   = 1                                             !
 impurity-number          = 1                                             ! properties of this impurity type have to be specified
below
 doping-concentration     = %dopingConcentration                          ! 150 * 10^18 cm^-3 = 1.5 * 10^20 cm^-3
 only-region              = %Barrier1 %region1                            ! doping only in QW
$end_doping-function                                                       !
                                                                           !
$impurity-parameters                                                       !
 impurity-number            = 1                                           ! impurity numbers labelled in doping-function
 impurity-type              = n-type                                      ! n-type, p-type
 number-of-energy-levels    = 1                                           ! number of energy levels of this impurity (only 1 is
currently allowed)
 energy-levels-relative     = %donorBindingEnergy                         ! energy relative to 'nearest' band edge (n-type ->
conduction band, p-type -> valence band)
 degeneracy-of-energy-levels = 2                                          ! degeneracy of energy levels, 2 for n-type, 4 for p-type
$end_impurity-parameters
!****** QUANTUM ****************************************************!
$quantum-regions                                                           ! Schroedinger equation is only solved inside this
region(s)
 region-number    = 1                                                     ! usually only one simulation region
 base-geometry    = line                                                  !
 region-priority  = 3                                                     !
 z-coordinates    = 0d0 %domain                                           ! can also be smaller than total simulation region
$end_quantum-regions                                                       !
$quantum-cluster                                                           ! again: regions can be grouped into clusters
 cluster-number    = 1                                                    !
 region-numbers    = 1                                                    !
 deactivate-cluster = no                                                  !
$end_quantum-cluster                                                       !
$quantum-model-electrons                                                   ! how to solve Schroedinger equation for electrons
```

```
 model-number                         = 1                          !
 model-name                           = effective-mass             ! quantum model, here: single band effective mass
approximation
 cluster-numbers                      = 1                          ! quantum cluster numbers to which this model applies
 conduction-band-numbers              = 1                          ! select conductions bands (minima), here: only gamma point
 number-of-eigenvalues-per-band       = 4                          ! how many eigenenergies are calculated for each band
 separation-model                     = eigenvalue                 ! to determine separation between classic and quantum
density
 maximum-energy-for-eigenstates       = 1d0                        ! has to be present but is ignored in separation model
"eigenvalue"
 quantization-along-axes              = 0 0 1                      ! directions in which charge carriers are quantized, here:
same as simulation direction
 boundary-condition-100               = Neumann                    ! mixed, Neumann or (Dirichlet|dirichlet|DIRICHLET).
Nonsens input means Neumann (default).
 boundary-condition-010               = Neumann                    ! mixed, Neumann or (Dirichlet|dirichlet|DIRICHLET).
Nonsens input means Neumann (default)
 boundary-condition-001               = Neumann                    ! periodic boundary conditions are necessary for
superlattices
$end_quantum-model-electrons                                       !
$quantum-model-holes                                              !
 model-number                         = 1                          !
 model-name                           = effective-mass             ! quantum model, here: single band effective mass
approximation
 cluster-numbers                      = 1                          ! quantum cluster numbers to which this model applies
 valence-band-numbers                 = 1 2 3                      ! select valence bands (maxima), 1 = heavy holes, 2 = light
holes, 3 = split-off holes
 number-of-eigenvalues-per-band       = 3 3 3                      ! how many eigenenergies are calculated for each band
 separation-model                     = eigenvalue                 ! to determine separation between classic and quantum
density
 maximum-energy-for-eigenstates       = 1d0 1d0 1d0                ! has to be present but is ignored in separation model
"eigenvalue"
 quantization-along-axes              = 0 0 1                      ! directions in which charge carriers are quantized, here:
same as simulation direction
 boundary-condition-001               = Neumann                    ! finite barrier .... infinite => Dirichlet
$end_quantum-model-holes                                          !
$binary-zb-default                                                !
 binary-type                    =AlN(zb)-zb-default                !
 apply-to-material-numbers      =1                                 !
 conduction-band-masses         =%lb_mass1    %lb_mass1    %lb_mass1    ! [m0] ml,mt1,mt2 for each band. Ordering of numbers
corresponds to band no. 1, 2, ... (Gamma, L, X)
                                 0.200000D+00    0.200000D+00    0.200000D+00      ! [m0]
                                 0.530000D+00    0.310000D+00    0.310000D+00      ! [m0]
 conduction-band-energies       = %Leitunsgband_AlGaN    7.78d0  3.38d0 ! 0K

 absolute-deformation-potentials-cbs = %ac_AlGaN  -4.95d0  3.81d0
 lattice-constants              = %g_AlGaN %g_AlGaN %g_AlGaN
 lattice-constants-temp-coeff   = 5.59d-6    5.59d-6    5.59d-6      ! [nm/K]
 elastic-constants              = %c11_AlGaN %c12_AlGaN %c44_AlGaN
 valence-band-masses            = %vb_mass1    %vb_mass1    %vb_mass1
                                  %vb_mass2    %vb_mass2    %vb_mass2
                                  %vb_mass3    %vb_mass3    %vb_mass3    ! [m0] ml,mt1,mt2 for each band. Ordering of numbers
corresponds to band no. 1, 2, ... (hh, lh, so)

 6x6kp-parameters               =     -0.480000D+01   -0.198000D+01   -0.510000D+01    ! [hbar^2/2m] [hbar^2/2m] [hbar^2/2m]
                                      %splitt_off!Splitt-off [eV]

 valence-band-energies          = %Valenzband_AlGaN                 ! A. Zunger, average valence band energy E_v,av [eV]
 varshni-parameters             = 0.593d-3 0.593d-3 0.593d-3        ! alpha [eV/K](Gamma, L, X) Vurgaftman1/Vurgaftman2
                                  600d0      600d0      600d0       ! beta  [K]    (Gamma, L, X) Vurgaftman1/Vurgaftman2

 absolute-deformation-potential-vb  = %av_AlGaN                     ! a_v [eV] Vurgaftman1 has different sign convention -> -
3.4
 uniax-vb-deformation-potentials    = %uniaxial_AlGaN -5.5d0        ! b,d [eV]  Vurgaftman2
$end_binary-zb-default
!_____
!_____
$binary-zb-default

 binary-type                    =GaN(zb)-zb-default                !
 apply-to-material-numbers      =2
 conduction-band-masses         =%mass_eGaN %mass_eGaN %mass_eGaN   ! [m0] ml,mt1,mt2 for each band. Ordering of numbers
corresponds to band no. 1, 2, ... (Gamma, L, X)
                                 0.200000D+00    0.200000D+00    0.200000D+00    ! [m0]
                                 0.500000D+00    0.300000D+00    0.300000D+00    ! [m0]

 conduction-band-energies       = %GaN_LB 4.870d0  3.800d0          !
 absolute-deformation-potentials-cbs = %ac_GaN  -7.46d0  -0.52d0
 lattice-constants              = %g_GaN %g_GaN %g_GaN              ! [nm]  including 'lattice-constants-temp-coeff'
 lattice-constants-temp-coeff   = 5.59d-6    5.59d-6    5.59d-6      ! [nm/K]
http://www.ioffe.ru/SVA/NSM/Semicond/GaN/basic.html
 elastic-constants              = %c11_GaN  %c12_GaN  %c44_GaN
 valence-band-masses            = %mass_hhGaN    %mass_hhGaN    %mass_hhGaN    %mass_lhGaN    %mass_lhGaN    %mass_lhGaN  0.29d0
0.29d0    0.29d0

 6x6kp-parameters               = -6.74d0    -2.18d0    -6.66d0     ! Vurgaftman2  L,M,N   [hbar^2/2m] (--> divide by
hbar^2/2m)
                                  0.015d0                           ! Vurgaftman1/Vurgaftman2 delta_(split-off) in [eV]

 valence-band-energies          = %GaN_VB                           ! A. Zunger, average valence band energy E_v,av [eV]
 varshni-parameters             = 0.593d-3 0.593d-3 0.593d-3        ! alpha [eV/K](Gamma, L, X) Vurgaftman1/Vurgaftman2
                                  600d0      600d0      600d0       ! beta  [K]    (Gamma, L, X) Vurgaftman1/Vurgaftman2
```

```
 absolute-deformation-potential-vb   = %av_GaN                              ! a_v [eV] Vurgaftman1 has different sign convention -> -
5.2
 uniax-vb-deformation-potentials     = %uniaxial_GaN   -3.7d0               ! b,d [eV]  Vurgaftman2
$end_binary-zb-default
!_____
!_____

!****** OUTPUT ***************************************************!
$global-settings                                                 !
 output-directory          = output/                             !
 number-of-parallel-threads = 4                                  ! 4 = for   quad-core CPU
$end_global-settings                                             !
$output-raw-data                                                 !
 destination-directory                = raw_data1/               !
 potential                            = yes                      !
 fermi-levels                         = yes                      !
 strain                               = yes                      !
 kp-eigenstates                       = no                       !
$end_output-raw-data                                             !
$output-1-band-schroedinger                                      !
 destination-directory                = Schroedinger_1band/      !
 shift-wavefunction-by-eigenvalue     = yes                      !
 sg-structure                         = yes                      !
 conduction-band-numbers              = 1                        ! only gamma point (as specified above)
 cb-min-ev                            = 1                        !
 cb-max-ev                            = 4                        ! four eigenvalues per band (as specified above)
 valence-band-numbers                 = 1 2 3                    ! heavy hole, light hole and split-off hole (as specified
above)
 vb-min-ev                            = 1                        !
 vb-max-ev                            = 4                        ! four eigenvalues per band (as specified above)
 complex-wave-functions               = no                       !
 scale                                = 2d0                      ! for psi_squared, no physical relevance
 interband-matrix-elements            = yes                      !
 intraband-matrix-elements            = yes                      ! electron-hole transition energies and wave function
overlaps
$end_output-1-band-schroedinger                                  !
$output-bandstructure                                            ! output for the band structure and the potential
 destination-directory                = band_structure/         !
 conduction-band-numbers              = 1                        ! conduction band edge at gamma point=1,L=2,X=3
 valence-band-numbers                 = 1 2 3                    ! valence band edge for heavy, light and split-off holes
 potential                            = yes                      !
$end_output-bandstructure                                        !
!***** END BAND STRUCTURE AND DENSITIES *************************************!
!***** OUTPUT STRAIN *******************************************************!
! This is the output for the densities.                         !
$output-densities                                                !
 destination-directory                = densities1/             !
 electrons                            = yes                      !
 holes                                = no                       !
 charge-density                       = no                       !
 intrinsic-density                    = yes                      !
 ionized-dopant-density               = yes                      !
 piezo-electricity                    = yes                      !
 pyro-electricity                     = no                       !
 interface-density                    = yes                      !
 effective-density-of-states-Nc-Nv    = yes                      !
 subband-density                      = yes                      !
$end_output-densities                                            !
                                                                 !
! This is the output for the strain.                            !
$output-strain                                                   !
 destination-directory                = strain1/                !
 strain                               = yes                      !
 strain-simulation-system             = yes                      !
$end_output-strain                                               !
                                                                 !
!***** END OUTPUT STRAIN ***************************************!
$output-current-data                                             !
 destination-directory                = current1/               !
 current                              = no                       !
 fermi-levels                         = yes                      !
 mobility-out                         = yes                      !
 IV-curve-out                         = no                       !
 recombination                        = no                       !
$end_output-current-data                                         !
                                                                 !
$output-material                                                 !
 destination-directory                = material/               !
 doping-concentration                 = doping_concentration1D.dat !
$end_output-material                                             !
```

D Appendix D - list of samples

Table D.1: List of samples

Sample GND...	Substrate	Date	Sample structure
2587	11CO063	14.12.2015	600 nm GaN
2620	UniPad11-01	29.03.2016	600 nm GaN
2621	UniPad11-01	30.03.2016	AlN calibration
2625	UniPad11-01	11.04.2016	150 nm GaN
2630	UniPad11-01	20.04.2016	GaN:Ge test
2631	UniPad11-01	21.04.2016	600 nm GaN:Ge(1000 °C)
2633	UniPad11-01	27.04.2016	600 nm GaN (for DBR test)
2634	UniPad11-01	28.04.2016	600 nm GaN (for DBR test)
2635	UniPad11-01	03.05.2016	260 nm GaN / few nm InN
2636	UniPad11-01	10.05.2016	260 nm GaN / few nm InN
2637	14CO144	11.05.2016	260 nm GaN / ≈200 nm InN
2638	14CO144	17.05.2016	260 nm GaN / ≈400 nm InN
2639	14CO144	18.05.2016	600 nm GaN
2640	14CO144	19.05.2016	600 nm GaN
2641	14CO144	24.05.2016	260 nm GaN / ≈400 nm InN
2642	14CO144	07.06.2016	260 nm GaN / ≈400 nm InN
2643	14CO144	08.06.2016	260 nm GaN / ≈400 nm InN
2644	14CO144	10.06.2016	260 nm GaN / ≈400 nm InN
2645	14CO144	14.06.2016	260 nm GaN / ≈400 nm InN
2646	14CO144	15.06.2016	260 nm GaN / ≈400 nm InN
2669	11CO192	18.10.2016	600 nm GaN
2671	14CO144	25.10.2016	GaN / AlN test
2672	14CO144	27.10.2016	GaN / AlN phonon mirror
2674	14CO144	07.11.2016	≈360 nm AlGaN 30% Al
2685	11CO192	21.11.2016	370 nm GaN
2691	12CO60	28.11.2016	AlN / AlGaN 15% Al test
2696	12CO60	06.12.2016	AlN / AlGaN DBR 5 periods
2697	12CO60	07.12.2016	500 nm GaN
2700	12CO60	12.12.2016	≈560 nm AlGaN 15% Al
2704	12CO60	20.12.2016	AlN / AlGaN DBR 5 periods
2721	12CO60	10.02.2017	AlInN 17% In
2722	12CO60	13.02.2017	AlInN 17% In
2723	12CO60	17.02.2017	AlInN 17% In
2724	12CO60	20.02.2017	AlInN 17% In

Table D.1: List of samples (continued)

Sample GND...	Substrate	Date	Sample structure
2727	12CO60	23.02.2017	AlInN 17% In
2728	12CO60	07.03.2017	AlInN 17% In
2735	12CO60	03.04.2017	450 nm AlGaN 27% Al
2736	12CO60	04.04.2017	GaN:Ge different doping levels
2741	12CO60	10.04.2017	AlN / AlGaN 27% Al test
2742	12CO60	11.04.2017	90 nm GaN/40x 1 nm AlN/1.8 nm GaN:Si(970 °C)
2752	12CO60	08.06.2017	GaN calibration sample
2753	12CO60	09.06.2017	440 nm GaN
2756	12CO60	14.06.2017	490 nm GaN
2759	12CO60	22.06.2017	580 nm GaN
2760	12CO60	23.06.2017	580 nm GaN
2764	12CO60	29.06.2017	550 nm GaN
2765	12CO60	03.07.2017	560 nm GaN
2766	X-6536-05	04.07.2017	580 nm GaN
2768	X-6536-05	06.07.2017	600 nm GaN
2769	TYN-B-06	07.07.2017	590 nm GaN
2770	TYN-B-06	12.07.2017	610 nm GaN
2781	12CO60	05.09.2017	600 nm GaN
2788	12CO60	28.09.2017	600 nm GaN
2789	12CO60	29.09.2017	AlN test sample
2791	12CO60	25.10.2017	300 nm GaN
2792	12CO60	27.11.2017	AlN test sample
2793	12CO60	27.11.2017	AlN test sample
2794	12CO60	28.11.2017	AlN test sample
2795	12CO60	28.11.2017	AlN test sample
2796	12CO60	29.11.2017	AlN test sample
2797	12CO60	30.11.2017	AlN test sample
2798	12CO60	01.12.2017	AlN test sample
2799	12CO60	04.12.2017	AlN test sample
2800	12CO60	05.12.2017	AlN test sample
2801	12CO60	05.12.2017	AlN test sample
2802	12CO60	07.12.2017	220 nm GaN
2803	12CO60	19.12.2017	AlN test sample
2807	16CO174	09.01.2018	AlN test sample
2808	16CO174	09.01.2018	AlN test sample
2810	16CO174	10.01.2018	AlN test sample
2812	16CO174	12.01.2018	AlN test sample
2813	16CO174	16.01.2018	AlN test sample
2814	16CO174	16.01.2018	AlN test sample
2816	16CO174	19.01.2018	AlN test sample

Table D.1: List of samples (continued)

Sample GND...	Substrate	Date	Sample structure
2817	16CO174	19.01.2018	AlN test sample
2818	16CO174	22.01.2018	AlN test sample
2819	16CO174	23.01.2018	AlN test sample
2820	16CO174	23.01.2018	AlN test sample
2823	16CO174	26.01.2018	AlN test sample
2824	16CO174	26.01.2018	AlN test sample
2826	16CO174	01.02.2018	AlN test sample
2827	16CO174	02.02.2018	AlN test sample
2828	16CO174	05.02.2018	AlN test sample
2829	16CO174	06.02.2018	AlN test sample
2830	16CO174	06.02.2018	AlN test sample
2833	16CO174	09.02.2018	AlN test sample
2834	16CO174	09.02.2018	AlN test sample
2835	16CO174	12.02.2018	AlN test sample
2836	16CO174	13.02.2018	660 nm GaN
2839	16CO174	16.02.2018	90 nm GaN/40x 1 nm AlN/1.8 nm GaN:Si(970 °C)
2841	16CO174	20.02.2018	AlN test sample
2842	16CO174	23.02.2018	AlN test sample
2843	16CO174	26.02.2018	GaN / AlGaN calibration sample
2845	16CO174	01.03.2018	AlN test sample
2846	TYN-B-06	01.03.2018	AlN test sample
2847	16CO174	02.03.2018	AlN test sample
2848	16CO174	02.03.2018	AlN test sample
2849	16CO174	05.03.2018	AlN test sample
2851	16CO174	09.03.2018	90 nm GaN/35x 1 nm AlN/1.8 nm GaN:Ge(900 °C)
2856	16CO174	22.03.2018	AlN test sample
2857	16CO174	23.03.2018	90 nm GaN/40x 5 nm AlN/1.8 nm GaN:Ge(900 °C)
2858	16CO174	26.03.2018	AlN test sample
2859	16CO174	27.03.2018	90 nm GaN/40x 2.5 nm AlN/1.8 nm GaN:Ge(900 °C)
2863	16CO174	03.04.2018	90 nm GaN/40x 2 nm AlN/1.8 nm GaN:Ge(900 °C)
2866	16CO174	10.04.2018	AlN test sample
2867	16CO174	10.04.2018	AlN test sample
2869	16CO174	12.04.2018	AlN test sample
2870	16CO171	12.04.2018	AlN test sample
2872	16CO174	17.04.2018	AlN test sample
2873	16CO174	18.04.2018	AlN test sample
2877	16CO174	25.04.2018	AlN test sample
2879	16CO174	27.04.2018	80 nm AlN
2880	16CO174	30.04.2018	80 nm AlN
2881	16CO174	30.04.2018	80 nm AlN

Table D.1: List of samples (continued)

Sample GND...	Substrate	Date	Sample structure
2882	16CO174	02.05.2018	30 nm AlN / 400 nm GaN
2884	16CO175-V2	09.05.2018	70 nm GaN
2885	16CO174	14.05.2018	580 nm GaN - absorption reference sample
2886	16CO174	16.05.2018	AlN test sample
2887	16CO174	16.05.2018	AlN test sample
2888	16CO174	18.05.2018	AlN test sample
2889	16CO174	18.05.2018	AlN test sample
2890	16CO174	22.05.2018	30 nm AlN / 400 nm GaN
2891	16CO174	25.05.2018	90 nm GaN/40x 2 nm AlN/1.8 nm GaN:Ge(900 °C)
2892	16CO174	28.05.2018	600 nm GaN:Ge (900 °C)
2893	12CO62	07.06.2018	AlN test sample
2894	12CO62	08.06.2018	AlN test sample
2895	12CO62	08.06.2018	AlN test sample
2896	12CO62	08.06.2018	AlN test sample
2897	12CO62	11.06.2018	AlN test sample
2898	12CO62	12.06.2018	AlN test sample
2899	12CO62	12.06.2018	AlN test sample
2900	14CO156	13.06.2018	AlN test sample
2901	14CO156	14.06.2018	AlN test sample
2902	14CO156	15.06.2018	AlN test sample
2903	14CO156	15.06.2018	AlN test sample
2905	16CO171	20.06.2018	460 nm GaN
2906	X-6536-05-V5	22.06.2018	70 nm GaN
2908	14CO156	25.06.2018	AlN test sample
2909	14CO156	25.06.2018	AlN test sample
2910	14CO156	26.06.2018	Substrate temperature calibration
2911	14CO156	28.06.2018	AlN test sample
2918	14CO156	18.07.2018	AlN growth rate calibration
2919	14CO156	19.07.2018	200 nm GaN / 200 nm AlGaN 37% Al
2920	14CO156	23.07.2018	200 nm GaN / 200 nm AlGaN 48% Al
2921	11CO192	30.07.2018	300 nm AlGaN:Ge (950 °C) 37% Al
2922	11CO192	31.07.2018	150 nm AlGaN:Ge (950 °C) 48% Al
2923	11CO192	31.07.2018	300 nm AlGaN:Ge (950 °C) 37% Al
2924	14CO156	02.08.2018	AlN test sample
2927	14CO156	14.08.2018	AlN test sample
2928	11CO192	15.08.2018	150 nm AlGaN:Ge (950 °C) 60% Al
2929	14CO156	17.08.2018	300 nm GaN + AlN / GaN:Ge SQW
2930	14CO156	20.08.2018	AlN test sample
2931	14CO156	23.08.2018	AlN test sample
2932	12CO62	28.08.2018	460 nm AlGaN 25% Al n.i.d.

Table D.1: List of samples (continued)

Sample GND...	Substrate	Date	Sample structure
2934	12CO62	30.08.2018	460 nm AlGaN 25% Al (Ge 700 °C)
2936	12CO62	03.09.2018	460 nm AlGaN 25% Al (Ge 800 °C)
2939	12CO62	06.09.2018	460 nm AlGaN 25% Al (Ge 850 °C)
2940	12CO62	07.09.2018	460 nm AlGaN 25% Al (Ge 900 °C)
2941	12CO62	11.09.2018	460 nm AlGaN 25% Al (Ge 950 °C)
2942	12CO62	12.09.2018	460 nm AlGaN 25% Al (Ge 1000 °C)
2945	12CO62	11.10.2018	410 nm GaN:Si (1150 °C)
2946	12CO62	12.10.2018	340 nm GaN:Si (1200 °C)
2948	12CO62	18.10.2018	360 nm GaN n.i.d.
2949	12CO62	19.10.2018	450 nm GaN:Si (1050 °C)
2951	12CO62	24.10.2018	360 nm GaN:Si (1150 °C)
2952	12CO62	25.10.2018	440 nm GaN
2953	14CO156	26.10.2018	AlN test sample
2954	14CO156	26.10.2018	AlN test sample
2958	14CO156	31.10.2018	AlN test sample
2959	14CO156	31.10.2018	AlN test sample
2960	14CO156	06.11.2018	AlN test sample
2961	14CO156	06.11.2018	AlN test sample
2962	14CO156	08.11.2018	60 nm AlN / 400 nm GaN
2963	14CO156	09.11.2018	60 nm AlN / 400 nm GaN
2964	12CO62	14.11.2018	480 nm AlGaN 25% (Ge 950 °C)
2965	14CO156	15.11.2018	300 nm GaN + AlN / GaN:Ge SQW (845 °C)
2966	14CO156	16.11.2018	300 nm GaN + AlN / GaN:Ge SQW (895 °C)
2967	12CO62	19.11.2018	390 nm AlGaN 25% (Ge 850 °C)
2968	14CO156	21.11.2018	100 nm GaN + AlN / GaN:Ge SQW (895 °C)
2969	14CO156	21.11.2018	100 nm GaN + AlN / GaN:Ge SQW (845 °C)
2970	14CO156	22.11.2018	Sticking coefficient measurements (Ga, Ge)
2971	14CO156	23.11.2018	Sticking coefficient measurements (Ga, Si)
2972	14CO156	26.11.2018	AlN test sample
2973	14CO156	27.11.2018	AlN test sample
2974	12CO62	28.11.2018	400 nm GaN:Ge (1050 °C)
2975	12CO62	29.11.2018	400 nm GaN:Ge (1000 °C)
2976	12CO62	04.12.2018	AlN test sample
2977	12CO62	05.12.2018	AlN test sample
2978	14CO156	14.12.2018	AlN test sample
2979	14CO156	18.12.2018	30 nm AlN
2980	14CO156	09.01.2019	480 nm GaN
2981	14CO156	10.01.2019	520 nm GaN
2982	14CO156	16.01.2019	100 nm GaN + AlN / GaN:Ge SQW (895 °C)
2983	14CO156	17.01.2019	50 nm AlN

Table D.1: List of samples (continued)

Sample GND...	Substrate	Date	Sample structure
2984	14CO156	23.01.2019	100 nm GaN + AlN / GaN:Ge SQW (895 °C)
2985	14CO156	24.01.2019	100 nm GaN + AlN / GaN:Ge SQW (895 °C)
2986	16CO126	11.02.2019	90 nm GaN/40x 2 nm AlN/1.8 nm GaN:Ge(900 °C)
2987	16CO126	12.02.2019	90 nm GaN/40x 2 nm AlN/1.8 nm GaN:Ge(850 °C)
2988	16CO126	14.02.2019	90 nm GaN/40x 2 nm AlN/1.8 nm GaN:Ge(800 °C)
2989	16CO126	15.02.2019	90 nm GaN/40x 2 nm AlN/1.8 nm GaN:Ge(950 °C)
2990	16CO126	18.02.2019	90 nm GaN/40x 2 nm AlN/1.8 nm GaN:Ge(1000 °C)
2991	16CO126	20.02.2019	90 nm GaN/40x 2 nm AlN/1.8 nm GaN (n.i.d.)
2992	16CO126	22.02.2019	90 nm GaN/40x 4 nm AlN/1.8 nm GaN:Ge(900 °C)
2993	16CO126	26.02.2019	90 nm GaN/40x 5 nm AlN/1.8 nm GaN:Ge(900 °C)
2995	12CO62	12.03.2019	450 nm GaN:Ge (1010 °C)
2996	12CO62	13.03.2019	450 nm GaN:Ge (1010 °C)
2997	12CO62	18.03.2019	450 nm GaN:Ge (1020 °C)
2999	12CO62	08.04.2019	450 nm GaN:Ge (1020 °C)
3000	12CO62	09.04.2019	450 nm GaN:Ge (1030 °C)
3001	16CO126	10.04.2019	90 nm GaN/40x 2 nm AlN/1.8 nm GaN:Ge(900 °C)
3002	16CO126	15.04.2019	90 nm GaN/40x 2 nm AlN:Ge(900 °C) / 1.8 nm GaN
3003	16CO126	16.04.2019	90 nm GaN/40x 2 nm AlN/1.8 nm GaN:Ge(δ770 °C)
3004	16CO126	17.04.2019	90 nm GaN/40x 2 nm AlN/1.8 nm GaN:Ge(δ1000 °C)
3005	16CO126	23.04.2019	90 nm GaN/40x 2 nm AlN/1.8 nm GaN:Ge(δ900 °C)
3007	16CO126	25.04.2019	450 nm GaN - absorption reference sample
3008	14CO156	26.04.2019	100 nm GaN + AlN / GaN:Ge SQW (895 °C)
3009	16CO126	02.05.2019	60 nm AlN / 400 nm GaN
3010	16CO126	03.05.2019	60 nm AlN / 400 nm GaN
3011	16CO126	09.05.2019	90 nm GaN/64x 1.5 nm AlN/1.8 nm GaN:Ge(850 °C)
3012	16CO126	20.05.2019	60 nm GaN + SQW 2.5 nm (Ge 875 °C)
3013	16CO126	22.05.2019	60 nm GaN + SQW 5 nm (Ge 830 °C)
3016	TYN-B-06	04.06.2019	20 nm GaN
3017	TYN-B-06	04.06.2019	20 nm GaN
3041	TYN-B-06	29.08.2019	740 nm GaN
3042	TYN-B-06	30.08.2019	75 nm AlN
3043	TYN-B-06	02.09.2019	90 nm GaN/40x 2 nm AlN/1.8 nm GaN:Ge(900 °C)

Publications

Scientific publications

1. **Michael Deppe**, Jürgen W. Gerlach, Dirk Reuter, and Donat J. As: 'Incorporation of germanium for n-type doping of cubic GaN'. *physica status solidi (b)* **254**, 1600700 (2017).

2. **Michael Deppe**, Jürgen W. Gerlach, Stepan Shvarkov, Detlef Rogalla, H.-W. Becker, Dirk Reuter, and Donat J. As: 'Germanium doping of cubic GaN grown by molecular beam epitaxy'. *Journal of Applied Physics* **125**, 095703 (2019).

3. Donat J. As, **Michael Deppe**, Jürgen Gerlach, and Dirk Reuter: 'Optical Properties of Germanium Doped Cubic GaN'. *MRS Advances* **2**, 283 (2017).

4. Elias Baron, Rüdiger Goldhahn, **Michael Deppe**, Donat J. As, and Martin Feneberg: 'Influence of the free-electron concentration on the optical properties of zincblende GaN up to 1×10^{20} cm^{-3}'. *Physical Review Materials* **3**, 104603 (2019).

5. **Michael Deppe**, Tobias Henksmeier, Jürgen W. Gerlach, Dirk Reuter, and Donat J. As: 'Molecular Beam Epitaxy Growth and Characterization of Germanium-Doped Cubic Al$_x$Ga$_{1-x}$N'. *physica status solidi (b)* **257**, 1900532 (2020).

6. Elias Baron, Rüdiger Goldhahn, **Michael Deppe**, Donat J. As, and Martin Feneberg: 'Photoluminescence Line Shape Analysis of Highly n-Type Doped Zincblende GaN'. *physica status solidi (b)* **257**, 1900522 (2020).

7. Elias Baron, Rüdiger Goldhahn, **Michael Deppe**, Fabian Tacken, Donat J. As, and Martin Feneberg: 'Optical evidence of many-body effects in the zincblende Al$_x$Ga$_{1-x}$N alloy systems (submitted)'. *Journal of Physics D* (2020).

Contributions to international conferences[1]

1. <u>Donat J. As</u>, **Michael Deppe**, Jürgen W. Gerlach, and Dirk Reuter: 'Optical Properties of Germanium Doped Cubic GaN'. *Oral presentation.* MRS Fall Meeting. Boston, MA, USA, 2016.

---

1   Presenting author is underlined

2. **Michael Deppe**, Jürgen W. Gerlach, Dirk Reuter, and Donat J. As: 'Incorporation of germanium for n-type doping of cubic GaN'. *Poster presentation.* International Workshop on Nitride Semiconductors 2016 (IWN 2016). Orlando, FL, USA, 2016.

3. Elias Baron, Martin Feneberg, Rüdiger Goldhahn, **Michael Deppe**, and Donat J. As: 'Plasmonic properties of degenerately Ge-doped cubic GaN'. *Oral presentation.* 12th International Conference on Nitride Semiconductors (ICNS-12). Strasbourg, France, 2017.

4. **Michael Deppe**, Fabian Tacken, Dirk Reuter, and Donat J. As: 'Photoluminescence characterization of germanium doped cubic $Al_xGa_{1-x}N$ grown by molecular beam epitaxy'. *Poster presentation.* 12th International Conference on Nitride Semiconductors (ICNS-12). Strasbourg, France, 2017.

5. Elias Baron, Martin Feneberg, Rüdiger Goldhahn, **Michael Deppe**, and Donat J. As: 'Plasmonic properties of degenerately Ge-doped cubic GaN'. *Oral presentation.* 10th Workshop Ellipsometry (WSE10). Chemnitz, 2018.

6. Martin Feneberg, Elias Baron, Elias Kluth, Karsten Lange, Donat J. As, **Michael Deppe**, Fabian Tacken, Matthias Wieneke, Jürgen Bläsing, Hartmut Witte, Armin Dadgar, and Rüdiger Goldhahn: 'Revision of the TO phonon frequencies in wurtzite and zincblende GaN'. *Oral presentation.* International Workshop on Nitride Semiconductors 2018 (IWN 2018). Kanazawa, Japan, 2018.

7. **Michael Deppe**, Fabian Tacken, Tobias Henksmeier, Jürgen W. Gerlach, Dirk Reuter, and Donat J. As: 'Germanium doping of Cubic $Al_xGa_{1-x}N$ Grown by Molecular Beam Epitaxy'. *Oral presentation.* 7th International Symposium on Growth of III-Nitrides (ISGN-7). Warsaw, Poland, 2018.

8. **Michael Deppe**, Tobias Henksmeier, Jürgen W. Gerlach, Dirk Reuter, and Donat J. As: 'Growth and Characterization of Germanium Doped Cubic $Al_xGa_{1-x}N$ Grown by Molecular Beam Epitaxy'. *Oral presentation.* 13th International Conference on Nitride Semiconductors (ICNS-13). Bellevue, WA, USA, 2019.

9. Elias Baron, **Michael Deppe**, Fabian Tacken, Martin Feneberg, Donat J. As, and Rüdiger Goldhahn: 'All-optical determination of free-carrier concentration and composition in cubic GaN and AlGaN'. *Poster presentation.* 13th International Conference on Nitride Semiconductors (ICNS-13). Bellevue, WA, USA, 2019.

Contributions to national conferences[1]

1. **Michael Deppe**, Jürgen W. Gerlach, Dirk Reuter, and Donat J. As: 'Germanium doping of cubic GaN'. *Oral presentation.* DPG Frühjahrstagung. Regensburg, 2016.

---

1 Presenting author is underlined

2. ELIAS BARON, MARTIN FENEBERG, RÜDIGER GOLDHAHN, **MICHAEL DEPPE**, and DONAT J. AS: 'Effective electron mass in cubic GaN'. *Oral presentation*. DPG Frühjahrstagung. Dresden, 2017.

3. **MICHAEL DEPPE**, JÜRGEN W. GERLACH, DIRK REUTER, and DONAT J. AS: 'Photoluminescence spectroscopy of Ge-doped cubic GaN'. *Oral presentation*. DPG Frühjahrstagung. Dresden, 2017.

4. **MICHAEL DEPPE**, JAN MUNDRY, FABIAN TACKEN, TOBIAS HENKSMEIER, JÜRGEN W. GERLACH, MARKUS BETZ, DIRK REUTER, and DONAT J. AS: 'Ge-Doping of MBE-Grown Cubic GaN and AlGaN Epilayers'. *Oral presentation*. 5th SFB/TRR142 Workshop. Bad Sassendorf, 2018.

5. **MICHAEL DEPPE**, FABIAN TACKEN, JÜRGEN W. GERLACH, DIRK REUTER, and DONAT J. AS: 'Structural and optical characterisation of germanium doped cubic $Al_xGa_{1-x}N$ grown by molecular beam epitaxy'. *Oral presentation*. DPG Frühjahrstagung. Berlin, 2018.

6. **MICHAEL DEPPE**, FABIAN TACKEN, TOBIAS HENKSMEIER, JÜRGEN W. GERLACH, DIRK REUTER, and DONAT J. AS: 'Optical and Electrical Properties of Germanium in Cubic $Al_xGa_{1-x}N$ Layers Grown by Molecular Beam Epitaxy'. *Oral presentation*. DGKK-Workshop 2018. Paderborn, 2018.

7. ELIAS BARON, **MICHAEL DEPPE**, FABIAN TACKEN, DONAT J. AS, MARTIN FENEBERG, and RÜDIGER GOLDHAHN: 'All-optical determination of free-carrier concentration and composition in cubic GaN and AlGaN'. *Oral presentation*. DPG Frühjahrstagung. Regensburg, 2019.

8. FELIX PASSLACK, MAHDI HAJLAOUI, STEFANO PONZONI, MIRKO CINCHETTI, THOMAS ZENTGRAF, DONAT J. AS, and **MICHAEL DEPPE**: 'Quantum well states of GaN/AlN studied by angle-resolved photoelectron spectroscopy'. *Poster presentation*. DPG Frühjahrstagung. Regensburg, 2019.

9. FELIX PASSLACK, MAHDI HAJLAOUI, STEFANO PONZONI, MIRKO CINCHETTI, THOMAS ZENTGRAF, DONAT J. AS, and **MICHAEL DEPPE**: 'Quantum well states of GaN/AlN studied by angle-resolved photoelectron spectroscopy'. *Poster presentation*. 6th SFB/TRR142 Workshop. Bad Sassendorf, 2019.

10. **MICHAEL DEPPE**, FABIAN TACKEN, JÜRGEN W. GERLACH, DIRK REUTER, and DONAT J. AS: 'Growth rate reduction of cubic III-nitrides at high doping levels in molecular beam epitaxy'. *Oral presentation*. DPG Frühjahrstagung. Regensburg, 2019.

Acknowledgments